In Silico Analysis of Flow and Dispersion in Ordered Porous Media

A thesis submitted in partial fulfilment of the requirements for the degree of

Doctor of Philosophy in Chemical and Process Engineering

University of Canterbury

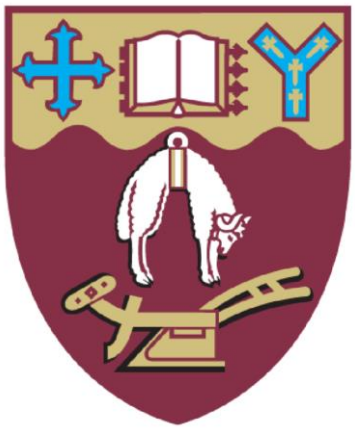

Written by

Fabian Dolamore

Department of Chemical and Process Engineering,

University of Canterbury,

Christchurch, New Zealand

2017

Abstract

The work herein investigates exciting new prospects for practical chromatographic systems which may be achieved using the rapidly evolving technology; three-dimensional printing. Previous studies in the literature have suggested that ordered chromatographic media can provide advantages over the traditional randomly packed column, an idea which is elaborated upon in this work. Numerical modelling coupled with high performance computing was used to investigate flow in ordered porous media via the Lattice Boltzmann method, to simulate the propagation and dispersion of solute species within these systems. Practical chromatographic metrics were derived from this model and used to contrast various media and analyse practical chromatographic phenomena.

There are four distinct bodies of work presented in this thesis. The first illustrates the chromatographic performance of ordered packed beds when using several different particle shapes, in various structural configurations. This chapter also highlights the influence of flow tortuosity in ordered packings and how this variable can be used to estimate system performance. The second focus is “wall effects” in confined ordered packing and how this detrimental phenomenon can be mitigated using “embedded” column walls, a prospect made possible via three-dimensional printing. The penultimate chapter considers ordered monolithic structures, more specifically, triply periodic minimal surfaces (TMPS) and a range of manipulations which can be used to optimise chromatographic performance of these structures. The fourth chapter further develops the model to observe full chromatographic separations by defining a permeable stationary phase and including adsorption and desorption behaviour of the solute species in the presence of an eluent. This facilitated systematic studies of practical chromatographic variables and laid the foundations for future work, using this model.

UNIVERSITY OF CANTERBURY
Te Whare Wānanga o Waitaha
CHRISTCHURCH NEW ZEALAND

Deputy Vice-Chancellor's Office
Postgraduate Office

Co-Authorship Form

This form is to accompany the submission of any thesis that contains research reported in co-authored work that has been published, accepted for publication, or submitted for publication. A copy of this form should be included for each co-authored work that is included in the thesis. Completed forms should be included at the front (after the thesis abstract) of each copy of the thesis submitted for examination and library deposit.

Please indicate the chapter/section/pages of this thesis that are extracted from co-authored work and provide details of the publication or submission from the extract comes:

Section 3.2 of this thesis contains work which is currently under review for the Journal of Chromatography A "Modelling Ordered Packed Beds of Spheres: The Importance of Bed Orientation and the Influence of Tortuosity on Dispersion" – Authored by Fabian Dolamore, Conan Fee and Simone Dimartino

Please detail the nature and extent (%) of contribution by the candidate:

All simulation work and first authorship was completed by the candidate. Revision and refinement of the work is attributed to the other authors.

Certification by Co-authors:

If there is more than one co-author then a single co-author can sign on behalf of all

The undersigned certifys that:

- The above statement correctly reflects the nature and extent of the PhD candidate's contribution to this co-authored work
- In cases where the candidate was the lead author of the co-authored work he or she wrote the text

Name: *Simone Dimartino* Signature: 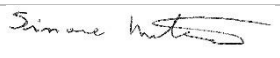 Date: *13-11-2017*

Acknowledgements

First and foremost, many thanks to my supervisory team: Prof. Conan Fee and Dr. Simone Dimartino for their invaluable knowledge, support and guidance through this project. It has been a great experience to work with you both.

Many thanks to the Ministry of Business, Innovation and Employment (New Zealand) for funding this project and the New Zealand eScience Infrastructure for supplying computational resources.

Thanks to Dr. Francois Bissey and Dr. Daniel Lavagra for their programming expertise and advice and Dr. Dimitrios Kontaxakis and Dr. Jonas Latt from Flowkit Ltd. for their support on the Palabos Library.

Thank you to my friends and family who have always shown their love and support throughout my academic endeavours. Most notably my mother, Dr. Barbara Dolamore, who is always able to provide insightful perspective on an array of matters.

I owe much of my success to the Garreg Road High Performance Centre.

Hannah, for her love and support and Maisie, for her excellent ball fetching abilities.

Table of Contents

Nomenclature

Variables in this thesis are listed below, in alphabetical order. Units are represented as Length [L], Mass [M], Time [T] and Amount (used for mol) [N]. Dimensionless variables have no stated units.

Roman alphabet

a, b, c, d, e, f	TMPS level-set constants	
a_c	Geometric channel shape factor	
A	Eddy dispersion coefficient	
A_c	Column cross sectional area	$[L^2]$
A_p	Wetted surface area	$[L^2]$
B	Axial Diffusion coefficient	
B_d	Displacement matrix	
c	Concentration	$[NL^{-3}]$
c_{CK}	Carman-Kozeny constant	
c_d	Drag coefficient	
c_i	Quadrature point	
c_s	Lattice speed of sound	
C	Mass transfer resistance	
$C(f)$	Collison term	
C_{ads}	Concentration of adsorbed species	$[NL^{-3}]$
C_{aq}	Concentration of solute in solution	$[NL^{-3}]$
C_{eluent}	Concentration of eluent species	$[NL^{-3}]$
C_{max}	Amplitude of the concentration pulse	$[NL^{-3}]$

C_o	Capacity of the stationary phase	$[NL^{-3}]$
$\bar{C}$	Average concentration of slice	$[NL^{-3}]$
d	Characteristic Length	[L]
d'	Distance between capillary centres	
d_c	Circumdiameter	[L]
d_{col}	Column diameter	[L]
d_p	Particle diameter	[L]
D	Number of dimensions in the LB model	
D_{axial}	Axial diffusion coefficient	$[L^2T^{-1}]$
D_m	Molecular diffusivity	$[L^2T^{-1}]$
D_{lb}	Molecular diffusivity (Lattice units)	
D_{pore}	Pore diffusion coefficient	$[L^2T^{-1}]$
D_{ref}	Reference diffusion	$[L^2T^{-1}]$
D_{TRT}	Diffusion coefficient for TRT LBM	$[L^2T^{-1}]$
$\widetilde{D}$	Diffusion deviation term	$[L^2T^{-1}]$
E	Separation Impedance	
f_i^{in}	Incoming lattice populations	
f_i^{out}	Outgoing lattice populations	
$f(x, \xi, t)$	Probability density function	
F	Body force term	$[MLT^{-2}]$
$F(s)$	Weierstrass–Enneper parameter	
F_d	Drag force	$[MLT^{-2}]$
F_i	Equilibrium density function	

g	Distance Function	
$G(s)$	Weierstrass–Enneper parameter	
h	Reduced Plate Height	
$HETP$	Theoretical Plate Height	[L]
H_w	Plate height of wall effect	[L]
k	System permeability	[L^2]
k_{ads}, k_{des}	Rate constant of adsorption/desorption	[L^3T^{-1}]
L_c	Length of the unit cell	[L]
L_p	Distance between particle centres	[L]
L_x, L_y	Transverse column lengths	[L]
L_z	Axial column length	[L]
n_p	Number of primary particles	
n_s	Number of spheres per unit cell	
N	Number of nodal points	
P	Periodic length of spring	
Pe	Peclet number	
Ps	Pressure	[$ML^{-1}T^{-2}$]
Q	Number quadrature points in the LB model	
Q_s	Source/sink term	[$NL^{-3}T^{-1}$]
Q	Volumetric flow rate	[L^3T^{-1}]
r	Level set porosity parameter	
r_p	Particle radius	[L]
r_{rxn}	Rate of reaction	[NT^{-1}]

R	Coil parameter of spring geometry	
R_c	Channel radius	[L]
Re	Reynolds number	
Rot	Rotational matrix	
R_x	Spatial resolution	
$\Re$	Real part of integral	
S	Collision matrix for MRT LBM	
S'	Bonnet transformation	
Sc	Schmidt number	
t	Time	[T]
t_i	Lattice weighting	
t_o	Dimensionless time	
T	Flow tortuosity	
T_{pore}	Pore tortuosity	
u	Local velocity	$[LT^{-1}]$
u_a	Advection velocity	$[LT^{-1}]$
u_d	Diffusion velocity	$[LT^{-1}]$
u_{sup}	Superficial velocity	$[LT^{-1}]$
u_z	Axial velocity component	$[LT^{-1}]$
$\bar{u}$	Average channel velocity	$[LT^{-1}]$
V	Empty column volume	$[L^3]$
V'	Dimensionless volume	
V_n	Normalized volume	

V_p	Particle volume	[L^3]
$x(x, y, z)$	Particle position vector	[L]
x, xo, y, yo, z, zo	lattice co-ordinates	

Greek alphabet

α_c	Volumetric fraction of bulk column flow	
α_w	Volumetric fraction of wall flow	
α_{lb}	Thermal diffusivity (lattice units)	
β	Particle overlap	
δ	Width of the wall flow zone	[L]
δ_c	Constrictivity	
δ_t	Time conversion factor	[T]
δ_x	Length conversion factor	[L]
Δv	Difference between column and wall velocity	[LT^{-1}]
ε	Interparticle porosity	
ε_c	Porosity of the bulk column packing	
ε_w	Porosity of the wall packing	
ε_t	Effective transport porosity	
θ	Angle of rotation	
κ	Desorption driving force	[NL^{-3}]
λ_e, λ_o	TRT relaxation parameters	
μ	Mean residence time of an RTD curve	[T]
ν	Kinematic viscosity	[L^2T^{-1}]

ν_{lb}	Kinematic viscosity (lattice units)	
$\xi(\xi x, \xi y, \xi z)$	Particle velocity vector	$[LT^{-1}]$
ρ	Fluid density	
σ^2	Variance of an RTD curve	$[T^2]$
Φ_b	Bonnet angle	
χ	Particle to diameter ratio	
ψ_{lb}	Lattice diffusive parameter (lattice units)	
Ψ	Sphericity	
ω	Collision operator	

List of Abbreviations

3D	Three-Dimensional
ADE	Advection Diffusion Equation
BB	Bounce-Back
BGK	Bhatnagar-Gross-Krook
CAD	Computer Aided Design
CFD	Computational Fluid Dynamics
CCS	Circular Cross-Section
DNS	Direct Numerical Simulation
FLOP	Floating Point Operation
HPC	High Performance Computing
IEC	Ion Exchange Chromatography
LB	Lattice Boltzmann
LBE	Lattice Boltzmann Equation
LBM	Lattice Boltzmann Method
LC	Liquid Chromatography
MRT	Multiple Relaxation Time
MPI	Message Passing Interface
MSUPS	Mega Site-Updates Per Second
NS	Navier-Stokes
PDF	Probability Density Function
RPC	Reverse Phase Chromatography

RTD	Residence Time Distribution
SCS	Square Cross-Section
SRT	Single Relaxation Time
TPMS	Triply Periodic Minimal Surfaces
TRT	Two Relaxation Time

Stationary Phase Morphologies

BCC	Body-Centred Cubic
DDS	Double Discrete Spring
DG	Double Gyroid
DP	Double Primitive
FCC	Face-Centred Cubic
SC	Simple Cubic
SD	Schwarz Diamond
SG	Schoen Gyroid
SP	Schwarz Primitive

Introduction

Porous media has an important role in both natural and artificial environments; from aquifers containing fresh ground water, to catalytic beds in large chemical processes. These systems comprise a solid and fluid phase which mediates highly laminar flow systems within the internal pores of the medium[1]. Each phase plays an important role in the duality of porous media, the fluid phase is where complex transport phenomena occur, while the solid phase has direct influence on the velocity field of the mobile phase and maintains the structural integrity of the system. Moreover, in the context of artificially manipulated media, the solid phase can be customized to have functionality which promotes chemical phenomena, such as: ion exchange, catalysis or reaction.

The applications of such systems in industrial settings naturally leads to the need for performance optimization, that is, the aim to increase system efficiency. Ultimately, there are two major concerns for process optimization: cost and time, however, in practice, these factors can be complex functions of multiple other process variables which are difficult, or even impossible, to optimize simultaneously[2, 3]. This work focuses on optimization of chromatographic systems, by reducing dispersion via manipulation of the solid phase morphology, which is directly beneficial to increasing the performance of liquid chromatography systems.

Liquid Chromatography (LC) is a unit operation which is used in both analytical and commercial systems as a method of solute separation[4, 5]. There are multiple variates of LC, including: ion exchange, size exclusion and affinity chromatography, each with a unique mechanism but all encountering the negative effects of dispersion. Dispersion is a naturally occurring phenomena and is the result of both molecular diffusion and advective transport of a solute in a liquid phase. This phenomenon impacts chromatographic systems by causing an effect known as “band-broadening” which reduces chromatographic performance by elongating the elution profile of the solute species and decreasing peak resolution[1, 4, 6]. This is an undesirable trait of a chromatographic media, because the chromatographic resolution determines the amount of column length/time to separate two or more chemical species.

It is hypothesized that the morphology of the stationary phase plays a critical role in controlling dispersion in the mobile phase, making this an important decision in selecting a chromatographic media. In the natural world, porous media is random, due to the chaotic nature and lack of control in formation processes[7, 8]. In fabrication of porous media, this same lack of control has led to manufactured packings suffering from random internal structures[9-11]. However, with the ongoing technological advancements in additive manufacturing, or more specifically, three-dimensional printing, a new level of control can

be applied to fabricating not only chromatography columns[12, 13], but other porous media applications, such as: filtration and heat exchange operations. The ability to create ordered packings with specifically designed flow channels in conjunction with a chemically purposed solid phase has the potential to create a large paradigm shift in the generation of porous media, with potential follow-on effects in various areas of analytical and commercial development. There has been previous simulation based work that has shown promise for ordered packing structures to provide benefit in these systems by minimizing dispersion[14]. These previous findings in the literature, coupled with the novel ability to feasibly produce these structures, promoted further investigation into ordered porous media, resulting in the findings of this thesis.

To understand the intricacies of such complex systems, computational fluid dynamics (CFD) was used as a tool to model and analyse flow phenomena, which are not able to be easily measured in real world systems. CFD works on the idea that fluid flow may be modelled using fundamental principles which are culminated into governing equations, better known as the Navier-Stokes (NS) equations[15-17]. These equations have been well studied and are known to provide accurate imitations of real world fluid systems, however, like all models, NS methods have certain limitations. The focus of this work is porous media, which is loosely defined as having equal or greater solid volume compared to the void volume[18]. These void spaces are distributed through the solid network, implying that there is a high amount of surface area within a given system, something that classical NS methods may struggle with due to computational intensity of boundary layer models[19-21].

A relatively new CFD technique, the Lattice Boltzmann Method (LBM), however, excels in this setting, because of its natively simple way of handling fluid/solid boundary conditions. This method takes a different approach to solving the same fundamental principles as NS, but from a different conceptual standpoint. The LBM is essentially a discretization of the Boltzmann Equation and uses elastic collisions of hard ball particles to model fluid behaviour, like the concept of Brownian Motion[22, 23]. From this basis, a probability density function (PDF) is calculated and all macroscopic variables are calculated as moments from this PDF and hence, phenomenological relations are not required. Although the LBM is relatively new method in the history of CFD, it has become an attractive alternative to NS when dealing with specific fluid systems, as it does not require complex meshing algorithms during pre-processing to achieve sufficient simulation accuracy. Instead, the LBM generally uses a homogeneous mesh, defining points as either solid or fluid and handling the interface between these points in a very simple, yet effective manner, eliminating the requirement of complex boundary layer models[24, 25]. Furthermore, all LBM calculations are performed locally and hence lend themselves well to parallel computing because of the simplicity in which a large domain may be fractured into smaller CFD problems which have little dependency on each other[26].

To harness the LBM, a front-end model was developed using Palabos (Flowkit Ltd, Lausanne, Switzerland) an open source C++ library, which solves complex CFD systems which can be coupled with other physical phenomena, such as dispersion. In fact, the first order LBM can be used directly to solve the advection-diffusion equation using a recently developed modification[27]. Palabos has been validated and benchmarked against widely accepted CFD software and is a powerful tool with a large potential for complex simulation in which multiple variables (velocity, temperature, pressure, etc.) can be solved simultaneously. To run the simulations which produced the results presented in this thesis, a variety of computing systems were used. Small simulations (~500,000 simulations points) could be run on several processors of a standard desktop computer in a matter of hours, however, large simulations (> 10,000,000 simulations points) were run using HPC systems to provide more memory and speed and complete simulations in a reasonable time frame (< 24 hours).

The first section of work in this thesis, Chapter 3, looks at ordered packed beds and elaborates on the work by Schure et al.[14] which investigates dispersion in random and ordered sphere packings. It is then shown that simply changing the orientation of the packing to the axial flow direction can provide substantial performance increase without altering the permeability of the system. The concept of spherical particles being the ideal for packed beds is then challenged by investigating alternative particle geometries, specifically octahedrons and tetrahedrons. Finally, in practical systems, it is suspected that ordered packed beds would be prone to column deformation, because of the limited physical contact between nearest neighbours. To reduce this concern, the concept of overlap was introduced which gradually blends the discrete particles in to a continuous, monolithic, structure. This provides dual benefit in chromatographic systems by increasing structural integrity of the bed and increasing column capacity.

Chapter 4 considers a more practical aspect of chromatography, wall effects. In practice, columns are contained by cylindrical walls to contain the mobile phase. However, this increases voidage at the column walls because of geometric constraints and causes channelling in the cross-sectional velocity profile. This is a well-studied issue for randomly packed columns[28-30], but its impact is unknown for confined ordered packings. From the work of Broeckhoven and Desmet[31, 32] the wall effect has a short and long-term effect, analogous to Taylor dispersion in a capillary[33]. For much of this chapter, only the short-term limit is observed because of the limitations of the computational power available to this work. Wall effects are quantified in this work for FCC packing of spheres confined by square cross section walls. The column diameter to particle diameter ratio was varied, to control the ratio of wall flow to bulk flow areas in the column and to observe the effect on the overall dispersion of the column for the short time limit. To mitigate this effect, 3D printing can be used to print particles into the walls themselves, thus eliminating the low porosity zones. These columns were identical to the initial square walled columns, except that partial spheres were embedded into the walls themselves as

if the packing was periodic in the transverse directions. To compare these findings to “real” columns, cylindrical columns with embedded walls were simulated and compared to the square cross section columns to show how this technique of embedded columns walls influences the magnitude of wall effects in a packed column.

Given new levels of manufacturing control, column fabrication is no longer restricted to using discrete particles to create a porous medium which led to the development of ordered monolithic structures (Chapter 5). The focus of this chapter is Triply Periodic Minimal Surfaces (TPMS), which minimize surface area for a continuous 3D volume. There are many TPMS structures[34, 35], many of which may be defined in Cartesian space by a level-set approximation[36]. These TPMS structures were characterised for flow and dispersion properties and compared with ordered particle packings. To further investigate the potential of TPMS structures, Schwartz Primitive was used as a test case for numerical (and consequently, geometric) manipulations of the TPMS structures to further reduce dispersion in these structures. Finally, investigation of the flow channels in the efficient TPMS structures led to the design of straight channel and spiral shaped flow channels, in which, the design focus was on the flow channels through the medium, as opposed to the stationary phase.

In the final section of work (Chapter 6), the model was further developed to incorporate a secondary porosity in the stationary phase, as observed for real chromatographic media. This secondary porosity is known to severely reduce chromatographic performance by increasing mass transfer resistance as defined by van Deemter’s analysis[6]. Subsequently, adsorption/desorption behaviour of the solute species onto the surface of the pores in the stationary phase was added to the model, thus simulating complete chromatographic simulations. In this context of these simulations, three solute species were simulated, the: inert (non-binding), selected (binding) and eluent (preferential binding) species, modelling a very simple chromatographic separation. Three variables of practical chromatography and their impact on performance were investigated using this new model: eluent concentration, stationary phase morphology and Peclet number. This new model creates new possibilities for modelling the chromatographic process and further optimization of practical systems.

1. Literature Review

1.1 Preface

This work explores solute dispersion in ordered porous media by analysing flow and mass transport metrics derived from computational fluid dynamics simulations, using the Lattice Boltzmann Method. Dispersion describes transport and dilution of a solute species via natural molecular movement and influence of an imposed velocity field and can be detrimental to the performance of some mass transport systems, such as liquid chromatography. The intention of chromatographic systems is to achieve the separation of one or more solutes through either: selective interaction with the stationary phase or interaction with pore networks within the stationary phase with a known size distribution. The performance of such processes is critically affected by the flow patterns of the mobile phase because dispersion increases the time and length scales required to reach sufficient chromatographic resolution between solute peaks.

The practical chromatographic separation of solutes is almost universally carried out in columns comprising randomly packed beds of adsorptive particles. However, it has been shown through numerical studies that ordered packings have the potential to improve performance over random packings, by homogenizing the distribution of path lengths which are present in a random medium and reducing eddy dispersion. It is the aim of this work to prove that chromatographic performance of ordered porous media can be further improved from ordered sphere packings by using: alternative particle shapes or ordered monolithic structures. To supplement these purely morphological optimizations, more practical concerns, such as: wall effects and adsorption/desorption of the solute species and their impact on chromatographic systems were characterised and mitigated.

1.2 Porous Media

A material that is described as porous is characterised by many small passages or channels, known as void space, within a solid matrix. Fig. 1.1. shows simple two-dimensional representations of porous media as an introductory visualization of the internal structure within these systems. However, real porous media exist in three dimensions, thus creating highly complex and intricate networks of pores that can be difficult to comprehend from a geometric perspective. For practical purposes, these pores allow fluid flow through the solid matrix, but because the channels are generally small and tortuous, these flow systems are highly laminar, because of the low permeability of the substrate[18].

Porous media exist naturally, but are also specifically manufactured to perform a variety of niche roles in engineering and medical applications[37].

A common factor in all porous media is the random nature of the void spaces, caused by uncontrolled fabrication processes[37]. For flow systems, this randomness correlates to irregular flow patterns, leading to the necessity of models to predict flow variables in these systems, such as Darcy's Law, the Ergun equation and the Carman-Kozeny equation[38]. Furthermore, disorder increases dispersion in mass transport systems by creating a diverse array of flow channel shapes and lengths, degrading the efficiency of the mass transport processes, such as chromatography. This leads to the question of whether ordered systems would perhaps be more efficient, because of the predictable flow channels and homogenization of path lengths.

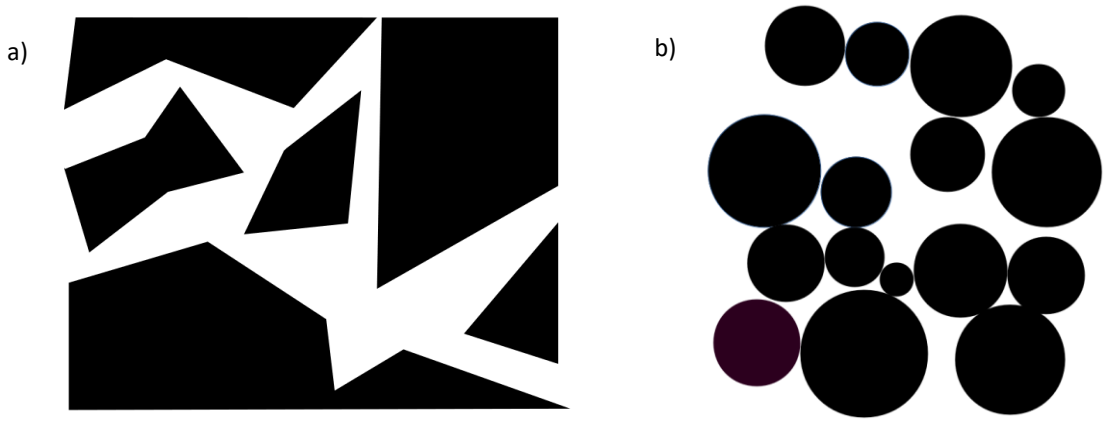

Figure 1.1 A two-dimensional illustration of a porous medium using a) random irregular polygons and b) spheres with an unknown size distribution. The dark areas represent solid material, while the white spaces in between represent the void space in which fluid flow may occur.

1.2.1 Natural Porous Systems

Natural porous media include non-living systems such as, soils and rock formations as well as biological structures such as animal tissues and bones[7, 39]. In natural systems, porous materials allow fluid flow and retention through their structurally rigid matrix, combing beneficial properties of both the solid and liquid phases. These properties are important as they both promote transport of soluble materials within their structure, while still retaining them[40]. For example, aquifers are made of porous rock and aggregate particles and retain groundwater below the water table, making them an important source of fresh water. Soil systems allow for water transport and retention of rainwater, which acts as a transport mechanism for important soluble minerals in this environment, such as their role in the nitrogen cycle[41]. In internal biological systems, organisms have evolved to harness the benefits of porous media, such as the controlled transport of proteins, minerals and other important nutrients through tortuous and porous networks is necessary to provide cells with the required materials to

perform their functional tasks. Bones are porous, allowing mass transport through the solid matrix, but also to reduce the weight of the bone, while maintaining structural strength[42].

Perhaps the most relevant natural porous media to this work are zeolites, a wide family of micro-porous aluminosilicates[8]. These materials are crystalline and are created by the interaction of volcanic material with an alkaline water source. Zeolites are renowned for their natural ability to exchange ions, making them an important natural regulator of chemical species and a precursor to modern chromatography and ion exchange.

1.2.2 Fabricated Porous Media

Fabricated media are created by manipulating materials to incorporate the characteristic void spaces into their structure. These materials are used in a wide range of applications in modern technology, including, but not limited to:

- Metal foams - heat exchange, force adsorption and catalytic systems[37]
- Ceramics - structural materials, heat resistance[43]
- Polymer foams – Low density, malleability, biological functionalization[44]

In the context of this work, these materials can be used to create important flow systems such as: catalytic beds, filters and chromatographic media (further explained in Section 1.3.1). These are examples of porous systems which can be used in conjunction with other chemical phenomena (adsorption and reaction) to provide important functionality for modern processing applications. Fabrication processes and the implications of said processes are further discussed in Section 1.4.1.

1.2.3 Ordered Porous Media

In 2004, Schure et al.[14] pioneered a theoretical study, using computational fluid dynamics (CFD) to analyse dispersion in ordered sphere packings, showing advantages over random jammed packing of spheres, which are regarded as an efficient medium in modern chromatography[45]. However, because of the difficulty of producing and maintaining the internal morphology of these ordered sphere packings coupled with the large pressure drop of the most efficient ordered packings, it was conjectured that this avenue of research was not feasible for practical use. Unfortunately, further investigation into ordered packings following from this research has been rare and only very recent[13, 46], perhaps stemming from current manufacturing limitations.

Congruent to the re-emergence of this research, the area of three-dimensional (3D) printing, or additive manufacturing, has gained major traction in the fabrication industry and has been the subject of rapid technological advancement[47]. This technological acceleration has renewed the idea of ordered

packings in porous media systems, as it has been proven that fabrication of these structures is achievable[13]. In this thesis, the functional application of the geometric optimizations is specifically applied to solute dispersion and chromatography. However, it is important to note that the investigated behaviours are transferable to other applications of porous media, such as heat exchange [48], perhaps making this work relevant beyond the intended scope.

1.2.4 Flow in Porous Media

Flow through porous media is studied across multiple scientific fields, including: soil science, groundwater flow and filtration[49]. Because the geometry of such systems is complex, analysis requires empirical correlations to describe the relationship between the pressure drop and rate of flow through the medium. Famously, Henry Darcy pioneered analysis of flow through porous media via his experimental findings, which culminated in the formulation of Darcy's Law (Eq. (1.1))[50]

$$-\frac{dP}{dZ} = u_{sup}\frac{\nu\rho}{k} \tag{1.1}$$

where dP/dZ is the pressure differential between two axial points in the medium [$ML^{-2}T^{-2}$], u_{sup} is the superficial linear flowrate of fluid [L^3T^{-1}], k is the permeability [L^2], ν is the kinematic viscosity [L^2T^{-1}] and ρ is the density of the fluid [ML^{-3}]. However, this expression is limited by the fact that the permeability of a specific medium must be determined experimentally and is not tied to characteristic features of the medium.

The Carman-Kozeny equation does not include the permeability term and was developed specifically for packed beds of particles[51-53]. The permeability variable from Darcy's law is replaced by a group of terms which are based on the packing efficiency and particle shape (Eq. (1.2))

$$-\frac{dP}{dZ} = u_{sup}\frac{c_{CK}\nu\rho}{\Phi^2 {d_p}^2}\frac{(1-\varepsilon)^2}{\varepsilon^3} \tag{1.2}$$

where c_{CK} is an empirical co-efficient (equal to either 150 or 180), Φ is the sphericity of particles in the bed, d_p is the characteristic particle diameter [L] and ε is the system porosity. Hence the pressure-drop of a given medium can be determined by analysing the particle shape and how these particles pack with each other, as opposed to using experimental data to calculate the permeability of a medium.

The Carman-Kozeny equation is only valid for laminar flow profiles, which is commonly observed for porous media flows, especially in natural systems. However, turbulent flow is seen in applications such as packed bed reactors involving gas species, where the onset of turbulent flow occurs at much lower flow rates because of small viscous forces in the mobile phase. In these cases, the Carman-Kozeny equation can be extended to the Ergun equation[54] (Eq. (1.3)).

$$-\frac{dP}{dZ} = u_{sup}\frac{c_{CK}\nu\rho}{{d_p}^2}\frac{(1-\varepsilon)^2}{\varepsilon^3} + {u^2}_{sup}\frac{1.75\rho}{d_p}\frac{(1-\varepsilon)}{\varepsilon^3} \quad (1.3)$$

The first term gives the laminar contribution to the pressure drop, while the second term gives the turbulent contribution. It is important to note that the standard Ergun equation does not include a sphericity term and is only used for packed beds of spherical particles, though there has been work which extends the Ergun equation for non-spherical particles[55, 56]. For systems in this work, the turbulent regime is not explored because chromatographic systems are operated at *Re < 1*.

When mass transport phenomena are coupled with flow in porous media, the analysis becomes more complex than the relationships described in this section. Taylor and Aris authored some of the earliest works which deal with dispersion in porous media systems, mostly dealing with the long-time limit solutions[57, 58]. With the constant increase in computational capabilities, the field of computational fluid dynamics (CFD) has become popular for producing accurate modelling of mass transport systems. The Lattice Boltzmann Method approaches CFD as a statistical description of particle motion and can be used to solve the flow field and dispersion behaviour in a simple decoupled model[27, 59, 60]. The advantage of CFD over analytical techniques is that the CFD can be applied to any column morphology, while in analytical methods any alteration of the morphology results in the model having to be adjusted.

1.3 Chromatography

Chromatography is a process which is used to separate a single, or multiple, chemical species from a given solution or mixture and is integral in both industrial and academic settings as a preparative or analytical method[4]. Chromatography causes a chemical or physical separation without requiring expensive heat energy, which occurs in processes such as distillation, making it suitable for heat-sensitive materials such as proteins[61]. A basic chromatographic system comprises a “mobile” and “stationary” phase. The mobile phase corresponds to the fluid in the pores of the medium and contains one or more chemical species that are the target of the separation process, while the stationary phase has characteristics which enable the separation process through either chemical or physical interaction(s) with the target solute(s).

Chromatographic systems can use various phase combinations, depending on the chemical species that are to be separated[1]. Gas-liquid, gas-solid, liquid-liquid and liquid-solid are all viable chromatographic phase combinations, in which, the less dense phase is defined as the mobile phase. This work focuses specifically on liquid-solid chromatography (LC), a method which generally uses an aqueous solution as the mobile phase and a packed bed of particles, as the stationary phase[1], which aligns with our definition of a porous medium.

Chromatographic systems are operated in the Stokes flow regime ($Re << 1$), a special case of laminar flow in which the velocity profile linearly scales proportionally to the superficial velocity of the system[15]. This is because the flow rate required to achieve optimal chromatographic performance for a given column satisfies the Stokes flow condition (discussed in Section 1.6.1). Additionally, high flow rates will impart high back pressures which can cause deformation of the stationary phase, thus creating a reduction in flow and loss of chromatographic efficiency[62]. The Stokes flow condition implies that the stationary phase dictates the flow profile of the mobile phase, because the inertial forces of the fluid are negligible compared to the viscous dampening. Hence, the morphology of a chromatographic directly affects the magnitude of dispersion in the mobile phase during the chromatographic process, which is directly related to column efficiency[63, 64].

For the systems investigated in this work, it is assumed that the stationary phase is rigid, because adding deformation behaviour adds extra complexity to the model. Though, it is noted that this would be an important area of study via both numerical and practical means.

1.3.1 Liquid Chromatography

Within LC, there are five distinct separation methods: ion exchange, affinity, reverse phase, hydrophobic interaction and size exclusion[4]. Each method has a distinct mechanism that causes the chromatographic process to occur, which provides a range of options when deciding how to best perform a desired separation. The first four methods use non-covalent chemical interactions between the solute species and the stationary phase to perform separations, whereas size exclusion chromatography uses physical means[65].

In chemical separations, once the selected species (analyte) is bound and the other species have exited the column (the effluent), the species must be unbound and sequestered, to complete the separation. This is achieved by using an elution step, in which, mobile phase conditions are manipulated to unbind the selected species using an eluent[66]. Common types of eluent involve manipulation of pH or introduction of a component with a higher affinity for the solid phase and/or higher mobility. When the analyte is unbound from the stationary phase, it is eluted from the column via the same advection and diffusion mechanisms as the effluent.

Dispersion affects practical chromatography by extending the amount of time which significant portions of the effluent and analyte are retained within the column, thus increasing the total amount of time required for the chromatographic process. The aim of reducing dispersion in these systems directly contributes to shortening the process time required for LC and minimizing costs associated with this process.

Ion Exchange

Ion exchange chromatography (IEC) uses charged functional groups to adsorb oppositely charged species from the solution. Ion exchangers are categorized by two variables, charge and strength[67]. Ions can either be positively (cationic) or negatively (anionic) charged, hence the respective exchanger has the opposite charge to its ionic counterpart. Secondly, the exchanger can be defined as solid or weak, much like an acidic or alkaline species[68]. Strong exchangers maintain their charge over the entire pH scale, whereas weak exchangers have a certain pH range over which they may be used or the risk of unbinding the solute becomes a factor. The benefit of weak exchangers, however, is the greater specificity they provide when targeting a certain solute for binding[69]. Common eluents for IEC are high concentration of salts or factors which alter pH (acidic or basic species).

Affinity

Affinity chromatography is commonly used for biological and pharmaceutical separations[70]. The target species in affinity separations has a specific type of binding which is unique for that solution, for example, a nucleic acid that binds to its complementary base pair could be separated from other nucleic acids[71]. This method provides highly specific selectivity but can require expensive ligands and is not suitable for high chromatographic throughput. Affinity chromatography is a highly specific and versatile method because of the variety of functional groups that may be selected for the affinity media. Elution from an affinity medium requires a species which has higher affinity to the medium than the selected species, giving preferential binding to the eluent.

Reversed Phase

For “normal phase” chromatography, the stationary phase is a hydrophilic substrate which binds hydrophilic substrates from the mobile phase by providing greater attraction that the solvent species. In “reversed phase” chromatography (RPC), the substrate has a hydrophobic functionality, while the mobile phase is polar. Therefore, the stationary phase attracts the more hydrophobic solutes, while the hydrophilic species are eluted first[4]. Reversed phase chromatography uses highly non-polar organic solvents for elution.

Hydrophobic Interaction

The stationary phase is functionalized with hydrophobic (non-polar) functional groups and the mobile phase contains high salt concentration. The hydrophobic groups of the solute molecules interact with the mobile phase. This technique is differentiated from RPC by having weaker hydrophobic interactions between the stationary phase and substrate and hence elution can be performed using a salt gradient, instead of harsher species which may degrade the substrate or stationary phase[72].

Size Exclusion

Size exclusion is the only isocratic technique presented here, meaning that there is no interaction between the solute and the stationary phase or chemical manipulation of the mobile phase to achieve separation. Instead, this method separates solute species based on their molecular size[73]. The matrix of a size exclusion medium has a distribution of pore sizes. Species which are small enough to fit into the smallest channels follow a highly tortuous path and spend a relatively long period of time in the column, while the large particles are excluded from these pores and hence are eluted from the column first, hence requiring a greater amount of time to elute from the column[65]. This method requires no chemical alteration of the sample, which is a benefit for samples which are sensitive to certain factors, such as pH. Species which have similar chemical functionality can be separated via this method, but conversely, separations of similar sized molecules do not occur.

1.3.2 Efficiency in Practical Chromatography

A common method of measuring efficiency in a practical chromatography column, is known as tracer study[74]. A tracer study is performed by injecting an inert species, known as a "pulse", into a column, which is modelled as a Dirac Delta Function, with a mean and variance of zero[75]. This pulse of tracer is transported through the column and is affected by a phenomenon known as dispersion. Dispersion occurs via two methods[33, 76]: advection, from the movement of the bulk flow of the mobile phase and molecular diffusion, which is caused by the random walk of particles (Brownian Motion) and describes how a solute is transported in a solution (further discussed Section 1.5). As the pulse moves through the column, dispersion causes the Dirac Function to "broaden" and become a Gaussian-like curve, known as a residence time distribution (RTD) or E-curve[77] (Fig. 1.2).

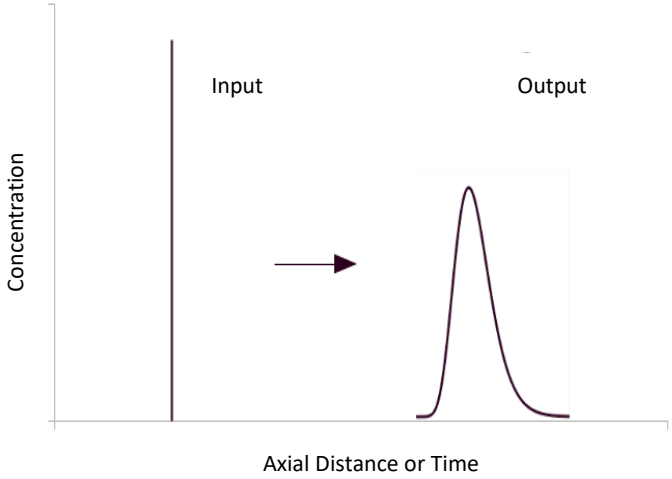

Figure 1.2. Illustration of band-broadening of the Dirac Pulse input into a Gaussian peak as the tracer moves through a column. This broadening causes inefficiency in the chromatographic process by increasing solute time spent in the column and dilution of the analyte.

Band-broadening increases the width and decreases the height of the RTD curve, which negatively effects column performance by both, increasing the amount time required for the solute to exit the column and diluting the solute species. For a chromatographic separation to be considered successful, the solute peaks should achieve baseline separation (Fig. 1.3), otherwise there is a period in which the analyte and effluent species are eluted together, reducing the analyte purity[77]. If the solute peaks are not resolved, the process must be altered by either: selecting a more optimal system flow rate, creating a longer column or delaying the introduction of the eluent species into the column[4].

To quantitatively analyse band-broadening, the concept of the height equivalent to the theoretical plate (*HETP*) is introduced. This value has been adapted from distillation processes and, although it has no direct physical meaning in a chromatographic setting, it is commonly used as a measure of column efficiency or band broadening[1]. It is mathematically defined as the ratio of the product of the standard deviation of an RTD curve and the axial distance travelled to the square of its mean residence time in the column. It is more commonly expressed in its dimensionless form, *h*, known as the reduced plate height (Eq. (1.4)).

$$HETP = \frac{\sigma^2 L_z}{\mu^2} \tag{1.4a}$$

$$h = \frac{HETP}{d} \tag{1.4b}$$

where, σ^2 is the standard deviation of the RTD curve [T^2], L_z is the axial length of the column [L], μ is the mean residence time of the RTD curve [T] and *d* is characteristic length of the system [L]. The mean and variance of the RTD curve are calculated using the method of moments (Eq. (1.5))[75].

$$\mu(t) = \int_0^\infty c\, t dt \Big/ \int_0^\infty c\, dt \tag{1.5a}$$

$$\sigma^2(t) = \int_0^\infty c\, (t-\mu)^2 dt \Big/ \int_0^\infty c\, dt \tag{1.5b}$$

where *t* is the time scale [T] and *c* is the scalar concentration [NL^3]. In practice, these integrals are solved numerically using the trapezoidal rule[78]. In an ideal chromatographic system, the HETP would be zero, meaning that band-broadening had not occurred during mass transport through the column. However, as diffusion occurs in any system where the solute is not in equilibrium, this is not possible in the current paradigm of chromatography. The goal is instead to minimize the reduced plate which allows for higher throughput for chromatographic systems, increasing the economic return of chromatographic processes[79].

It is known that the reduced plate height is dependent on the system Peclet number, or reduced velocity, which is the ratio of advective to diffusive transport[6] (Eq. (1.6)).

$$Pe = \frac{d\bar{u}}{D_{mol}} \quad (1.6)$$

where *Pe* is the Peclet number, $\bar{u}$ is the average channel velocity [LT^{-1}] and D_{mol} is the molecular diffusion coefficient of the solute species [L^2T^{-1}]. Plotting reduced plate height against the system Peclet number for a given column morphology yields a Van Deemter plot[6], which can be used to find the optimum operating conditions of a chromatographic medium (Fig. 1.3). It is noted that a classical van Deemter plot compares flow rate and HETP, whereas this work uses *Pe* and *h*. This is a common modern interpretation of van Deemter's analysis that is used to remove the dimensional dependence of reported data.

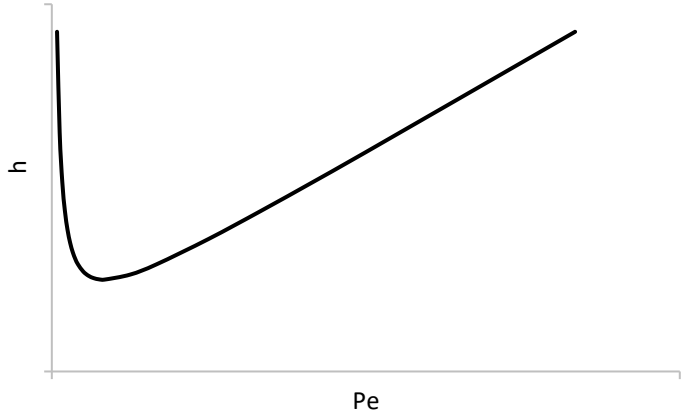

Figure 1.3. A van Deemter Plot shows the optimum Peclet number for minimizing the reduced plate height for a given column morphology. A van Deemter plot is produced by varying the axial velocity of the system, which has direct influence on the Peclet number.

Fig. 1.3 shows a clear optimum Peclet range, in which, the reduced plate height is minimal. Below this Peclet number, diffusive transport starts to dominate, meaning that the RTD broadens as a result of the natural motion of particles being more influential on solute motion than the axial flow through the column[76]. Conversely, if the Peclet number is increased from this point then advective transport dominates and the RTD is broadened by the increased velocity gradients across the flow channels. Van Deemter proposed that this curve can be modelled using the Van Deemter equation (Eq. (1.7))[6].

$$HETP = A + B/u + Cu, \quad (1.7)$$

where *A* is the eddy diffusion coefficient [L], *B* is the axial diffusion coefficient [L^2T^{-1}] and *C* is the mass transfer resistance coefficient [T] which each contribute toward band broadening in specific Peclet regimes (Fig. 1.4).

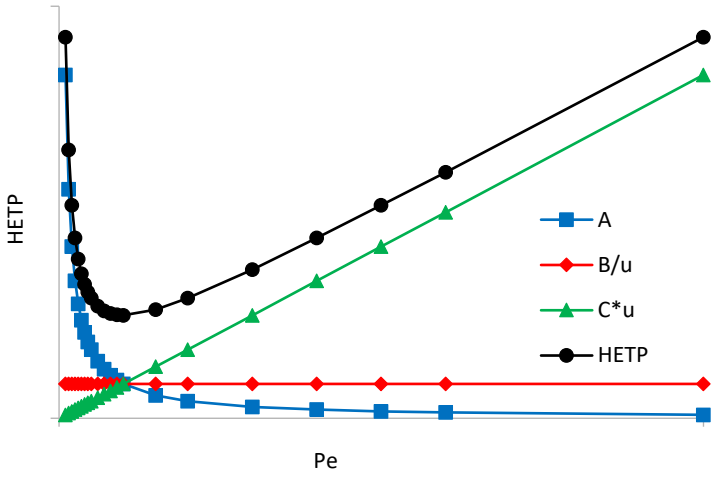

Figure 1.4. Illustrating the contribution of each term in the Van Deemter Equation toward the system performance of a given column morphology. The A term applies across all Peclet values, the B term is dominant in low Peclet regimes and the C term is dominant in high Peclet regimes.

The A term – Eddy Diffusion Coefficient

The A term is known as the Eddy Diffusion term, though it is important to note that chromatographic systems are in the laminar regime. This term is defined here as being independent of system velocity, though some reports challenge this[80], and does not relate to eddies in the bulk flow of the mobile phase, but instead describes the differences in particle path length through the column caused by the disruption of bulk flow by the stationary phase. A high value for the A term can indicate a poor distribution of packing, leading to phenomena such as channelling[6]. Channelling occurs when a dominant flow channel carries the solute through the column at a much higher rate than the remaining bulk flow. Channelling can distort an RTD curve by creating multiple peaks, which severely increases the standard deviation of an RTD curve which in turn increases the reduced plate height.

The B term – Axial Diffusion Coefficient

When the rate of diffusion is higher than the rate of advection ($Pe < 1$), axial diffusion becomes a major factor in solute transport. Molecular diffusion is a process which occurs naturally and acts to increase the entropy of a solute system[81]. Hence, when the velocity scale is low, band broadening occurs because the advective transport cannot elute the analyte before diffusion has a pronounced effect. Diffusion occurs in both the positive and negative axial direction, meaning that the RTD curve is stretched in both directions, causing the solute to be diluted to low levels when it is collected at the column outlet.

The C term – Mass Transfer Resistance Coefficient

This term can be expressed as the sum of two parts, C_m describes the dispersive convection, while C_s describes the adsorption/desorption of the analyte[82]. To describe C_m, consider a particle

traveling at the maximum velocity – in the centre of the flow channel, this particle will move through the column at a faster rate than a particle stuck in a zone of low or no flow, such as a dead zone or inside the pores of the solid phase. C_s, describes the dispersion caused when a solute molecule is adsorbed compared to one which is not bound, causing a variation of the elution time. An increase in average system velocity causes an increase in velocity gradients across the flow channels, because of the no-slip boundary condition at the surface of the stationary phase. Therefore, as the Peclet number increases, this term starts to dominate the Van Demeter plot and become the main source of band-broadening.

Ordered Non-Porous Systems

In a practical chromatographic process, the stationary phase is a porous and active material that is responsible for the separation process. For previous computational investigations of dispersion in porous media, however, the solute in the mobile phase has been mostly modelled as an inert tracer and the stationary phase has been non-porous[14, 45]. In doing this, the impact of the C_m term is reduced, because the pores of the stationary phase are not accessible to the analyte and the C_s term is completely disregarded, as the tracer is mathematically defined as being inert.

Real chromatographic systems are randomly packed, which contributes to the eddy diffusion (A term) of the system by creating flow channels with a distribution of path lengths through the medium. Ordered systems are characterized as being repetitious in nature with respect to both, the solid matrix and the flow channels. In theory, creating ordered packings should create a reduction in the eddy diffusion based on the homogenization of the flow channel lengths[14].

Confined Porous Systems

Another source of dispersion, which is specific to confined systems, are wall effects[28-30]. Walls are necessary for fabricated porous media for containment of the mobile phase but have been shown to decrease column performance in randomly packed beds. Walls disrupt the local packing efficiency resulting in a higher void space and consequently skewing the velocity profile toward the walls. The result of this phenomena is a length dependence on the magnitude of dispersion because of the divergence solute within the faster wall flow and the slower bulk column flow.

It is hypothesized that this phenomenon would also be present in confined ordered packed beds. When fabricating columns via 3D printing, it is more efficient to print the column walls simultaneously with porous medium itself, as a complete structure. It has been suggested in the literature that partial particles can be printed into the column walls to homogenize the column velocity profile and mitigate wall effects[14].

1.4 Fabrication of Porous Systems

Although natural porous materials exist, such as zeolites and activated carbon, these are generally inferior to their fabricated counterparts because of impurities and irregularities caused by the natural fabrication process[8]. For example, lower grade zeolites are used in applications such as agriculture and water softening, but for sensitive applications, such as chromatography, higher quality synthetic zeolites are required[83]. Furthermore, there is only a small range functional porous media which is naturally occurring, meaning that fabrication is a necessary facet of chromatographic research[84-86].

The scale of a chromatographic process depends on the overall process aim. Generally, production scale chromatography uses column diameters which are orders of magnitude larger than analytical columns[87]. The optimization in these cases is between throughput vs. accuracy, where analytical systems are more focused on accurate results and preparative chromatography is aimed at high throughput[88].

1.4.1 Production of Synthetic Media

Products such as zeolites and activated carbon can have both chemical functionality and physical integrity, meaning they can be used as both the solid matrix and active species for a chromatographic medium[83]. However, many functional groups, especially in affinity chromatography, cannot be produced as a stand-alone solid phase and hence must be attached to a physical matrix to maintain the morphology of the medium[5, 89]. Therefore, the solid material is first fabricated and subsequently functionalized to create the chromatographic medium. For size exclusion, however, no functionalization is required for the matrix, as the process is purely a physical one.

There are two approaches to creating a porous medium, either individual particles may be physically conglomerated into a column, known as a packed bed, or the medium may be created as a continuous porous structure, known as a monolith[90].

Packed beds

A packed bed consists of many tightly packed particles. These particles may be also porous themselves, creating two paradigms of porosity in these systems; inter-particle and intra-particle porosity[91]. Packed beds with porous beds experience greater band broadening than their non-porous and pellicular counterparts due to the slow nature of diffusion in the solid phase[82], however, the porous particles provide a greater column capacity[92]. In these systems, it is ensured that the column to particle diameter ratio is large to reduce the impact of the “wall effect”[28, 29]. In practice, packing efficient columns is difficult to achieve, as there is a low amount of control in the fabrication process at the micro-scale level[93]. It is also important to note that once a column has been packed, the specific internal

morphology is unknown and the probability of replicating the exact packing is all but impossible. This means that in practice, every packed bed must go through quality control before it is useable[94].

There are two methods of creating a packed bed: dry packing or slurry packing[4]. Dry packing involves simply pouring particles into the column, while applying some form of vibration to settle particles into a more efficient arrangement. This method is generally restricted to larger particles (>25 μm) and is faster than the alternative. Slurry packing introduces packing particles intro the column as a slurry (solid/liquid mixture). The slurry is then dried, leaving behind the solid phase particles. In general, slurry packing produces a more uniform packing[11], making the slurry packing more efficient for separations, but requiring more time for preparation of the columns[9, 10]. However, for both procedures, there is no control over how a specific particle is arranged with respect to another and hence, the probability of these methods producing ordered arrangement is effectively zero. Therefore, these packings will always be non-uniform, contributing to band broadening by increasing the eddy dispersion of the packing. It has been shown in literature that spheres are the superior particles shape when observing chromatographic performance of randomly packed beds, based on their ability to pack efficiently while maintaining the permeability of the medium[95].

Monoliths

A less common method, is the production of monolithic structures, which has been proven to have advantages over the traditional packed bed[96, 97]. Monoliths eliminate inter-particle porosity, as the structure can be considered as one large particle with a large network of randomly distributed intra-particle pores. Monoliths generally have a higher porosity than packed beds, leading to lower pressure requirements for monolithic columns, thus can support faster chromatographic throughput.

Monolithic materials have several modes of creation, including: hydrogels, foams, compressed beads and monolithic discs[96]. However, these methods still suffer from the lack of control over the location of pore structures and all processes produce random structures, though the order is arguably better than packed beds. Of interest to this work, are monolithic structures which can be applied to ordered porous media. Triply Periodic Minimal Surfaces (TPMS) are promising candidates for such applications because of their minimal surface area and tortuous flow paths to promote transverse dispersion. These structures are not found in natural porous media systems but instead have physical relevance in soap films because of the system's tendency to minimize its total energy[35].

1.4.2 Additive Manufacturing

3D printing is a specific subset of additive manufacturing, a group of methods which create objects by adding material as opposed to removing material from a starting block[47]. This method is like the household technique of two-dimensional printing, but the vertical dimension is created by building layers of material on top of the previous layers. The benefit of 3D printing is that the geometric

control is far superior to any other fabrication technique for producing porous media, and allows for construction of the column walls, stationary phase and distributor as a single unit[12]. 3D printing often uses a geometric model, generated using computer aided design (CAD) software or otherwise, as an input and produces this object in accordance to the printer's specific method and material[98].

3D printing encompasses many materials in the families of: metals, plastics and other polymers. These materials require various fabrication methods including (but not limited to): deposition, stereolithography, sintering and binder jetting. Deposition methods accurately extrude small amounts of the printed material which fuse to create an object. The structure is created by heating and extruding the material through the printer head making this method appropriate for thermoplastics[99]. It is imperative in this technique that the sections of deposited material can physically bind to each other, to produce an object with sufficient structural integrity[100]. Structures with overhanging parts require support materials to maintain the appropriate geometry while the deposited material solidifies and can maintain its own weight without deformation[101] .

Stereolithography begins with a vessel of the printing material, a light sensitive resin, and a printing stages. UV lasers are then used to accurately solidify the resin at the appropriate locations on the stage. Once a layer is completed, the printing stage moves downward into the bath, so that a fresh layer of liquid resin is exposed on top of the hardened structure[102]. For sintering, the method is analogous to lithography. Instead of a liquid precursor, sintering techniques use a powder which is sintered using focused lasers to melt and fuse the material. This method can be used for both thermoplastics and metals and has many variations, such as selective laser melting and electron beam melting[103]. Binder jetting is comparable to sintering methods, but instead of using heat energy to fuse the material, a chemical binding species is secreted onto the powdered material to create the solid structure[104]. This method can be used on many common materials (metals and plastics) but also extends to ceramics.

Investigation into materials which may be printed and functionalized is a current focal point for Fee et al.[12], who are exploring multiple avenues that 3D printing has opened. This work aims to numerically prove the superiority of ordered packings for both preparative and analytic chromatography to supplement the practical studies performed by this group.

1.5 Computational Fluid Dynamics

To study the benefits of ordered packings, both quantitative and qualitative analysis of flow characteristics and dispersion is necessary. However, observation of these phenomena at the chromatographic scale is difficult and only provides limited insight into the internal workings of the column. To gain a comprehensive understanding of ordered packing systems, this work endeavoured to develop a CFD model which illustrated the chromatographic process at the inter-particle pore scale,

producing novel data to improve applications of porous media in chromatography by both reducing band broadening and increasing system permeability.

1.5.1 Fluid Dynamics Background

CFD uses a numerical description of fluids to predict flow behaviour and can couple this with other complex physics involved in both static and dynamics systems. Traditionally, most CFD models are based on the Navier-Stokes (NS) equations which are accepted as fundamental governing equations of fluid flow[15-17]. The NS equations themselves are very complex and have no known analytical solution which is universally applicable to any domain morphology[105]. In conjunction with this, Direct Numerical Simulation (DNS), which is full resolution of a flow field with the pure NS equation set, is rarely used because of its immense computational requirements. Turbulence and boundary layer models are very common in applied NS simulations to increase computational efficiency at the cost of accuracy[19-21]. Complex meshing is also required to achieve sufficient accuracy when using NS methods, which is a time-consuming process that must occur before iterative solution of the NS equations begins[106]. This meshing time is dependent on how fine a mesh is required, leading to highly accurate simulations requiring a huge amount of computing resources for pre-processing. For incompressible fluids, the NS equations take the following form (Eqs. (1.8) and (1.9)):

$$\nabla . u = 0 \tag{1.8}$$

$$\frac{\partial u}{\partial t} + (u.\nabla)u = \nu\nabla^2 u - \frac{1}{\rho}\nabla P_s + \frac{F}{\rho} \tag{1.9}$$

where u is the velocity vector [LT^{-1}], P_s is the system pressure [$ML^{-1}T^{-2}$] and F is the body force term [MLT^{-2}]. Eq. (1.8) is commonly known as the continuity equation (conservation of mass) and Eq. (1.9) represents the conservation of system momentum (which can be written separately for each dimensional velocity).

Although NS is an established and reliable CFD method, this subject of this thesis lends itself to an alternative approach. The Lattice Boltzmann Method (LBM) is a discretized form the Boltzmann equation (Eq. (1.10)), which is a statistical description of the kinetic theory of gases[22]. In this approach, gases are not considered as a continuum - as the NS approach does, but as a collection of particles. Although the theory is based on gaseous species, it can be extended to incompressible liquids by using an artificial sound speed to converge to the incompressibility limit[107]. In fact, the NS equations themselves are contained within the LBM and may be produced by the “Chapman-Enskog” expansion of the Boltzmann equation[108].

There are three main reasons that the LBM has multiple advantages over traditional NS CFD methods in the context of this work:

- Simple meshing, boundary conditions and fully resolved flow for low porosity systems[109]
- Effective coupling with multiple physical phenomena[110-112]
- High level of computational parallelization[26]

Each of these factors provides a performance increase of the CFD model which allows for a greater time efficiency for collection of simulated data.

1.5.2 Lattice Boltzmann Theory

Consider a system containing a rarefied gas which is modelled using hard balls with elastic collisions (Fig. 1.5). In this system, any particle can be defined by its position $x(x,y,z)$, velocity $\xi(\xi_x, \xi_y, \xi_z)$ at a given time, t. From this definition, we define a probability density function, $f(x, \xi, t)$, which describes the probability of finding at a given location, with a given velocity[23], converting the discrete particle system into a macroscopic continuity.

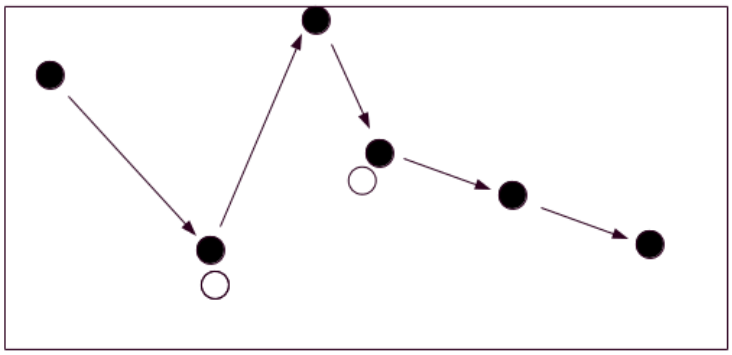

Figure 1.5. Depicted motion of Brownian motion of a single gas particle in a closed rarefied gas system. The white particles represent other gas particles which have collided with the black particle, at the illustrated locations.

Essentially, the Boltzmann equation (Eq. (1.10)) is a statistical model of the Brownian Motion of particles[60].

$$\frac{\delta f}{\delta t} + \xi \frac{\delta f}{\delta x} = C(f) \tag{1.10}$$

where $C(f)$ is the collision term, a function that describes particle collisions in the rarefied system. Much like the NS equations, we are unable to solve this equation analytically and require numerical solvers for the Boltzmann Equation, meaning that a discretization is required[113].

Initially, this is done by converting the integral in a series of Hermite Polynomials, which are commonly used to evaluate complex integrals[114]. From here, Gauss-Hermite quadrature rules are used to remove the velocity dependence of the integral, leaving the "velocity-discrete" Boltzmann Equation, which is evaluated at each quadrature point, c_i (Eq. (1.11)). The collision term is approximated using

the Bhatnagar-Gross-Krook (BGK) collision model, a common single-relaxation time (SRT) method which is second order accurate in space and time[115]. This is not the only collision model which can be applied to the LBM, but the simplest and is viewed as adequate to solve laminar velocity fields, such as in a chromatographic medium[45].

$$\frac{\delta f_i(t,x)}{\delta t} + c_i \frac{\delta f_i(t,x)}{\delta x} = -\omega(f_i(t,x) - F_i[f]) \tag{1.11}$$

where $f_i(t, x)$ is equivalent to $f(t, x, c_i)$ is the probability density function at a discrete quadrature point i, ω is the collision operator (Eq. (1.12)) and F_i is the value of probability density function at equilibrium, according to the Maxwell-Boltzmann equilibrium distribution[116].

$$\omega^{-1} = \frac{\nu_{lb}}{c_s^2} + \frac{1}{2} \tag{1.12}$$

where ν_{lb} is the lattice viscosity and c_s is the lattice speed of sound, a theoretical concept which is used to sustain lattice isotropy[59]. In lower order lattices, such as D2Q9 and D3Q19, cs2 takes a constant value of 1/3, a value which is used exclusively in this work. Literature suggests that the relaxation time for any given lattice should be equal to one for the BGK model using Bounce-Back boundary conditions (Section 2.3.3), with simulations become inaccurate when the condition is not me[117]. The amount of quadrature points used to evaluate the integral depends on the accuracy of the model that is required for the problem. In basic Lattice Boltzmann (LB) simulations the D2Q9 and D3Q19 are standard lattices that are used for two- and three-dimensional domains, respectively[118], where D represents the number of spatial dimensions and Q is the amount of quadrature points used (Fig. 1.6). To evaluate the governing equation, the domain must be discretized in space, that is, the continuous domain is approximated by discrete nodes (Section 2.2.1), which are subsequently used as the quadrature points.

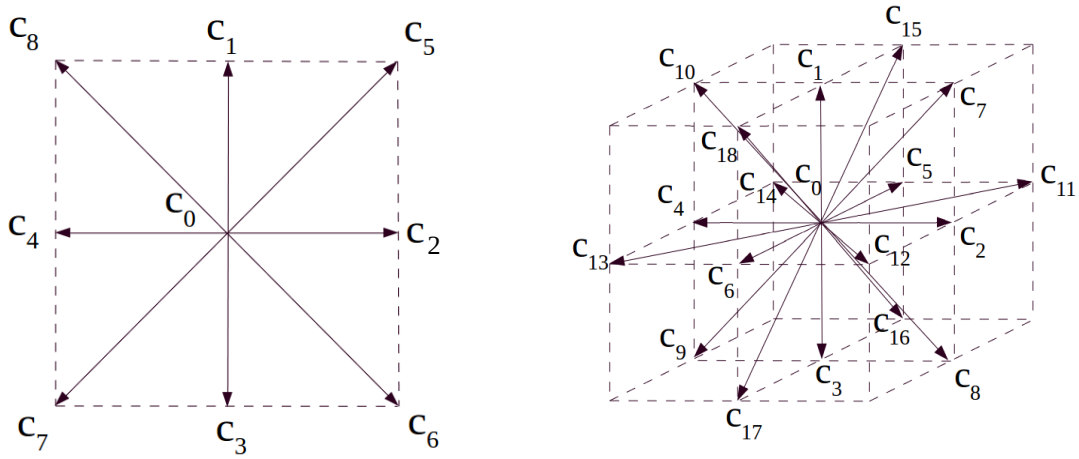

Figure 1.6. Illustration of the a) D2Q9 and b) D3Q19 lattices models represented in discrete lattice space.

In Fig. 1.6., the point c_o corresponds to the lattice node itself and c_i are the nearest neighbours ($i = 1, \ldots Q-1$), as illustrated. Increasing Q is a useful feature of this discretization, because including more terms in the Hermite expansion also increases the number of physical phenomena that may be

observed by the model. For example, at low order expansions, incompressible flows are solved, but at high orders we can solve compressible and non-isothermal flows[119]. Though, as *Q* increases, so too does the amount of contributions to the equilibrium term (Eq. (1.13)), noticeably increasing computational demand. For this thesis, only low order expansions are required, as flow in porous media is highly laminar and iso-thermal.

$$F(x,\xi,t) = \frac{n(x,t)}{(2\pi RT(x,t))^{(3/2)}} . e^{\left(\frac{(\xi - u(x,t))^2}{2RT(x,t)}\right)} \tag{1.13}$$

To complete the discretization, both sides of Eq. (1.11) must be integrated, and the left-hand side approximated using the Trapezoidal rule, yielding the Lattice Boltzmann Equation (LBE) using the BGK approximation (Eq. (1.14)).

$$f_i(x + c_i, t + 1) - f_i(x,t) \; = \; -\omega \left(f_i(x,t) - F_i\big(\rho(x,t), u(x,t)\big)\right) \tag{1.14}$$

More simply, the left-hand side of Eq. (1.14) describes the change in the probability density function in discrete time and space. While the right-hand side is the BGK approximation of the collision term[115]. The Maxwell-Boltzmann distribution (Eq. (1.13)) must also discretized (Eq. (1.15))

$$F_i \; = \; \rho t_i \left(1 + \frac{c_i.u}{{c_s}^2} + \frac{(c_i.u)^2 - c_s^2|u|^2}{2{c_s}^4}\right) \tag{1.15}$$

where t_i is the lattice weighting, based on the position of the contributing point relative to the node in the lattice space (Fig. 1.7)[60]. To commence a LB simulation, an initial "guess" value for *f* is required. For laminar solutions, Eq. (1.14) is solved iteratively until convergence of the function at each simulated point to a given tolerance.

There are shortcomings to the standard LBM-BGK model compared to the NS methods, such as: an increased amount of computational memory[120] and lesser maturity and compressibility issues when approaching turbulent flows (without using further modifications)[121]. Considering this, it was decided that the strengths of the method outweigh these factors, especially when modelling creeping flows in porous media.

Macroscopic Variables

When obtaining macroscopic data from the LBM solution, the probability density function itself has no physical meaning. However, macroscopic variables such as velocity and pressure are calculated as moments of the distribution function, since the LBM uses a much larger set of 'primitive' variables than standard NS methods. Hence, no phenomenological laws are required when producing results at the macroscopic scale. For example, the steady state pressure and velocity field are calculated as in Eqs. (1.16) and (1.17)[60].

$$\rho(x) \; = \int f(x,\xi)\, d^3\xi \tag{1.16}$$

$$u(x) = \frac{1}{\rho}\int \xi f(x,\xi) d^3\xi \quad (1.17)$$

1.6 Mass Transport

1.6.1 Advection-Diffusion

The focal point of this work is analysis of advection, diffusion and adsorption of solute species within porous media, or more specifically, a chromatographic system. Advection and diffusion are phenomena in which heat or mass are transported in fluid systems, but as this work is only interested in isothermal systems, heat transfer is ignored, though it is noted that it is an analogous case to mass dispersion[33]. Here, it is assumed that the advection-diffusion behaviour is passive and does not affect the velocity field, though the buoyancy effects of heat and mass transport are relevant in some contexts. For a solute, the mass transport is modelled by the advection-diffusion equation (ADE) (Eq. (1.18)).

$$\frac{\partial C}{\partial t} = \nabla.(D_m \nabla c) - \nabla.(uc) + Q_s \quad (1.18)$$

where D_m is the molecular diffusivity of the solute [L^2T] and Q_s is a source/sink term [$NL^{-3}T^{-1}$]. Ignoring the source term, Eq. (1.18) is comprised of two terms: advection and diffusion. Diffusion (first term on the RHS), describes how a solute is transported as described by Fick's law, which describes dissolution because of concentration gradients and the random walk of molecules[33]. The second term, advection, describes how the momentum of the bulk fluid transports the solute entrained in the streamlines of the velocity field[33].

The ADE can be naturally solved using the first order LBE (Eq. (1.14)) as a separate set of equations to those used to resolve the velocity field[122]. However, when solving the ADE with the LBM using the BGK model for mass transport, instabilities and numerical diffusion are commonly encountered[123, 124]. To understand this, Eq. (1.12) is modified, to Eq. (1.19):

$$\omega = \left(\frac{\psi_{lb}}{c_s^2} + \frac{1}{2}\right) \quad (1.19)$$

where ψ_{lb} is the diffusive parameter for the specific lattice, in lattice units. For the velocity lattice, ψ_{lb} takes the value of ν_{lb} or the momentum diffusivity (dynamic viscosity), giving Eq. (1.12). For mass transport, this parameter becomes molecular diffusion, D_{lb}, and for heat transport this is the thermal diffusion, α_{lb}. For any ψ, the dimensional units are given as L^2T^{-1} and so to convert to lattice units, Eq. (1.20) is used.

$$\psi_{lb} = \psi \frac{\delta_t}{\delta_x^2} \quad (1.20)$$

where, δ_x is the length conversion factor (Section 2.2.1) and δ_t is the time conversion factor (Section 2.3.1). For the velocity lattice, it has been previously stated that ω should be equal to one, to provide simulation accuracy[117], though we do not know the impact on the advection-diffusion lattice, it is assumed to be analogous to the velocity field because of the similarities between the fundamental equations. Given that each diffusive parameter is converted into lattice units in the same manner (Eq. (1.20)), it is impossible for each relaxation parameter to achieve a value of one, unless the diffusive parameters are equivalent.

This thesis investigates fluid systems nominally using sodium chloride (NaCl) as a solute tracer in water (H_2O). At STP, $v = 1.0 \times 10^{-6}\ m^2s^{-1}$ [125] and $D = 2.0 \times 10^{-9}\ m^2s^{-1}$ (though the Na^+ and Cl^- ions have different diffusion coefficients, the more diffusive species is used)[126], which differ by over two orders of magnitude. In real chromatographic systems, when dealing with proteins and other large molecular species, these diffusion coefficients can range from values 1×10^{-10} to 1×10^{-12}[127] which creates a large discrepancy between the relaxation time in each lattice. This discrepancy leads to large instabilities in the mass transport lattice, causing oscillation, mass loss and divergence of the system when directly solving the ADE.

It is also noted that for thermal systems, that the conductivity of water, α, is around the magnitude 1.0×10^{-7}[128] and hence would also encounter instabilities, but to a lesser extent. Furthermore, the impact of heat dispersion on the density gradient of the fluid is perhaps greater than the concentration, as the magnitudes of concentration used in this study are small, compared to the potential for temperature variation[129, 130]. An accurate solution could potentially require redefinition of the fluid properties at every iteration for each grid point, requiring greater computational resources than the mass transport case.

1.6.2 Advection-Diffusion Equation Models

Solving the ADE in a stable and accurate manner requires an alternative approach to natively using the first order LBM. There are multiple options presented in the literature and each method has positive and negative aspects, as discussed.

Particle Tracking

A popular method is not to directly solve the ADE itself for bulk motion of solute, but to simulate individual particles and their transposition through the domain[14, 45, 131]. Each particle is defined as an inert tracer molecule and has no interaction with the solid phase or other tracer particles while it moves through the domain and exits at a measured time. Multiple particles are simulated, and their frequency is plotted (analogous to concentration) for a time interval spent in the column. This frequency data can be used to build a histogram, in which when the time intervals become small enough, is

equivalent to an RTD curve. The motion of an inert particle is tracked using the differential equation (Eq. (1.21)):

$$dx(t) = u\big(x(t)\big)dt + B_d dW(t) \tag{1.21}$$

where B_d the displacement matrix, a tensor with diagonal values equal to $(2D_m)^{1/2}$ and dW is a function representing Brownian Motion (the Wiener process). Random Walk Particle Tracking (RWPT) is a Lagrangian method, as opposed to the Eulerian methods which are used for a standard approach to solving the ADE[132]. Eulerian methods observe parts of the fluid which are fixed in space, whereas Lagrangian Methods track an observed fluid "packet" and its motion through the domain. As with the LBM, a discretization on the continuous model is required[45] as in Eq. (1.22)

$$x(t + \delta_t) = x(t) + u(x)\delta_t + (2D\delta_t)^{(1/2)}N \tag{1.22}$$

where N is a vector whose components are randomly generated from a normal distribution with mean zero and variance of one. This model excels with LBM as it does not require a relaxation time, as the velocity field does, meaning that RWPT does not experience instabilities, granted that δ_t is small enough to solve the DE accurately[45]. The RWPT method also does not suffer from mass loss because the tracer is modelled discretely and hence, can always be accounted for. Finally, using the RWPT approach means that modelling a single particle only requires simulation at the location of the particle, as opposed to the entire domain, which requires a fraction of the computational resources. Conversely, a large sample of individual tracers must be simulated to approximate the bulk motion which would be produced by solution of the ADE[133]. This last factor can lead to large simulation times when collecting large sets of data which would be required when examining residence time distributions.

Multiple Relaxation Time Models

The issue with the stability of the advection-diffusion lattice stems from the inability of the BGK model to satisfy the required relaxation time for multiple lattices with varying ψ. To counteract this, alternative models have been suggested, in which multiple relaxation times are used to express the collision operator, as opposed to one (as in the BGK model). These methods are known as Multiple Relaxation Time (MRT) methods[134, 135], with the simplest being a Two Relaxation Time (TRT) Method[136, 137]. It is important to note that these MRT methods are not only applicable to using LBM for modelling of advection-diffusion behaviour, but can be used for solving the velocity field in turbulent flows[138].

A common TRT model, introduced by Ginzburg, uses two relaxation parameters, λ_o ("odd") and λ_e ("even")[139] . The standard BGK model can be retrieved from this model in the case of the two eigenvalues being identical, as such (Eq. (1.23)).

$$\omega^{-1} = -\frac{1}{\lambda_o} = -\frac{1}{\lambda_e} \tag{1.23}$$

Recalling the *D3Q19* system (Fig. 1.7), each quadrature point is paired with the opposite velocity in the quadrature space (excluding C_o), for example, C_1 is paired with C_3. The unknown population at each point is then split into two components, known as the symmetric and anti-symmetric denoted by f_q and $f_{\bar{q}}$ (Eq. (1.24)) (note the difference between f_q^- and $f_{\bar{q}}$).

$$f_q = f_q^+ + f_q^-,\ f_q^\pm = \frac{1}{2}\left(f_q \pm f_{\bar{q}}\right) \tag{1.24}$$

The exception is the rest population, where $f_0 = f_0^+$ and $f_0^- = 0$. The population pair can then be used to calculate the symmetric and anti-symmetric components of each population in their pairs. A numerical parameter, Λ, is introduced (Eq. (1.25)).

$$\Lambda = \Lambda_e \Lambda_o \tag{1.25a}$$

$$\Lambda_e = -\left(\frac{1}{2} + \frac{1}{\lambda_e}\right), \qquad \Lambda_o = -\left(\frac{1}{2} + \frac{1}{\lambda_o}\right) \tag{1.25b}$$

Λ is generally the user defined parameter in these simulations and commonly takes an empirically determined value of *1/4*[140]. The component, A_o is used to calculate the effective diffusion coefficient of the system[141] (Eq. (1.26)).

$$D_{TRT} = \frac{D}{\Lambda_O} \tag{1.26}$$

where D_{TRT} is the diffusion coefficient for the TRT system [L^2T^{-1}]. One relaxation time is applied for half of the populations and the counterpart relaxation time for the opposite member of the population pair. This method increases the resilience of the LBM by decreasing the isotropic nature of the collision term presented by the BGK model. Presented here is a very brief explanation and does not cover the intricate details of the method, for a full explanation, refer to the stated references.

To further develop this idea MRT models become even more complex, by using a diagonal collision matrix, *S*, of size *Q* by *Q* (where *Q* is equal to the number quadrature points) to represent the collision operator[142] (Eq. (1.27)).

$$f_i(x + c_i, t + 1) - f_i(x, t) = -S\left(f_i(x, t) - F_i\left(\rho(x, t), u(x, t)\right)\right) \tag{1.27}$$

As before, the BGK and the TRT models are can be recovered from the MRT, where the eigenvalues are either identical (BGK) or take on one of two values per their position in the quadrature pair. However, not all the members in the collision matrix are required to be different and many combinations of parameters can be used[143].

The issue with MRT models, however, is that that choice for these relaxation parameters seems to be more of a tuning exercise as opposed to a choice based on physical parameters of the system[144] and increased simulation time because of the added level of complexity[124]. For simulations in novel

domains, it becomes difficult to verify the results. It is well known the BGK model does have compressibility issues, which, in terms of solving the ADE, results in instability and mass loss (as discussed previously). The MRT method provides a large benefit here, providing superior stability and accuracy over the simple BGK model, but can be viewed as unnecessarily complex when considering other models which are available.

Reference Diffusion

For this work, a third approach was used. Instead of focusing on the complexities of the collision operator, this method equivocates the diffusion parameters of each lattice and subtly changes the LB framework for solving the ADE[27]. The details of this method are covered in Section 2.4.1.

1.7 System Variables

To understand the characterization of the flow systems studied in this work, a more in-depth introduction to some aspects of the process variables is required. These variables are organized into three broad categories: flow parameters, solute properties and morphology characteristics.

1.7.1 Flow Parameters

Flow parameters encompasses the following variables: kinematic viscosity, density, (inlet) velocity and outlet pressure. For this work, we exclusively investigate isothermal systems involving H_2O (an incompressible fluid), which restricts the kinematic viscosity and density to their defined physical values at STP. The only flow parameter that is altered in this work is the inlet velocity, which in conjunction with the characteristics of the stationary phase, defines the average channel velocity. The average channel velocity is one of the most important variables in the presented studies, as it defines both the Reynolds (Eq. (1.28)) and Peclet (Eq. (1.6)) numbers, given the constant values of d, D and v within any system.

$$Re = \frac{d\bar{u}}{\nu} \tag{1.28}$$

where Re is the system Reynolds number. These two dimensionless numbers are crucial when it comes to defining a mass transport system. The channel Peclet number describes ratio of mass transport via advection and molecular diffusion and has direct impact on the system performance (Section 1.3.2). The Reynolds is defined as the ratio of inertial to viscous forces in a fluid and is used to gain an estimate of which flow regime the system is in: turbulent flow ($Re > 500$ for porous media[145]), laminar flow ($1 < Re < 500$) or Stokes Flow ($Re << 1$), which is also known as creeping flow[33]. For this thesis, and in practical chromatography, systems are operated in Stokes flow, in which viscous forces are greater in magnitude than inertial forces.

1.7.2 Solute Properties

For this work, the solute is considered an inert tracer (excluding Chapter 6) and is used to investigate the extent of band-broadening in the mobile phase for a given morphology and flow rate. To give the study physical relevance, sodium chloride (NaCl) was selected as the tracer species, because of its high rate of molecular diffusion. The molecular diffusion coefficient defines the rate at which the solute passively diffuses through the solvent and is analogous to the kinematic viscosity of a fluid, which describes momentum diffusion[76]. For actual chromatographic processes, there are a variety of solutes which are used, depending on the process objective. The diffusion of a solute species depends on the size of the solute molecules, as larger molecules experience a greater number of collisions both, with each other and solid boundaries, causing them to have an overall slower diffusion in solution[127]. As a solute, NaCl is dissociated into Na^+ and Cl^- ions, which are small ionic species consisting of only a single nucleus and its associated electrons. In practice, these species have separate diffusion coefficients, but for simplicity, we assume one coefficient for the system as $D_m = 2.0 \times 10^{-9}\ m^2s^{-1}$[126]. Proteins and other chemical species of relevance to chromatography are much larger than simple ionic species, meaning that most practical solutes will have smaller diffusion coefficients than in this study. However, if the molecular diffusion coefficient is altered, both the Peclet number and the Reynolds number cannot be conserved, based on observation of the Schmidt number

$$Sc = \frac{Pe}{Re} = \frac{\nu}{D} \tag{1.29}$$

where *Sc* is the Schmidt number. Therefore, to scale both the Reynolds and Peclet numbers equivalently, the viscosity must be reduced by the same factor as the diffusion coefficient, though this is not possible in practice, as these values are predetermined. However, these systems are already in Stokes flow and when decreasing the Reynolds number, the velocity field scales linearly. Hence, we can say that the systems modelled in this work can be equivocated to systems involving species with lower diffusion coefficients, given that the Peclet number is conserved and $Re << 1$.

In scenarios where the stationary phase is also considered as a porous medium (Chapter 6), a secondary (intra-particle) diffusion is experienced by the solute particles, also known as pore diffusion. Pore diffusion has previously been defined as being a function of a number of factors and consequently has a lower value than the bulk solute diffusion (Eq. (1.30))[40].

$$D_{pore} = \frac{D_m \varepsilon_t \delta_c}{T_{pore}} \tag{1.30}$$

where D_{pore} is the pore diffusion coefficient [L^2T^{-1}], ε_t is the effective transport porosity (< 1), δ_c is the constrictivity factor of the pores (< 1) and T_{pore} is the tortuosity of the pores (> 1). There is a very broad range for the values of the presented variables depending on the characteristics of the solid phase material and the way it has been fabricated, which is not explored in this work.

1.7.3 Morphology Characteristics

The morphology of a porous medium, has an important effect on the dispersion behaviour[14, 45, 46]. In this work, a specific morphology is characterized by three main variables, as follows.

Porosity

The system porosity is defined as the ratio between the fluid volume and the total volume of the system. For random packings, the entire domain must be used to calculate the true porosity, but for ordered packings, it may be calculated using a single unit cell. In the discretized environment (Section 2.2.1) this volume is approximated using the prescribed solid and fluid nodes

$$\varepsilon = \frac{V_{fluid}}{V_{total}} = \frac{\Sigma N_{fluid}}{\Sigma N_{total}} \tag{1.31}$$

where *N* represents the nodal points in the sample volume. The porosity of a system is important, as a greater amount of solid phase represents logically a greater number of binding sites for chromatographic separation from the increase in the amount solid phase material. However, a lower proportion of fluid also represents a lower permeability of the media, per the Carman-Kozeny relation[38].

Permeability

The permeability of a system describes the ease at which fluid travels through a porous medium and is defined from Darcy's Law (Eq. (1.1)). For a fluid with constant properties, such as an isothermal and incompressible liquid, the permeability is constant within the Stokes flow regime.

The permeability indicates the amount of work required from the system driving force (generally a pump) to generate the required channel velocity (or *Pe*). A system with high permeability requires less applied pressure and hence, lower pumping costs in a practical setting. The permeability is also important when considering the deformation limits of the solid matrix material[62]. Some structures may require a pressure which would cause the column to deform at an optimum Peclet number. In this work, deformation is not considered, and it is assumed that the solid phase is rigid under all conditions.

Tortuosity

Tortuosity is a factor that has many definitions[146, 147] and is often derived from the geometry of the stationary phase. In this work, a variant is considered, known as the flow tortuosity[148], which is defined as the ratio of total velocity to the axial velocity

$$T = \frac{\Sigma u}{\Sigma u_z} \tag{1.32}$$

where T is the system tortuosity and u_z is the axial velocity component [LT^{-1}]. It is thought that this metric could be a strong indicator of channelling in a column, as these systems tend to have a low tortuosity caused by the axial channel dominating flow profile.

1.8 Direction of Current Work

Based on literature findings, ordered packing has the potential to revolutionize fabricated porous media systems by using additive manufacturing. It has already been proven by Schure et al.[14] that ordered packed beds can provide less band-broadening than randomly packed spheres under optimal conditions. However, beyond this, there is very little literature which further investigates ordered packings of both particles and monoliths. For example, in random packings, non-spherical particles are inferior in performance, but it is unknown whether this is still an applicable result for ordered packings. Another consideration for ordered packed beds is the orientation of the axial flow direction within the bed, as this will alter the velocity field, whereas this is not applicable concept for randomly packed beds because of their lack of order (Chapter 3).

For scenarios in which a packed bed has infinite width, which is not the case for practical chromatography, ordered packing has been shown to have better performance than its randomly packed counterpart, under optimal conditions. However, it is known the walls can also contribute to dispersion beyond the measured dispersion of the bulk packing in practical chromatography of randomly packed beds, because of the "wall effect". It is therefore important to explore how the wall effect contributes to dispersion in ordered packings and if this differs from randomly packed beds (Chapter 4). It is important to note that confined randomly packed beds are not explored in this work, as this work focuses almost exclusively on ordered packings.

Monolithic structures have become increasingly popular in modern chromatography, which can be attributed to their ability to produce low amounts of band broadening while reducing pressure drop when compared to packed beds. Therefore, it is appropriate to hypothesize that ordered monolithic structures could show better performance than ordered packed beds. Of specific interest in this work are triply periodic minimal surfaces, which provide both minimal surfaces (to increase permeability) and tortuous flow paths (to promote transverse mixing). These structures have not yet been considered for use as a chromatographic medium making it a promising area of investigation for improving chromatographic efficiency in practical systems (Chapter 5).

Finally, current CFD studies in the literature often use two assumptions which differ from practical chromatography. First, many of these studies assume that the stationary phase is non-porous, i.e. the intraparticle porosity is equal to one. This is done because the band broadening contribution of the stationary is assumed to be additive, thus can be determined at a later stage. Second, the tracer is inert and does not interact with the stationary phase. As these two phenomena are practically relevant,

it is important to understand how these effect band broadening in ordered packings compared to the simplistic models used in this study and other literature sources (Chapter 6).

2. Numerical Methods

2.1 Model Overview

This chapter describes, in detail, the simulation and analysis methods used to generate the results presented in this thesis. The simulation process can be categorized into four serial steps:

1. Pre-processing - generation of simulation domain and porous medium (Section 2.2)
2. Solution the laminar flow profile at the pore scale (Section 2.3)
3. Simulation of dynamic advection-diffusion of the solute species (Section 2.4)
4. Post-processing/analysis (Section 2.5)

The model was developed using an open source C++ library, Palabos (FlowKit Ltd., Lausanne, Switzerland), a highly parallelized LB solver (Section 1.5.2). To use this library, a front-end script was written to perform pre-processing (Section 2.2), data collection for post-processing as well as calling the iterative solver. The iterative solver first developed the flow profile (Section 2.4 and secondly, simulated the advection-diffusion (and adsorption) behaviour of an introduced solute species in the porous medium (Section 2.4). Finally, post-processing used analytical tools developed from spreadsheet and visualization software, to generate the results presented in this work (Section 2.5).

2.2 Pre-Processing

Pre-processing includes all tasks performed prior to the solution of the velocity field, including: space discretization, defining the morphology of the stationary phase and defining all system boundary conditions.

2.2.1 Space Discretization

To solve the LBE for our specific purposes, the continuous physical domain was approximated by a homogeneous grid of "nodes" at which the fundamental equations of the model were solved, using each other as the quadrature points (Section 1.5.2). The number of nodes which are used to resolve the defined characteristic length is described as the space resolution[149] (not to be confused with chromatographic resolution), which is a user defined parameter

$$\delta_x = \frac{d}{R_x - 1} \tag{2.1}$$

where *R* is the spatial resolution. This thesis mainly deals with repeating geometries; hence, the length factor and resolution are defined for individual particles or periodic unit cells as opposed to the entire domain. Resolution is an important ingredient in LB simulations because of the method utilizing a homogeneous meshing technique, requiring curved and angled surfaces to be approximated by voxels (Fig. 2.1).

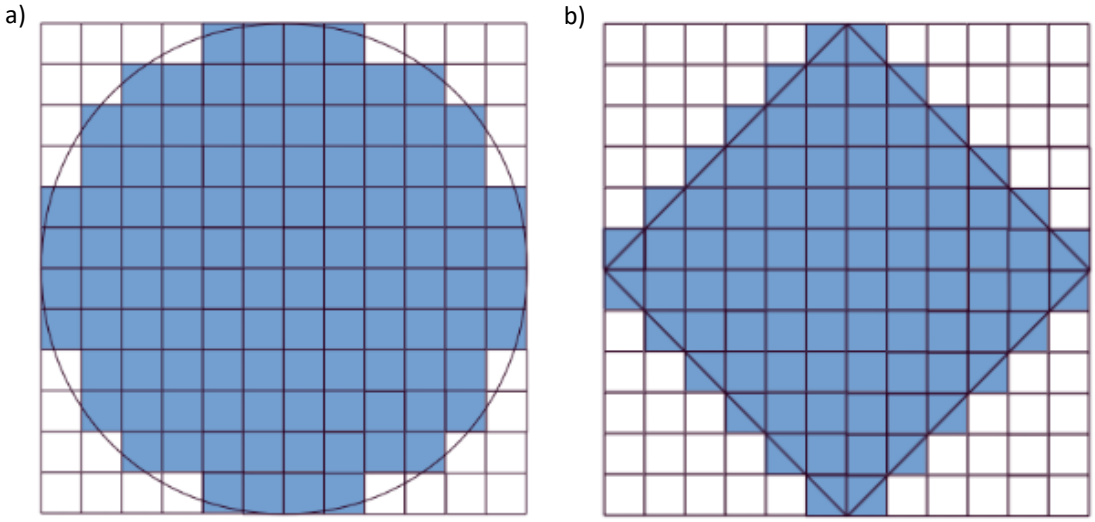

Figure 2.1. Two-dimensional voxelization at a resolution of 12, for a) a sphere and b) a rhombus. Each square represents a single voxel and physical grid locations are located at voxel centres.

Resolution defines the number of voxels that are used to define the characteristic length and hence is an optimization between the representation of the actual geometry, which relates to accuracy, (Fig. 2.2) and a more refined mesh requiring greater memory for more simulation nodes and simulation time to solve the LBM at a greater number of points.

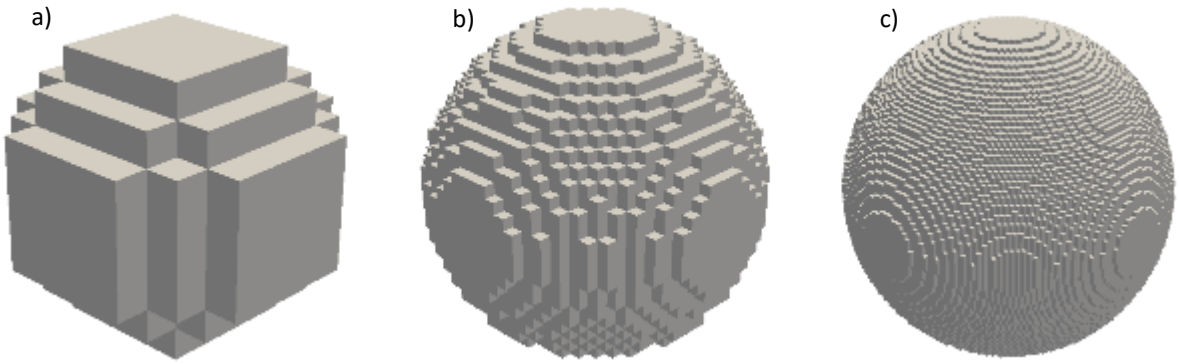

Figure 2.2. Voxelization of a sphere at varying grid resolution. Spheres are resolved at: a) 10, b) 30 and c) 90 grid nodes in each spatial dimension.

A recent study focusing on random sphere packings by Khirevich, suggested that a resolution of 30 nodes (Fig. 2.2b) across a particle diameter gives sufficient accuracy[45], while an older study on ordered and random sphere packings by Schure et al, used roughly 30 nodes for random packings, but (an estimate of) 60 to 80 nodes for ordered packings[14]. There is no comment regarding the chosen resolutions in the work of Schure, however, it is assumed that higher resolutions are used for the ordered packings because the repeating unit cell contains few spheres when compared to a large randomly packed column. Hence, for ordered packings there are more computational resources available to increase the resolution to match the number of nodes used in a random packing. For this thesis, a mesh independence study was performed to determine an appropriate resolution.

Mesh independence is an important aspect of discretized systems and is defined as the point at which the further grid refinement no longer influences the data produced by the model, to within a specified tolerance[150]. In this study, three ordered sphere arrangements were investigated: SC, BCC and FCC, to observe the effect of resolution on both the permeability and reduced plate height of these systems (Fig. 2.3). A prior study used a reference resolution of 90 nodes, for the mesh independence study[45], a practice which was mirrored in this study.

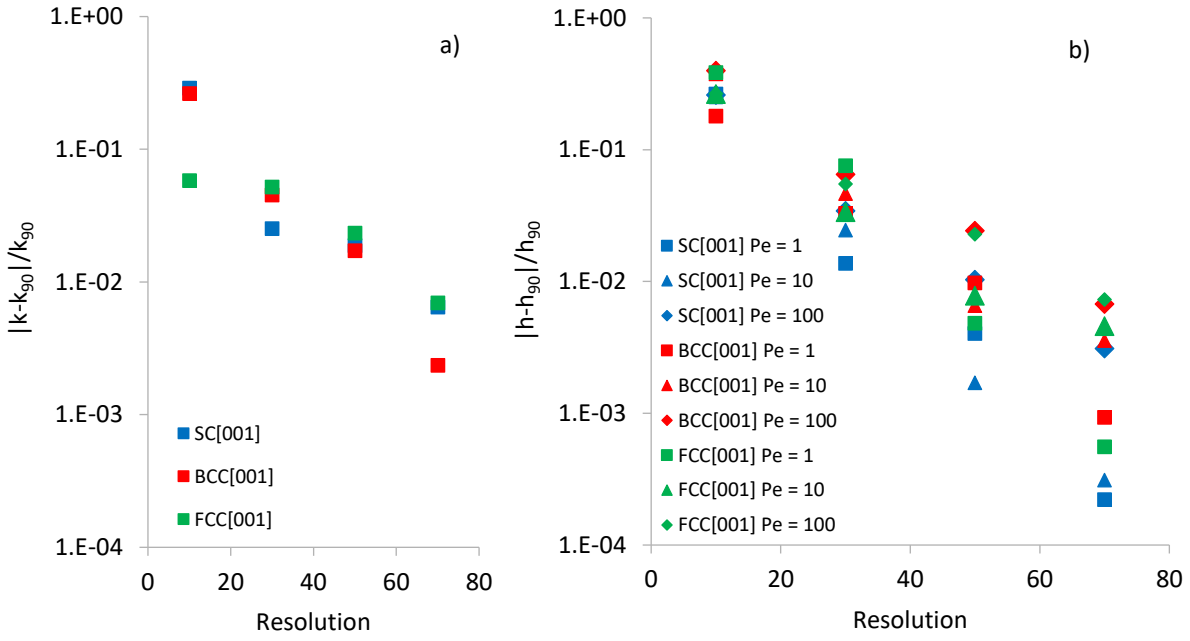

Figure 2.3. Mesh independence investigation for a) permeability and b) reduced plate height for crystal cubic packing of spheres; SC, BCC and FCC. A resolution of 90 nodes resolving each sphere is used as the reference solution for both permeability and reduced plate height.

Permeability is constant within Stokes flow and therefore, is not presented for multiple Peclet values. For the convergence of permeability in random packings it has been shown that there is an inverse correlation between porosity and rate of convergence for LBM-BGK schemes[45]. However, for

the ordered packings studied here, there appears to be no distinct trend for convergence of permeability and reduced plate height between packing types (which vary in porosity). For the reduced plate height, convergence appears does appear to be inversely proportional to the Peclet number, which was observed for random packing in literature[45]. This result was expected, because the advection, which is dominant at high *Pe*, is dependent on the morphology of the stationary phase, via the velocity field, whereas the rate of molecular diffusion, which dominates at low *Pe*, is less influenced by the morphology of the medium when occurring in the bulk fluid.

Unlike these previous studies, this work does not use periodic boundary conditions in the axial dimension and requires multiple particles to be modelled in this dimension so that steady column flow is achieved within the medium. When selecting a simulation resolution, it is also important to note that for increasing the resolution of a simulation, time cost increases by at least $O(R^5)$ and the memory requirements by $O(R^3)$. For this mesh independence study, the largest recorded error was for 7% for both permeability and reduced plate height values with an average of around 5%. It was decided that optimization between speed and accuracy suggested a resolution of 30 nodes for each particle was sufficient for producing results within an acceptable time frame, especially when simulating larger domain sizes and producing many data sets.

2.2.2 Solid Phase Declaration

Two distinct categories of column morphology were investigated in this study: discrete particles and monolithic structures, both of which required a subtly different declaration, as described in the following section. It is important to note that the Z axis is defined as the axial direction in this work.

Initially, for any geometry, a 3D Boolean grid of zeros was declared. The size of this matrix was defined by the number of repeating unit cells in each physical dimension for ordered packings, or the predefined size of a random pack. Discrete particles were initially defined by their geometric centre - as all particles used in this study were symmetrical, this was equivalent to the centre of mass, assuming a particle of homogeneous density. For random sphere packing, an external program, developed by Vasili Baranau[151], was used to locate particle centres. This program generated binary outputs for sphere centre locations which were imported into our solver and transposed into our discretized domain. As random packing was used as a starting point for this research and validation for our CFD model, it was deemed unnecessary to develop our own random packing algorithms and programs, when such a useful open source tool had already been created. For ordered packings, the particle locations were calculated using the specific orientation and arrangement of the specific packing type (Section 3.1).

Once the particle locations had been defined, the physical particles were generated by defining solid nodes around each centre point, using the Cartesian inequality in which satisfying the inequality yielded a solid node (a value of one in the Boolean grid), e.g. spherical particles (Eq. (2.2))

$$(x - x_o)^2 + (y - y_o)^2 + (z - z_o)^2 \leq {r_p}^2 \quad (2.2)$$

where *x, y z* are the lattice co-ordinates, x_o, y_o and z_o are the co-ordinates of the particle centre and r_p is the radius ($d_p/2$) of the particle. Using an inequality assured that no fluid nodes were located within the particle, which would both use extra computational resources and lack the specific chemical functionality for diffusion and adsorption, where applicable.

For continuous structures, solid nodes were located with a Cartesian inequality that defined the solid phase without the need for particle centres, making this a less intensive process than for discrete particles. The equation for a given surface in this work, for example "Schwartz Primitive" (Eq. (2.3)), is valid for all *x, y, z*.

$$sin(x) + sin(y) + sin(z) < 0 \quad (2.3)$$

The continuous structures studied in this thesis are periodic in nature and hence, the concept of repeating unit cells is also used when defining these morphologies.

2.3 Velocity Field Simulation

2.3.1 Time Discretization and Simulation Stability

To reflect practical chromatography, only laminar flow systems were examined in this and were non-transient. However, achieving a laminar solution requires iteration using the dynamic solver until convergence of the flow field (to a specified tolerance). For solving the LBE, a time discretization is required, in which real time is approximated by discrete time steps. For the LBE, to produce a stable, accurate and convergent solution, an appropriate time step must be selected[152]:

$$\delta_t = \delta_x \frac{u_{lb}}{u} \quad (2.4)$$

where u_{lb} is the lattice velocity ($u_{lb} << 1$). It is important to note that the spatial and time units of the lattice system, δ_x^{lb} and δ_t^{lb} respectively, are both equal given a value of one, for simplicity and hence no further conversion is required between dimensionless and LB unit systems[153]. It is crucial that dimensionless quantities, such as Reynolds and Peclet numbers, remain constant between physical and lattice units, therefore this was used as a check for maintaining the dimensional consistency within the numerical framework.

Recalling Eq. (1.12), v_{lb} is the variable which defines the velocity lattice relaxation time and affects the stability of the simulation for the BGK model. As previously stated, it has been shown that inaccuracies occur for simulations in which ω diverges from unity ($v_{lb} = 1/6$)[117]. To achieve this, v_{lb} is manipulated by the dimensional conversion factors (Eqs. (2.1) and (2.4)), but as in Section 2.2.1, the

choice for δ_x is already decided by computational factors. In the framework presented, δ_t is chosen by the value of u_{lb}, hence this is appropriately selected to satisfy $\omega = 1$.

2.3.2 Collision and Streaming

Practical LBM solvers commonly utilize a two-step iterative process. The iterative method is composed of two main steps: collision and streaming[23, 60, 113, 152]. In the collision step, all values for the distribution function are calculated (Eq. (2.5)).

$$f_i^{out}(x,t) = (1-\omega)f_i^{\text{in}}(x,t) + \omega f_i^{eq}(x,t) \tag{2.5}$$

where f_i^{out} is the outgoing populations and f_i^{in} is the incoming populations for each quadrature point. This step is where the LBE is solved, while the streaming (or propagation) step, which is the updating of the populations at each site per the lattice velocities and weights (Eq. (2.6)).

$$f_i^{\text{in}}(x + c_i, t+1) = f_i^{out}(x,t) \tag{2.6}$$

These two steps are required to avoid over-writing populations that are still required in the specific iteration step. It is also worth noting, for all simulations, that the streaming step is constant and is separate from any dynamics specific to that simulation node, while the collision step can vary between both simulations and specific areas of the simulation domain.

In basic LBM codes, the outgoing populations may be saved as temporary values, though this increases the amount of memory required for simulation. In Palabos, the steps are integrated without overwriting populations or requiring temporary values, which creates a more efficient solver with respect to both memory and simulation time[152].

2.3.3 Boundary Conditions

Excluding Chapter 4, periodic boundary conditions were used in the transverse dimensions, to simulate columns of infinite width while only requiring a single unit cell in these dimensions. This cannot be emulated in practice, as column walls are required to contain the mobile phase within the column. Walls have a negative impact on chromatographic performance, due the "wall effect" [28, 29]. In Chapter 4, wall effects were investigated by using solid boundaries in the transverse dimensions and varying the column diameter. To reduce the computational impact of the increase in domain size two of the orthogonal planes used symmetry boundary conditions, simulating a column with twice the length in each transverse dimension. This reduced both simulation time and memory requirements by a factor of four when modelling confined packings.

For the axial boundary conditions, a Dirichlet inlet and Neumann outlet were used. The superficial velocity of the system was defined by applying a uniform velocity profile across the Dirichlet

inlet, while the outlet boundary was defined as a zero pressure, a common configuration for CFD problems[154]. For all simulations, the stationary phase of the column was defined with no-slip boundaries using the (LBM specific) "Bounce-Back" boundary condition.

Bounce-Back Boundaries

The distribution of void spaces in porous media often creates complex column geometries characterised by the prevalence of solid-fluid boundaries. From the "no-slip" boundary condition[155], a zone of the fluid called the laminar boundary layer is created, in which there is a velocity gradient from zero, at the solid boundary, to the channel maximum velocity, which is parabolic in nature[156] (Fig. 2.4).

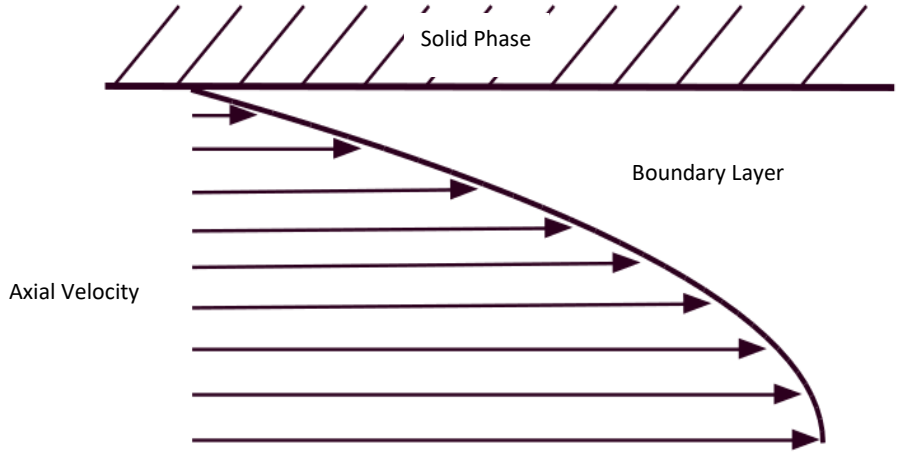

Figure 2.4. Illustration of a boundary layer in a laminar flow system. The magnitude of the axial velocity increases from zero at the wall to the maximum, in the centre of the flow channel, with a parabolic profile.

In LB schemes, a boundary condition known as "Bounce-Back" (BB) is commonly used to model no-slip boundaries[25, 109]. BB models an interface which is located half-way between the defined BB node and adjacent fluid nodes (Fig. 2.5). These boundary conditions reflect incoming particles populations back to their node of origin at the microscopic level, which at the macroscopic level, equates to a no-slip boundary[24]. LBM employs a homogeneous meshing system, so BB provides an advantage by creating a boundary that does not have to be explicitly defined; the boundary is created by a solid node being adjacent to a fluid node. The implications of this are two-fold, complex geometries are easily meshed (although resolution is important) and solid and fluid nodes are easily re-defined during simulation, allowing for in situ manipulation of the solid phase[157]. This provides a large advantage of traditional NS methods, which must apply more rigorous methods for moving boundaries[158].

Although the BB method is employed in this thesis, it is acknowledged that there are inaccuracies associated with the method. BB degrades the accuracy of LBM to first order in space[159], which creates longer convergence times for laminar flow systems and potential inaccuracies in dynamics systems. The halfway BB also means that the size of objects is inaccurate at lower resolutions. Moreover, for the BGK method, the location of the wall is not always half-way between the solid and fluid nodes, but it is dependent on the lattice viscosity[117]. However, these factors were ultimately outweighed by the computational efficiency of using BB as opposed to other boundary conditions which are available to the LBM.

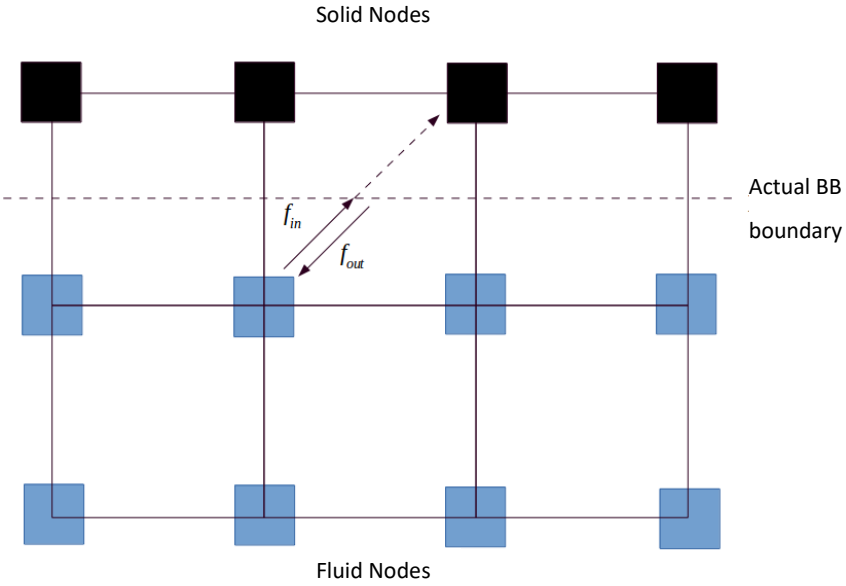

Figure 2.5. The True Bounce-Back boundary is located halfway between the solid and fluid nodes and (on average) reflects the streamed values back to the node of origin.

2.4 Mass Transport

Once the velocity field reaches its steady state profile, mass transport of the tracer is modelled using the ADE (Section 1.6.1). However, for our systems, naturally solving the ADE using first order LBE is non-trivial because of instability issues caused by the discrepancy between the relaxation parameters of the two lattices. To resolve this issue, a modified single relaxation time (SRT) method was used (Section 2.4.1).

The advection-diffusion lattice also used the collision and streaming iterative system (Section 2.3.2) and boundary conditions (Section 2.3.3) as the solid phase, but to different effect. Here, the Dirichlet inlet boundary was used to define the concentration of solute species entering the column and the Neumann outlet allowed flow of tracer out of the system. In this context, the Bounce-Back boundary was equivalent to an adiabatic boundary condition, simulating a non-porous stationary phase[160].

2.4.1 Reference Diffusion (SRT) Model

A solution to the instability issue of the ADE is with the use of a "reference diffusion" model, developed by Perko and Patel[27]. In this simple SRT model, the molecular diffusion coefficient is represented by two terms, the reference diffusion and a deviation term (Eq. (2.7)).

$$D = D_{ref} + \widetilde{D} \tag{2.7}$$

where D_{ref} is the reference diffusion value [L^2T^{-1}] and $\widetilde{D}$ is the deviation term [L^2T^{-1}]. The reference diffusion term is a user defined parameter that is substituted in place of the molecular diffusion term in the ADE, which then becomes (ignoring source/sink) (Eq. (2.8)) and the flux of the deviation term is converted into an advection term (Eq. (2.9)).

$$\frac{\partial C}{\partial t} = \nabla.\left(D_{ref}\nabla C - \widetilde{D}\nabla C\right) - \nabla.(uC) \tag{2.8}$$

$$\widetilde{D}\nabla C = u_d C, \quad u_d = \frac{\widetilde{D}\nabla C}{C} \tag{2.9}$$

where u_d is defined as the diffusion velocity [LT^{-1}]. Finally, the diffusion velocity is inserted into the ADE as part of the advective term (Eq. (2.10)).

$$\frac{\partial C}{\partial t} = \nabla.\left(D_{ref}\nabla C\right) - \nabla.\left((u_a - u_d)C\right) \tag{2.10}$$

where u_a is the advection velocity [LT^{-1}] (the standard velocity term in the ADE). From this formulation, the mass balance of the ADE is still respected, however, an extra unknown term is present in the governing equation. To determine the diffusion velocity, a first order Chapman-Enskog expansion is used. For further derivation, refer to the original work by Perko and Patel[27].

Although this method is not as computationally efficient as the standard BGK model, because of the extra operations required for the diffusion velocity, it was found that the BGK is not adequate for producing meaningful results when solving the ADE within the context of this work. Even so, the SRT is less computationally intensive than the previously mentioned MRT models[27] and when compared with the RWPT, a popular method in the literature, this method holds the advantage of being able to model the bulk motion of a solute, as opposed to individual particles. Being able to model the bulk motion not only improves simulation time efficiency[133], but the model can be developed to incorporate solute interaction with the solid phase (non-inert tracer). This feature is useful when the model is used to investigate adsorption behaviour, a phenomenon which occurs in practical chromatographic systems.

The reference diffusion method does have limitations. It is shown that the model is not particularly accurate for accelerated coefficients, i.e. when the reference diffusion is smaller than the true molecular diffusion, becoming unstable, in some cases, when the two values differ by an order of magnitude[27]. However, in the inverse case, for basic advection-transport problems, the method is

shown to be stable for cases in which the reference diffusion is five orders of magnitude greater than the molecular diffusion value. Therefore, the reference diffusion model is used for the lattice which has the smaller diffusivity value - in this case this is the ADE lattice and the molecular diffusion coefficient.

For optimum stability and accuracy of the method, we define $D_{ref} = v_{H2O}$, meaning that the relaxation time is equal to one for both lattices, ensuring stability and accuracy of the model. In the case of an inert tracer, nominally NaCl, this creates $D_{ref} = 500D_{mol}$, which is within the stated stability boundaries[27]. For a protein species, which is a more realistic analyte for chromatography, this becomes $D_{ref} \approx 10000D_{mol}$, which begins to exceed the limit of the model's stated capabilities. Hence, further investigation is required for the stability and accuracy of mass transport in protein-based systems.

2.4.2 Adsorption-Desorption Behaviour

In Chapter 6, the concepts of porous stationary phase and solute binding are introduced, a concept which has been previously implemented with the LBM[161-163], but not for systematic studies of 3D chromatographic media. By introducing interactive properties between the solute and stationary phase, this study enters the field of reactive transport, as adsorption and desorption are effectively chemical reactions which occur at the liquid-solid phase boundary. Here, we begin to apply this behaviour to ordered packings, with specific aim of digitally recreating the chromatographic process and producing comparisons between different morphologies and column operating conditions.

Model Adjustments

To model the porous stationary phase, the BB condition in for the ADE lattice for the stationary phase was removed and instead the pore diffusion coefficient was introduced as in Eq. (1.30) (Section 1.7.2). However, the BB condition on the velocity field remains, meaning that mass transport in the solid phase occurs exclusively by pore diffusion.

In the original work by Grathwohl, the ratio between the pore transport and bulk fluid transport is introduced (Eq. (2.11)) with some empirical values for porous media[40].

$$D' = \frac{D_{pore}}{D} \tag{2.11}$$

where D' is the mass diffusion ratio. This work does not endeavour to prescribe any physical properties to the solid phase, as this is dependent on the material comprising the stationary phase. Therefore, this ratio will vary based on how the fabrication of a medium is targeted toward a specific separation. For most studies involving intra-particle porosity, a value of 0.1 was selected for D' as this was deemed a fair estimate of both: remaining within the boundaries of the reference diffusion model and approximating a material with a realistic internal porosity (around 0.2 ~ 0.4)[164, 165].

Previously, concepts of ordered porous media and additive manufacturing were introduced (Sections 1.2.3 and 1.4.2). The term "ordered packing" describes extra-particle order, as opposed to intra-particle order which would occur within the stationary phase. Intra-particle order is not investigated in this work, because of the physical limits of current 3D printing technology. Therefore, when simulating porous particles, the intra-particle characteristics are estimated by using D_{pore}, instead of modelling the system at the intra-particle pore scale. Modelling at this scale would only feasible for, perhaps, a handful of particles, because a much higher resolution would be required to accurately resolve the pore features. Much like the extra-particle pores, a comparison between ordered and random internal porous structure would be valuable for understanding the effects on mass transfer within the stationary phase.

Adsorption-Desorption Model

Various models are used in the study of surface binding, known as isotherms[166]. Each of these models differs in complexity, both numerically and conceptually, and are applicable to different adsorption systems. In this work, the Langmuir isotherm was used because of its simplicity and effectiveness[167]. The isotherm was modelled by a modified rate equation (Eq. (2.12))[168], where the influence of the eluent is added to the desorption term:

$$r_{rxn} = k_{ads} C_{aq} \left(1 - \frac{C_{ads}}{C_o}\right) - k_{des} C_{Eluent} \frac{C_{ads}}{C_o} \tag{2.12}$$

where, r_{rxn} is the rate of surface reaction [NT^{-1}], k_{ads}, k_{des} are the rate constants for adsorption and desorption [L^3T^{-1}], C_{aq} is the concentration in the solution [NL^{-3}], C_{eluent} is the concentration of the eluent [NL^{-3}], C_{ads} is the adsorbed concentration [NL^{-3}] and C_o is the binding capacity of the stationary phase [NL^{-3}]. This rate equation provided dual functionality between adsorption (first term RHS) and desorption (second term RHS), dependent on the presence of the eluent. Because these processes are mass transfer limited, it is hypothesized that the adsorption model is not highly influential in chromatographic systems.

The values for k_{ads}, k_{des} and C_o were not prescribed from observations of a specific physical system, but as realistic estimates. The rate constant for adsorption was chosen to be large enough so that the adsorption process was mass transfer limited, not rate limited, as is the norm for surface reactions[169]. However, when the rate constant becomes too large, this creates instabilities in the simulation because the time step is too large to accurately resolve the rapid reaction. The desorption constant was chosen so that $k_{ads} >> k_{des}$, meaning that adsorption was dominant under standard column flow and the desorption term could only become dominant if the eluent had been introduced into the column.

2.4.3 Multi-Scale Model

A multi-scale model describes a model in which phenomena are solved at different time or spatial scales[170]. In the framework of this model, both lattices were iterated under the same global scheme, meaning that separate time steps were unable to be prescribed to each lattice. However, dispersion of the solute occurs at longer time scales than the global time step required to achieve a relaxation time of one (Section 2.4.1). This meant that the advection velocity, which was passively passed to solve the ADE, could be linearly scaled for low velocity systems. To maintain the system *Pe* with the scaled velocity field the Diffusion coefficient was also increased accordingly. To create a speed increase, global iterations were then "skipped" creating a pseudo larger time step for the ADE lattice.

To implement this technique, an integer factor was introduced which scaled all variables involved in the mass transport process while proportionally iterating at a less frequent rate, to compensate. It is important to note that the reference diffusion value was not scaled, to maintain a relaxation parameter of one, but the deviation term was altered. For simple cubic (SC) packing of spheres, the speed up of this method was found to be proportional to scale factor (Fig. 2.6a), however, the reduced plate height deviated from the non-scaled value (Fig. 2.6b). As the product of the Reynolds number and the scale factor approaches one, the error becomes large. Considering this, for all simulations the scale factor was chosen to keep the discrepancy below one percent, based on Fig. 2.6b, while providing a valuable saving in computational resources and time.

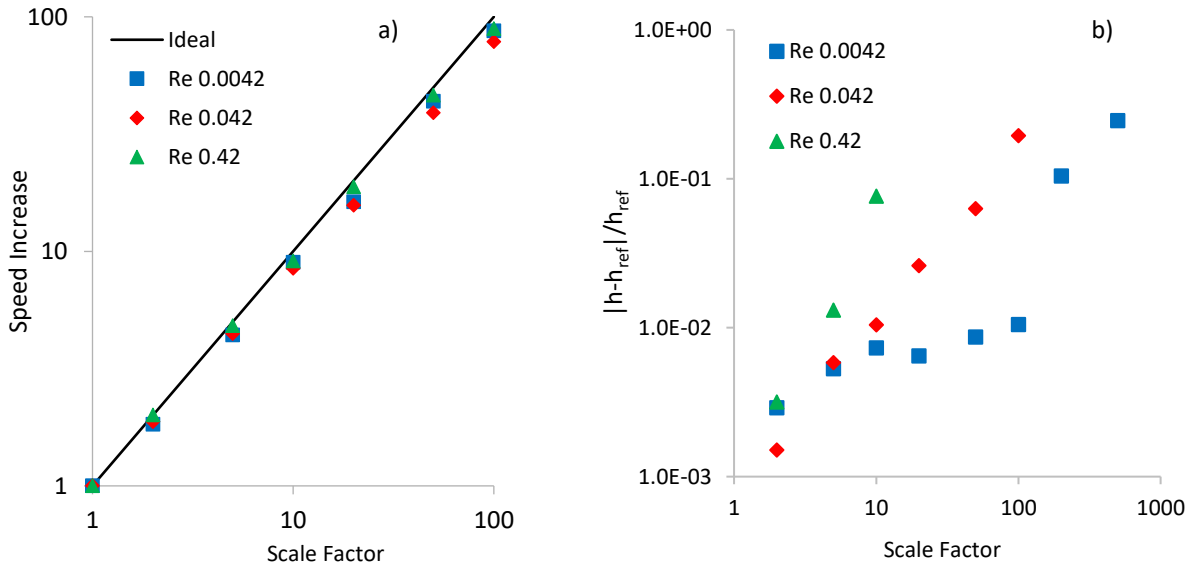

Figure 2.6. Impact of the scaling factor periodic sphere in the SC arrangement comparing: a) speed increase using the multi-scale method compared to systems in which no scale factor is used and b) deviation from the reference solution when using the scaling factor (missing values are because of divergence of the advection-diffusion lattice).

2.5 Post Processing and Analysis

2.5.1 RTD Curves

For quantifying dispersion in the bulk phase using an inert tracer species (Chapter 3-5), the RTD method was used (Section 1.3.2). However, as discrete approximation of the physical chromatographic process was used, some modifications were applied.

In a practical column, samples may only be taken at the column outlet as taking samples within the column could produce an observer effect[171]. Furthermore, in situ measurement of concentration is difficult to perform across the cross section of a porous medium because of the low system porosity. In conjunction with this, the scale of the pores being in the micro-scale and smaller requires precise instrumentation to acquire accurate measurements. For these reasons, in a practical column, it is assumed that the inlet pulse is injected with the properties a Dirac function (a mean and variance of zero), because the true values cannot be practically quantified. To counteract this, the column must be long enough to negate the relative importance of this assumption.

In a simulated environment, passive sampling may be performed at any location in the column, without influencing the results. This provides a major advantage over practical tracer studies, because dispersion can be measured at any point in the column and hence the HETP is calculated using the difference between two points[172] (Eq. (2.13)).

$$HETP = \frac{\sigma_2^2 - \sigma_1^2}{(\mu_2 - \mu_1)^2}(L_2 - L_1) \tag{2.13}$$

where the subscripts 1 and 2 represent the value of the variable at the upstream and downstream locations, respectively. Because of this adjustment, the shape of the inlet pulse was no longer influential on the measured dispersion and the Dirac pulse was no longer necessary. In the context of modelling, the Dirac pulse creates a large concentration gradient at the inlet, promoting instabilities in the numerical model. Instead of the Dirac pulse profile, a function comprised of two hyperbolic tangent terms was used, smoothing the gradients preceding and proceeding the bulk solute pulse (Eq. (2.14)).

$$C(t) = C_{max}\left(tanh\left(\frac{t}{a} + b\right) + tanh\left(\frac{-t}{c} + d\right)\right) \tag{2.14}$$

where $C(t)$ is the concentration value at the inlet [NL^{-3}], C_{max} is the amplitude of the concentration pulse [NL^{-3}] and a, b, c and d are constants which manipulate the steepness and length of the pulse. For ordered packings, multiple sampling points were chosen at geometrically periodic locations along the axial length of the column to capture the dispersion effect of each axial period (Fig. 2.7). For random packings, periodic axial lengths did not exist, so sampling points were placed at greater intervals to attenuate the fluctuating dispersion which occurs in a randomly packed column.

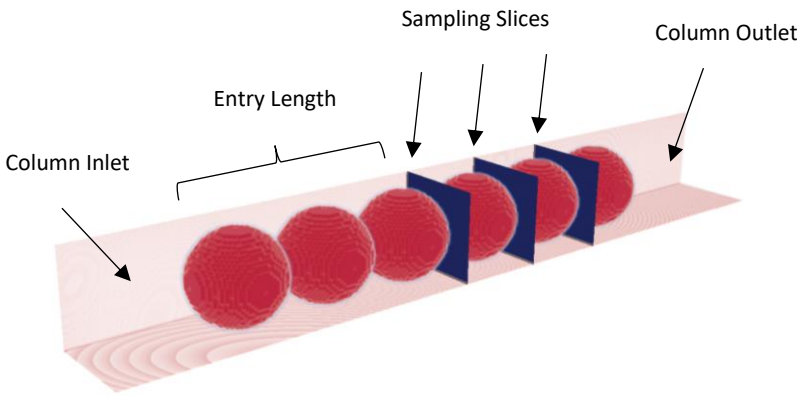

Figure 2.7. Column layout in the simulation process as illustrated for a periodic array of spheres in the SC arrangement. The column inlet and outlet allow for smooth flow resolution of the velocity profile through the Dirichlet inlet and Neumann outlet for both lattices. The entry length signifies the area in which the inlet flow develops into bulk column flow.

Another important difference between practical and simulation sampling was the determination of the average sample concentration. Practically, a sample volume is collected over a short period and the concentration of the stagnant sample is measured. The RTD is then developed using these data points and the solute mass balance is respected. In the simulation environment, samples were taken as the average concentration flux measured over "two dimensional" (1 node in thickness) slices, to measure axial dispersion over the periodic length (Eq. (2.15)).

$$m = \int_0^{\infty} \int_{[0,0]}^{[L_x,L_y]} cv \; dA_c dt \tag{2.15}$$

where L_x and L_y are the lengths of the domain in the transverse dimensions [L], m is the total amount of solute [N], dA represents the differential across the sample slice [L^2]. At each time step, the average concentration used to construct the E-curve was defined as in Eq. (2.16)

$$\bar{C} = \int_{[0,0]}^{[Lx,Ly]} cv \; dA_c \Big/ \int_{[0,0]}^{[Lx,Ly]} v \, dA_c \tag{2.16}$$

where the denominator is equal to the superficial velocity in the column. Dividing by the superficial velocity has no effect on the mean residence time or the standard deviation of the E-curve, however, it is required to maintain the appropriate units of the numerical system.

2.5.2 Chromatograms

For simulations in Chapter 6, where the chromatographic separation process is modelled, singular RTD curves were no longer used to analyse the system performance. Instead, a chromatogram was produced, which illustrated the flow concentration of each species at measured sections of the

column for the duration of the process[173] (Fig. (2.8)). This is more of a qualitative approach than using reduced plate height and is more open to interpretation, however, this is a more representative approach to real chromatographic systems than using RTD curves for non-porous solid phases.

Convention for the independent variable of the chromatogram uses time or volume[4]. Time is used as an absolute quantity, while volume is converted to a dimensionless quantity (Eq. (2.17)).

$$V'(t) = t\frac{\dot{Q}}{V} \tag{2.17}$$

where V is the empty column volume [L^3] and $\dot{Q}$ is the volumetric flow rate [L^3T^{-1}]. Which variable to use is a subjective decision; V' shows the most optimal process with respect to the amount of eluent which is used to flush the column, whereas using time shows the relative speed of one process to another (not considering the amount of eluent used). An important aspect of a chromatogram is ensuring baseline separation, i.e. the peaks of the chromatogram do not overlap. If baseline separation is not achieved this corresponds to an impure analyte sample and the process must be repeated or the affected portion of the sample discarded.

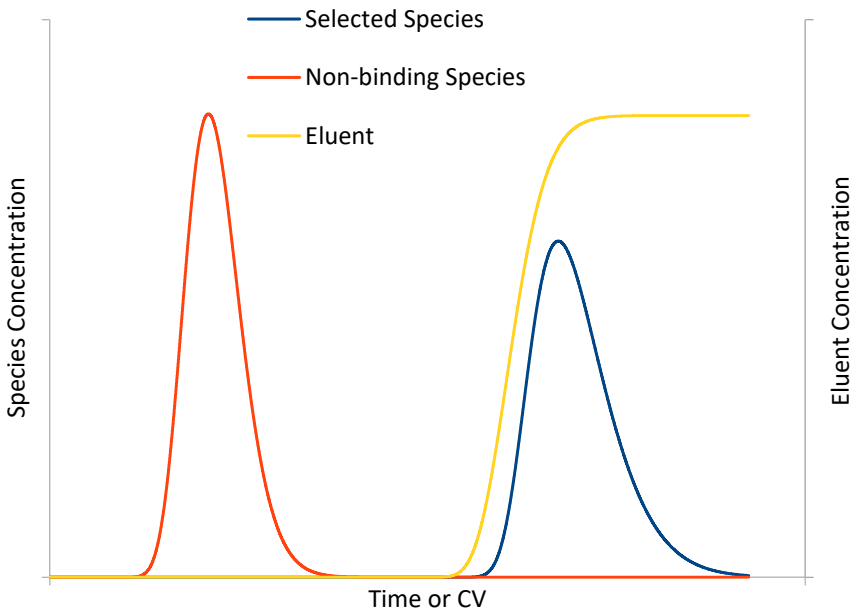

Figure 2.8. Illustration of a chromatogram which has achieved baseline separation between the selected and non-binding chemical species. The selected species is only observed once the eluent has been introduced into the column, as is the expected behaviour in a chromatographic process.

2.6 Computational Data

CFD simulations can be computationally intensive, as a result of the large number of floating point operations (FLOP) that are performed when iteratively solving the governing equations[174]. In

this study, it was found that the important factors determining the amount of FLOP required for a complete simulation were the system velocity and the domain size (measured in nodes). From the method outlined in Section 2.4.3, speed increases in lower *Re* systems made the ratio of time step to linear velocity equivalent for all systems and the total time of completion instead became a function of the reduced plate height instead of the system velocity. This meant that the fastest simulation for any given morphology had the lowest simulation time and shifting from the optimum, either to a lower or higher *Pe*, increased the simulation time (and FLOP required).

The number of simulation nodes was a function of the number of unit cells in each dimension and the spatial resolution of the domain. In the axial dimension, the number of unit cells was determined by the Reynolds number and for the transverse dimensions it was determined by the boundary type (confined vs. periodic). The spatial resolution was determined by the trade-off between simulation accuracy and time. Even at low resolution, simulations with large domains involved millions of simulation nodes, leading to the necessity of using high performance computing (HPC) to solve these complex systems.

2.6.1 Hardware

For this thesis, multiple HPC systems at the New Zealand eScience Infrastructure were used, as follows:

- "Pan" - Sections of the cluster used were up to 6 nodes of 24 core (2.7 GHz) Intel Ivy Bridge
- "Beatrice" (retired) – P755 cluster 13 x 4 CPU (8 core 3.3 GHz)
- "Foster" (retired) – 2,048 CPU (4 core) Blue Gene/P

2.6.2 Parallelization and Performance

Parallelization is a method used in modern computing, in which a larger task is fragmented into smaller tasks and distributed, using message passing interface (MPI), to be separate processors[175]. Parallelization has also become more utilized in common computing, because of the increased use of multi-core processors in domestic computers, meaning that programs like Palabos can show improved performance on these systems. However, large simulations still require HPC systems, which use parallelization by aggregating large "clusters" of computing cores.

For parallelization to be effective, the task must be able to be effectively broken into smaller, (semi)discrete tasks, so that there is minimal dependency of one task on another. If a task requires information from another task, this creates simulation bottlenecks, which lead to a reduction in parallel efficiency[176]. For the LBM, all calculations are performed locally, making it a prime candidate for parallelization and HPC systems.

Performance

The Pan system uses Red Hat Enterprise Linux v6.3 and g++ 4.4.7 as the C++ compiler. For the internal network, QDR InfiniBand is used, which is rated at 40 Gb/s. Performance of the model is here measured using Mega Site-Updates Per Second (MSUPS), which is the number of sites in the LB lattice on which the governing equation is solved, per second (x 10^{-6}). Using a single node (24 cores) of the Pan system, achieved a performance of around 20 MSUPS for the velocity lattice and 34 MSUPS for the ADE lattice. The stationary phase in these simulations was non-porous, meaning that solid nodes only required a fraction of the computational time, compared to fluid nodes.

Using the multi-scale method improved the overall simulation speed but, did not directly influence the site updates. This is because the multi-scale method reduced the rate at which the lattice was updated with respect to the global iterations scheme. The pseudo increase in MSUPS would be < 34 x n, where n is the scaling factor, which would be less than the ideal case (equal to the scaling factor) because of operations in the main iterative loop which are not involved with the collision and streaming processes. These speeds are comparable to the Palabos benchmarks[177].

Scalability

The property of scalability is how efficiently a code is performed by a variable number of processors and is considered as a quantitative measure of parallelization[45, 178, 179]. A program with perfect scaling will experience a speed up proportional to the increase in computational power, however, this is only theoretical and is not achieved in practice because of MPI requirements. It is first noted that this work uses multiple computing systems, domain sizes, geometries and physical phenomena, making it difficult to judge specific performance of the model with a single test. To gain an estimate of the performance, a single morphology was scaled on the Pan system (Fig. 2.9). A domain of 12 x 30^3 unit cells at a porosity around 0.5 was used, meaning the domain comprised approximately 160,000 fluid nodes and 160,000 solid nodes.

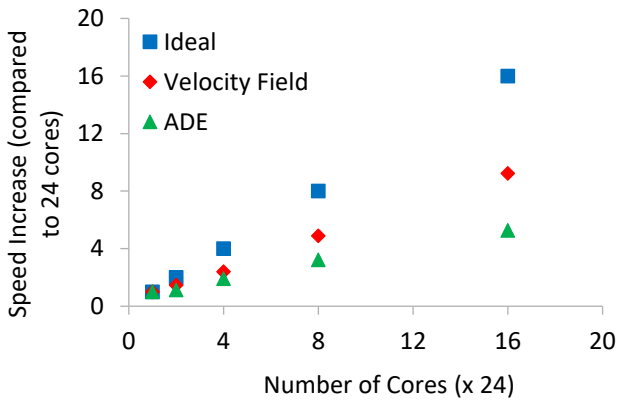

Figure 2.9. Scaling performance of the model on the Pan system. Each core contained 2 x 2.7 GHz Intel Ivy Bridge processors.

For the Pan system, increasing the number of cores improved the performance for both the velocity and the ADE lattice. The speed increase of both lattices scaled linearly with the number of cores and the parallel efficiency decreased as more cores were used. At the maximum number of cores tested (16 x 24), the parallel efficiency for the velocity field was 50%, while the concentration lattice was at around 30% (which is considered poor scaling). The difference between the performance for the two lattices was thought to be a result of the extra operations involved with the advection-diffusion lattice, such as manipulating the boundary conditions for the tracer and a monitoring convergence criteria, the latter of which was not well parallelized.

For pre-processing and I/O operations, however, it was found that increasing the number of cores decreased performance, showing that these functions are not well parallelized. Although the performance of these functions was decreased, the relative time loss compared to the time saved from the collision and streaming processes of the two LB lattices was minimal. This became more of a factor for larger simulations, such as random packings and is an area which would benefit from an optimization of the parallelization methods.

The final consideration, especially when using shared clusters is the amount of traffic and the scheduling process which is used. Generally, these systems favour jobs using less cores and the computational advantage provided by using extra cores is outweighed by the amount of consequent queue time. Hence, for this system, the number of cores per job was selected to increase the simulation throughput.

2.7 Independence Studies

Analogous to the mesh independence study (Section 2.2.1) several simulation variables were investigated to verify the model's independence from their value. Failure to prove independence would contradict physical behaviour and indicate an error in the model. Each of these studies were conducted using periodic spheres in the SC arrangement.

2.7.1 Length Scale

The length scale (diameter) of the spherical particles was altered while the system velocity was adjusted so that both the *Pe* and *Re* were maintained (Table 2.1). As the LBM nondimensionalizes all physical variables to lattice units before simulation, these simulations should be numerically identical within the LB framework; producing identical dispersion data. From the results, the model was confirmed to be independent of the length scale, meaning that all equivalent *Re* and *Pe* systems produce equivalent results.

Table 2.1. Effect of the physical particle size on the reduced plate height for SC packing of spheres at Pe = 10.

Length Scale [m]	0.002	0.0002	0.00002
h	0.674	0.674	0.674

2.7.2 Inlet concentration

In a physical study, the quantity of tracer species would be measured by the number of moles introduced into the system[74]. In the simulation environment, the amount of solute is defined by the integral of the pulse function (Section 2.5.1), which is simulated by manipulating the inlet Dirichlet boundary of the advection diffusion lattice. For all simulations, the maximum concentration of the pulse function was arbitrarily chosen as 1 mol/L to maintain consistency. However, it was shown that altering the max concentration through a range of five orders of magnitude did not deviate by more than 1% (Table 2.2.) meaning that the dispersion data can be considered independent of the inlet concentration.

Table 2.2. Effect of the inlet concentration on the reduced plate height for SC packing of spheres at Pe = 10.

Concentration [mol/L]	10	1	0.1	0.01	0.001
h	0.668	0.674	0.675	0.673	0.675

2.7.3 Sampling Interval

The sampling time was the interval between which the average concentration for each slice was calculated, measured in iterations. Ideally, samples would be calculated at every iteration, but this would increase simulation time, because of the poor scalability of I/O operations. However, increasing the sampling period was found to compromise the accuracy of the model (Fig. 2.10).

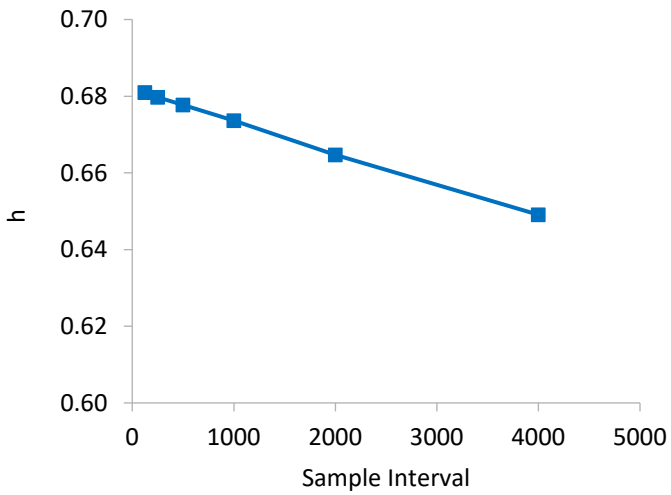

Figure 2.10. The Influence of sampling interval on the reduced plate height for SC packing of spheres at Pe = 10.

An interesting trend is observed, which shows that the reduced plate height is negatively proportional to the sample interval within this range, a result which was also confirmed for other morphologies and Peclet numbers. The percentage error of *h* was also found to be roughly proportional to the product of the Peclet number and the sample interval:

$$\%Error = N_{sample}\frac{Pe}{10^5} \tag{2.18}$$

where N_{sample} is the sample interval. For this study, Eq. (2.18) was used as a guideline to keep the error below 1% for any given simulation. A result of this relationship is that the data can be linearly extrapolated to the y-axis, signifying the limit as the sample time approaches zero giving an infinitely small sample time. However, because this is a discretized system with respect to time, it is unknown if this is an accurate result.

2.8 Model Validation

Before the model was used to produce novel data, as presented in Chapters 3-6, it was first validated by using three test cases, each of which had contextual relevance to this work. Initially, the BGK-LBM solver was used to determine the permeability of ordered sphere packings compared with studies using both the same model and other methods. Secondly, the ADE model was used to model Taylor-Aris dispersion in a cylindrical capillary, which has an analytical result. Finally, the model was compared with two important studies in the literature, which investigate dispersion in random jammed packing of monodisperse spheres.

2.8.1 Permeability of Sphere Packings

This section investigates the Darcian permeability (Eq. (1.1)) data for ordered sphere packings: SC, BCC and FCC as well as random jammed packing. This is a well-studied area for both the LBM and other methods. Comparison of the results produced here with literature data (Table 2.3), shows the close agreement between all data sets with no greater than a 2% discrepancy between results.

Table 2.3. Comparison between dimensionless permeability of ordered sphere packings between this work and literature.

Packing	This Work	Schure et al.[14]	Khirevich[45]	Zick et al.[181]	Sangani et al.[182]
SC	2.51E-03	2.46E-03		2.52E-03	2.52E-03
BCC	4.93E-04	4.96E-04	4.92E-04	5.01E-04	5.04E-04
FCC	1.71E-04	1.70E-04		1.72E-04	1.71E-04
Random	6.91E-04	6.44E-04	6.97E-04		

It is noted that the LBM can cause a slightly lower observed permeability because of the way in which the viscosity is handled when using BB boundaries[45, 180]. The work of Schure[14] and

Khirevich[45] also used the LBM-BGK method to calculate the velocity fields, while Zick et al.[181] and Sangani et al.[182] used analytical methods.

It should also be noted that Zick et al. and Sangani et al. represent their data in terms of the drag coefficient, c_d. To convert this to permeability, we use Darcy's Law (Eq. (2.19)) and the Stokes drag equation for a sphere (Eq. (2.20)).

$$\dot{Q} = -k\frac{A_c}{\nu\rho}\frac{dP}{dZ} \tag{2.19}$$

$$F_d = 6\pi\nu\rho\frac{d}{2}\bar{u}c_d \tag{2.20}$$

where F_d is the drag force for a single sphere [MLT^{-2}]. From the definition of pressure (P = F/A), the pressure drop across the unit cell is related to the drag force, Eq. (2.21)

$$\frac{dP}{dZ} = \frac{n_s F_d}{L_c^3} \tag{2.21}$$

where n_s is the number of spheres in the unit cell and L_c is the length of the unit cell [L]. Combining Eqs. (2.19), (2.20) and (2.21) yields a relationship between k and c_s (Eq. (2.22)).

$$k = \left(\frac{L_c}{d}\right)^3 \frac{1}{(3n_s\pi c_d)} \tag{2.22}$$

where, L/d is the ratio between the unit cell length and particle diameter for a given sphere packing which can be analytically defined by trigonometric relationships within the unit cell (Table 3.1).

As a final validation, recall the pressure drop expressions for dimensionless permeability (Eq. (2.23)) and the Carman-Kozeny equation (Eq. (2.24)):

$$\frac{dP}{dz} = \frac{-1}{k}\frac{\mu}{d^2}u_{sup} \tag{2.23}$$

$$\frac{dP}{dz} = -c_{CK}\frac{(1-\varepsilon)^2}{\varepsilon^3}\frac{\mu}{d^2}u_{sup} \tag{2.24}$$

where c_{CK} is the Carman-Kozeny coefficient, which can have a value of either 150 or 180, as stated in the literature[51-53]. Combining Eqs. (2.23) and (2.24), this yields and expression which allows us to compare between the observed k and the equivalent Carman-Kozeny expression (Eq. (2.25)).

$$\frac{1}{k} = c_{CK}\frac{(1-\varepsilon)^2}{\varepsilon^3} \tag{2.25}$$

The Carman-Kozeny estimations, using the two different coefficients, was plotted against the permeability data from the LBM simulations in Fig. 2.11, showing a strong correlation between the two data sets.

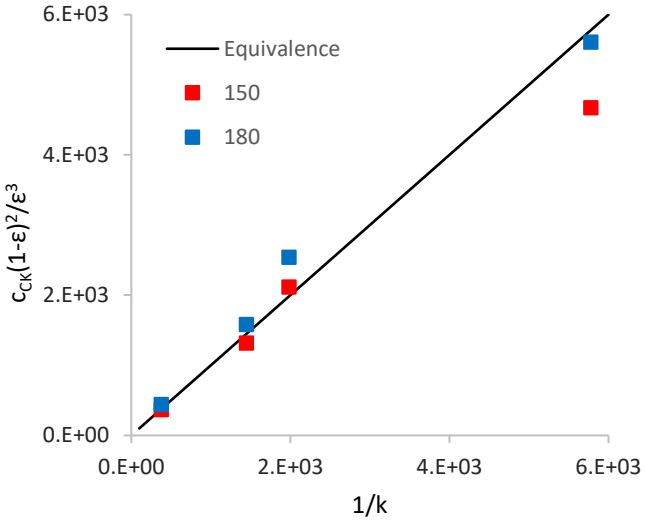

Figure 2.11. Comparison of inverse permeability from each packing family with the empirical terms from the Carman-Kozeny equation. These terms correlate with the LHS and RHS of Eq. (2.25), respectively. The equivalence plot represents the points at which these terms are equal.

2.8.2 Taylor Dispersion in a Cylindrical Channel

As an initial case for the ADE solution method, a simple case of Taylor dispersion in a cylindrical channel was observed. Taylor dispersion describes the scenario in which a shear flow causes an increase in effective diffusivity as a result of the velocity gradient in boundary layer[183]. Bird et al.[33] provide a comprehensive overview of these systems (refer to Section 20.5 of this reference). Before an analytical solution is obtained, there are two important variables which dictate the appropriate method. First, the dimensionless time (Eq. (2.26)) is calculated, which describes the importance of the θ-dependence of the mass fraction and corresponds to the contributions from radial diffusion, as such:

$$t_o = \frac{tD_m}{R^2} \tag{2.26}$$

where t_o is the dimensionless time and R_c is the radius of the channel. When the dimensionless time is greater than one, this importance diminishes, and Taylor's analysis may be applied. Taylor proposed that the effective axial diffusion coefficient in a cylindrical tube (Eq. (2.27)).

$$D_{axial} = \frac{Pe^2 D_m}{48} \tag{2.27}$$

where D_{axial} is the effective axial diffusion coefficient [L^2T^{-1}]. However, this term is proportional to the Peclet number and only appropriate for high Reynolds numbers, where advection is dominant. This is

confirmed by Bird et al.[33] showing that below a Peclet of roughly 100, that a correction term is needed, as proposed by Aris[57] (Eq. (2.28)):

$$D_{axial} = D_m \left(1 + \frac{Pe^2}{48}\right) \tag{2.28}$$

The relation between effective diffusivity and reduced plate height, as stated by Giddings (Eq. (2.29))[184], can be equated to the Taylor and Taylor-Aris relationships, to yield an expression for the reduced plate height for capillary flow (Eq. (2.30)).

$$D_{axial} = \frac{Pe\ h\ D_m}{2} \tag{2.29}$$

$$h = \frac{Pe}{24} \tag{2.30a}$$

$$h = \frac{2}{Pe} + \frac{Pe}{24} \tag{2.30b}$$

The model developed in this work is compared to the analytical data (Fig. 2.12) and shows great agreement to the Taylor-Aris expression (Eq. (2.30b)) for most of the Peclet range presented here. These two data sets also converge to the original Taylor expression (Eq. (2.31a)) as the Peclet number increases. However, as the Peclet number decreases and diffusion begins to dominate, the Taylor-Aris expression no longer predicts the solute behaviour, which again, agrees with the analysis presented by Bird et al[33].

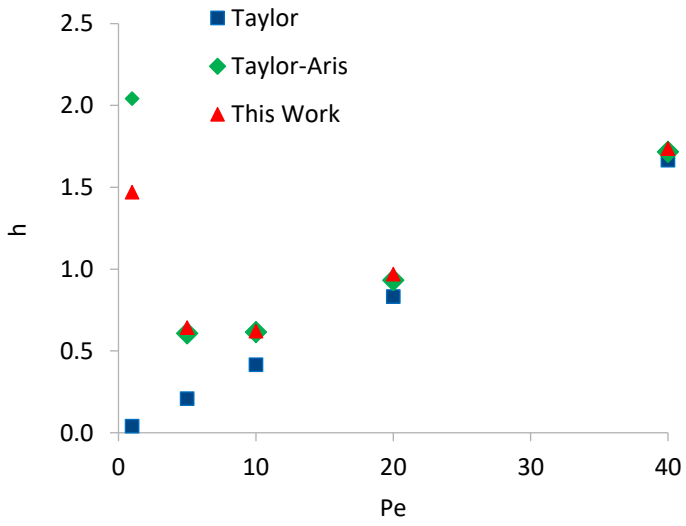

Figure 2.12. Comparison of dispersion in a cylindrical capillary as analytically defined by the Taylor and Taylor-Aris analyses and modelled using the ADE solution method from this study.

2.8.3 Dispersion in Random Sphere Packing

The final validation comes from comparison with recent literature, investigating dispersion in jammed random packing of equally sized spheres[14, 45]. Using the developed model, five different

random packings were modelled, and the results averaged for each Peclet number. For our simulations, the resolution was 30^3 LB nodes to resolve a single particle and an overall domain size of $7d_p$ in the transverse dimensions and $11d_p$ in the axial dimension (to include the inlet and outlet) (Fig. 2.13a). To accommodate for periodic boundary conditions, particles which intersected with the transverse boundaries were copied to the opposite domain boundary to complete the periodicity.

Comparing with the literature (Fig. 2.13b), shows that these sources present very different numerical results from one another, though both utilize the BGK model for flow field calculation. The numerical results from this study show close agreement between this work and from the thesis of Khirevich[45]. Although the results differ from the work of Schure et al[14], taking the numerical differences into account, it can be see that the trends and turning points of the of each curve are quantitatively similar. The source of these quantitative differences is not investigated here.

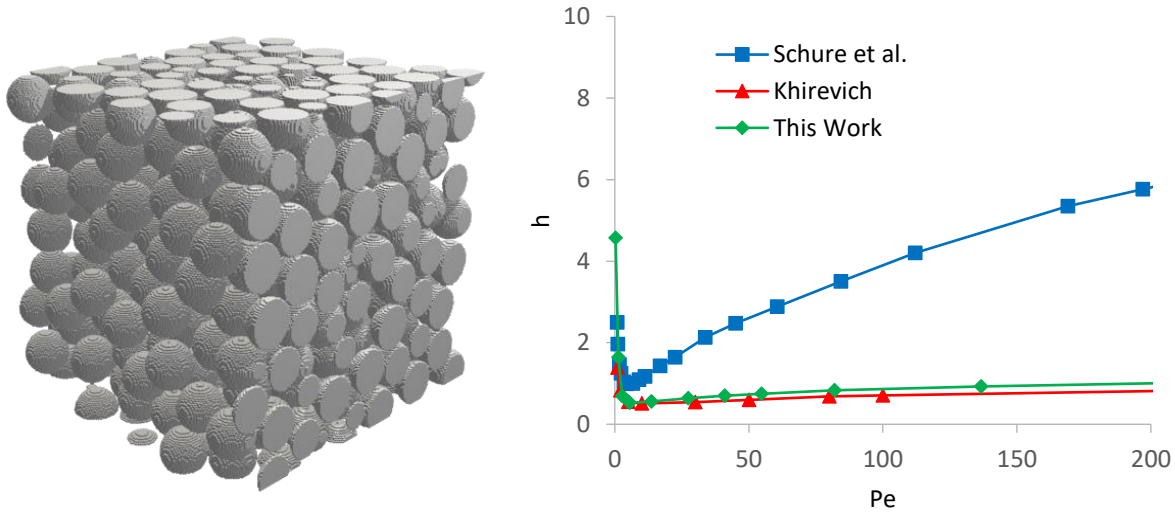

Figure 2.13. a) Illustration of a jammed random packing of monodisperse spheres using periodic boundary conditions and b) Comparison of data for reduced plate height of jammed random sphere packing between: Schure et al. (blue), Khirevich (red) and this work (green).

It is noted that all data presented here is generated from numerical simulation, as opposed to measured physical results. This is a recurring theme throughout this thesis (excluding Sections 2.8.1 and 2.8.2) because of the increased complexity in practical systems that are difficult to accurately replicate in numerical systems. Most notable differences include: non-uniform inlet distribution, inaccuracies in the fabrication process, column confinement and practical sampling limitations. Furthermore, based on the work of Schure et al.[14], the focus of this work is the optimization of ordered packings and hence, there is no scope in this study for an extensive validation for randomly packed beds. It is noted that there is at least one practical study that investigates ordered packings[13] and there is planned published work that compares simulation based results of TPMS structures with physical studies from 3D printed columns.

3. Chromatographic Performance of Ordered Packed Beds

3.1 Introduction

Packed beds are the practical standard in functional porous media because of their versatility and simple fabrication (Section 1.3.1). An important packed bed morphology in literature is the jammed random packing of mono-disperse spheres[45, 185], which is considered as a benchmark for practical performance due to efficient packing which creates a low voidage system, while maintaining permeable flow channels. However, the idealization of jammed random sphere packings has been challenged by the work of Schure et al.[14], who demonstrated that under certain flow conditions, a face-centred cubic (FCC) packing of spheres demonstrated lower band broadening than jammed random packing. This increase in efficiency was thought to be due to a reduction in eddy dispersion, based on van Deemter's analysis of dispersion in porous media (Section 1.2.2). Proceeding these initial findings by Schure, there has been little simulation based work investigating dispersion in ordered packings[46], perhaps due to the complications involved with producing physical analogues of the simulated structures. However, using additive manufacturing (Section 1.3.2), ordered packings are now a physically feasible and attractive concept[12, 13], which incentivises further inquiry into the capabilities of ordered packed beds.

This chapter begins by revisiting the work of Schure et al.[14], which focused on comparison of dispersion in jammed random packing and basic ordered sphere packing arrangements: simple cubic (SC), body-centred cubic (BCC) and FCC, each of which is based on the atomic crystal lattice[186]. From this starting point, the novel concept of orientation was introduced, which described the orientation of the axial flow direction with respect to the cubic crystal cell and chromatographic metrics were ascertained for each of these systems (Section 3.2).

Continuing investigation into packed beds, based on a recent work by Nawada et al.[13], the idea of spheres as the ideal shape for ordered packed beds was challenged. In this work, octahedral and tetrahedral particles packs were simulated for the same orientations and arrangements as for sphere packings, with the aim of further solidifying the physical findings of Nawada et al. and demonstrating the feasibility of alternative particle packings for ordered systems (Section 3.3).

Finally, the concept of particle overlap was investigated (Section 3.4), a feature that has been introduced into the 3D printing process to avoid potential physical instabilities that could occur by movement of individual geometric elements within ordered packed beds[13]. To create overlap in packed

bed systems, the particle size was increased while the distance between the particle centres is maintained. This distorted the distinction between packed beds and monolithic structures when using 3D printing as a fabrication method.

3.1.1 Ordered Packed Bed Characteristics

To understand ordered packings on a geometric level, several variables must first be defined. The characteristic length of a particle (d_p) is an important factor, because it is used to calculate both the Peclet and Reynolds numbers. For a sphere, this is simply defined as the particle diameter, but as the particle shape becomes less homogeneous, defining the value for this length becomes more ambiguous and is covered in Section 3.3.

In a packed bed, the location of particles with respect to one another defines the configuration of the ordered packing and is a focal point of the current chapter. Two parameters, arrangement and orientation, are used to define the location of each particle's centre. In this work, arrangement refers to how particles were placed with respect to each other, based on the cubic crystal arrangements: SC, BCC and FCC. Orientation refers herein to how the axial flow aligns with the crystal cubic cell and is denoted using Miller Indices[187]. The orientation can also be conceptualized as a rotation of the packed bed with respect to a constant axial flow; for technical purposes, the two scenarios are analogous. In this work three orientations were studied, which were assumed to be limiting cases and the dispersion properties of another rotated system would be bounded by these results:

- [001] – axial dimension is normal to the cubic cell face
- [011] – axial dimension aligns with the edges of the cubic cell ($\pi/4$ rotation in the YZ plane)
- [111] – axial dimension aligns with the opposite vertices of the cubic cell ($\pi/4$ rotation in the YZ plane and $\tan^{-1}(1/\sqrt{2})$ in the XZ plane)

where Z represents the axial and X and Y represent the transverse dimensions. To visualize these rotations, spheres are used to more clearly illustrate the particle configurations (Fig. 3.1), but these configurations apply equally to other particle shapes. For random packing, particle locations must be specifically generated for a given domain size and particle shape, but for ordered packings the domain can be extended infinitely in any dimension because of the periodic properties of the defined unit cell (Table 3.1). It is interesting to note that some configurations show similar structure, particularly: BCC [001] - FCC [011] and FCC [001] - BCC [011] and hence, they would perhaps be expected to have similar performance.

Table 3.1. Packing properties of the sphere packings studied in this section.

Packing Configuration	Cell Length[a] (x, y, z)	Particles per unit cell	Porosity
SC [001]	1, 1, 1	1	
SC [011]	1, √2, √2	2	0.48
SC [111]	2√3/√2, √2, √3	6	
BCC [001]	2/√3, 2/√3, 2/√3	2	
BCC [011]	2/√3, 2√2/√3, 2√2/√3	4	0.32
BCC [111]	2√2, 2√2/√3, 1	6	
FCC [001]	√2, √2, √2	4	
FCC [011]	√2, 1, 1	2	0.26
FCC [111]	√3, 1, 2√3/√2	6	
Random	7, 7, 7	416	0.36

[a] Dimensionless length, 1 corresponds to one particle diameter

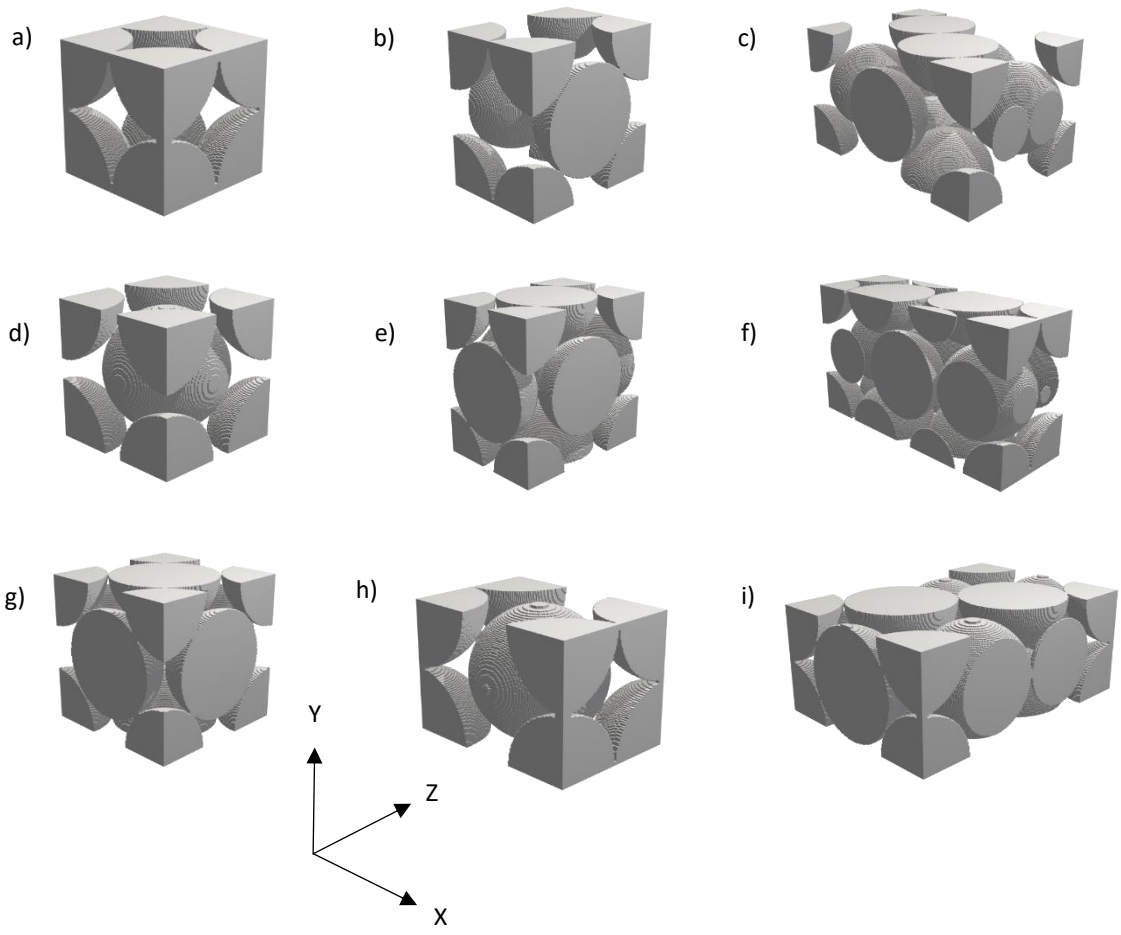

Figure 3.1. Visualization of the packing configurations in this study: a) SC [001], b) SC [011], c) SC [111], d) BCC [001], e) BCC [011], f) BCC [111], g) FCC [001], h) FCC [011], i) FCC [111].

The particle location was then used to generate the volume of the particle within the simulated environment. The shape of each particle was defined by either a single or a combination of Cartesian inequalities to define solid nodes (grid locations which satisfy the inequality) (Eqs. (3.1) – (3.3)).

Sphere:

$$(x - x_o)^2 + (y - y_o)^2 + (z - z_o)^2 < r^2 \tag{3.1}$$

Octahedron:

$$|x - x_o| + |y - y_o| + |z - z_o| < r^2 \tag{3.2}$$

Tetrahedron:

$$x_{norm} = x - x_o,\ y_{norm} = y - y_o,\ \ z_{norm} = z - z_o \tag{3.3a}$$

$$x_{norm} + y_{norm} + z_{norm} < r \tag{3.3b}$$

$$-x_{norm} - y_{norm} + z_{norm} < r \tag{3.3c}$$

$$x_{norm} - y_{norm} - z_{norm} < r \tag{3.3d}$$

$$-x_{norm} + y_{norm} - z_{norm} < r \tag{3.3e}$$

These numerical definitions of the octahedral and tetrahedral particles were not unique, meaning that the shapes could equally be defined by an alternative set of equations that would retain the characteristic shape but change the "alignment" of the particle with respect to the cubic cell. It is hypothesized that changing the alignment of the particle would cause different results from those presented in this chapter. The choices for the declarations are discussed in the relevant chapters examining alternative particle shapes (Section 3.3).

In the model, the particle and the unit cell it was contained within were defined separately. To explain this design choice, consider the simplest orientation, SC [001], in which there is one particle per unit cell. Now consider BCC [001], there are two particles per unit cell – but the physical particle size has not changed, hence, it is simpler to manipulate the size of the unit cell rather than reducing the particle size (which would affect the system resolution). More importantly, this accommodated the ability to manipulate the particle size without increasing the size of the unit cell, creating a factor known as particle overlap. Overlap is a technique that has been used in 3D-printed, ordered column packings to maintain structural integrity of the packing[13] (Eq. (3.4))

$$\beta = \frac{d_c}{L_p} \tag{3.4}$$

where β is the particle overlap, d_c is the circumdiameter of the particle [L] and L_p is distance between nearest particle centres [L]. A value less than one would be infeasible in a practical setting, as there would be no physical contact between particles and an imposed pressure field would cause reconfiguration of the bed geometry. As well as improving structural integrity, increasing the overlap decreases void space and increases column capacity, but it has been practically shown that higher overlap increases peak skewness for beds of octahedrons[188]. The fabrication process for both discrete and overlapped columns is the same when using additive manufacturing, meaning that packed beds and monolithic columns are part of a continuum of column morphologies instead of existing as distinct packing types.

3.1.2 Defining Particle Locations

Arrangement

The centre of the seed particle for any packed bed was defined at one radius from the origin in each spatial dimension (ignoring the empty inlet length), so that the particle surface was in contact with the domain boundaries. From this seed particle, the other particles in the bed were located using the characteristics of the specified particle arrangement. To more clearly describe the packing methodology, the concept of primary and secondary particles is defined, based on their location in the unit cell (Fig. 3.2). For Simple Cubic (SC) packings, primary particle centres were placed at a length of d_p from one another in each spatial dimension, while secondary particles did not apply for this case. For Body Centred Cubic (BCC) and Face Centred Cubic (FCC), the unit cell length distance was extended to $2/\sqrt{3}*d_p$ and $\sqrt{2}*d_p$ respectively, causing the primary particles to lose contact. For BCC, a single secondary particle was added at diagonal vector of $d_p/\sqrt{3}*(1, 1, 1)$ from the origin, while in FCC three particles were added at vectors: $d_p/\sqrt{2}*(1, 1, 0)$, $d_p/\sqrt{2}*(0, 1, 1)$ and $d_p/\sqrt{2}*(1, 0, 1)$.

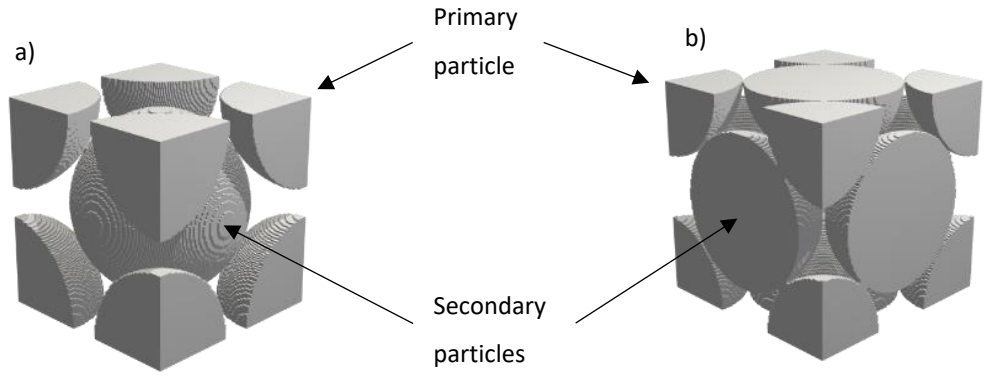

Figure 3.2. Illustrating the definition of primary and secondary particles, specifically in: a) BCC and b) FCC particle packings.

Orientation

To change the orientation of the axial flow, the packed bed itself was rotated to keep the overall domain as a cuboid, which was necessary to retain periodic boundary conditions within the framework of the model. Rotations were performed on the standard [001] orientation using either a singular (for [011]) or a combination of two rotational transformations (for [111]). These transformations were performed using 2D rotational matrices (Eq. (3.5))[189].

$$Rot = \begin{bmatrix} cos\theta & -sin\theta \\ sin\theta & cos\theta \end{bmatrix} \tag{3.5a}$$

$$x'_1 = x_1 cos\theta - x_2 sin\theta, \qquad x'_2 = x_1 sin\theta + x_2 cos\theta \tag{3.5b}$$

where *Rot* is the rotational matrix, x_1, x_2 are the coordinates in two spatial dimensions in which the rotation takes place (e.g. X and Y) [L], x'_1, x'_2 are the transformed coordinates in the corresponding spatial dimensions [L] and θ is the angle of rotation. Because this transform was exclusively for particle centres, for non-spherical particles, a rotation was also required for the particle declaration itself. For example, for an octahedral pack in the [011] orientation, Eq. (3.2) would be modified as such:

$$|x - x_o| + \left|(y - y_o)cos\left(\frac{\pi}{4}\right) - (z - z_o)sin\left(\frac{\pi}{4}\right)\right| + \left|(y - y_o)sin\left(\frac{\pi}{4}\right) + (z - z_o)cos\left(\frac{\pi}{4}\right)\right| < r^2 \tag{3.6}$$

Before the rotational transform was performed, the centre of the particle bed was translated to the origin and following from the single or combination of rotations, the centre of the particle bed was translated back to its initial location. This was done because the rotational process occurs about the origin and this process retained the centre of mass of the particle bed within the domain. However, the process still caused particles to be positioned outside of the simulation domain due to the incongruence of the domain and the transformed particle bed. To counteract this, a surplus of particles was initially defined so that the resultant particle field after rotation would be sufficient to describe the rotated packing. This did not cause issues at small bed sizes and low resolution, however, when these variables were increased, this would cause a large increase in pre-processing time. To minimize this factor, the particles which no longer intersected the domain boundaries after rotation could be transposed into the domain by a multiple of the unit cell length, depending on their distance from the domain.

Alignment

A sphere has the property of infinite rotational symmetry on any axis which intersects the centre of mass, i.e. the particle is identical from any angle – given homogenous internal particle morphology. However, for tetrahedrons and octahedrons do not have this property, and altering the particle alignment with respect to the unit cell is likely to change the properties of the medium. The alignment of non-

spherical particles with respect to the unit cell in the SC [001] packing, is not investigated in this work, but is expected to impact on both the porosity and dispersion characteristics of a packed bed of non-spherical particles.

3.1.3 Entry Length

The Neumann and Dirichlet boundary conditions selected at the entrance and exit of the packed bed are descriptive of a chromatography column with a "real" inlet and outlet. This choice has the benefit of monitoring the flow and concentration profiles at various points within the column, which is particularly advantageous when extending these models to real adsorption problems. This is an element of novelty with respect to previous work, where periodic boundaries were employed in the axial direction[14, 45]. Accordingly, the domain was composed of an appropriate series of unit cells aligned in the axial direction. In such domains, a transition from flat velocity profile and fully developed bulk flow occurs in an entrance region downstream of the column inlet[33]. In this work, the entry length was determined by comparing the reduced plate height between two consecutive sampling cross-sections and checking if this remained unchanged within 1% for each sampled section thereafter. For ordered packings, the relevant RTD curves were simulated at cross-sections positioned at periodic intervals along the axial length (Fig. 3a).

For ordered sphere packings, the entry length decreased as bed porosity decreased from SC to BCC to FCC (Fig. 3.3, Table 3.1). This result indicates that a more compact bed, with less evidence of straight channel flow patterns, has the capability to more efficiently disrupt the inlet linear flow profile. This same observation can be made in terms of tortuosity (Fig. 3.3, Table 3.2), where a more tortuous flow pattern favours transverse mixing, thus reducing the entry length. This is particularly apparent with the SC configuration, where the [001] orientation was characterized by a larger entrance region and a lower tortuosity with respect to the [011] and [111] orientations. The entry length was also correlated with *Re*, where higher velocities required longer entry lengths. At relatively low *Re*, i.e. close to Stokes flow conditions, all packing types had an entry length of a single unit cell. In this case, viscous forces are more relevant than inertial forces, hence favouring the rapid establishment of a fully developed flow profile. Clearly, upon exceeding Stokes flow, the entry length extended beyond the first unit cell. It is worth noting here that the entrance length does not have a significant impact on practical chromatography columns with ordered packing configurations.

Interestingly, the entry length for random packing did not extend beyond the first bead diameter. This is consistent with the tortuous nature of random configurations, where the flat velocity profile is immediately disrupted by the packed bed. Because of variations in the geometry from one sampling section to the following (one particle diameter distance), the reduced plate height and permeability varied markedly between consecutive segments. This problem was overcome by evaluating the key

performance indicators as the average between several longer sampling sections over five different random packings.

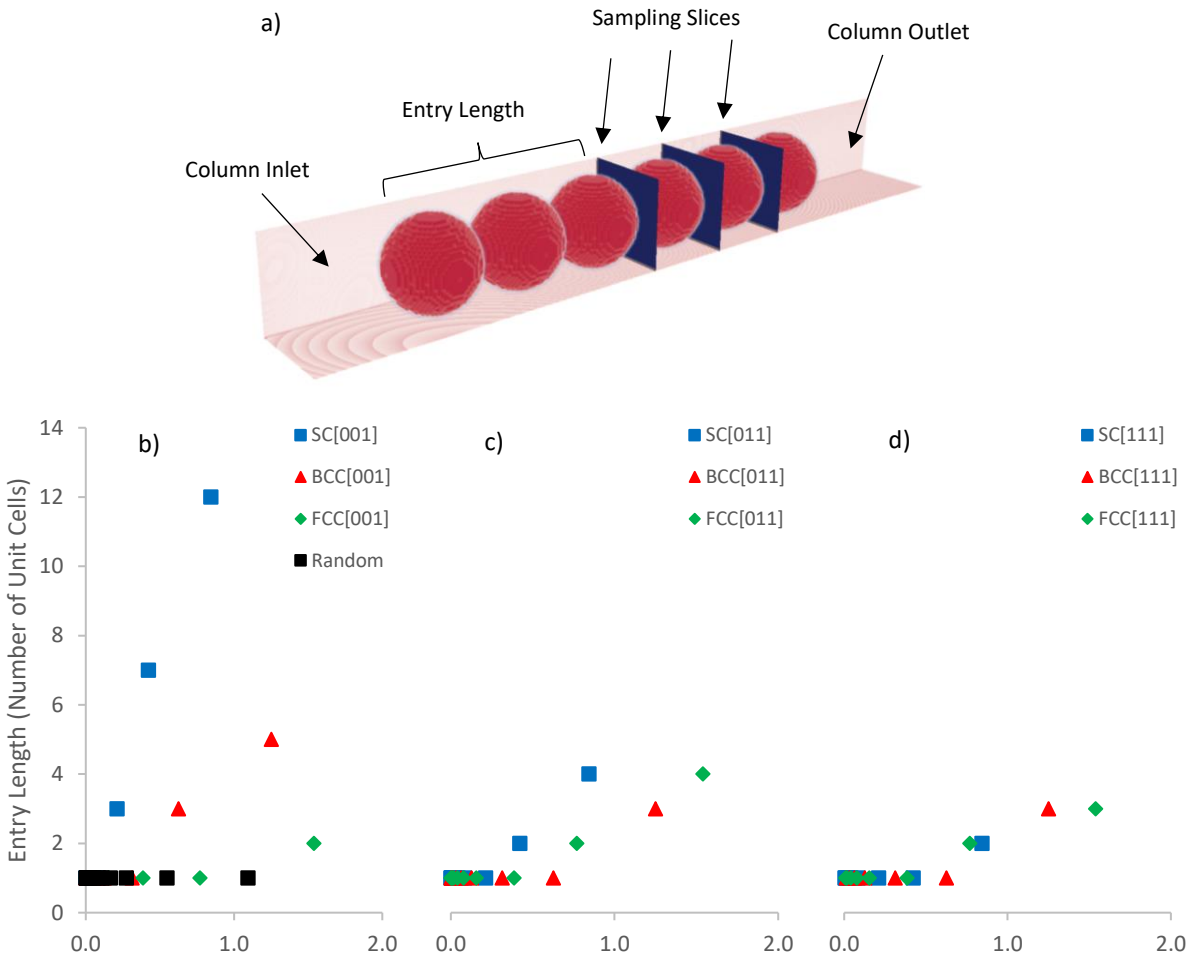

Figure 3.3. a) Illustration of the method used to calculate the height equivalent of a theoretical plate between two sampling slices, and entry length for ordered sphere packings: b) [001] orientation, c) [011] orientation and d) [111] orientation.

3.2 Ordered Sphere Packings

For randomly packed beds, spheres have been proven to be the most efficient shape in terms of chromatographic performance[95]. This is because, if well packed, spheres form structures with low void space and it has been shown that the chromatographic performance (both pressure drop and dispersion) is decreased when particle shapes deviate from spherical. The idea of using spheres for ordered packing was initiated by Schure et al.[14] to draw comparison to these randomly packed beds. This was also an appropriate starting point for this work, because initial data produced by the model could be more thoroughly compared with literature data.

3.2.1 Chromatographic Performance of Sphere Packings

The jammed random packing of monodisperse spherical particles is a limiting case, with the minimal bed porosity of *~36%*, reached only in extremely well-packed columns. Bed porosity is a key parameter in conventional, randomly packed chromatography columns. For example, packing operations aim to achieve a target porosity of *37-40%*, because higher porosities correlate to loose packing, which is prone to channelling and bed non homogeneities[190]. This practical aspect was validated by Khirevich through computational simulations, showing that, for random packings of monodisperse particles, plate height increases with void fraction[45]. However, it is suggested that this correlation is a function on the more tightly restricted and hence even flow channels that come with decreased voidage in random packings.

Similar arguments were put forth for ordered packings of monodisperse spheres by Schure et al., who observed an improvement in plate height as the void fraction decreased progressively from SC, BCC and FCC configurations of particles[14]. While this trend is consistent with the behaviour of random packings, such ordered configurations were only investigated in the basic [001] orientation, and the influence of other important packing factors was not considered. In fact, ordered arrangements of particles have a completely different freedom that random packings, defined not only by particle arrangement, but also orientation, shape of particles, and careful combination of appropriately polydisperse particles. To date, the full variety and combinations of ordered packing and their effect on chromatographic performances has not been thoroughly investigated. In turn, no definitive methods or packing parameters are available to help predict the chromatographic performance of an ordered packing of particles. To this aim, Van Deemter plots were constructed for ordered packings in the range of *Pe 0.5* to *~800* for each configuration and orientation investigated (Fig. 3.4).

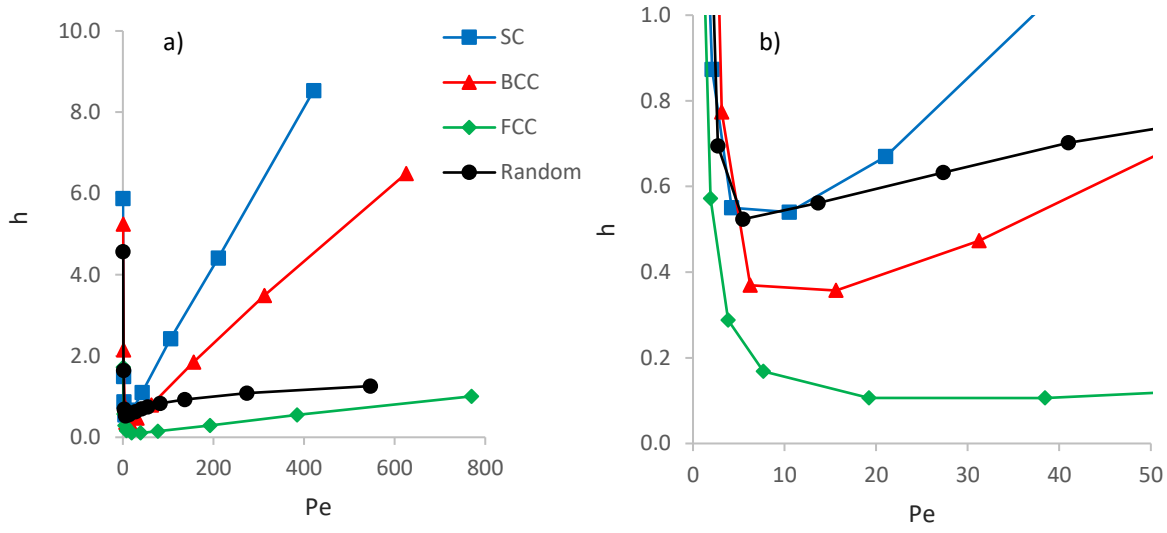

Figure 3.4. van Deemter plots of ordered sphere packings in the [001] orientation, and of jammed randomly packed spheres: a) over the entire simulated Peclet range and b) zoom on the minima for the reduced plate heights.

In Fig. 3.4, van Deemter curves for ordered packings (in the [001] orientation) were compared with random sphere packing. The curves have a characteristic concave upward shape with minimum reduced plate height located in the Peclet region between *5* and *10*, except for FCC, which presents its minimum at *Pe* between *20* and *40*. In general, FCC [001] produced the lowest h_{min} value, followed by BCC [001] and SC [001]. Compared with ordered packings, random packing displayed the minimum plate height, comparable to the SC [001] configuration, and progressively outperformed SC [001] at around *Pe = 20*, BCC [001] at around Pe = 100 and trended to outperform FCC [001] at *Pe > 1000*. In the [001] orientation, the axial flow direction is orthogonal to the standard cubic cell face (Fig. 3.2).

Orientation of the ordered packing with respect to the axial direction, i.e. the main direction for fluid flow, is one of the key degrees of freedom which was expected to produce significant changes in the flow profile of a packed bed. In turn, this should impact the dispersion behaviour within the packing and consequently, chromatographic performance. Given the regular structure of the cubic unit cells in ordered packings, only three alignments with respect to the main direction of flow were investigated, namely the [001], [011] and [111] orientations. These constitute principal positions for a regular lattice, and any other transitional alignment would be expected to result in intermediate performance between these limiting cases. van Deemter plots for these orientations within each of the packing arrangements are presented in Fig. 3.5.

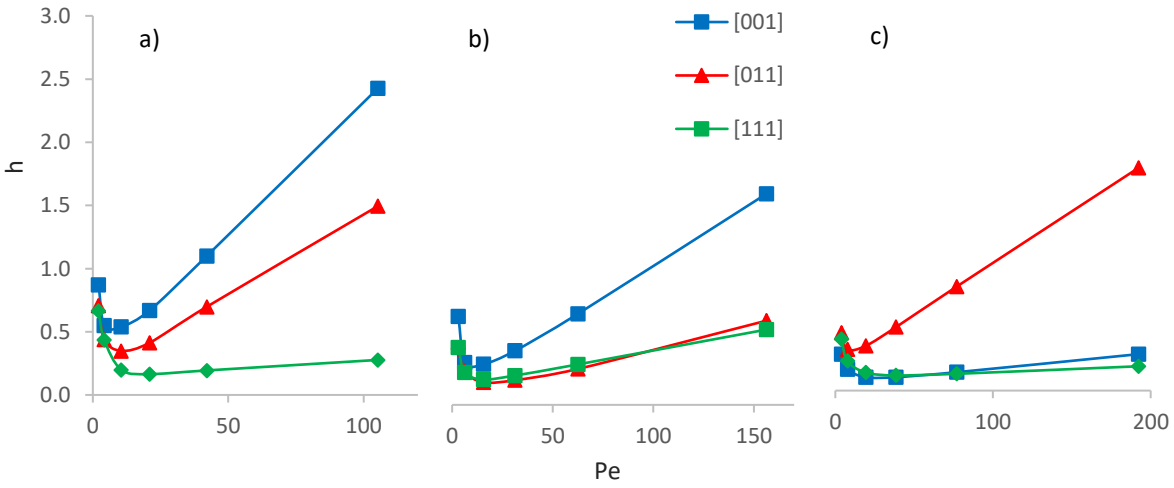

Figure 3.5. van Deemter plots for each family of packing at different orientations with respect to the main flow direction: a) SC, b) BCC and c) FCC.

Fig. 3.5 highlights the influence of lattice orientation on chromatographic performance. Rotation of the [001] orientation decreased the reduced plate heights of both SC and BCC arrangements, while the performance of FCC remained relatively unchanged for the FCC [111] orientation but was impaired in the FCC [011] orientation. Ultimately, FCC [001] displayed the lowest reduced plate height, but other rotated configurations also resulted in comparatively small h_{min}, such as SC [111], BCC [011], BCC [111] and FCC [111]. These results suggest that, while porosity may be a strong indicator of

chromatographic efficiency for random packings, other factors should be considered for ordered packings.

Orientation also has a strong impact on the magnitude of the mass transfer resistance term, i.e. the gradient of the van Deemter curve at greater *Pe* than the optimum operating point. This is most effectively illustrated by the SC series, where SC [001] and SC [011] showed a sharp drop in efficiency as the Peclet number increased above 20, whereas in the case of SC [111], the plate height remained relatively low even at higher reduced velocities. This same behaviour can also be observed for the FCC [111] configuration, endowed with a shallower gradient than FCC [001]. Because these simulations only consider non-porous particles, the increase in mass transfer resistance must be caused by an increased variance from the average channel velocity across the total velocity field. A deviation term was calculated as the average of the deviated velocity for each nodal point and normalized by the average channel velocity (Eq. (3.7)).

$$\tilde{v} = \frac{\Sigma|v-\bar{v}|}{N\bar{v}} \tag{3.7}$$

where $\tilde{v}$ is the average velocity deviation from the mean channel velocity. This term is analogous in theory to the mass transfer resistance term in van Deemter's plate height equation. This is shown by the linear correlation between the two variables (Fig. 3.6), though there are differences that can be explained by Eq. (3.7) using the total velocity, while perhaps the C term correlates to the axial velocity component. Ultimately, these results indicate that it is possible to operate columns with ordered beds at relatively high velocities without significant loss in performance, with consequent benefits in terms of column throughput in preparative and industrial applications.

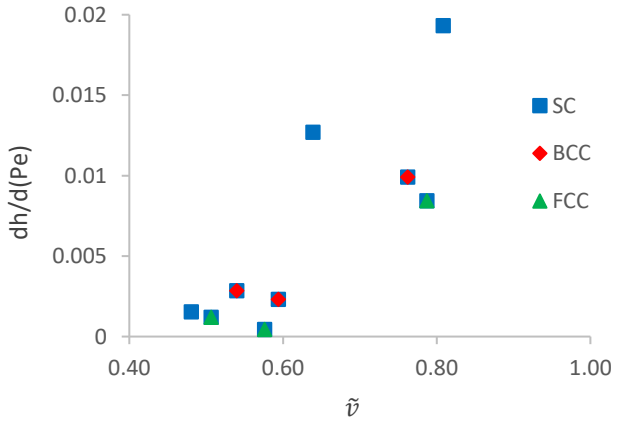

Figure 3.6. Correlation between the rate of increase in reduced plate height with Peclet number and the deviated velocity fraction for packed beds of spheres.

Pressure drop across a column is another key factor in chromatographic operations. The relatively low voidage of random beds (*37-40%*) causes high resistance to flow, thus limiting

operational flow rates, particularly for soft materials subject to deformation and compressibility issues. A similar degree of flow resistance is expected also for the ordered packings, with porosities ranging from *26%* for FCC to *48%* for SC (Table 3.1). Table 3.2 shows that each family of ordered packing shared very similar permeability and hence, was unaffected by orientation of the bed. Yet, the different particle arrangements were characterized by seemingly different permeability values, with the SC being the most permeable and the FCC the configuration with the highest flow resistance. Through the analysis performed in Section 2.8.1, these results were found to agree with the permeability predicted by the Carman-Kozeny equation.

Table 3.2. Simulated properties of the studied sphere packings.

Packing Configuration	h_{min}	k	E_{min}[a]	T
SC [001]	0.54	2.64E-03	53	1.02
SC [011]	0.35	2.63E-03	22	1.18
SC [111]	0.16	2.60E-03	5	1.30
BCC [001]	0.36	5.04E-04	81	1.12
BCC [011]	0.17	5.04E-04	19	1.25
BCC [111]	0.19	5.02E-04	24	1.24
FCC [001]	0.10	1.73E-04	17	1.37
FCC [011]	0.33	1.71E-04	161	1.14
FCC [111]	0.12	1.72E-04	22	1.25
Random	0.52	6.91E-04	145	1.30

[a] *Separation impedance is estimated at h_{min}. Please note the difference to table 2.3, due to lower spatial resolution being used here.*

In terms of separation impedance, SC [111] was by far the best performer – with values more than three times lower than its closest competitor - followed by FCC [001] and BCC [011]. The SC [111] configuration is endowed with a reasonably good h_{min} of *0.16*, within the range of other well performing configurations (*0.10* for FCC [001] – *0.19* for BCC [111]). This, coupled with the remarkably high permeability of the SC family, explains the exceptional performance of SC [111] in terms of separation impedance. These results suggest that such an arrangement is particularly attractive for use in real chromatographic stationary phases. In addition, practical limitations in 3D printing capabilities, such as the large file size needed to describe the entire internal geometry of the packing[12], and the fidelity of the printed objects[13], are more easily overcome in a looser configuration of particles, making this arrangement a realistic goal in practical manufacturing terms. A potential drawback with SC packing is the physical instability of the bed, wherein the high voidage might cause the particles to move under the influence of physical vibration, thus disrupting the ordered bed arrangement. In 3D

printing practice, this drawback can be overcome by slightly overlapping the individual particles to increase the structural stability of the bed[188].

3.2.2 Impact of Orientation and Tortuosity

Low bed voidage has generally been considered critical to ensure good chromatographic performance in randomly packed beds[45]. Approaching the theoretical limit of random close packing is the goal in conventional packed columns, as this mitigates the occurrence of channelling or dead zones in the column. The results herein challenge, for the first time, the concept that excellent chromatographic performance is only possible at low bed porosities. A simple correlation between porosity and reduced plate height does not hold in ordered arrays of spheres, and other parameters must therefore be taken into consideration.

In a chromatography column, dispersion can occur in both the transverse and axial directions[191]. Good transverse dispersion is desirable because it ensures a uniform concentration profile across the column cross-sections and helps reduce variations in axial velocity associated with defects in the packing[192]. On the other hand, axial dispersion is responsible for band broadening effects and should be kept as low as possible[184]. Coupling of these two parameters finds an analogy in the tortuosity, a metric that describes the axial deviation of the flow paths in a system. In porous media, tortuosity gives an indication of how the flow paths differ, on average, from straight flow channels. Several methods have been proposed to determine the tortuosity of a flow system using the shape of the flow channels. In this study, the procedure proposed by Matyka and Koza was used, in which the tortuosity is computed from the flow field itself, as the ratio between the sum of the magnitudes of the velocity vectors and the sum of their axial components[148]. This is known as flow (or hydraulic) tortuosity, which is an anisotropic variable that describes differences in flow patterns stemming from orientation changes and indicate the degree of transverse dispersion. Tortuosity in ordered packings was calculated in a single unit cell after the entrance region, while in random packing it was averaged over ten samples of 50^3 simulation nodes in size multiple samples in the 5 variants considered. It was first verified that, for any given packing beyond the entry length, the tortuosity was independent of reduced velocity and column location. This is also reasonable considering all systems are in the Stokes flow regime and hence the flow characteristics should not change while under this condition. The resulting flow tortuosity values, T, are summarized in Table 3.2.

The streamlines for each packing show the relative axial and transverse velocity components through the unit cell (Fig. 3.7). Qualitatively comparing these figures with the performance of each medium shows that larger transverse contributions correlates lower mobile phase band broadening. This observation led to the postulation of an inverse relation between tortuosity and minimum reduced plate, with the data sets obtained in the simulations plotted in Fig. 3.8.

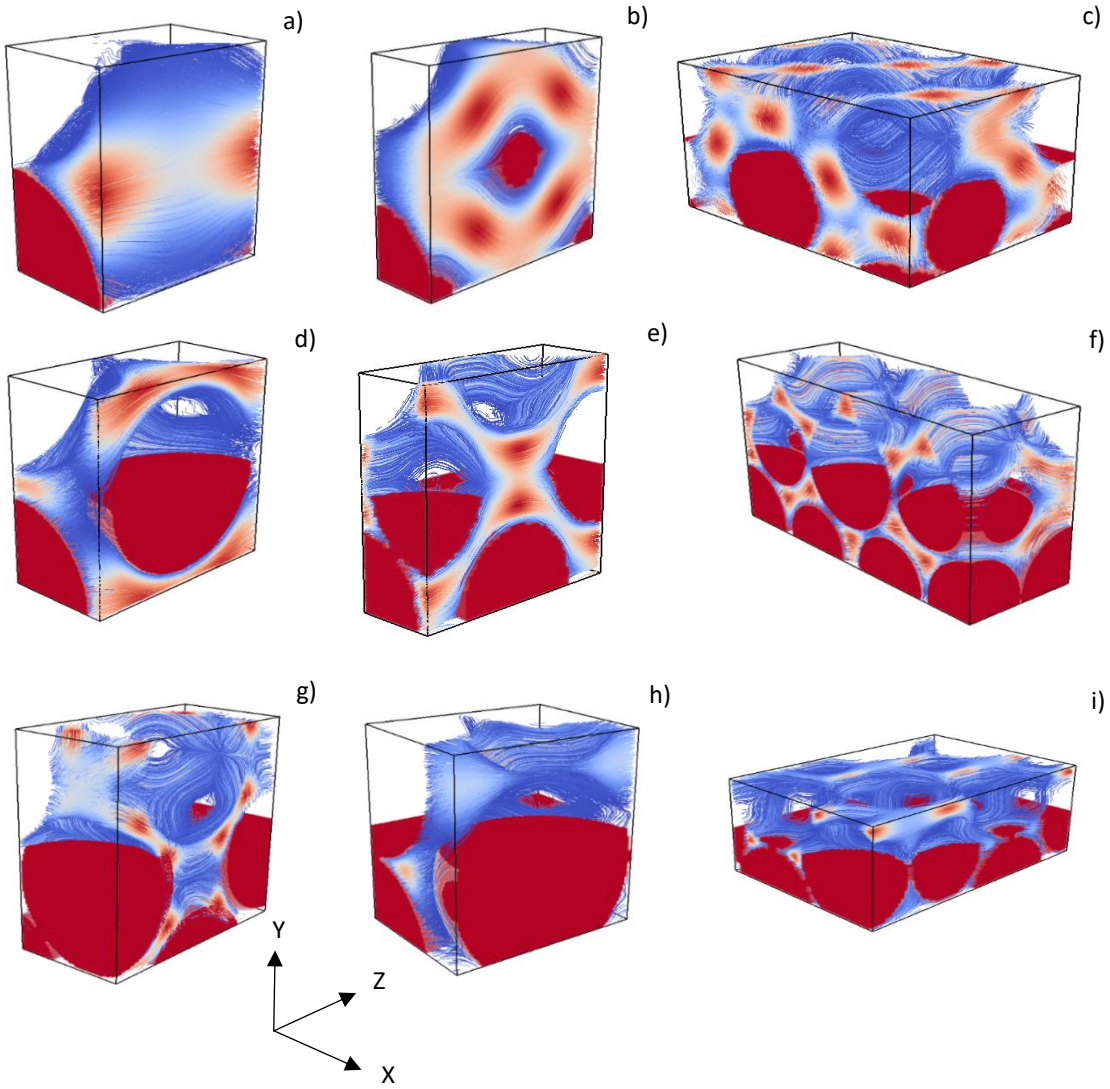

Figure 3.7. Representative stream lines of a produced by unit cells of: a) SC [001], b) SC [011], c) SC [111], d) BCC [001], e) BCC [011], f) BCC [111], g) FCC [001], h) FCC [011], i) FCC [111] unit cells. The [001] and [011] have symmetrical channels reflected by YZ face (in the positive X direction) while the [111] orientations show the whole unit cell. Red and blue represent high and low velocity, respectively.

Strikingly, a simple linear correlation captures the general trend observed. The SC [001] geometry, endowed with the lowest tortuosity due to its relatively straight channel-like paths, was also characterized by the highest h_{min}, indicating lower performance in chromatographic applications. In contrast, FCC [001], i.e. the configuration with the smallest $h_{\min}$ amongst the geometries investigated, was the configuration with the highest tortuosity. The correlation proposed here offers a strong clue for directing further research efforts into the design of ordered packings for chromatography. While this correlation has been established for ordered packings of monodisperse spherical particles, it is reasonable that an inverse relation will still hold for other types of ordered packings, with improved geometries characterized by higher tortuosity factors. For example, improved chromatographic beds could be composed of poly-disperse spheres, whose particles have appropriate dimensions and suitable

3D arrangement[193] or the use of ellipsoids with the major axes aligned in the transverse directions, i.e. similar to the trapezoidal pillars proposed in 2D chromatography[194]. Beds with greater performances might not even be composed of particles at all, but being monolithic in nature, with a tortuous lattice of appropriately designed channels that improve radial dispersion while limiting axial band broadening.

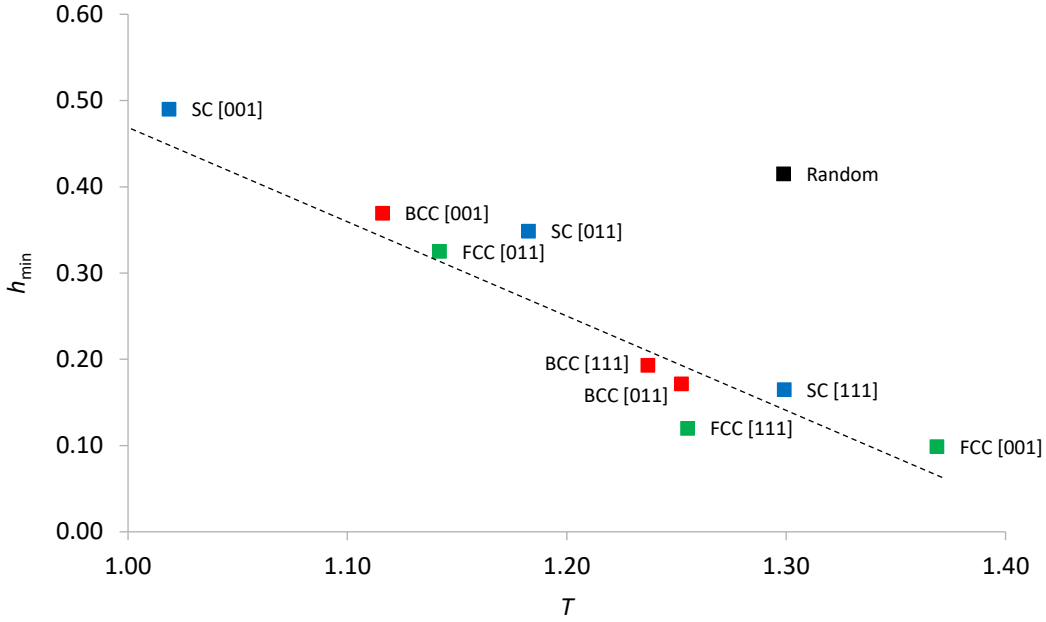

Figure 3.8. Correlation between minimum reduced plate height and tortuosity in the ordered packings considered: SC in blue, BCC in red, and FCC in blue. Also reported, is the data for random packing, in black.

Interestingly, random packing did not follow the trend observed for the regular packings, with relatively large reduced plate height, despite its high tortuosity. This inefficiency is suspected to be a product of the greater eddy dispersion present in random packings. Eddy dispersion is closely related to the *A* term in van Deemter's plate height equation, and is also linked to the disparity between path lengths within a porous medium[6]. This observation again demonstrates that the performance of random beds is, in general, lower than that of ordered packings.

3.3 Alternative Particle Geometries

As previously discussed, a sphere provides a minimum surface for any discrete volume. As a particle's shape deviates from spherical, literature states that this can be described by sphericity (Eq. (3.8))[195]. From the Carman-Kozeny equation (Eq. (3.9)), the drag coefficient of a particle is inversely correlated with square of sphericity and by this definition, spheres produce the minimum pressure drop in a packed bed.

$$\Psi = \frac{\pi^{\frac{1}{3}}(6V_p)^{\frac{2}{3}}}{A_p} \tag{3.8}$$

$$\frac{dP}{dz} = \frac{-c_{CK}}{\Psi^2}\frac{(1-\varepsilon)^2}{\varepsilon^3}\frac{\mu}{d^2}u_{sup} \quad (3.9)$$

where Ψ is the sphericity, V_p is the volume of the particle [L^3] and A_p is the wetted surface area of the particle [L^2]. For an individual octahedron and tetrahedron, sphericity is analytically defined as 0.846 and 0.671, respectively. Comparison of random packing of spherical particles and irregular particles[95] shows that sphere packings also minimize dispersion, based on the greater efficiency with which spherical particles can pack, which minimizes non-homogeneities in the packed bed and minimizes eddy dispersion. However, for ordered packings, an opposing trend has been found both numerically and practically; showing that elongation of spherical particles[46] and using alternative particle shapes[13] can reduce dispersion in a porous medium. Here, this hypothesis is further developed by observing dispersion for ordered packed beds using both octahedral and tetrahedral particles (Fig. 3.9).

In this study, octahedrons were defined to contact their nearest six neighbours in a SC packing at each of six vertices of the particle (Fig. 3.9b), however, tetrahedrons could not mimic this behaviour, because they only have four vertices. To account for this factor, the six edges were instead used to create contact between particles with each edge being located along the diagonal of the six faces of the unit cell (Fig. 3.9c). Upon observing dispersion in the various orientations of sphere packings (Section 3.2), it was proposed that deviations from these specific alignments pictured in Fig. 3.9 would also cause deviations in the pressure drop and dispersion data, a phenomenon not encountered for sphere packings, though it was not studied here.

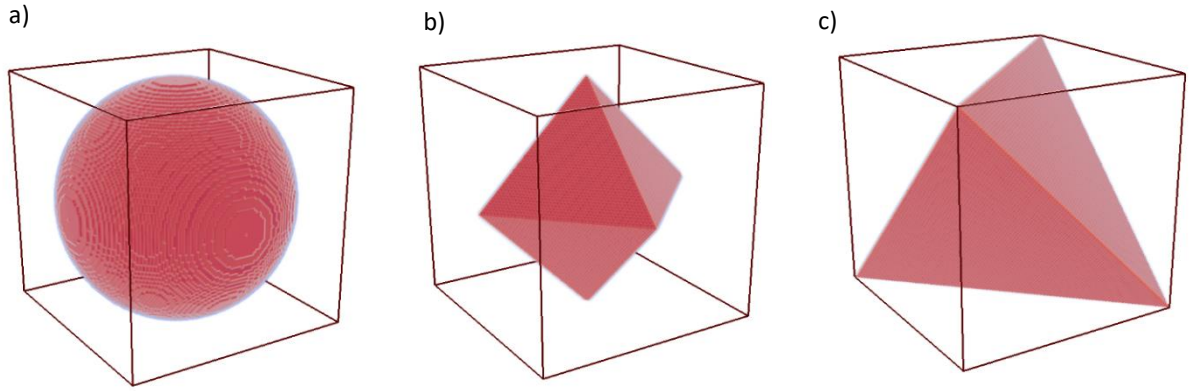

Figure 3.9. The three particle shapes studied in this chapter and their alignment to the unit cell for the SC [001] configuration: a) spherical, b) octahedral and c) tetrahedral.

3.3.1 Octahedral Particles

The declaration of octahedral particles maintained the equivalent characteristic dimension of a spherical particle, i.e. a constant circumdiameter, resulting in a decrease in solid volume and increase of void fraction for the packed bed from *0.48* to *0.82* in the SC [001] configuration. As would be

expected, for any porous medium, this increase in void space corresponded to an increased system permeability (Table 3.3). The arrangement and orientation of octahedral packings was also tested, with the exception being for FCC packings as this would result in impermeable packings for the specified alignment. For spherical particles, the permeability was found to be independent of the orientation, which was thought to be correlated to the fact that spheres have infinite rotational symmetry. For non-spherical particles, rotation caused the axial flow to encounter a different face of each particle and literature suggests that the orientation of the particle is relevant to permeability, but there is a distinct lack of data about the relevance of orientation for isometric particles[196-198]. From the model, it is shown that there are only minor differences in permeability between the orientations of octahedral packings (Table 3.3). This suggests that, in the Stokes flow regime, the orientation of isometric particles is a negligible factor when determining permeability. The BCC arrangement decreases the voidage and, as expected, the permeability of the medium compared with SC packings, which is consistent with sphere packings.

Table 3.3. Flow Characteristics of Tetrahedral packings.

Packing Configuration	ε	k	T	E_{min}
SC [001]	0.82	2.15E-02	1.02	4.6
SC [011]	0.82	2.18E-03	1.08	2.8
SC [111]	0.82	2.20E-02	1.10	0.7
BCC [001]	0.62	3.98E-03	1.13	0.9
BCC [011]	0.62	3.95E-03	1.10	3.6
BCC [111]	0.62	3.92E-03	1.07	5.8

Dispersion in octahedral packings was decreased when compared with the equivalent sphere packings for each orientation of the SC arrangement (Fig. 3.10). This was consistent with the findings of Nawada et al.[188] and further argues that performance is not directly correlated to system voidage in ordered packings. Quantitatively, this can be observed from the van Deemter plots, in which, the curves for each packing diverged at high Peclet numbers. Much like sphere packing, the orientation of the packed bed also influences the measured dispersion in octahedral packs. The order of performance of minimum reduced plate height for both particles shapes was: SC [001] > SC [011] > SC [111], again with increasing tortuosity.

For BCC, the octahedral pack experiences the opposite trend to the spherical pack and the optimum performance deteriorated when the orientation was altered (Fig. 3.11). This trend was seen previously for FCC spheres, but the occurrence in this case suggests that the relationship between combination, orientation and particle shape is a complex one and there is no absolute performance trend between the packing variables. Moreover, for octahedral particles, each BCC orientation achieved a

lower minimum plate height than each of the SC orientations, unlike for sphere packings in which the most efficient orientation for each arrangement produced similar minimum reduced plate heights.

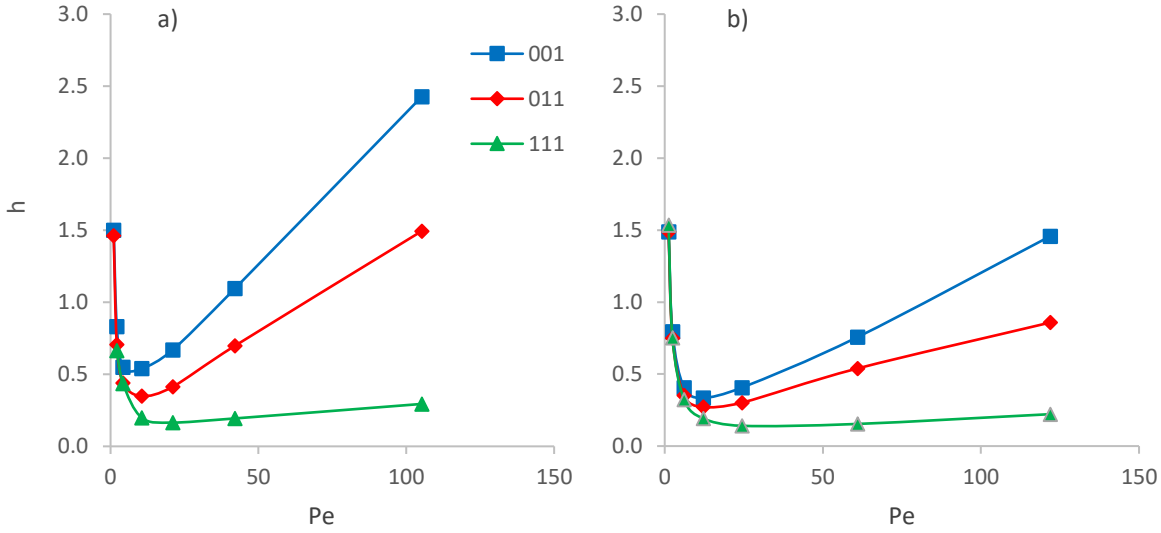

Figure 3.10. Comparison of performance between: a) Spherical particles and b) Octahedral particles in the SC packing arrangement

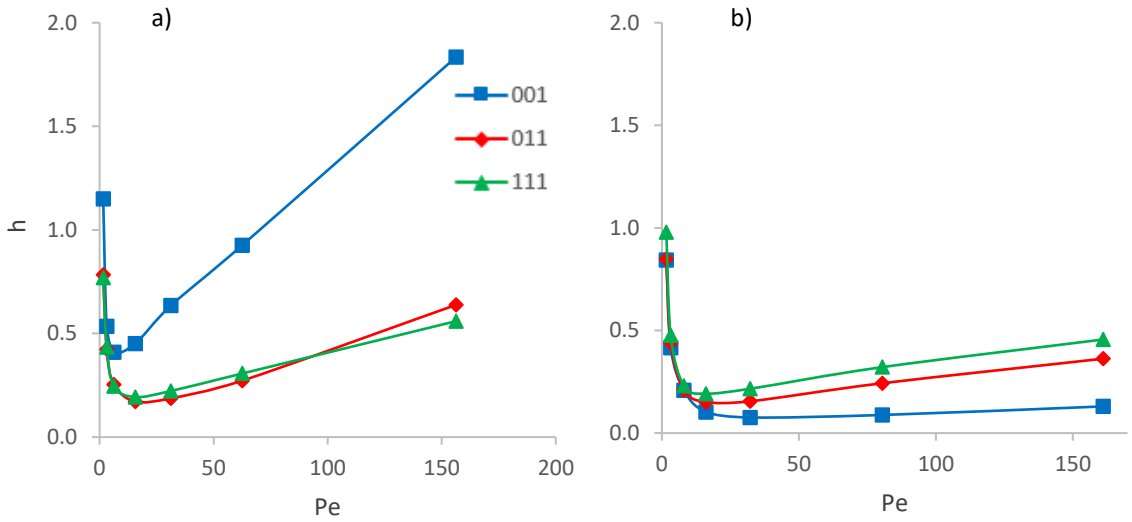

Figure 3.11. Comparison of performance between: a) Spherical particles and b) Octahedral particles in the BCC packing arrangement.

Finally, the minimum separation impedance was achieved by the SC [111] (*0.7*) and BCC [001] (*0.9*) packings – which were over five times lower than the best sphere packing; SC [111] (*5.0*). This was a definitive result in the comparison between spherical and octahedral particles for the reduction of band broadening and pressure drop in packed beds. However, there is an important factor to consider for practical applications of these packings; the higher amount of void space in octahedral packings. This correlates to a reduction in chromatographic capacity and earlier column saturation which would require in a more frequent adsorption-elution cycle in the practical setting, perhaps could lead to a less effective system.

3.3.2 Tetrahedral Particles

The length of the unit cell which contained the tetrahedron was used to define its characteristic length, as opposed to the circumdiameter, which would be larger. For SC configurations, this created a particle volume which was greater than an octahedral packing, but less than for a sphere packing.

An interesting property of the tetrahedral particles and the ordered packed beds that they form in this study, is that the SC packing has a lower voidage than the BCC and FCC packings; the inverse of the trend for sphere and octahedral packings. This occurs because the length between the particles along the axes on which these particles contact is no longer constant, as they are for sphere packings. Therefore, the size of the unit cell is increased, due to the length of the tetrahedral particle being greater along the unit vector which intersects the particle centres in these packings. As for all packed beds investigated so far, the permeability decreases with void space for each packing arrangement (Table 3.4). Like other particle shapes, the orientation of a tetrahedral pack has little impact on the bed permeability, which again suggests that this factor is not important in Stokes flow regimes.

Table 3.4. Flow Characteristics of Tetrahedral packings.

Packing Configuration	ε	k	T	E_{min}
SC [001]	0.66	3.30E-03	1.19	4.0
SC [011]	0.66	3.77E-03	1.16	13.8
SC [111]	0.66	3.60E-03	1.13	10.5
BCC [001]	0.72	5.26E-03	1.10	14.6
BCC [011]	0.72	5.20E-03	1.13	6.3
BCC [111]	0.72	5.15E-03	1.11	9.7
FCC [001]	0.81	1.10E-02	1.14	2.0
FCC [011]	0.81	1.09E-02	1.07	10.4
FCC [111]	0.81	1.11E-02	1.06	4.6

For the [001] orientation of tetrahedral packing, dispersion is comparable for both the SC and FCC packing across the measured domain (Fig. 3.12). Interestingly, manipulating the packing orientation did not improve the performance of either SC or FCC and did not reduce dispersion in worst performing BCC packings to the levels already achieved by SC [001] or FCC [001]. Again, this shows that the performance trends of a packed bed cannot be estimated by using orientation, arrangement and particle shape. The lowest separation impedance was achieved by FCC [001] at a value of *2.0*, which was better than any sphere packing, but worse than the best octahedral packings.

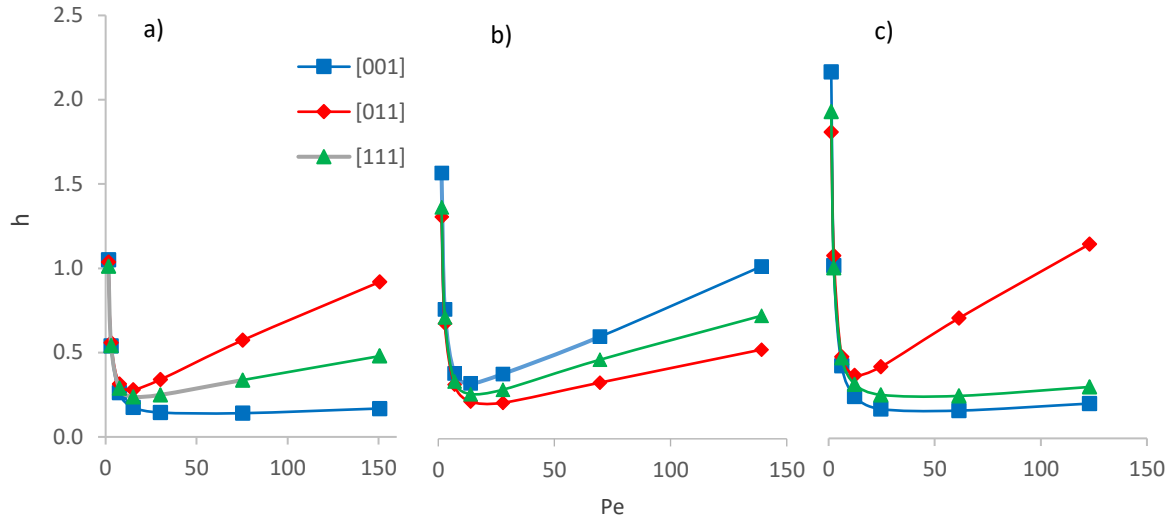

Figure 3.12. Comparison of performance in ordered tetrahedral packing between for varying orientation and arrangement: a) SC, b) BCC and c) FCC.

3.3.3 Feasibility of Alternative Particles

The Carman Kozeny relationship was previously used to validate the model for sphere packings (Section 2.8.1). For non-spherical particles, the relationship is modified to include the sphericity term (Eq. (3.10)).

$$\frac{1}{k} = \frac{c_{CK}}{\Psi^2}\frac{(1-\varepsilon)^2}{\varepsilon^3} \tag{3.10}$$

Neither of the alternative particles behaved well in this comparison and the pressure drops of these packings were greater than the predicted value, even when accounting for the sphericity of the particle (Fig. 3.13a). Using the data from the work of Sangani et al.[182], it was shown that when the porosity of sphere packings is increased, the permeability of the bed starts to strongly deviate from the Carman-Kozeny prediction (Fig. 3.13b). This suggests that in lower porosity systems, the Carman-Kozeny equation, using the standard literature coefficients, loses its capacity as an accurate predictor of permeability. It was found a coefficient of around *300*, created a more suitable fit to the non-spherical data (not shown here), while for disperse SC spheres, the trend is non-linear.

Because of the low levels of symmetry in non-spherical particles, there are alternative particle alignments that alter the porosity of the unit cell. For example, if the concept of the unit cell is maintained, the largest normalized volume for a single octahedron is *0.56* (compared with *0.18* for the alignment used in this study), which is greater than for spherical particles at *0.52*. However, changing the alignment for any non-spherical shape causes an alteration in the contact points between particles, which subsequently alters how a certain arrangement (SC, BCC or FCC) is formed. This becomes a

non-trivial relationship, which is perhaps worthy of further investigation but was outside the scope of this work.

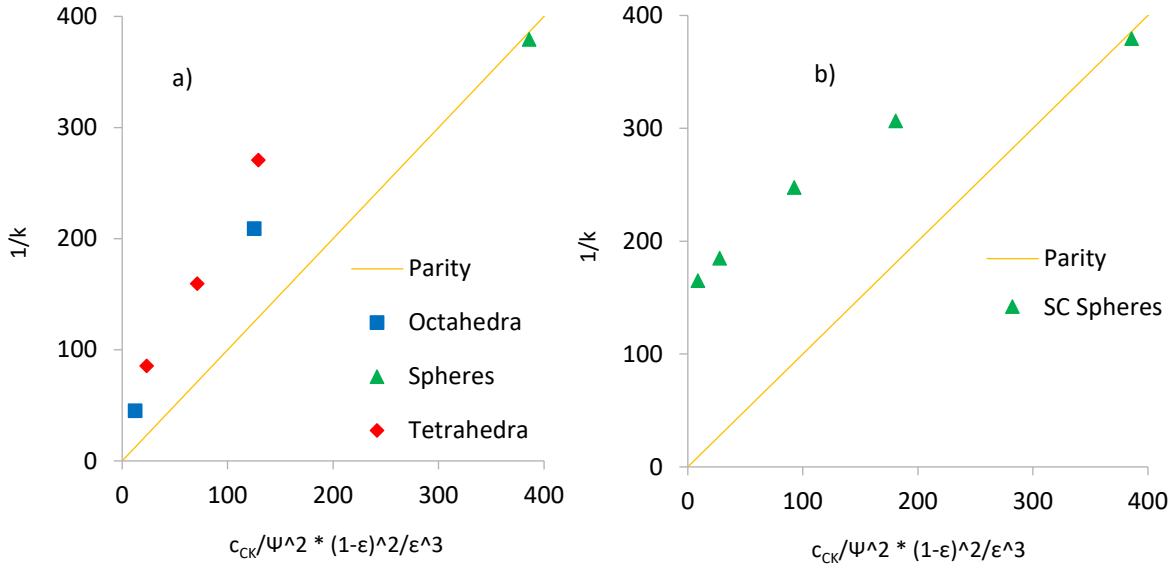

Figure 3.13. Carman Kozeny comparison for: a) ordered non-spherical packing and b) expanded SC packings of spheres which illustrates the poor performance of the Karman Cozeny equation in high porosity systems. Parity shows an accurate prediction from the Carman Kozeny equation.

For both dispersion and separation impedance, it has been shown that both octahedral and tetrahedral beds provide an improvement over sphere packings for certain arrangements. Conversely, sphere packings provide a much lower porosity, which translates to a larger column capacity for practical purposes. Therefore, when selecting a stationary phase morphology, it is perhaps ideal to minimize both separation impedance and voidage (inverse capacity) (Fig. 3.14). Clearly, some packings are better than others for both criteria, however, there is no clear packing which has both the lowest voidage and separation impedance. This means that each practical system must be evaluated on the specific operating objectives and conditions.

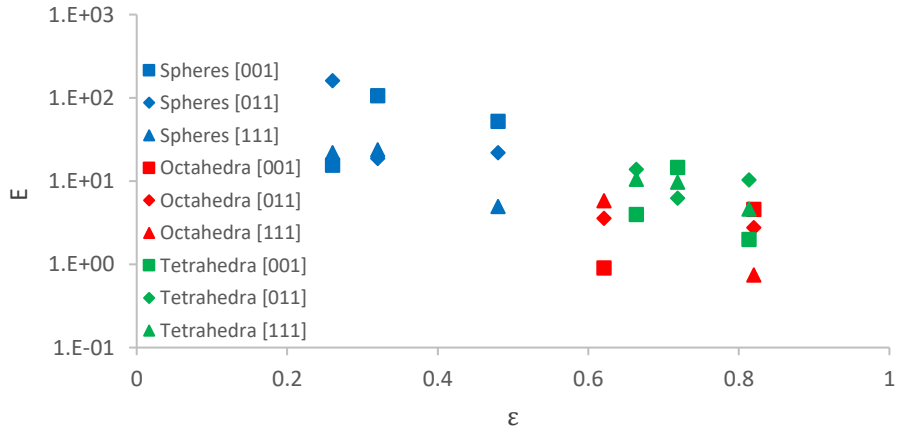

Figure 3.14. The relationship of separation impedance and voidage (assumed to be directly proportional to column capacity) for all ordered particle packings.

-For sphere packings, it was shown that tortuosity is a good indicator of the minimum reduced plate height for a given morphology (Fig. 3.8). However, for alternative particle shapes, this trend becomes weaker (Fig. 3.15a), though there is linearity within each particle shape, suggesting that each data set differs by a characteristic factor. Because the T vs. h plot of the tetrahedral packings lie in between the spherical and octahedral data, sphericity was not the factor, contrary to expectations. Many other factors were tested, and it was found the minimum reduced plate height showed strong correlation with the cubed root of the normalized volume, V_n (Eq. (3.11)) (Fig. 3.15b). V_n was calculated using the unit cells illustrated in Fig. 3.9 (for a SC [001] packing) and hence was only unique for each particle shape. The particle shapes with lower relative volume were prone to low tortuosity, because there was a greater amount of void space present in these packings. Hence, V_n was used to equivocate the relative volume of each particle.

$$V_n = \frac{V_{solid}}{V_{cell}} \tag{3.11}$$

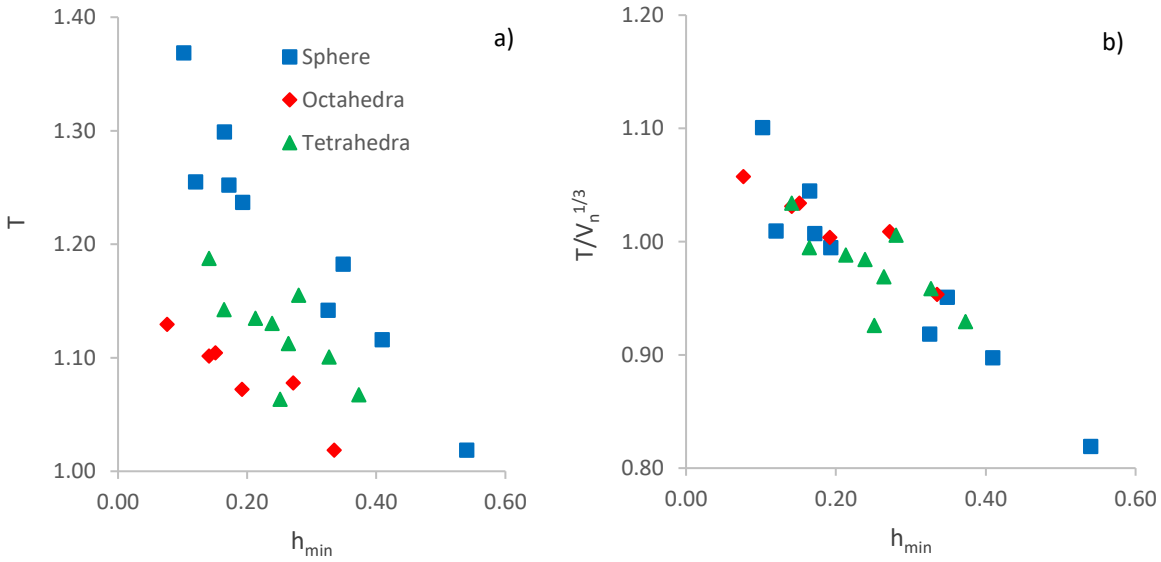

Figure 3.15. Illustration between minimum reduced plate height and a) tortuosity and b) the ratio of tortuosity to the cubed root of the normalized volume for all particle packings.

However, minimum reduced plate height is not the only important characteristic of a packing. Arguably just as important, the mass transfer resistance is the rate at which dispersion increases with the Peclet number (at higher velocity than the turning point of the van Deemter plot). If the increase is small, then perhaps the absolute efficiency is less important, and a faster system is preferred. From each van Deemter plot presented in this chapter, the lowest reduced plate heights are correlated to the systems with the lowest mass transfer resistance. For any infinitely wide ordered packing, it can be assumed that the eddy dispersion is similar because every flow channel is identical. In conjunction with this, diffusion in the bulk phase is also independent of the solid phase morphology. Therefore, the deviation between

each ordered packing is primarily dependent on the mass transfer resistance, which is function of the pore velocity profile in the context of the non-porous systems in this study.

To illustrate this, the velocity profile in the unit cell of SC [001] packing for each particle shape was observed at a constant superficial velocity (Fig. 3.16). Although this Peclet value does not produce the minimum reduced plate height for each packing, the hierarchy at this operating condition is the same as when comparing h_{min} for each packing (tetrahedrons < octahedrons < spheres). Although the porosity difference between the packings causes a variation in the average pore Peclet number, the channel velocity for sphere packing reaches ten times the magnitude of the superficial velocity, while in the XY plane intersecting the particle centre there is relatively stagnant flow. This suggests that this packing experiences a high amount mass transfer resistance, causing an increase in dispersion at lower Peclet flows. The octahedral pack shows a much smaller velocity gradient in the main channel and noticeable flow in the XY plane. Finally, the tetrahedral packing shows the most even velocity distribution across each of the observed planes and it is proposed that the lowest amount of mass transfer resistance leads to the superior performance over the other two packing shapes for this case.

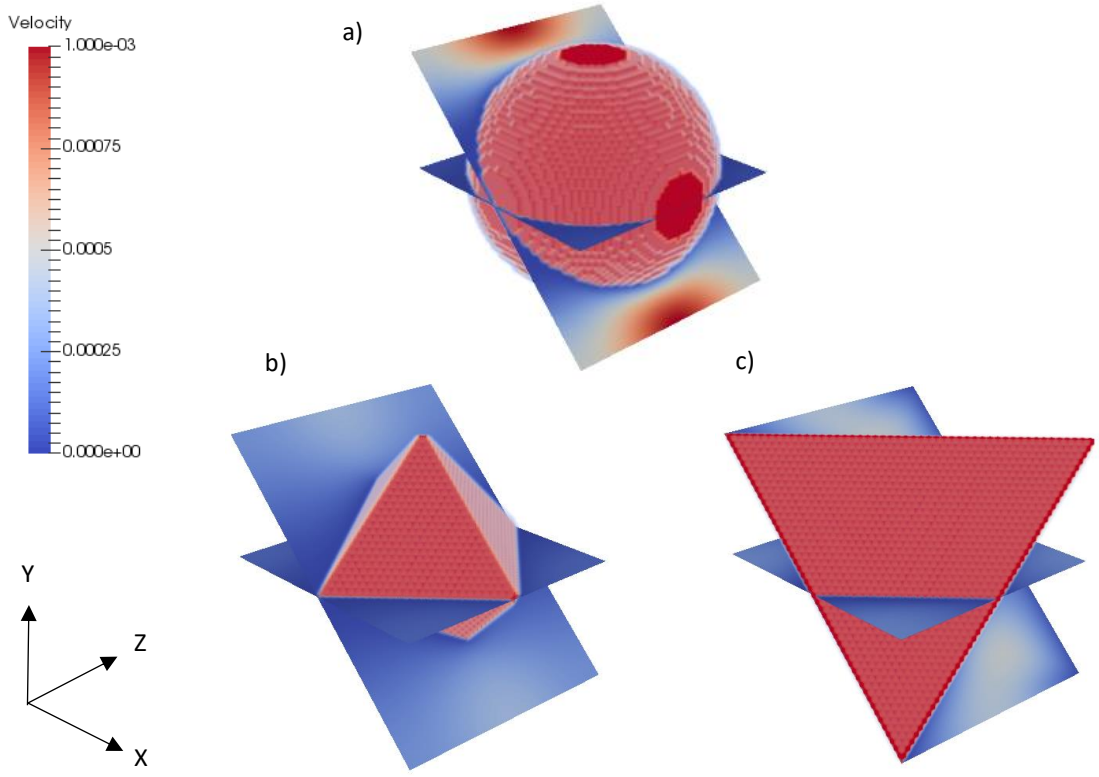

Figure 3.16. The velocity profile at an axial superficial velocity of $1.0e^{-4}ms^{-1}$ for particle shapes: a) sphere, b) octahedron and c) tetrahedron.

In this work, only three symmetrical particle shapes were investigated. However, symmetry is not a prerequisite for producing ordered packings, which presents the opportunity for work which considers ordered packings of monodisperse but irregular-shaped particles. Based on the findings of

this section, particles which maximize both tortuosity and particle volume, have the potential to create more efficient packed beds. This thesis does not explore this optimization, though it is a potential avenue for future work.

As a final point for alternative particle geometries, the high porosity and sharp contact points of these packings make them even more susceptible to deformation than sphere packings. For physical studies of non-spherical particles[13] the overlap required for non-spherical particles is much greater than for spherical particles.

3.4 Particle Overlap

For a printed column, particle overlap (Fig. 3.17) is a necessary feature to ensure the morphology of the bed is not compromised by movements induced by drag under the pressure of the flow system[13]. However, the extent of the overlap required to ensure bed rigidity for a particle type has not been investigated, which would require the inclusion of deformation behaviour to be coupled with the CFD model. Instead, below, the impact of overlap on dispersion and pressure drop is examined.

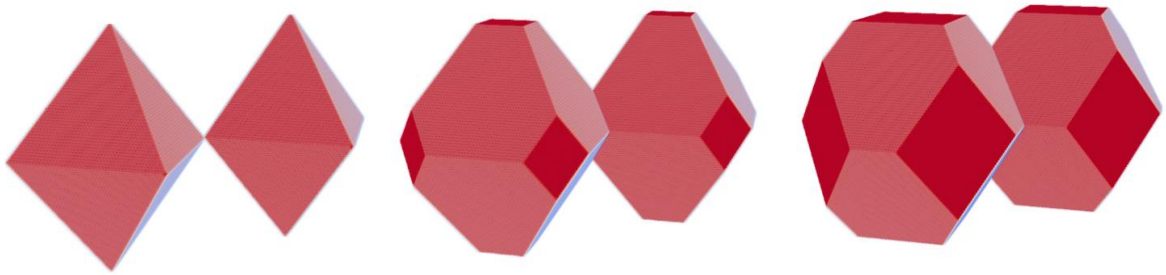

Figure 3.17. Illustration of effect of overlap on particle shape in octahedral SC [001] packing for overlap values of: a) 1, b) 1.33 and c) 1.66.

In this section, instead of using the circumdiameter to calculate the overlap using Eq. (3.4) (Section 3.1.1), the length of the particle along the vector which intersected particle centres was used. This was done to create all packings with flush particles surfaces with an overlap value of one. Decreasing particle diameters from this reference size would define an overlap less than one, creating a packed bed with loose particles which would not maintain its structure under flow conditions. Conversely, increasing the particle size from this reference point created packings with an overlap greater than one, meaning that particle volumes began to merge into a continuous structure. This specific definition was not important for spheres, because each surface point is equidistant from the particle centre in these packings. However, for non-spherical particle shapes, this meant that the unit cell size differed from the spherical equivalent when creating BCC and FCC arrangements. Particle overlaps less than one, were not studied here as they are not practical for a real column, although they have been studied in the literature[181, 182].

For sphere packings, it was decided that overlap would only be investigated for the SC arrangement, because of the low porosities reached when applying overlap to BCC and FCC beds. For octahedral particles, overlap was tested for constant arrangement and varying orientation and finally for tetrahedral particles, overlap was tested for constant orientation and varying arrangement. The conclusiveness of these results provided justification to not test overlap for every arrangement/orientation/particle shape combination but only a representative sample of the previously investigated packed beds, to reduce the amount of simulations required.

3.4.1 Pressure Drop

Particle overlap increases the individual particle volume and hence, decreases the system voidage. Logically, this increases the measured pressure drop of the porous medium, as has been observed for all packing prior to this section (Fig. 3.18). As for packings with an overlap of one, the orientation does not alter the permeability of packings with higher overlap values, as illustrated for spheres and octahedrons.

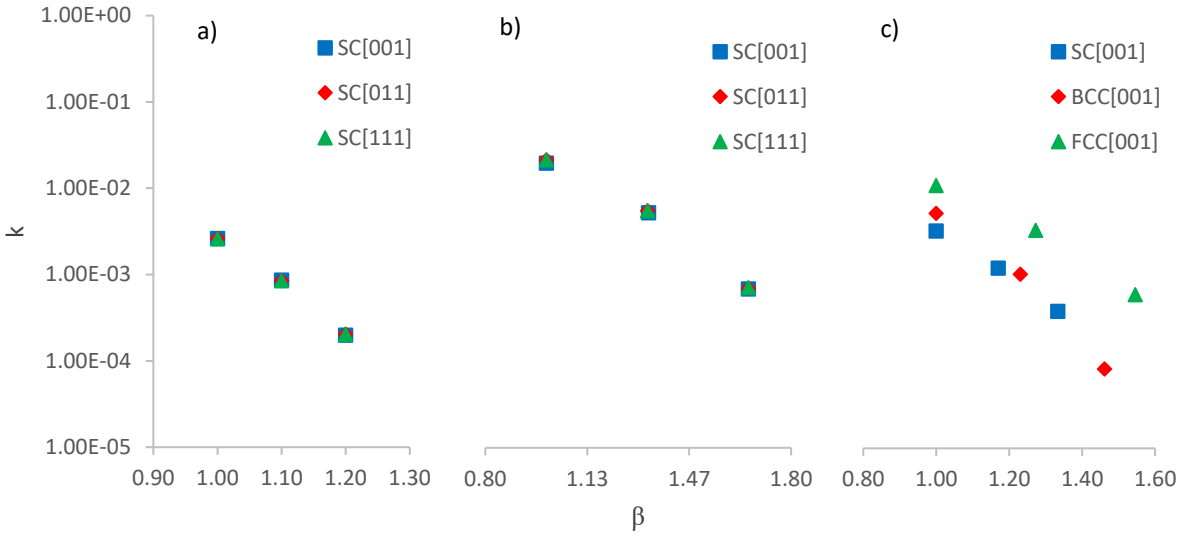

Figure 3.18. Decrease in system permeability with respect to overlap factor in ordered particle packings: a) spheres, b) octahedrons and c) tetrahedrons.

As overlap increased in the packed beds, the particle shape is altered because of the intersection with other particles (Fig. 3.17). Because sphericity is dependent on the wetted surface area, overlap causes an increase in sphericity, which should cause a proportional decrease in permeability, as predicted by the Carman-Kozeny equation. For the Carman-Kozeny analysis, only spheres and octahedral particles are observed, as overlap is simple and only increases the size of the contact points between the particles, whereas overlap in tetrahedral particles causes the sphericity to become much more complex. Previously in this work it has been shown that the Carman-Kozeny equation is not an accurate predictor for ordered non-spherical packings, which is also the case for overlapped packings

(Fig. 3.19). It is suspected that because the Carman-Kozeny equation was developed for close packing of spheres, it loses its ability as a predictor of permeability when the morphology is dramatically altered from this case, such as when the particle shape is a simple polygon.

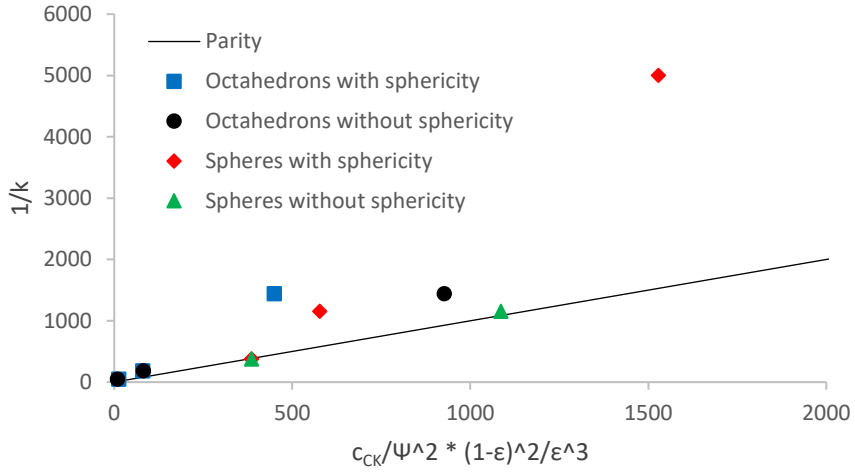

Figure 3.19. Comparison of simulated permeability in packings with overlap and prediction using the Carman Kozeny equation. This shows the inaccuracy of the Carman-Kozeny equation as a model when using particle overlap.

3.4.2 Dispersion

Practical morphologies in literature have shown that overlap increased peak skewness[188] which suggest higher levels of band broadening. Overlap was first observed for SC spheres, of which, the SC [111] configuration showed the lowest separation impedance out of all the sphere packings (Section 3.2.2). For SC [001] and SC [011] packings, the minimum amount of dispersion was not changed by using overlap (Fig. 3.20). For SC [111], the performance was slightly improved, but the separation impedance was still increased, due to the proportionally larger magnitude of the pressure increase (Fig. 3.21).

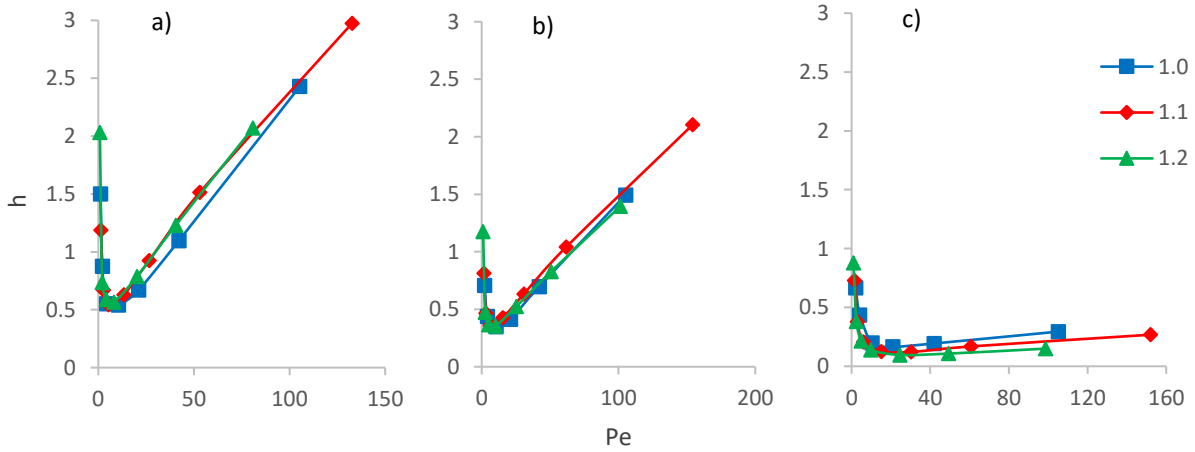

Figure 3.20. Effect of overlap on dispersion in sphere packings for: a) SC [001], b) SC [011] and c) SC [111] orientations. Legend denotes the degree of overlap.

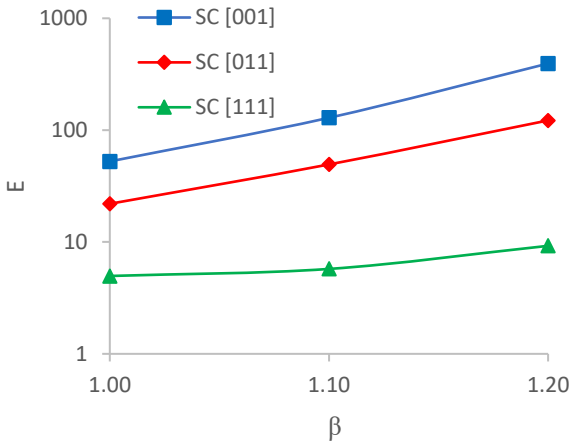

Figure 3.21. Effect of overlap on separation impedance in sphere packings.

As octahedral particles had a much lower volume than spherical particles, more overlap could be applied to these beds without having a detrimental effect on the voidage of the bed. For SC arrangements, it was found that overlap increases both reduced plate height and pressure drop for both SC [001] and SC [011] orientations (Figs. 3.22a and 3.22b). However, for the SC [111] orientation, there was little effect on the dispersion behaviour (Fig. 3.22c).

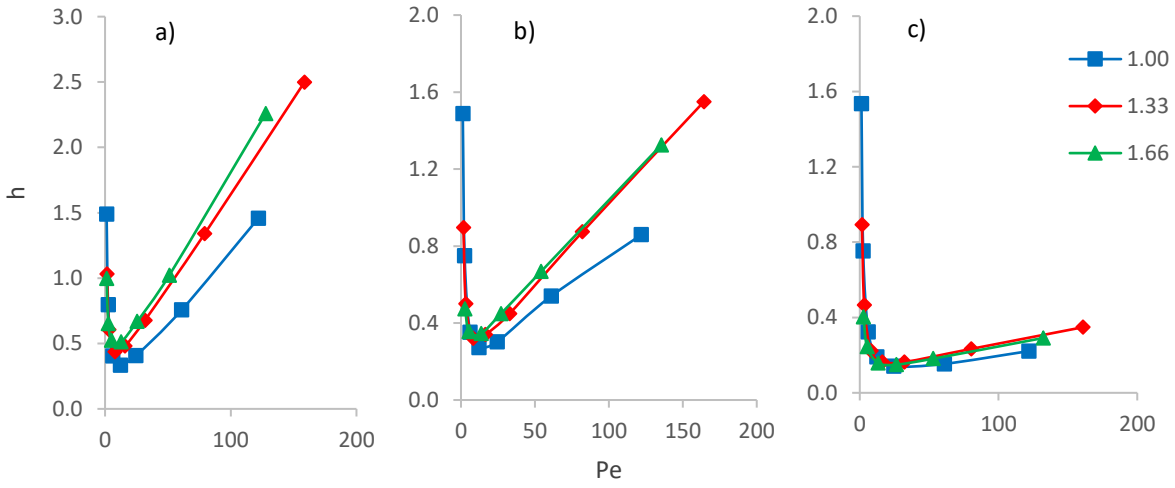

Figure 3.22. Effect of overlap on dispersion in octahedral packings for: a) SC [001], b) SC [011] and c) SC [111] orientations.

Finally, for tetrahedral packings, the dispersion for SC [001] and BCC [001] arrangements was marginally decreased, while for the FCC [001] packing, it was increased (Fig. 3.23). Interestingly, the packings which did not experience higher dispersion when introducing overlap were those with high tortuosity, which was also increased by overlap, while the packings whose performance deteriorated had both low tortuosity and high porosity (Table 3.5).

As overlap increases, the characteristic shape of the particle itself became distorted, for example octahedrons began to resemble a higher-level polygon (Fig. 3.17). Furthermore, the SC [001] octahedral packing at an overlap value of 1.66, shows similar performance to spherical packings with an overlap value of one, which supports the theory of particle packings losing their characteristic flow channels with increasing overlap.

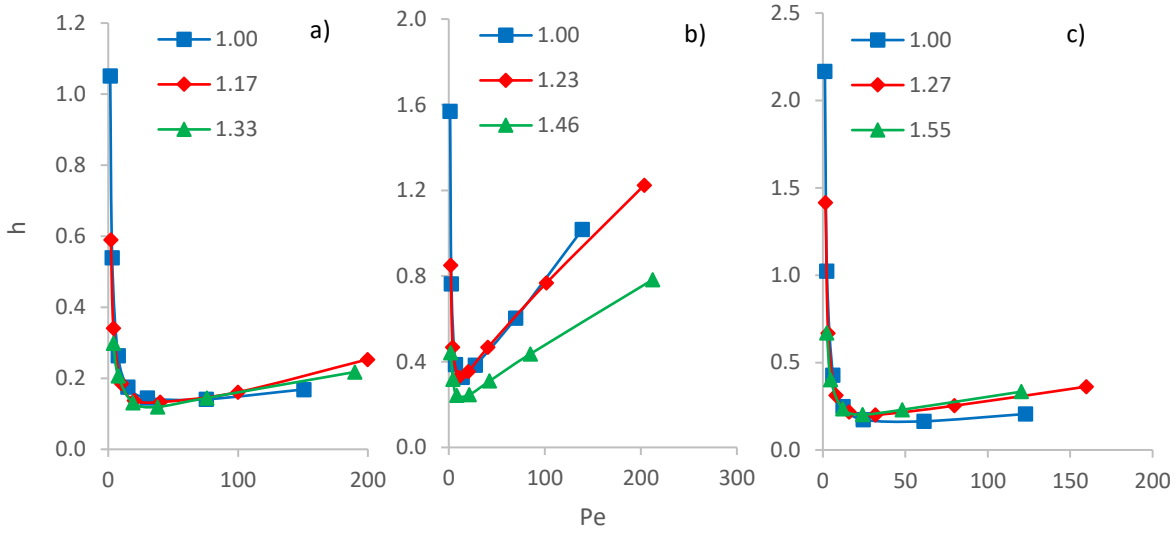

Figure 3.23. Effect of overlap on dispersion in tetrahedral packings for: a) SC [001], b) BCC [001] and c) FCC [001] arrangements.

Table 3.5. Comparison of the effect of overlap in low tortuosity packings (SC [001] Octahedrons) and high tortuosity packings (SC [111] spheres).

SC [001] Octahedrons				SC [111] Spheres			
Overlap	h min	Tortuosity	Porosity	Overlap	h min	Tortuosity	Porosity
1.00	0.33	1.02	0.82	1.00	0.16	1.30	0.48
1.33	0.44	1.03	0.63	1.10	0.12	1.38	0.33
1.66	0.51	1.04	0.39	1.20	0.10	1.45	0.20

Although dispersion was reduced in some packings when introducing higher levels of overlap, the separation impedance was increased in all observed cases (Fig. 3.24). Therefore, it is recommended that the overlap in practical systems should be minimized by finding the pressure deformation limit of the packed bed and comparing to the desired operating conditions. However, as the overlap also manipulates the capacity of the stationary phase, perhaps the pressure increase is acceptable when the band broadening is not increased. This optimization would require deformation behaviour of the solid phase in the CFD model, which is beyond the scope of this thesis, but is a prospect for future work.

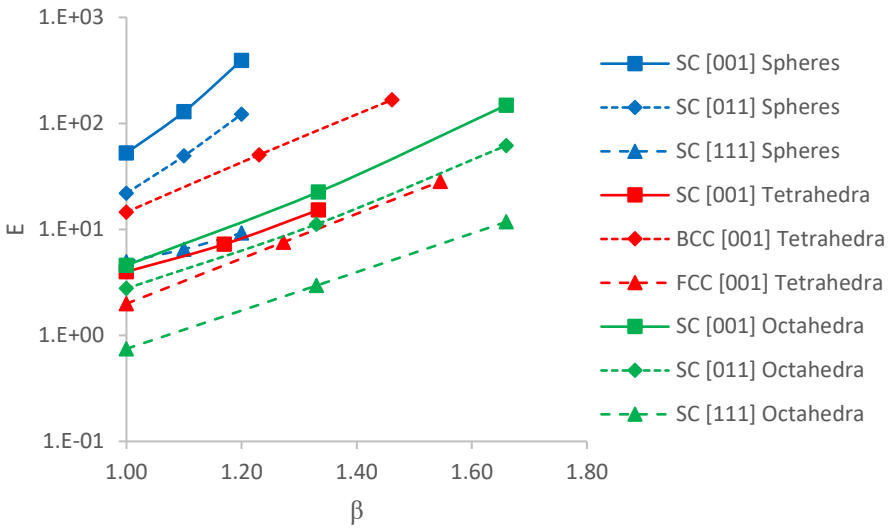

Figure 3.24. Comparison of overlap and separation impedance for various packed beds, showing the negative impact which overlap has on the performance of packed beds.

3.5 Conclusions

This chapter provides important insight into the chromatographic performance of packed beds using ordered particles. Initially, the work of Schure et al.[14] was replicated, proving that, in infinitely wide columns, the BCC and FCC arrangements of ordered packings can reduce band broadening when compared with jammed random packing of spheres. It was hypothesized that this occurs by homogenizing the velocity field within the packed bed, which minimizes the eddy dispersion effect caused by random flow channels.

From this proof of concept, the idea of bed orientation was introduced, dictated by the angle of incidence of the axial flow relative to the standard unit cell of the packed bed. Here, three limiting cases were analysed: [001], [011] and [111] for each packing arrangement, which demonstrated that band broadening can be reduced without altering the permeability of the packed bed. This was an important result, because the separation impedance of any given medium can potentially be reduced by changing its orientation with respect to the axial flow direction. A strong correlation between the minimum plate height and the flow tortuosity for sphere packings was found. It was proposed that this was because these systems promote transverse mixing, which acts to maintain uniformity of the tracer pulse, reducing dispersion.

Although literature states that spheres are superior for jammed random packings[95], a recent physical study has challenged the legitimacy of this hypothesis for ordered packings[13]. This result was confirmed herein, where it was shown that BCC [001] packings of octahedral particles produced lower reduced height and separation impedance values than any tested sphere packing. For tetrahedral

packings, the reduced plate height was not improved, but some configurations achieved lower separation impedance than the most optimal sphere packings. It was proposed that the discrepancies in performance of ordered packed beds was predominantly influenced by mass transfer resistance because packings which had the lowest reduced plate heights also demonstrated a lower increase of reduced plate height with increasing Peclet number. It was also found that for ordered packed beds of non-spherical particles, the Carman-Kozeny equation was a poor predictor of the system permeability. Although these alternative particles produced greater performance than sphere packings, it must be noted that lower volume particles would correlate directly with the column adsorption capacity. Hence, a larger column would be required for non-spherical particle columns to achieve an equivalent capacity to that of packed beds of spherical particles.

Finally, when fabricating ordered packed beds, the stability and structural integrity of the bed is an important issue. When flow is introduced, or other physical trauma is applied to the ordered packed beds, bed deformation can occur by particles being displaced within the bed, which impedes system performance by increasing eddy dispersion. To counteract this behaviour, the particle size was increased while maintaining the unit cell size, which created overlap of the physical space occupied by the particles; fusing them into a continuous structure. Overlap is necessary for ordered packed beds but causes large increases in pressure drop which corresponds to an increase in separation impedance when compared with the non-overlapped case. Therefore, in a physical system, overlap should be minimized to ensure bed stability while maintaining the lowest possible pressure drop and solute dispersion.

4. Wall Effects in Ordered Packed Beds

4.1 Introduction

In Chapter 3, the packed beds morphologies were assumed to have infinite width, which is an idealized scenario that does not occur in practical columns. This behaviour was implemented by using periodic boundary conditions in the transverse column dimensions, transferring momentum and solute concentration exiting through these boundaries into the opposite boundary, to conserve mass and momentum of the system. However, this scenario is unrealistic in practical chromatography, because a column must be confined to retain the mobile phase within the porous medium. The negative aspect of this practical requirement is that these wall boundaries de-homogenize the bulk column flow and create what is known as the "wall effect" creating a dichotomy between the wall and bulk flow zones.

The wall effect is well documented as being detrimental to column performance in both practical and simulated environments[28-30]. Walls reduce column performance by disrupting the packing of the particle bed and locally altering the void space (Fig. 4.1) and hence, the transverse velocity profile within the packed. Therefore, the column has two flow zones with different characteristic velocity profiles. In practical chromatography, solute matter that enters either zone with experience different rates of elution, further contributing to band broadening over the characteristic dispersion of the packing itself.

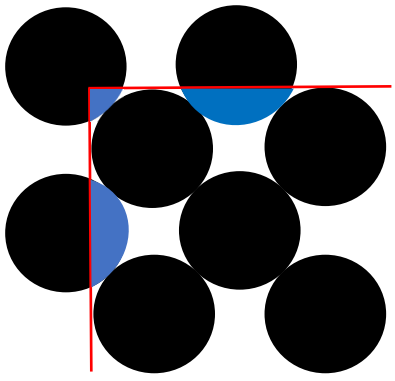

Figure 4.1. Cross section of an FCC sphere pack which illustrates how walls require particles to be removed from the bulk packing (shown in blue) creating low porosity zones.

Because low bed porosity is favoured in bulk packings, the wall flow is usually attributed with higher porosity and lower flow resistance, causing higher velocity in these areas of the column. A

practical implication of this, is that the faster movement of the solute causes less potential to be adsorbed onto the stationary phase and breakthrough may occur before the bulk packing is saturated. Furthermore, in random packings, it has been shown that walls do not only disrupt packing directly at the walls, but also extends out into the packed bed for a distance before the true bulk packing porosity is established[30, 45]. For the ordered packings in this study, this secondary effect was mitigated by using a square cross-section column, allowing the cubic unit cell to fit into the confines of the walls.

To reduce wall effects, practical columns have a large column-to-particle diameter ratio, which has two benefits. First, smaller particles pack more efficiently into any confined space, which is especially true for curved walls and hence, the porosity differential is minimized. Second, decreasing the particle size decreases the radial extent of the wall effect because of greater attenuation from the particles of packed bed[45]. A CFD study by Maier et al. showed that for random packing of spheres, the wall effect can be observed on total column dispersion even for columns in which the column-to-particle diameter ratio is greater than 100[199] making it an important consideration for the optimization of practical chromatography. The practical manifestation of wall effects is the plate height is length dependent over the “short-range” timescale, which is the regime that the results of this chapter deal with.

There are practical studies in the literature that investigate wall effects in randomly packed columns[29, 30, 200]. However, randomly packed beds are not the focus of this thesis and hence, we do not try to reproduce these physical works. Confined random packings have also well been studied in the thesis of Khirevich[45] and hence, this would not be a novel piece of work. Moreover, replicating practical randomly packed system requires much larger simulation domains than possible for the computing systems available for this work. There has also been research into creating columns with varied flow resistance across their diameter, to reduce wall effects in gas-liquid chromatography[201, 202]. Using 3D printing, achieving these kinds of media is a much easier process meaning that manipulation of these wall flow zones will be a very important aspect for the future of chromatographic systems.

In this chapter, the impact of confinement was investigated for ordered FCC [001] sphere packings. FCC [001] was selected because of the low amount of dispersion observed in this study and success in previous physical studies[13, 14]. FCC packs also had the lowest voidage out of any of the ordered packed beds from Chapter 3, meaning that walls caused the largest porosity difference when in confined geometries. Because ordered packings are based on the cubic crystal cell, confined packings with a square cross-section (SCS) were explored, to ensure that the packing arrangement was not dependent on the column diameter. For systems with curved cross-sections the ordered nature of the packing would be degraded, which is not the aim of this work.

The column-to-particle diameter ratio was increased, and the amount of mobile phase band broadening was measured at various axial distances from the packing entrance to observe the short-time dispersion behaviour. From this, the concept of embedded walls was implemented, based on the recommendations of Schure et al.[14] and Fee et al.[12], to mitigate the negative impact of wall effects on ordered packed beds. This method altered the confined packing by embedding particles into the walls, as if the bulk packing continued in the transverse dimensions to conserve the porosity and impede wall channelling. Finally, to draw comparison between this study and "real world" columns, the square embedded columns were compared with embedded circular cross-sectioned columns, to explore the potential of using alternative column geometries for practical applications.

4.1.1 Model Adjustments

The axial boundary conditions remained unchanged from Chapter 3 - Dirichlet velocity inlet and Neumann pressure outlet. To simulate the solid walls, Bounce-Back boundaries were used in place of periodic boundary conditions for both the velocity and advection-diffusion lattice and the inlet section was no longer implemented before the start of the packed bed packing. This region was previously used to reduce the velocity gradients caused when the imposed boundary velocity interacted with the stationary phase. This section was removed because the walls of the inlet region would form a parabolic flow profile from the "no-slip' boundary condition – contrary to the ideal homogeneous inlet profile that practical chromatography strives to achieve. Removing this entrance section reduced the rate of convergence for the velocity field, because of a larger instability between the interaction of the Dirichlet inlet and the packed bed. The void space between the bed and the outlet was maintained, so that the simulation results were independent of the Neumann outlet.

When varying the column-to-particle diameter ratio, the size of the domain was increased to maintain the resolution of each spherical particle. Because of this, the number of simulation nodes was increased by a factor of ~O(L_c), increasing the required memory and simulation time for larger packed beds. To counteract this, the medium's symmetrical properties were leveraged to simulate only a representative fraction of the column. Symmetry boundary conditions were used for two of the orthogonal transverse boundaries, as opposed to the bounce back condition (which were used for the other two boundaries), effectively simulating a column twice as large in each axial dimension. Numerically, symmetry boundaries enforced zero flux across the boundary plane and are analogous to "free-slip" boundary conditions (Fig. 4.2).

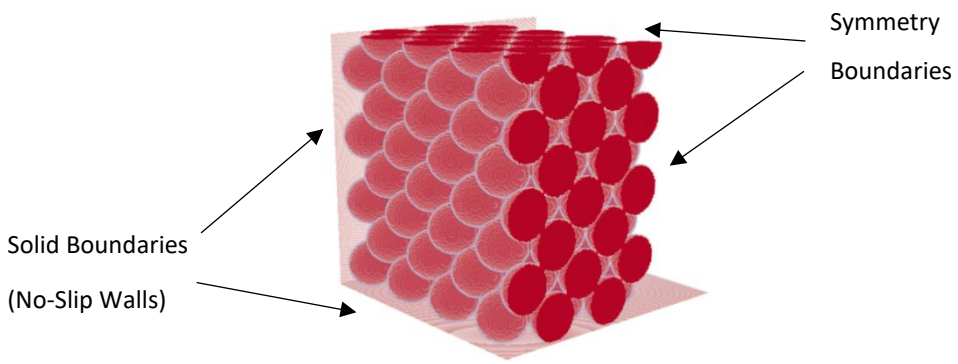

Figure 4.2. Illustration of a confined packed bed of FCC packing with a square cross-section. Two transverse boundaries are defined as symmetry planes to replicate a column of twice the size in each transverse

4.2 Column-to-Particle Diameter Ratio

The smallest representative number of primary spheres of a confined FCC pack consisted of two primary particles in each linear dimension, corresponding to a column-to-particle diameter ratio, χ, of $1+\sqrt{2}$. This ratio increased by $\sqrt{2}$ for each additional unit cell added in the transverse dimensions and if the number of primary particles is defined as n_p, then a relationship for χ can be defined (Eq. (4.1)).

$$\chi = \frac{d_{col}}{d_p} = 1 + (n_p - 1)\sqrt{2} \qquad (4.1)$$

where d_{col} is the column diameter [L]. Such a relationship can be written for any ordered packing, given that only whole particles are used, meaning that χ takes discrete values for any configuration. For random packings, this ratio can technically be any value greater than the particle diameter, although this does affect the packing efficiency. For the packing generation program used[151], randomly packed beds with dimensions less than $7d_p^3$ could not be generated for the specified porosity ($\varepsilon = 0.36$).

The ordered packing efficiency for the square cross-section was also found to be dependent on χ, which subsequently altered the system Peclet number when comparing systems with a constant superficial velocity. Accordingly, the lower total porosity caused a higher permeability with respect to the periodic case, which asymptotically decreased with χ (Fig. 4.3). In conjunction with this, the velocity profile across the transverse length (L_{trans}) of a confined ordered packing showed that the velocity field was dramatically skewed toward the wall, which suggests a severe channelling effect (Fig. 4.4). In these system, there were two distinct flow zones; wall and bulk column flow, the magnitude of which increased with χ for a constant superficial column velocity. The practical effect of these wall channels, for a pulse input, was that amount of dispersion increased through each section of the column causing a length dependence on the reduced plate height of the system.

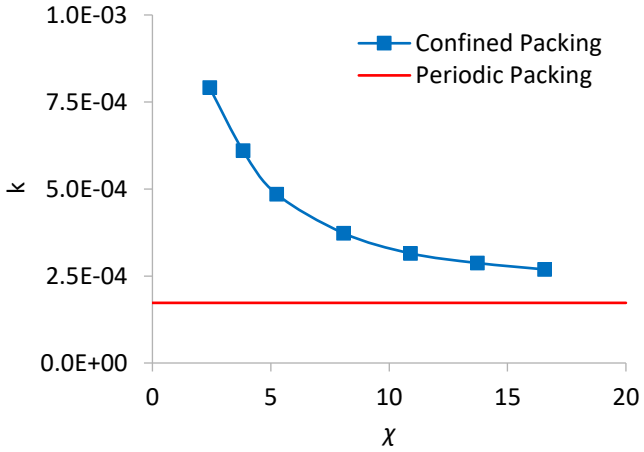

Figure 4.3. Permeability of confined FCC sphere packings. As the particle to column diameter ratio increase, the system permeability tends toward the value for the periodic case.

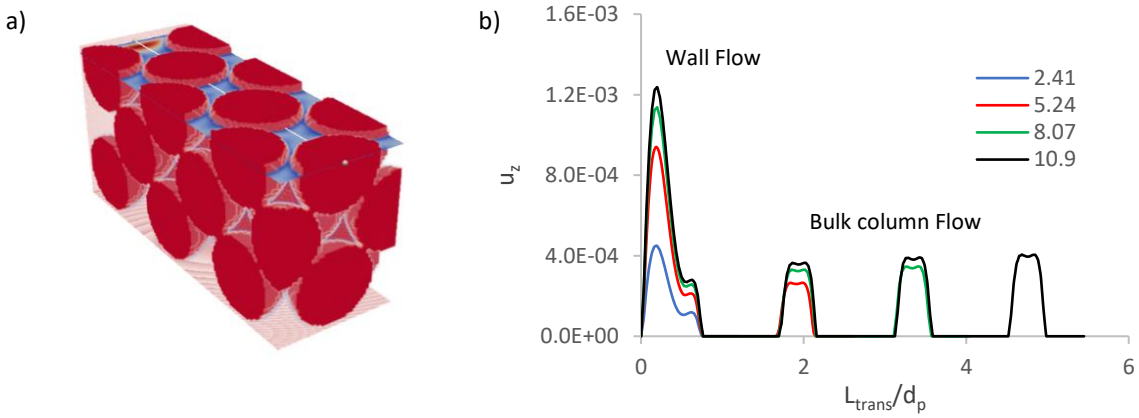

Figure 4.4. Velocity profile across the transverse axis in a confined FCC pack for a constant superficial velocity - a) depicts the location of the x axis for b) which shows the total magnitude of the velocity along the transverse column dimension for changing χ (χ values in legend).

For ordered packing systems, it was found that the reduced plate height increased with column length, in agreement with data for confined random packing systems in the literature using LBM methods[45]. Broeckhoven and Desmet[31, 32] showed that the length-dependence of the plate height in a packed bed can be modelled for both the short or long (length independent) range behaviour. Of relevance to the behaviour of FCC systems observed here, they proposed a two-zone plug flow model in which the additive plate height contribution caused by the wall can be analytically defined by three regions of the h vs. t (or $L = \bar{u}t$) relationship (Fig. 4.5).

The first is a linear plate height increase, in which the bands of solute species entrained in the two zones travels away from each other at a constant velocity dictated by the difference in channel velocity between the two zones. Following this, the transitional regime describes system behaviour as the rate of the plate height increase gradually tends to zero as radial equilibration of the concentration

gradient occurs, and the long-time limit is reached. This long-time limit was estimated in the work of Knox[203] (Eq. (4.2)).

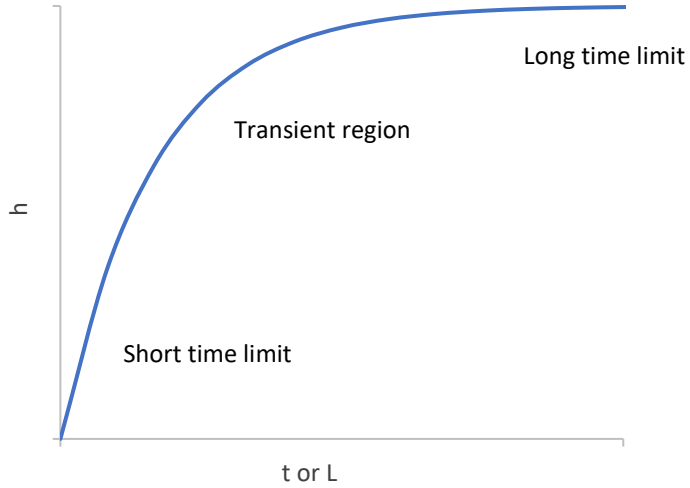

Figure 4.5. Evolution of the reduced plate height of confined packed columns which develops through equilibration of transverse diffusion between the wall and bulk flow zones.

$$t \cong \frac{{d_{col}}^2}{32 D_{rad}} \tag{4.2}$$

where D_{rad} is an estimate of the radial dispersion [L^2T^{-1}] (Eq. (4.3)).

$$D_{rad} = 0.7 D_{mol} + 0.03 u d_p \tag{4.3}$$

When investigating wall effects, the two variables of interest were the channel velocity (expressed in terms of the Peclet number) and the column diameter. The radial equilibration time was therefore important to consider here, because the column velocity determines the axial column length required to reach the limit ($L_z = \bar{u}t$) and increasing the column diameter increases the time required to achieve radial equilibration. For low *Pe* and χ systems the long-time limit solution is achieved in short columns, but for most systems, the results presented here are for the linear region of plate height increase because it was infeasible to achieve the long-time limit for systems with large *Pe* and χ given the model and computing resources.

To support Broeckhoven and Desmet's findings[31], the ordered packing systems were analysed, showing the behaviour for each region of plate height development from Fig. 4.2. First, the linear region was caused by the growing distance between the RTD curve contributions where radial dispersion has not yet become a factor. This can be verified simply from the development of the axial RTD profiles in a high Pe environment (Fig. 4.6).

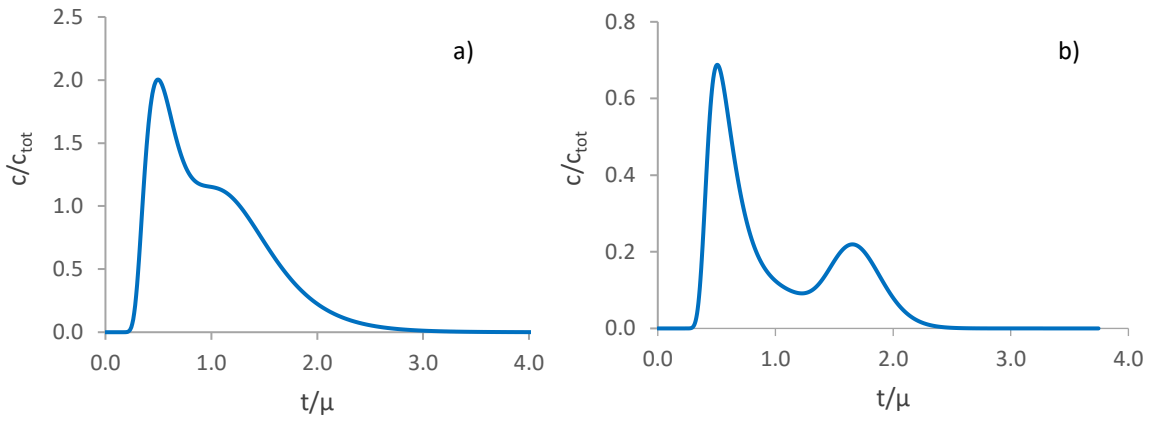

Figure 4.6. The divergence of RTD peaks caused by the difference in velocity between the bulk and wall regions of a confined FCC sphere pack (Pe = 32, χ = 8.07) after a) one unit cell and b) five unit cells from packing entrance, in the axial direction.

Once the solute enters the transition regime, radial diffusion between the bulk and the wall flows becomes influential on the plate height – reducing the magnitude of total column dispersion. To observe this effect, the sampling slices were split into an RTD of the wall channel flow, and an RTD of the bulk flow (Fig. 4.7). While the solute pulse propagates through the column, solute particles in the channel flow and the bulk flow separate, because of the skewed velocity profile across the column. Subsequently, radial equilibration starts to ensue because of the transverse concentration gradient caused by the solute separation. This occurs in two ways, first, the solute in the wall flow diffuses into the bulk flow, which causes an increasing amount of fronting on the RTD for the bulk flow (Fig. 4.8b). Second, solute in the bulk flow diffuses into the channelled flow causing large amounts of tailing in the wall flow (Fig. 4.8a).

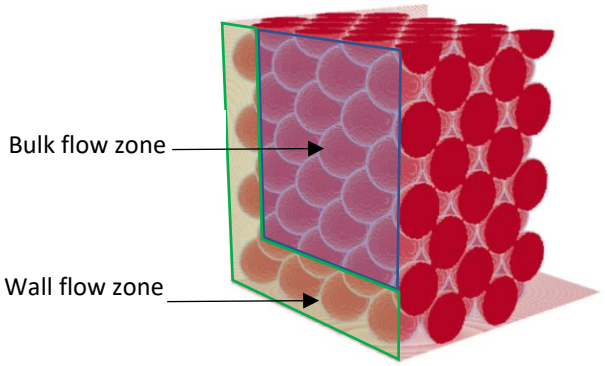

Figure 4.7. Illustration of RTD sampling slices for observing wall (green) and bulk flow (blue) regions. Flow runs left to right.

The magnitude of both fronting and tailing increased with the column length, because there was more time for solute to diffuse between the flow systems. Evaluating the plate height of each zone,

showed that the wall flow had a significantly larger contribution to the overall system HETP when compared to the mobile phase band broadening of the periodic FCC packing.

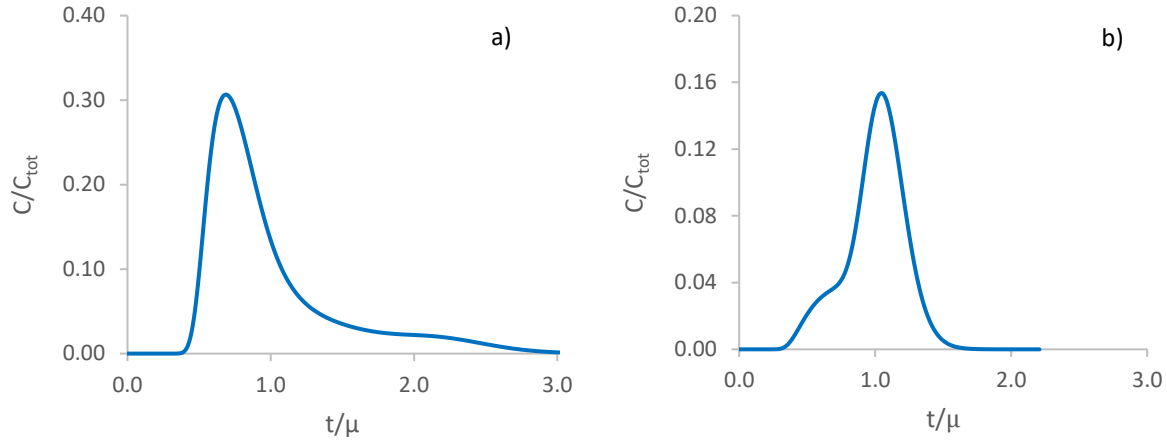

Figure 4.8. RTD of the a) wall flow and b) bulk flow in a FCC sphere pack (Pe =29, χ =5.24) 5 unit cells downstream of the packed bed entrance. This illustrates tailing for the wall flow RTD and fronting for the bulk flow RTD.

Finally, once the long-time limit is reached, the major solute differentials between the two flow systems are attenuated and the amount of band broadening becomes constant. In the systems of FCC packed spheres, the long-time limit was observed over short axial lengths for low *Pe* and χ. Instead of the characteristic dual peak in the linear and transition zone (Fig. 4.9b), the RTD curve for a radially equilibrated column has a single distinct peak and a long tail (Fig. 4.9a).

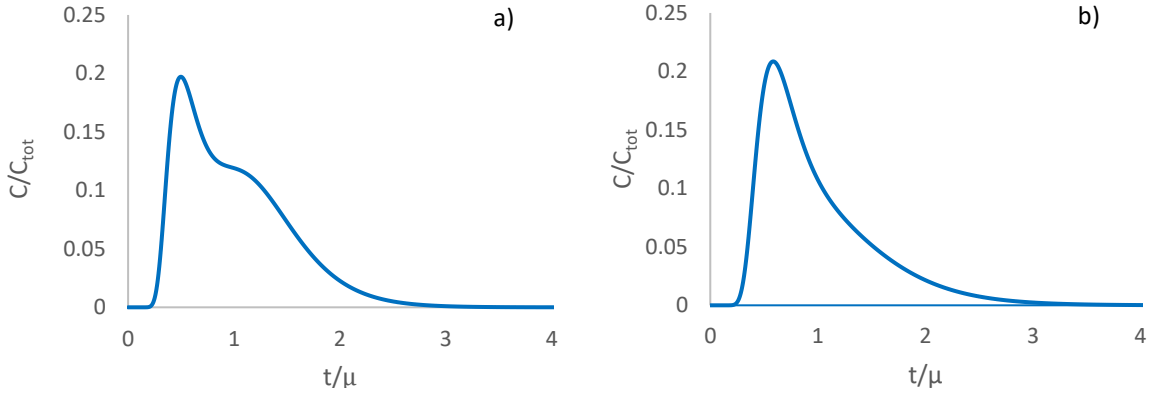

Figure 4.9. RTD profiles of a) Long Time Limit (Pe = 2) and b) Transition region flow (Pe = 23) in packed beds of FCC spheres (χ = 2.41).

From the CFD data, it was found that most of the simulated systems were in the linear regime of the plate height increase (Fig. 4.10), the few exceptions being the smaller and slower flow systems. This corresponded well with the long-time limit predicted by Knox's work (Eq. (4.2)). The model developed by Broeckhoven and Desmet can predict short-range (Eq. (4.4)), transition and long-range (Eq. (4.5)) contributions of the wall effect in packed beds that exhibit two-zone plug flow velocity

profiles (Fig. 4.4b). However, this model was stated to be valid for systems in which the width of the wall flow zone, δ, was less than *5%* of the total column width. For FCC packings, the wall flow zone was found to be constant for all χ at a value of $d_p/2$. Therefore, within the context of this work, the model can only be used to model behaviour for columns in which $\chi > 10$. The plate height data from periodic and confined FCC packings from this study shows strong agreement with the two-zone plug flow model in the short time limit region (Fig. 4.11). This suggests that the wall effect produces the dominant contribution to the overall system dispersion compared with the dispersion in the bulk column packing itself.

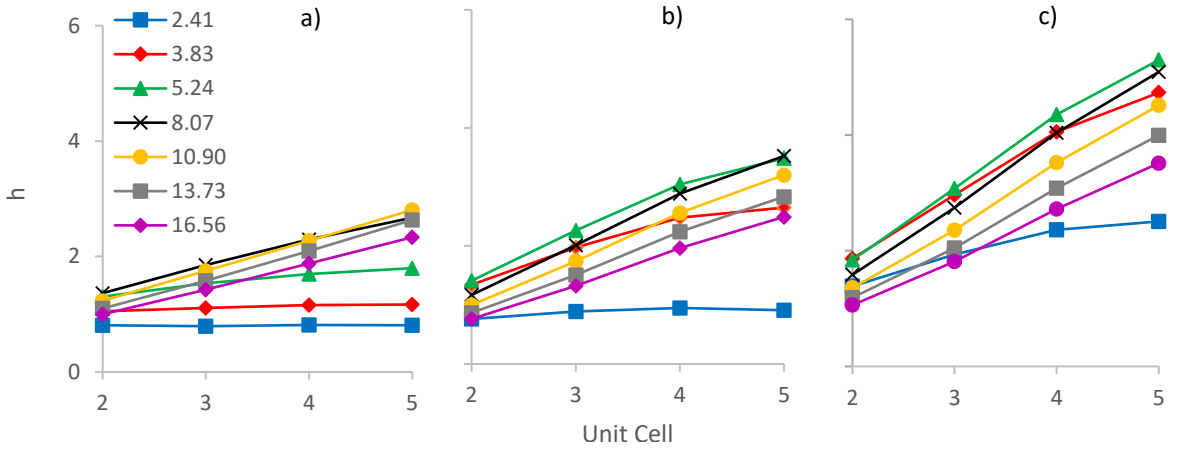

Figure 4.10. Evolution of reduced plate height for confined FCC packing for varying χ at a superficial velocity of a) $1e^{-5}$ ms^{-1}, b) $1e^{-4}ms^{-1}$ and c) $5e^{-4}$ ms^{-1}. The x axis corresponds unit cell in the axial direction over which the reduced plate height was measured. The legend denotes values of χ. The particle diameter is 200 μm.

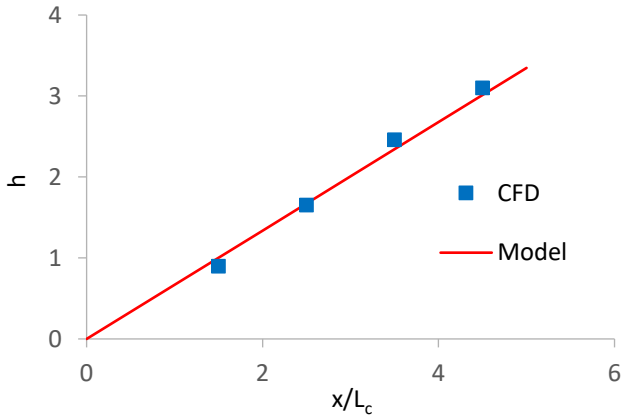

Figure 4.11. Example of agreement between CFD data and the two-zone plug flow model from literature for FCC sphere packing (Pe = 33 χ = 10.9). x refers to the axial co-ordinate on the sample.

$$H_W(t \rightarrow 0) = 2\alpha_c\alpha_w\Delta v^2\bar{u}t \tag{4.4}$$

$$H_{W,\infty} = \frac{32}{a}\frac{\Delta v^2 \bar{u}}{D_{rad}}\,\delta^2\left(\frac{\varepsilon_w}{\varepsilon_c}\right)^2 \tag{4.5}$$

where H_w is the additive plate height contribution from the wall effect [L], α_c and α_w are the volumetric fluid fractions of the column and wall zones, respectively, Δv is the difference between the column and wall flow [LT^{-1}], ε_c and ε_w are the void fractions of the column and wall zones respectively and a is a geometric factor defined by the channel shape.

For a practical chromatographic column, it is not a certainty that the long-time limit will be reached, but it is not infeasible. For example, assume a χ value of *100* and a *Pe* value of five (around the optimum or random sphere packing), this would require an axial column length nearly $2000d_p$ meaning that the aspect ratio of the column would be *1:20* (width to length). In fact, given the observed increase in plate height with column length, long columns are detrimental to performance. Therefore, minimizing column length in the axial direction and increasing χ becomes an attractive concept for reducing dispersion in confined columns, although it is noted that this can reduce chromatographic resolution because the solute peaks have less time to separate. In conjunction with this, it is already common practice to minimize length, because this reduces the pressure drop when compared to increasing column diameter[204]. Based on the findings for entry length in ordered packings (Section 3.1.2), it was assumed that this was not a factor past the first unit cell for confined FCC packings. The reduced plate height was analysed for varying *Pe* and χ across the second and fourth unit cells from the column entrance (Fig. 4.12).

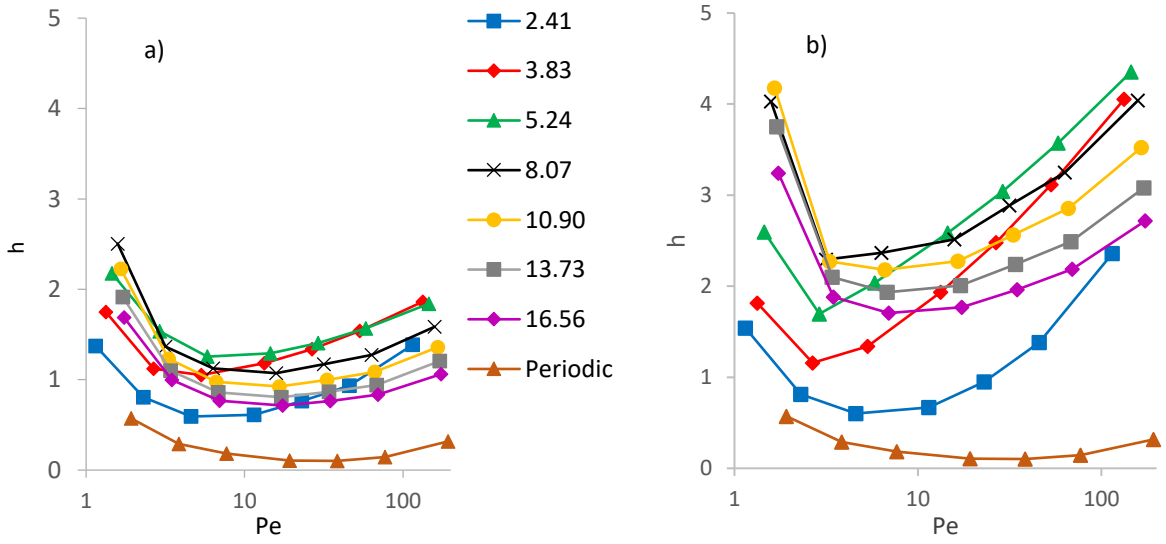

Figure 4.12. van Deemter plots for varying χ for a) the second unit cell and b) the fourth unit cell downstream of the packing entranced of confined FCC sphere packing. The legend denotes the value of χ for each curve.

As discussed earlier, most simulations were carried out within the short-time region, which was further echoed by the increase in the local plate height across the second and fourth unit cells. A noticeable trend was that the minimum reduced plate height for the larger columns was shifted to lower Peclet numbers, meaning that the wall effect is more severe at higher Peclet numbers. It is important to

note that for both unit cells, the minimum reduced plate height did not monotonically increase with χ. Instead there is a clear hierarchy, in which, the worst performance is observed when $\chi = 5.24$ and $\chi = 8.07$ for the second and fourth unit cells, respectively. This means that larger columns exhibit less band broadening at shorter length scales. However, as the axial length column length increases, wider columns exhibit a greater degradation of performance, meaning the dispersion at the long-time limit is larger. To more clearly illustrate this point, a clear trend between the plate height and χ shows how larger columns had superior performance at shorter axial lengths (Fig. 4.13).

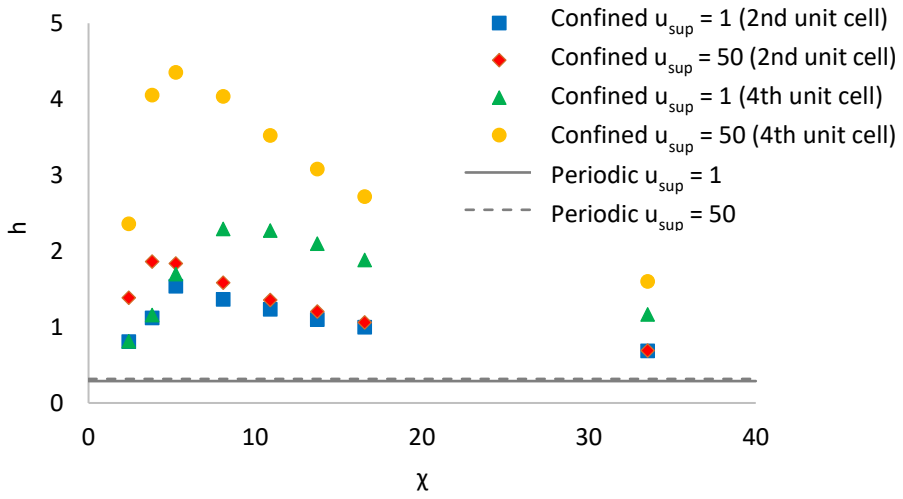

Figure 4.13. Comparison of the reduced plate height at two different axial lengths and two superficial velocities at varying χ, illustrating the more rapid increase of dispersion in smaller and faster systems.

This observation agrees with the model proposed for the long-time limit (Eq. (4.4)). This increase in band-broadening with column diameter also agrees with literature results for randomly packed showing the same trend[205]. For FCC packing with a square cross-section and constant Peclet number, it can be assumed that the shape factor and radial dispersion are constant for a given bed morphology. The long-term plate height is therefore determined by the velocity difference between the wall and channel flow, the average channel velocity, the thickness of the wall flow and the porosities of the bulk and channel regions. The radial thickness of the wall flow zone and the porosities of each zone were both found to be constant for FCC packings, meaning that the plate height contribution from the wall effects in the long range is purely determined by the average channel velocity and the velocity difference between the wall and bulk column flow. It was found the both the channel and wall flow velocities increase with χ because of the overall decrease in column porosity, but the wall flow increases at a greater rate (Fig. 4.4b). This means that both Δv and $\bar{u}$ both increase with χ and larger columns will always have a greater plate height at the long-time limit. However, because these factors increase to an asymptotic threshold (because the porosity decrease is limited by the periodic case) this suggests that the long-term plate height will also reach an asymptotic limit for both column length and width, though

we cannot simulate columns of this magnitude. As the long-time limit (Eq. (4.2)) is determined by the column diameter, the asymptotic limit described is approached at a slower rate in columns with larger χ.

Ultimately, the dispersion caused by wall effects is due to a portion of the solute input that travels faster through the packed bed than the remaining solute because of the difference in velocity profiles. Therefore, columns with a larger χ experience a slower increase in band broadening because of the proportion of the solute in the bulk flow is larger and the radial dispersion process takes longer. Inspection of the RTD profiles at equivalent unit cells for increasing χ shows a clear transition from the dominance of the wall flow component in the RTD at low diameter and the dominant bulk flow at large diameters (Fig. 4.14).

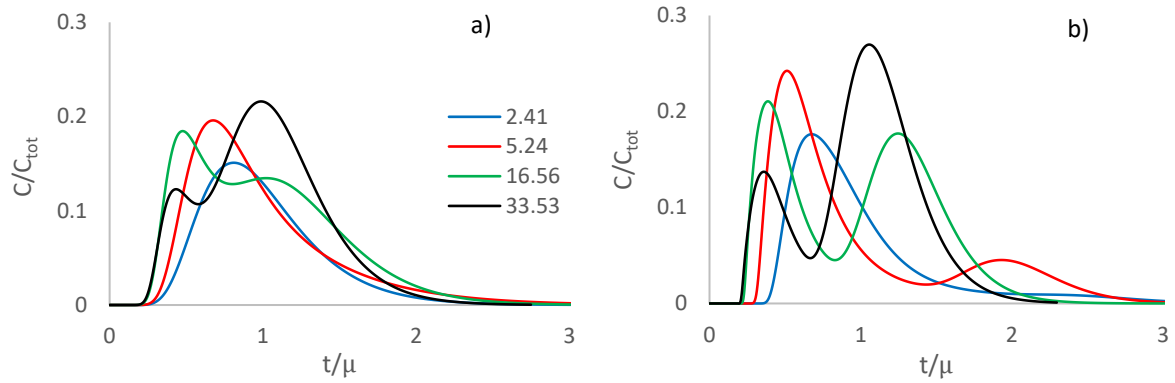

Figure 4.14. Illustration of distribution of solute between the wall (left peak) and bulk (right peak) in the RTDs for varying χ (denoted by legend) at: a) u_{sup} = 1 and b) u_{sup} = 50 measured after the fourth unit cell of the packed bed. The key denotes the value of χ.

In this work, only confined FCC [001] packings of spheres were studied, which were attributed with the lowest bulk voidage of all ordered packings studied in Chapter 3. If the findings here were applied to other packing configurations, the theory suggests the impact of walls would decrease with the difference in voidage between the bulk packing and wall zones. This can be explained by the difference in velocity between the wall channels and the bulk flow, which would be lower, resulting in a lower rate of divergence of the RTD peaks. The opposite case to the observations described in this section is also possible, in which the walls zones have lower voidage compared with the bulk packing, causing slower flow in the wall channels (e.g. the extreme case of an empty column). Ultimately, these systems would experience the same channelling issues, but for chromatographic purposes this case would arguably be less detrimental because solute from the wall flow would not prematurely leave the bed.

The model proposed by Broeckhoven and Desmet only considers the additive contribution of wall effects to the plate height of a confined packing. Therefore, the true dispersion behaviour for a

given packed bed is a combination of the wall effects and the behaviour of the bulk packing itself. In Chapter 3, FCC [001] was proven to the have the lowest band broadening properties out of all sphere packings but, did not show the highest performance when compared to other packing configurations. For example, octahedrons in the BCC [001] configuration and tetrahedrons in the FCC [001] configuration, produced lower band broadening and more importantly for the context of this chapter, lower porosity than FCC [001] spheres. The bed porosity dictates the magnitude of the wall effect through the discrepancy of the velocity profile across the transverse column dimension so packed beds with higher voidage would have a lower voidage difference between the wall packing and bulk column packing.

As a final thought on confined packings, Chapter 3 highlighted the importance of transverse flow by identifying a correlation between tortuosity and minimum reduced plate height. However, the traditional column wall runs in the axial dimension and resists transverse flow, meaning that practical columns may cause greater flow disruption in high tortuosity packings. Providing evidence to this point is outside of the scope of this work but, would be an important piece of future research for the practical applications of confined ordered packings.

4.3 Embedded Column Walls

In Section 4.2, it was shown that wall effects cannot be completely ignored at any column width. However, the plate height increases at a lower rate for larger columns and hence, in practice, the long-time limit should not be reached – lowering the observed dispersion caused by the bed. However, columns that cannot achieve high values of χ are fated to poor performance because the long-time limit is achieved at much shorter time and length scales. In the work of Schure et al[14] and Fee et al.[12], it was suggested that wall effects could be alleviated to some extent by embedding the walls with particles. This concept had little physical relevance for the former study, but it was suggested by Fee et al. that it is achievable through 3D printing particles into the walls. Embedded walls are created by extending the particle packing by calculating particle centres beyond the confines of the domain and creating fractional particles that protrude through the walls (Fig. 4.15). This creates beds with constant porosity across the cross-section and hence more uniform flow through the column, much like the periodic ideal.

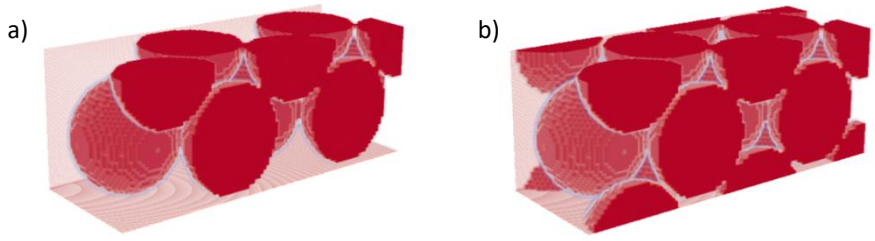

Figure 4.15. Visual comparison of: a) non-embedded and b) embedded packing of FCC spheres.

The embedded packings are no longer constrained by strict values of χ to create a uniformly packed column, because of the ability to print particles into the wall. However, varying the point at which the wall intersects the packing was not tested, because this work aims to instead provide a pure comparison at the specific values of χ from the non-embedded columns. The permeability is higher than for the bulk case because the walls themselves provide increased resistance because of the "no-slip" boundary, and this effect decreases with increasing χ (Fig. 4.16b). Although this relates to a higher pressure drop than for non-embedded packings, it implies heterogeneity of the velocity field, which suggest that wall effects are mitigated.

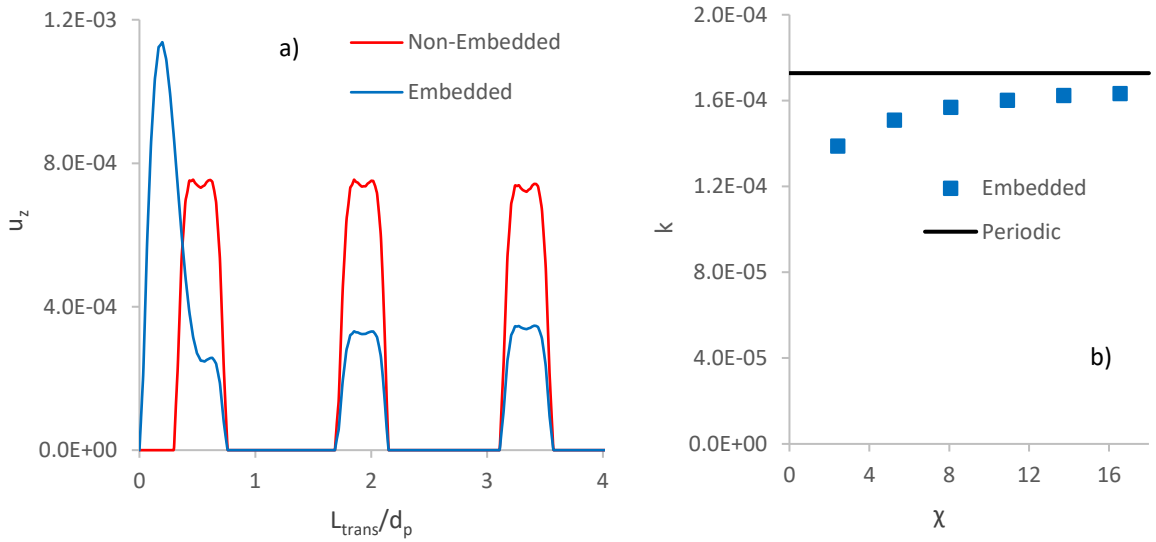

Figure 4.16. a) homogenization of the transverse velocity profile in ordered FCC packings of spheres by using embedded walls and b) the lower permeability caused by no slip walls which tends to the periodic value.

It should be noted that the reduced plate height does again increase with column length, as observed for the non-embedded case, but at a much lower rate - especially as χ increases. In these systems, the walls created the opposite effect, in which the wall channels exhibited slower flow than the bulk, which amounted to tailing in the RTD profile. However, the wall effect in this scenario is demonstrated as having a much lower magnitude than the case for non-embedded packings (Fig. 4.17). It is also important to note that the reduced plate height monotonically decreased toward the periodic case, unlike non-embedded columns, because of the more homogeneous transverse velocity profile.

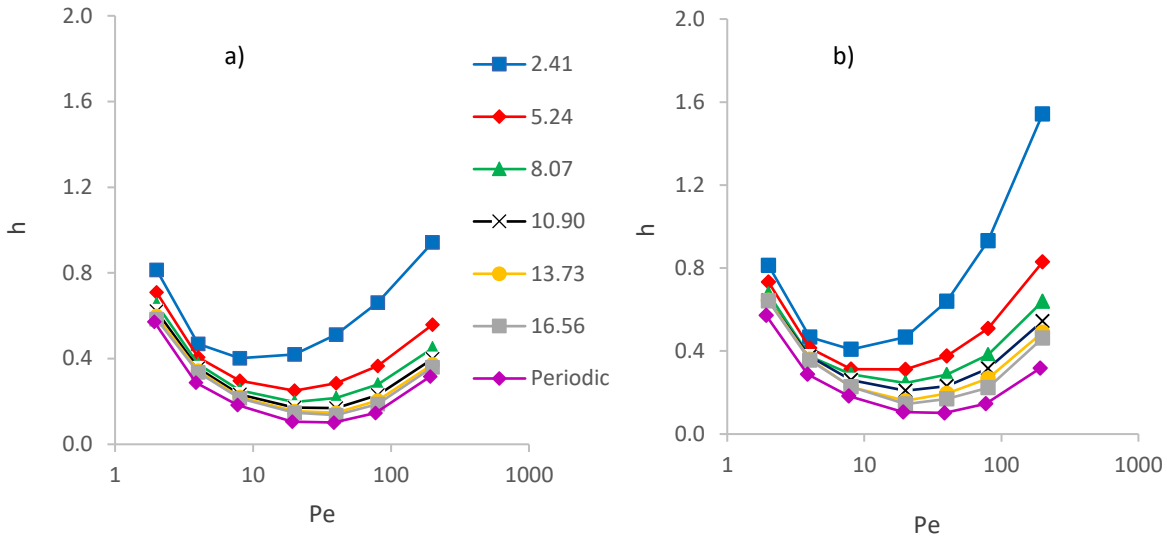

Figure 4.17. van Deemter plots for varying χ for a) the second unit cell and b) the fourth unit cell downstream of the packing entranced of confined FCC sphere packing with embedded walls and square cross-section. The key denotes the value of χ for each curve.

FCC spheres were considered a limiting case for wall effects in confined ordered packings because they have the lowest voidage and being most disrupted by column walls. For some other packing configurations, embedded walls were not applicable. For example, if SC [001] packing is defined as being flush with the walls (Fig. 4.18a), then the packing is not disrupted by the walls, but the wall effect still exists. Alternatively, the packed bed could be translated so that the walls intersect the particle centres (Fig. 4.18b), creating a more uniform velocity profile across the width of the column for this packing configuration (Fig. 4.18c).

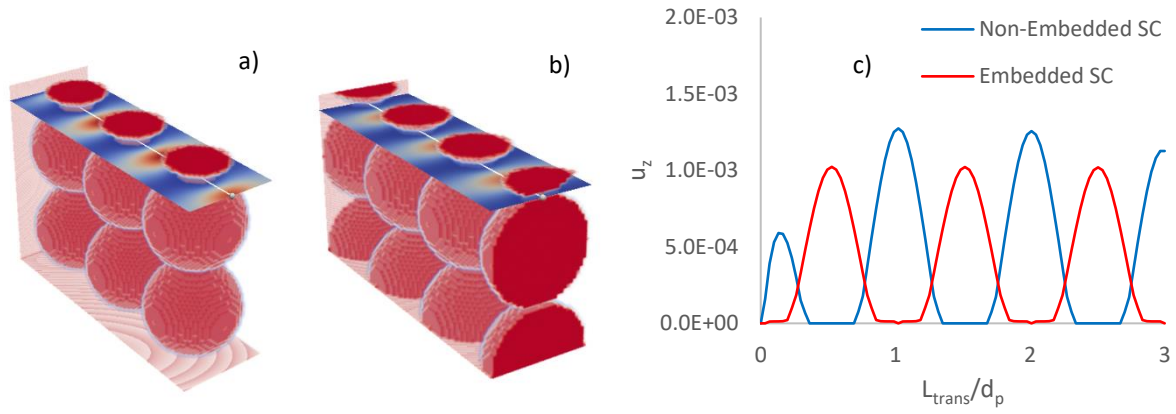

Figure 4.18. SC [001] packing, a) flush with the walls and b) embedded into the column walls. c) compares the transverse velocity profile for each packing along the displayed axis.

For the future of confined packings, a beneficial area of research would be to consider further methods of manipulating walls to remove the increasing amount of dispersion with the column length. The location of the wall with respect to the packed bed is a variable that can be applied to any packing type.

Manipulating this factor could further minimize walls effects in confined ordered packed beds and is an important subject for future investigation of confined ordered packings.

4.4 Square vs. Circular Cross-Section

In pipe flow, a circular cross-section (CCS) minimizes the drag forces on the flow system[206]. For randomly packed chromatographic systems it has also been shown that a CCS minimizes dispersion because channelling is much more pronounced in 2D cross-sectional geometries that have corners[45]. In this chapter, only square cross-sections (SCS) have so far been used to compare embedded and non-embedded wall packings because the SCS causes less disruption to the particle packings, which are based on the crystal cubic cell. It could therefore be argued that the above results do not pertain to practical chromatographic systems, which use circular cross-sectioned geometries. To address this point, a comparison between circular and square columns is an important step for proving the effectiveness of embedded walls at mitigating the wall effect in ordered packed beds.

CCS columns were created with an equal diameter to the equivalent SCS column (Fig. 4.19a). Although this created columns with a lower cross-sectional area, the value of χ was retained when comparing columns. The issue for non-embedded cylindrical columns is that the curved surface of the column wall made it infeasible to efficiently pack particles at the column walls in a system of monodisperse particles, especially at low χ. When using embedded walls, however, this is no longer an issue, because partial particles can be printed into the column. Compared with square cross-sectioned columns, the permeability is marginally higher, but this was roughly the same size the error of the model at that resolution (Fig. 4.19b). Therefore, it cannot be stated with certainty that the pressure drop is in fact lower. Regardless, the difference in pressure drop is small, meaning that the embedded packed bed also mitigates the increased pressure of a non-cylindrical cross-section column.

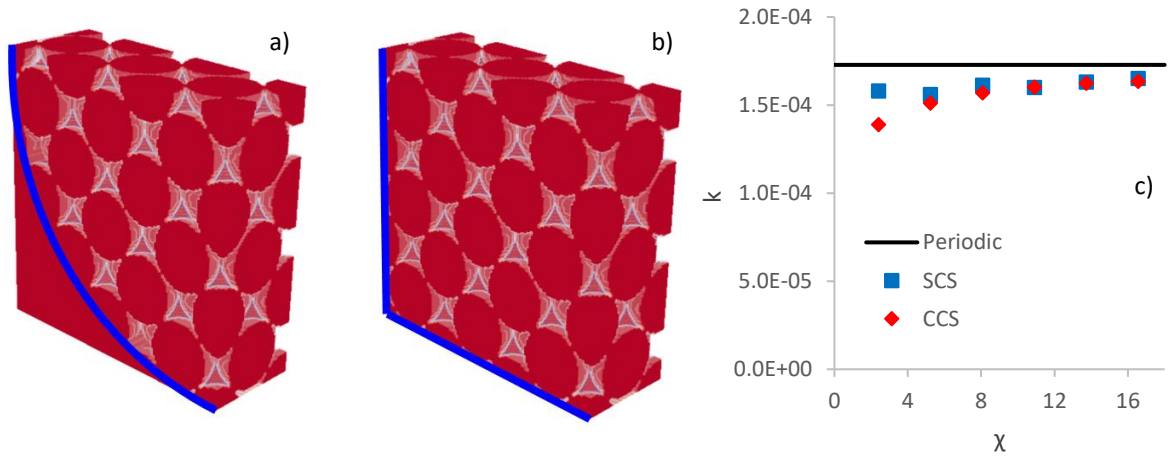

Figure 4.19. Illustration of a) circular cross-section (CCS), b) square cross-section (SCS) and c) the comparison between the permeability between the two systems for varying χ.

Comparison between the dispersion properties of the column morphologies shows that CCS slightly outperforms SCS at high Pe values, but otherwise the systems are comparable (Fig. 4.20). The observed variance was thought to be because of the corners that are present at the intersection of the transverse boundaries in SCS columns. The proportion of corner flow in SCS systems decreases with increasing χ meaning that the increased band broadening caused by these zones is reduced and the performance of the two morphologies converges. An interesting observation can be made at $\chi = 1+4\sqrt{2}$ for the CCS column, at which value the reduced plate height increases compared with the smaller columns. This behaviour does not occur in SCS columns and hence, must logically be a product of the geometric interaction between the curved wall surface and the crystal cubic cell. Furthermore, this small increase does not occur at lower Peclet numbers where diffusion is dominant, suggesting that is caused by an advective process. It could be argued that this anomaly is within the amount of error observed in the model, but this is a consistent trend, which noticeably increases with Pe, suggesting the trend is real. Geometrically, the resultant shape of the spheres when intersected by the walls differs with χ, which creates a region of the velocity field which is slower than the analogous channels elsewhere in the medium (Fig. 4.21).

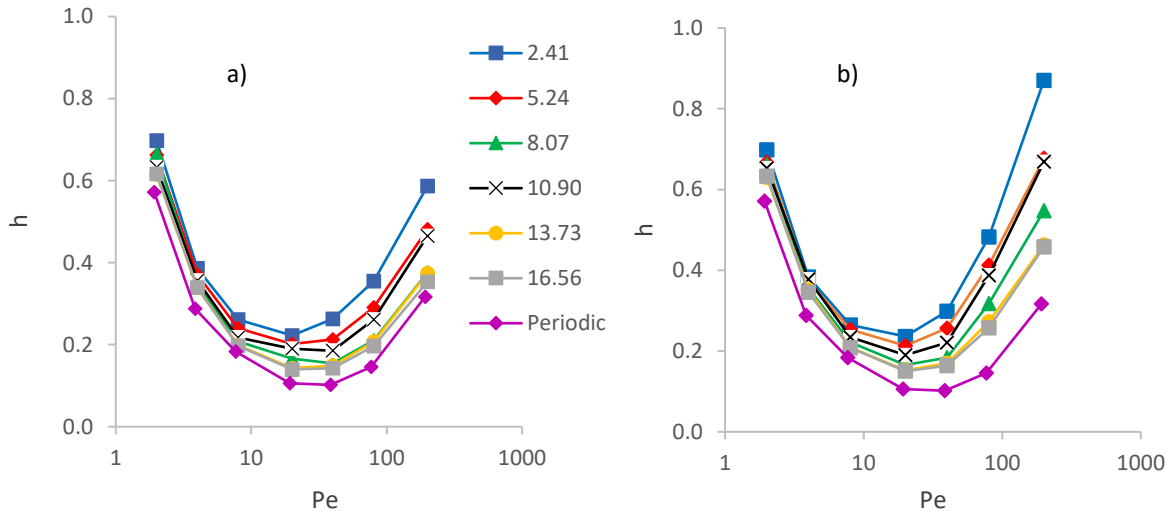

Figure 4.20. van Deemter plots for varying χ for a) the second unit cell and b) the fourth unit cell downstream of the packing entranced of confined FCC sphere packing with embedded walls and circular cross-section. The key denotes the value of χ for each curve.

Although there is a slight difference in the performance between the column cross-section shapes, it has been shown here that the performance of these systems is similar for low values *Pe* and large χ, suggesting that the wall shape becomes less influential on mobile phase band broadening for embedded ordered packing systems. This is also expected to be the case for embedded randomly packed systems, although this was not explored in the current work. Although it is slightly less efficient, the SCS offers a more efficient geometry for utilizing a given characteristic length and provides a greater volumetric flow rate for its characteristic dimensions than the CCS columns. Overall, the implications

of this finding are substantial for applications which use alternative column cross-sections, such as in HPLC microchips[45].

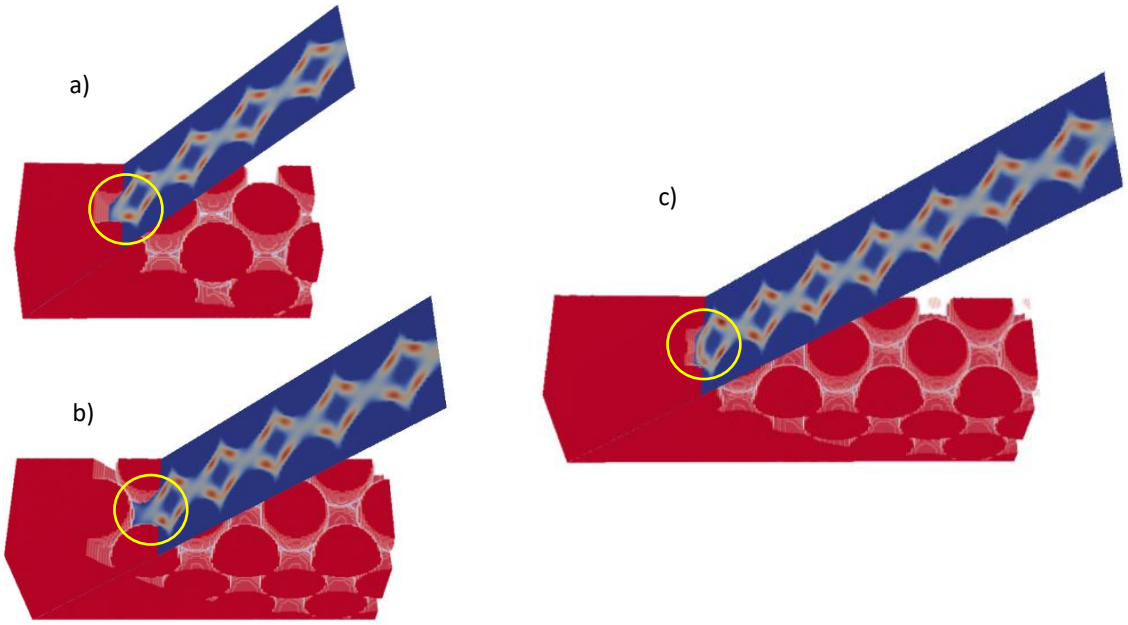

Figure 4.21. Comparison of the channel velocity profile in CCS for a) χ = 8.07, b) χ = 10.9 and c) χ = 13.73 showing the greater velocity difference for χ = 10.9 at the wall due to the packing interface, highlighted by the yellow circles. For the slices illustrating the velocity magnitude, red illustrates high velocity while blue is low velocity.

4.5 Conclusions

In this chapter, it has been shown that the length dependence of dispersion in confined ordered packing is consistent with the trends found in a two-zone plug flow model[31]. This is also a phenomenon seen in random packing, but because FCC has a much larger discrepancy in the characteristic voidages near the wall and bulk flow regions, the effect has larger impact on column performance in FCC than in randomly packed columns. The long-time limit of dispersion increases with the column-to-particle diameter ratio, meaning that larger columns ultimately result in poorer performance. The rate of the increase in dispersion occurs in three stages: short-time (linear), transition and long-time (constant) limit. Most systems in this study were in the short-term limit because the long-time limit is unachievable using the developed model for high Pe and χ values, because of computational resource constraints. However, the RTD curve behaviour from this study agrees with the proposed mechanism for wall effects from the literature, in which the divergence of the RTD peaks in the wall and bulk zones causes linearly increasing dispersion. The rate at which dispersion increases is gradually offset by the diffusion of solute between the two flow systems, until the long-time limit is reached because transverse concentration gradients have been eliminated.

Although larger columns are less efficient, based on the long-term limit, the rate at which the wall effect increases dispersion is reduced. This was found to be because the proportion of solute that is entrained in the wall flow decreases with χ and hence has less effect per unit distance. Therefore, in practice it is preferential that the long-time limit is not reached, by increasing the column width while reducing the axial length, though the column length must be long enough to achieve sufficient chromatographic resolution.

To further mitigate this effect, is was found that partial particles located at the wall boundaries, practically achievable using 3D printing, homogenized the transverse flow profile of the column, thus dramatically reducing the amount of dispersion caused by packing confinement. Although the wall effect is still observed in these systems, its magnitude has much lower impact on column performance when compared to non-embedded systems. A focus for future work in this field, is to determine the most effective point in the cross-section of the unit cell at which the walls intersect an embedded packing.

Finally, when comparing the square and circular cross-sectioned columns it was found that the circular cross-section showed better performance at lower values of χ, which was attributed to the corner flow in rectangular columns remaining relevant in embedded columns. Even so, within standard operational Peclet numbers, the performance of both systems was comparable, suggesting that perhaps column performance can be considered independent of the wall shape for practical scenarios. This is particularly useful for applications such as HPLC microchips and maximizing chromatographic throughput for a given characteristic length because these systems aim to use irregular cross-sections and hence are more negatively impacted than traditional circular cross-section media. Ultimately, the process of embedding column walls is an important advance toward reducing dispersion.

5. Chromatographic Performance of Triply Periodic Monoliths

5.1 Introduction

The use of monolithic structures as chromatographic media is becoming commonplace in practical applications, because of their low band broadening and high permeability characteristics[207]. However, the drawback of monoliths is that their manufacturing process is more difficult than for packed beds and, currently, the cost and time of manufacturing can outweigh the performance gain[208]. In the context of this work, when 3D printing is used to fabricate a porous medium, the fabrication process of monoliths is identical to creating a packed bed and hence, the manufacturing concerns which previously hindered the use of monoliths, become irrelevant.

Excluding straight channel structures, which can be created by extrusion[209], practically used monolithic beds have random internal structures, much like randomly packed beds, because pore geometry cannot be controlled during the manufacturing process[210-212]. From the promising results for ordered packed beds in this thesis (Section 3), the idea of geometric order was transposed to monolithic structures with the aim of producing morphologies with low band broadening and increased permeability compared with ordered packed beds of discrete particles. Furthermore, for packed beds, it was clear that particle overlap was necessary to maintain the integrity of the ordered packed beds, though the extent of overlap required was thought to be dependent on the structural properties of the medium. This overlap factor was shown to degrade separation impedance by increasing the pressure drop, while the reduced plate height was only slightly decreased, unaffected or increased. For conventional monolithic structures, bed integrity is less of a concern because monolithic structures are continuous and do not have specific areas of structural weakness.

Triply Periodic Minimal Surfaces (TPMS) are an attractive candidate for porous media because they provide minimal surface area for a continuous volume (the monolithic equivalent to a sphere), hence reducing the pressure drop of these systems. Discovery of these surfaces was pioneered by Schwarz[213] and Neovius[214] and further major works have been published in modern times by Schoen[34, 35] and others[215-218], who have built on the earlier works by discovering further minimal surfaces and also applying them to practical scenarios. There are many TPMS surfaces described in the literature that can be approximated by a level-set equation[36] (i.e. a description in Cartesian Space), removing the need for a surface evolver to define the geometry for the CFD model to use. For practical

applications of these structures, there is published data on the permeability of TPMS structures in flow systems[216] and the structural properties[219], however, there has been nothing published to date about flow dispersion properties.

This chapter begins by using multiple TPMS structures in the CFD model to determine if there are performance improvements over ordered packed beds of particles. The simplest TMPS structure, "Schwarz Primitive" was then used as a case study for numerical manipulations of the level set equation, creating geometric alterations of the TPMS morphology and altering the flow properties of the structure. Finally, observation of the flow channels in TPMS and straight channelled monoliths led to the development of structures which focused on definition of the shape of the flow channel itself. Helical shaped flow channels comprised a single or multiple tortuous flow channels through the axial length of the column, increasing flow tortuosity when compared with straight channels, a morphology that is currently used in monolithic structures.

5.1.1 Model Adjustments

For the flow lattice, the axial boundaries were defined with a velocity inlet and pressure outlet, while the transverse boundaries were periodic. For the advection-diffusion lattice, the inlet used a Dirichlet boundary to define the solute pulse and a Neumann outflow for the solute to exit the column. The solid phase used no-slip (bounce-back) conditions for both lattices, to simulate an impermeable stationary phase.

The definition of the solid phase for monoliths was a much simpler process and involved a single equation to define the entire domain, as opposed to calculating the location of each particle individually. Additionally, the non-dimensionalization of HETP was no longer related to a characteristic particle size and instead the axial periodic length was used in these scenarios – which was a close equivalent to d_p.

5.2 Triply Periodic Minimal Surfaces

A minimal surface is defined as having a mean curvature of zero, i.e. every point on the surface is a geometric saddle point and there is equal "bending" at opposite sides of every point on the surface[220]. These structures are of interest in this work because of the promising performance shown by random monolithic structures in liquid chromatography when compared with randomly packed beds[207]. These surfaces minimize the surface area for a given volume, which in theory, reduces the pressure drop because of there being a minimal amount of liquid-solid interface. But, as opposed to spheres, TMPS structures are not discrete and can only minimize the ratio of surface area to volume for a morphology of infinite size in each spatial dimension. Although minimizing the surface area to volume

ratio does not directly correlate to reduction in band broadening, e.g. octahedrons and tetrahedrons vs. spheres, it does increase permeability when comparing media with constant void space. An interesting mathematical property of TPMS, is the characteristic of being embedded, meaning that they do not intersect themselves[221]. Geometrically, this means that TPMS structures are smooth and do not have unnecessary obstructions in the flow field which could cause decreases in permeability.

Minimal surfaces are classified into "Bonnet families" (or associate families), that share Weierstrass–Enneper parameterization, in which, each family member can be differentiated by specific Bonnet transformations[222]. The Weierstrass–Enneper parameterization is essentially a parametric equation which describes the location of the surface co-ordinates using complex analysis (Eq. (5.1)).

$$x(r,\theta) = \mathrm{R}\int \frac{1}{2}F(s)(1-G(s)^2)ds \quad (5.1a)$$

$$y(r,\theta) = \mathrm{R}\int \frac{1}{2}iF(s)(1+G(s)^2)ds \quad (5.1b)$$

$$z(r,\theta) = \mathrm{R}\int F(s)G(s)ds \quad (5.1c)$$

$$s = re^{i\theta} \quad (5.1d)$$

where *F(s)* and *G(s)* are functions which define the minimal surface, R is the real part of the integral, *i* is equal to $\sqrt{-1}$. A Bonnet transformation is mathematically defined as the weighted sum of two minimal surfaces (Eq. (5.2)).

$$S' = \cos\Phi_b S^{90} + \sin\Phi S^0 \quad (5.2)$$

where *S'* is the Bonnet transformation of S^0, S^{90} is the unique point which makes *S'* isometric to S^0 and Φ_b is the Bonnet angle. To conceptualize this process, consider a simple example of a Bonnet family, the catenoid and helicoid; two of the first minimal surfaces to be discovered (not including the flat plane) (Fig. 5.1). For the catenoid $F = 1$, $G = s^{-1}$ and the helicoid $F = 1$, $G = i.s^{-1}$, which are defined as being adjunct surfaces, i.e. the Bonnet angle is 90° between each structure. A Bonnet rotation does not cause stretching or wrinkling and in the case of the catenoid-helicoid family, the rotation process can be easily visualized.

For modern studies, minimal surfaces can be developed using an iterative surface evolution process, based on specific initial conditions provided by the user. A program developed by Kenneth Brakke[223] is a popular open source surface evolver, which is used by researchers to study minimal surfaces. However, an alternative option was used for defining geometries in this chapter, using level-set approximations in Cartesian space to approximate the TPMS structures, as developed in the work of Wohlgemuth et al.[36]. The level-set equations are characterized as specific combinations of

trigonometric functions, as defined in the referenced work, which can be combined to create interesting new surfaces.

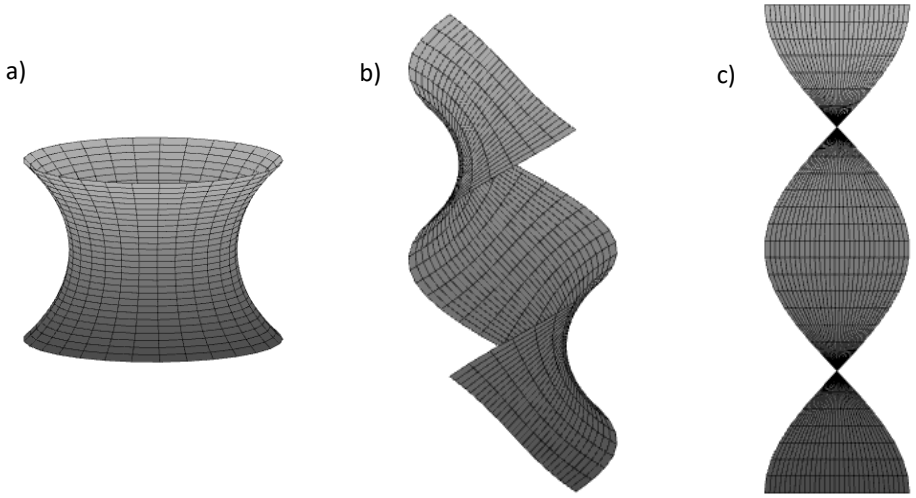

Figure 5.1. A simple example of a Bonnet family: a) catenoid, b) π/4 Bonnet rotation of a catenoid and c) helicoid (π/2 rotation of a catenoid).

5.2.1 P-G-D family

The most well-known and geometrically simple group of TPMS, is the P-G-D family, which is comprised of: Schwarz Primitive (SP) (Eq. (5.3a)), Schoen Gyroid (SG) (Eq. (5.3b)) and Schwarz Diamond (SD) (Eq. (5.3c)), each of which are represented by their level-set equations. The members of this family are all of genus three; the minimum genus for any embedded TPMS. Genus is a non-trivial concept which can roughly be interpreted as the amount of "holes" which a three-dimensional object has[224], meaning that a higher genus relates to a TPMS with a greater number of flow channels in the unit cell.

$$\cos(x) + \cos(y) + \cos(z) = 0 \tag{5.3a}$$

$$\sin(x)\cos(y) + \sin(y)\cos(z) + \sin(z)\cos(x) = 0 \tag{5.3b}$$

$$\cos(x)\cos(y)\cos(z) + \sin(x)\sin(y)\cos(z) + \sin(x)\cos(y)\sin(z) + \cos(x)\sin(y)\sin(z) = 0 \tag{5.3c}$$

These equations describe surfaces with infinitely small width; hence, to create volume for a physical structure each level-set equation was made into to an inequality. The P-G-D family are symmetrical about zero, i.e. < 0 is equivalent to > 0, meaning that both possibilities do not have to be explored for flow and dispersion properties (Fig. 5.2). These three surfaces are related to the SC, BCC and FCC cubic cells, respectively, making for an interesting comparison between these surfaces and the ordered particle packings. The permeability of these packings is similar to that of sphere packings at

the equivalent voidage (Table 5.1) and shows similarity with published values for previous flow studies of TPMS using Navier-Stokes based methods[216].

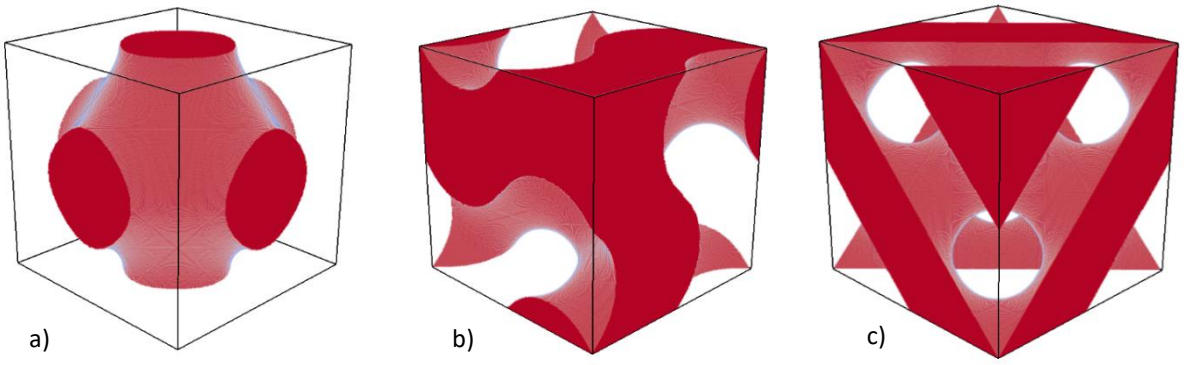

Figure 5.2. Illustration of the PGD family as solid structures: a) Schwarz Primitive, b) Schoen Gyroid and c) Schwarz Diamond.

Table 5.1. Flow properties of the P-G-D family of triply periodic minimal surfaces as calculated from the LBM model used in this study. Literature permeability data was calculated using a Navier-Stokes model[216].

TPMS	T	ε	Ψ	k	Literature k
SP	1.03	0.50	1.30	3.25E-03	3.47E-03
SG	1.25	0.50	0.98	2.21E-03	2.29E-03
SD	1.30	0.50	0.79	1.38E-03	1.43E-03

Like packed beds, the void fraction can be controlled, though it is not as much of a concern for the stability of the packed bed but, is relevant for increasing column capacity. This is performed by manipulating the parameter on the right-hand side of the inequality, *r*. For the P-G-D family, 50% porosity is achieved using $r = 0$, however, manipulating *r* also alters the mean curvature of each structure, meaning that it is no longer minimal[225]. For $r = 0$ each member of the P-G-D family differs in permeability, though they have identical porosity, meaning that this difference must somehow be accounted for. In Chapter 3, the concept of sphericity was introduced, which describes the volume to surface area ratio for a particle relative to a sphere (which itself has a value of one). The validity of using sphericity for analysis of TPMS is unknown, because discrete particles no longer exist in these systems. However, if the sphericity value is used to fit the coefficients of the Carman-Kozeny equation (using $c_{CK} = 180$), the modelled permeability is less than the Carman-Kozeny prediction (Fig. 5.3). It is also interesting to note the sphericity value of SP is greater than for a sphere, meaning continuous structures can minimize surface area more efficiently than discrete particles. To more accurately fit the data a coefficient of $c_{CK} = 230$ can be used.

When measuring solute dispersion, there was a clear hierarchy for the P-G-D family: SP > SG > SD (Fig. 5.4). Moreover, the SD surface produced a lower reduced plate height than any of the packed bed structures from Chapter 3, contributing to the evidence of monoliths being superior to packed beds

for chromatographic applications. These results reflect the trends shown by sphere packings, but each TPMS structure is an improvement over its spherical analogue. Although the minimum reduced plate height is not drastically improved (aside from SG vs BCC), the performance at high *Pe* flows exhibits the superior performance of monolithic structures.

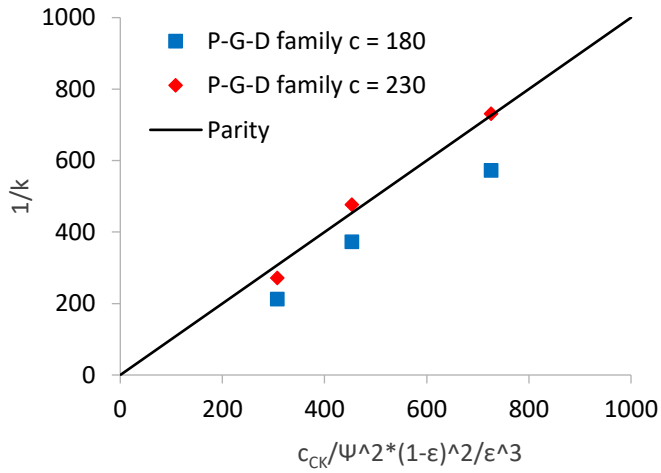

Figure 5.3. Comparison of the P-G-D permeability data with the prediction using the Carman Kozeny equation.

As observed for the various particle shapes in Chapter 3, spheres create a large velocity gradient in the flow channels, which directly influences the mass transfer resistance term of the van Deemter plot. For sphere packings, each particle must contact neighbouring particles to create structural integrity of the bed, reducing the magnitude of the local velocity field at these points. For the monolithic TPMS structures, the solid phase has more uniformly size flow channels, which is thought to minimize the mass transfer resistance.

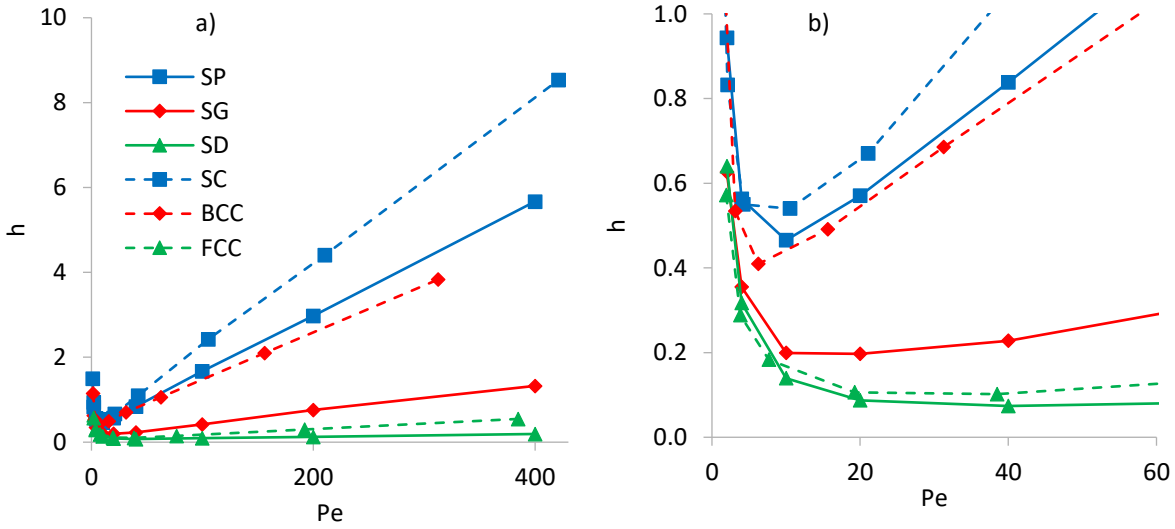

Figure 5.4. van Deemter curves for P-G-D TMPS family and basic sphere packings: a) over large Pe range and b) focusing on the optimal operating conditions for each curve.

Finally, an analysis that has been important throughout this work is the relationship between tortuosity and minimum reduced plate height in periodic packings. The P-G-D family appears to fit the trend when compared to results obtained from sphere packings in Chapter 3 (Fig. 5.5), further reinforcing the observation that column performance is dependent on the tortuosity of the medium.

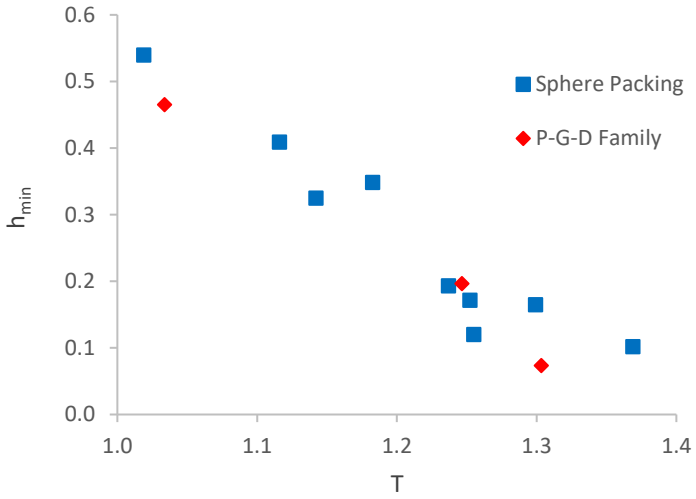

Figure 5.5. Tortuosity vs. minimum reduced plate height for the P-G-D family compared to sphere packings from Chapter 3.

5.2.2 Other TPMS Structures

From the work of Alan Schoen and Kenneth Brakke, there are many TPMS structures that have been discovered outside of the P-G-D family. An important property of the P-G-D family is that the morphology of the volumes occupied by the stationary and mobile phases is identical, meaning that the flow and dispersion properties of the medium are identical regardless of the direction of the inequality that is defined to create the volume of the morphology in this work. However, this is not a property held by all TPMS structures, meaning that the flow properties are dependent on how the inequality is defined. For example, Schoen's I-WP surface (Eq. (5.4)) produces a different structure when the equality is substituted by either the greater than or less than equality (Fig. 5.6a and 5.6b).

$$\cos(x)\cos(y) + \cos(y)\cos(z) + \cos(z)\cos(x) = -0.25 \qquad (5.4)$$

These definitions have notably different structures, which translates to different flow properties (Table 5.2) and dispersion behaviours (Fig. 5.6c) This shows that TPMS structures that are not symmetrical about r must be evaluated for both scenarios (or modes) to determine which definition exhibits the superior chromatographic properties.

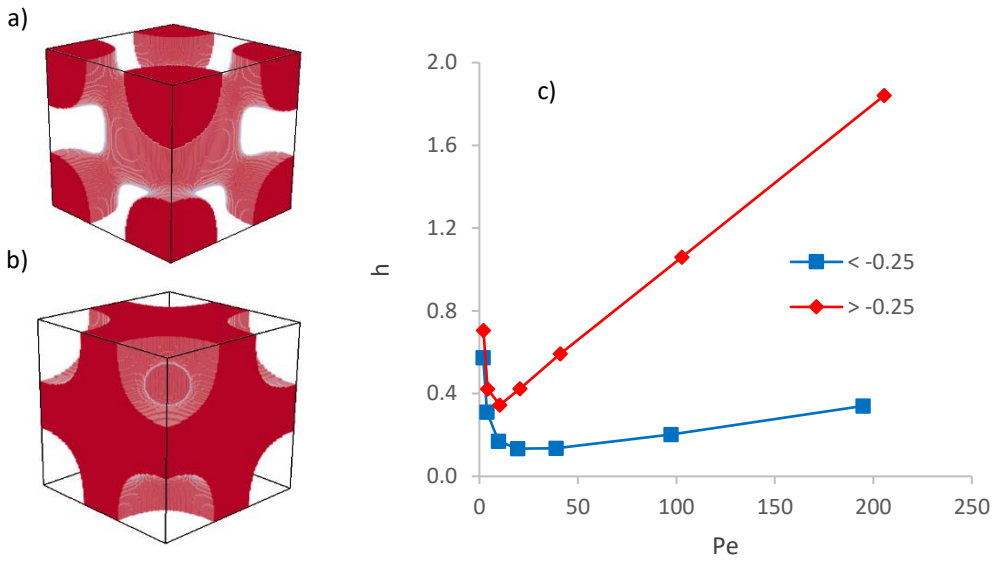

Figure 5.6. Solid structures for Schoen's I-WP surface using a) >-0.25 and b) <-0.25 and c) van Deemter plots for each structure.

Table 5.2. Difference in flow properties between the defined I-WP structures, illustrating the importance of the solid definition for non-symmetrical monolithic structures.

I-WP structure	T	ε	k	E
> -0.25	1.05	0.49	1.65E-03	11.1
< -0.25	1.29	0.51	8.32E-04	35.0

The work by Wohlgemuth et al.[36] defined many level-set approximations for TP structures (not necessarily minimal surfaces), but testing all structures would be an inefficient use of computational resources, if a less intensive screening process could be employed instead. Tortuosity was found as a reliable indicator for chromatographic efficiency in packed beds and for the P-G-D family. A qualitative observation made during these systematic studies showed that a porous medium exhibits low tortuosity if it contains straight pores though the medium, aligned in the axial direction. For example, SP and SC [001] spheres were strong exhibitors of straight channels, whereas SD and FCC [001] were highly tortuous morphologies. This can be shown by observing each unit cell morphology from the axial direction (Fig. 5.7). Hence, CFD simulations were only performed on TPMS structures which did not exhibit straight channels, because this characteristic implied higher tortuosity and lower band broadening. The selected structures were: F-RD, P2-DG, Double Gyroid (DG), L and the D' surface (Fig. 5.8) as defined in the referenced work[36].

Using these surfaces with higher tortuosity resulted in lower medium permeability, as observed for previous media (Table 5.3). For dispersion, three structures achieved a h_{min} value of less than *0.1* (Fig. 5.9), which was equivalent to the best performing packed beds (assuming an overlap of one),

showing that TPMS have great potential in chromatographic applications. The lowest separation impedance value was *2.3*, for DG > 0, however, this did not outperform SC [111] octahedral particles. As previously discussed, octahedral particles were packed with high void space and would require a large overlap factor to retain their structure in practical columns. Hence, the highest performing packed bed structures are not physically feasible, while the monolithic structures are.

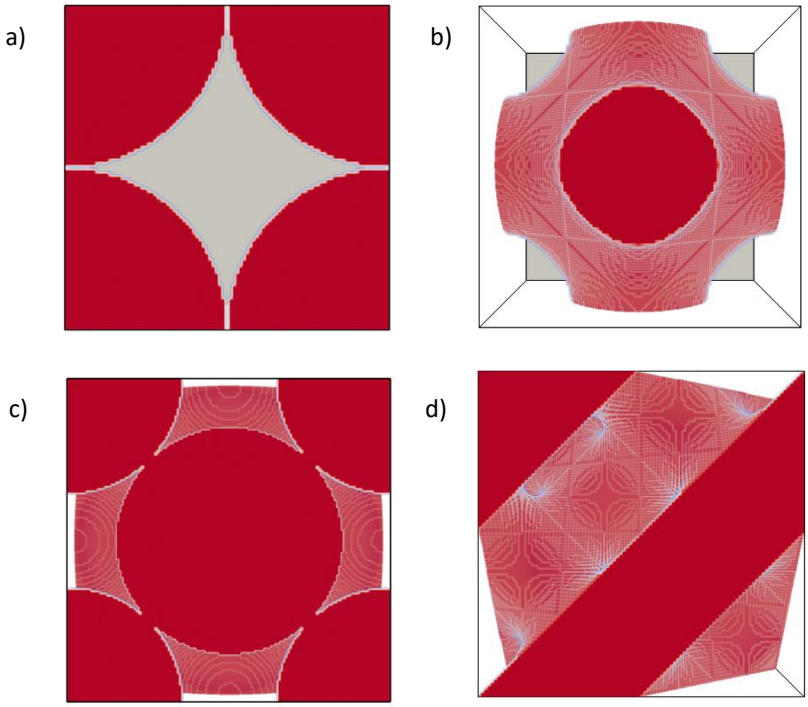

Figure 5.7. Axial view of a) SC (Spheres), b) SP, c) FCC (spheres) and d) SD. The grey planes in the transverse dimensions illustrate the opposite face of the unit cell, if this is visible (a and b), the tortuosity of the medium will be low.

Table 5.3. Flow properties of the five studied surfaces for each mode.

Surface	Mode	T	ε	k	E
F-RD	> 0	1.27	0.48	4.97E-04	6.4
	< 0	1.18	0.52	7.32E-04	14.8
P2-GD	> 0	1.14	0.53	8.81E-04	18.8
	< 0	1.21	0.47	6.40E-04	18.5
DG	> 0	1.15	0.56	1.20E-03	2.3
	< 0	1.33	0.44	5.18E-04	24.4
L	> -0.15	1.35	0.39	1.82E-04	6.6
	< - 0.15	1.22	0.61	1.02E-03	14.9
D'	> 0.2	1.32	0.54	6.41E-04	45.7
	< 0.2	1.14	0.46	3.87E-04	22.5

A remarkable feature of the DG (> 0) structure was the optimum operating *Pe*, which was slightly less than *100*; higher than any other medium in this work. This would provide huge benefits to practical chromatography because the flow rate directly influences the speed of the chromatographic process. Furthermore, the structure has two physically independent matrices which could be printed using different materials and uniquely functionalized to perform different sequestrations in the same column. This opens a new paradigm for chromatographic methods, such as affinity chromatography, in which two distinct species could be adsorbed and eluted separately using the same medium. Using current chromatography technology, this process would require two separate chromatographic media and two chromatographic processes to achieve the same result. Conversely, the DG (< 0) structure contains two separate, non-interacting flow channels. This is also a useful feature, though perhaps not for chromatographic purposes. These discrete flow channels could be applied to unique reactor design or heat exchange operation because of the high amount of contacting surface area between the two intertwined channels allowing for exchange of mass or heat.

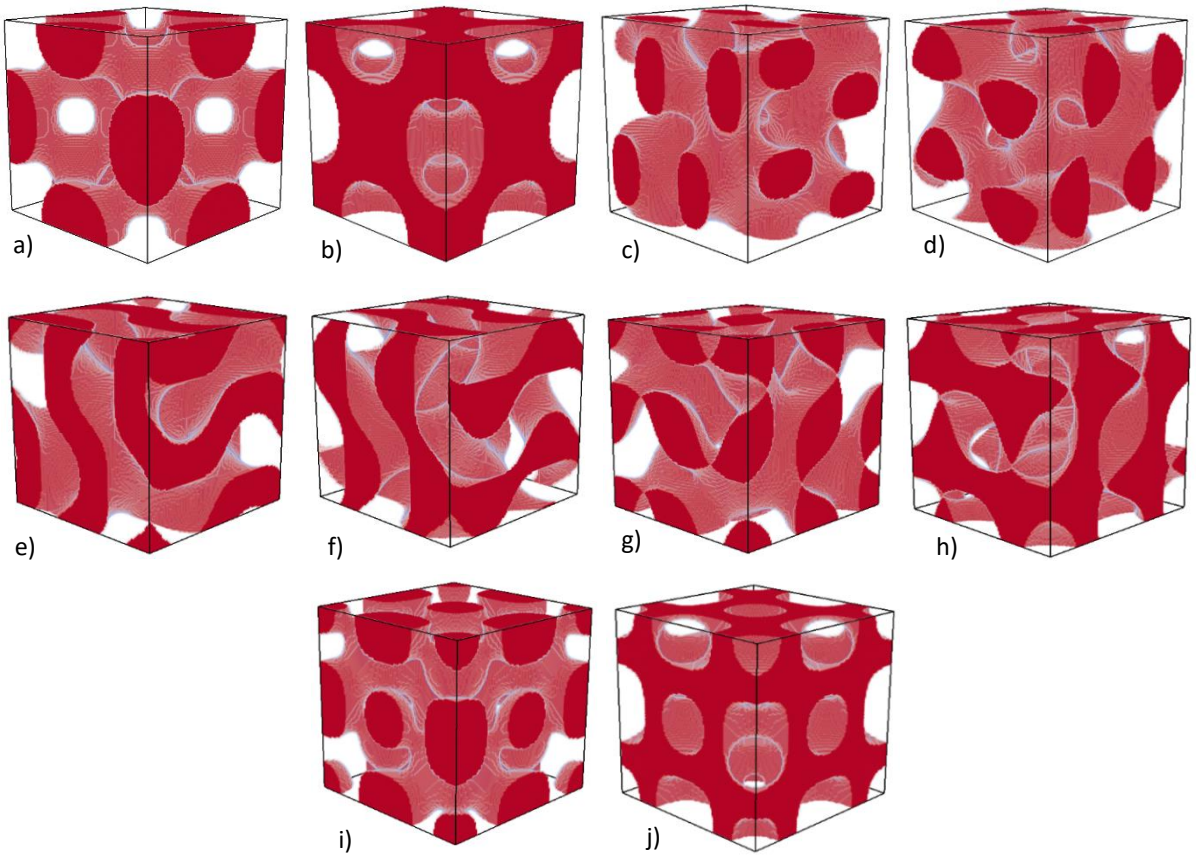

Figure 5.8. Illustration of the studied surfaces as solid morphologies: F-RD a) < 0 and b) >0, P2-GD c) < 0 and d) > 0, DG e) < 0 and f) > 0, L g) < -0.15 and h) > -0.15 and D' i) < 0.2 and j) > 0.2.

Finally, some of these surfaces weaken the standing correlation between the system tortuosity and minimum reduced plate height, although the improvement in performance with increasing

tortuosity still appears to hold overall (Fig. 5.10). The main outliers of this trend were found to be opposite modes of the same surface, suggesting that there are additional factors that contributes to this trend in some monolithic packings. This factor was not further investigated, but it was thought that it could be related to the genus of the morphology (a non-trivial calculation).

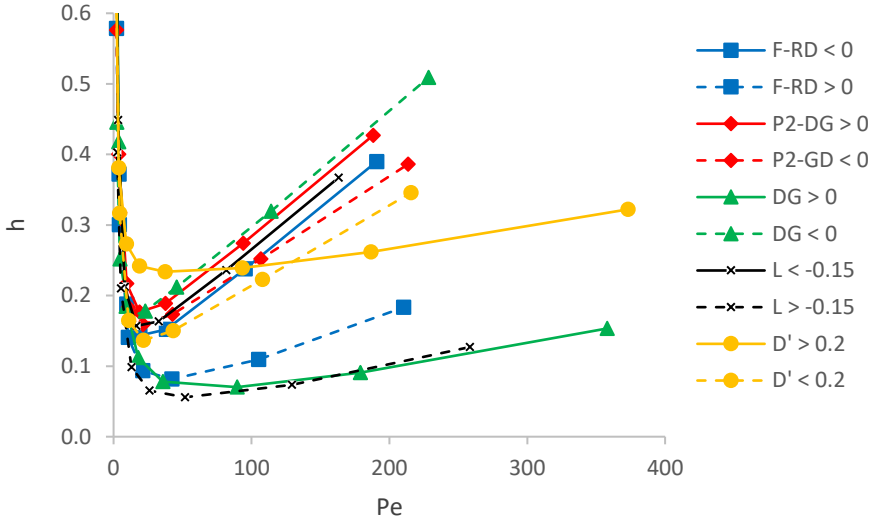

Figure 5.9. van Deemter curves for ordered monolithic packings based upon each mode of level-set equations for TPMS.

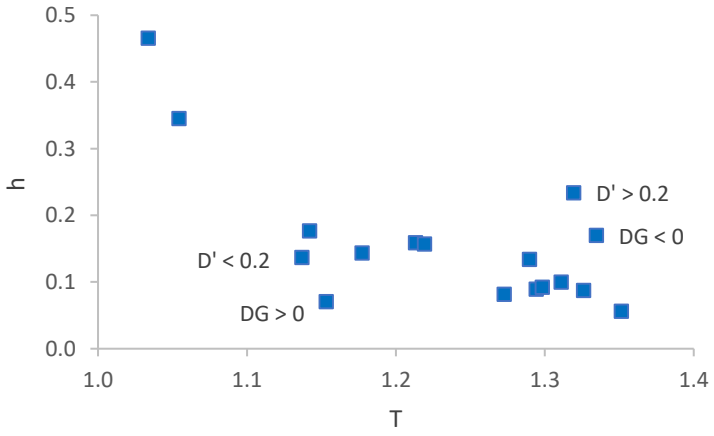

Figure 5.10. van Deemter curves for ordered monolithic packings. The labelled packings are the primary outliers of the linear trend.

5.2.3 Extensions of Level-Set Equations

Several of the level-set equations in the previous section are created by combining distinct groups of trigonometric expressions from other surfaces, e.g. P2-DG combines the SP and DG level set equations. By extending this idea, new structures can be created through various combinations of these groups, although it is important to note that these surfaces will not likely be minimal. This concept was explored by adding the terms from the high performing structures SD and DG, yielding a unique structure, which is referred to as “SD + DG” (Fig. 5.11a and 5.11b). Alternatively, the terms can be

subtracted to create “SD – DG” (Fig. 5.11c and 5.11d). Though these two structures have different morphologies, they have similar dispersion and permeability values (Table 5.4 and Fig. 5.12).

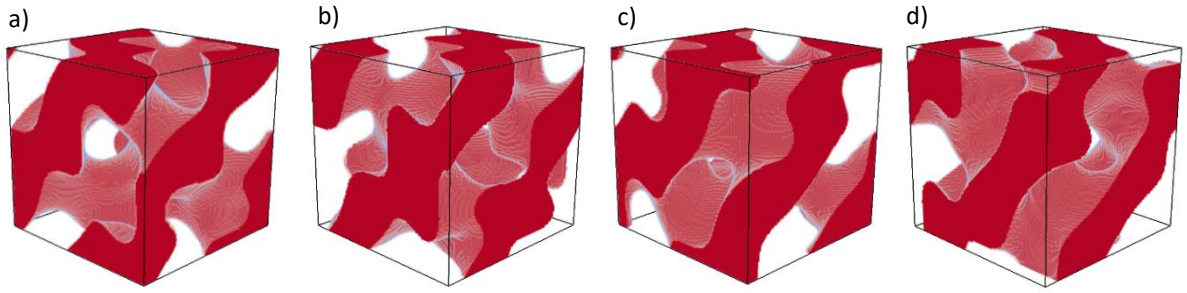

Figure 5.11. Illustration of the new produced surfaces: SD + DG, a) < 0 and b) > 0 and SD – DG, c) < 0 and

Table 5.4. Flow characteristics of the SD+GD and SD-GD surfaces

Surface	Mode	T	ε	k	E
SD+DG	< 0	1.31	0.49	9.86E-04	4.9
	> 0	1.29	0.51	1.13E-03	3.6
SD-DG	< 0	1.30	0.52	1.17E-03	3.8
	> 0	1.33	0.48	9.35E-04	3.9

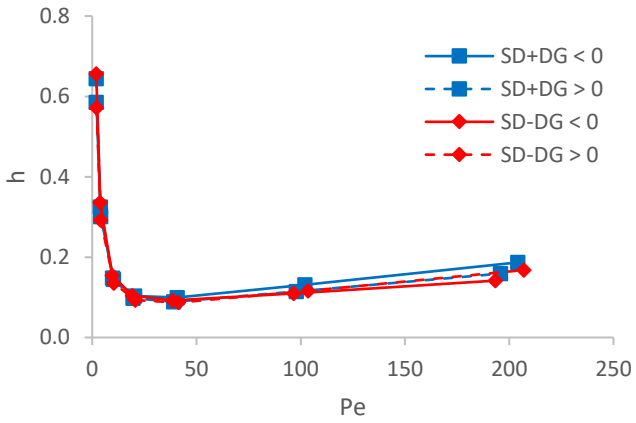

Figure 5.12. van Deemter curves of the SD + DG and SD-DG morphologies for each mode.

Although the performance of these structures is good, they are not quite as good as the best performing parent structures. However, it is noted that the performance of DG (< 0) is worse than both SD + DG (< 0) and SD – DG (< 0). Moreover, each of the four morphologies are very similar in their behaviour, which suggests that SD is the dominant contributor to these new structures because each of its modes are identical. This opens a new paradigm for creating surfaces which may have the potential to improve upon the most efficient surfaces in this chapter.

5.3 Manipulation of Schwarz Primitive

Continuing the idea of manipulating the level set equations, three further manipulation methods were explored. Because Schwarz Primitive is approximated by the simplest level-set equation and attributed with the worst band broadening of all the TPMS structures it is used a case study for observing the potential in optimization of monolithic structures which are defined by a level-set equation.

5.3.1 Geometric Coefficients

The first manipulation technique was adding parameters to the level-set equation. Recalling the level-set equation of the SP surface (Eq. (5.1a)), coefficients can be added to manipulate the physical structure (Eq. (5.5)).

$$a * \cos(b * x) + c * \cos(d * y) + e * \cos(f * z) < r \qquad (5.5)$$

where *a*, *b*, *c*, *d*, *e*, *f* are constants and *r* manipulates the porosity of the structure. In this work, three of these coefficients were investigated: *a*, *e* and *r* (Fig. 5.13). The bounding values for these variables were selected qualitatively by observing the connectivity between the solid phase in the manipulated medium.

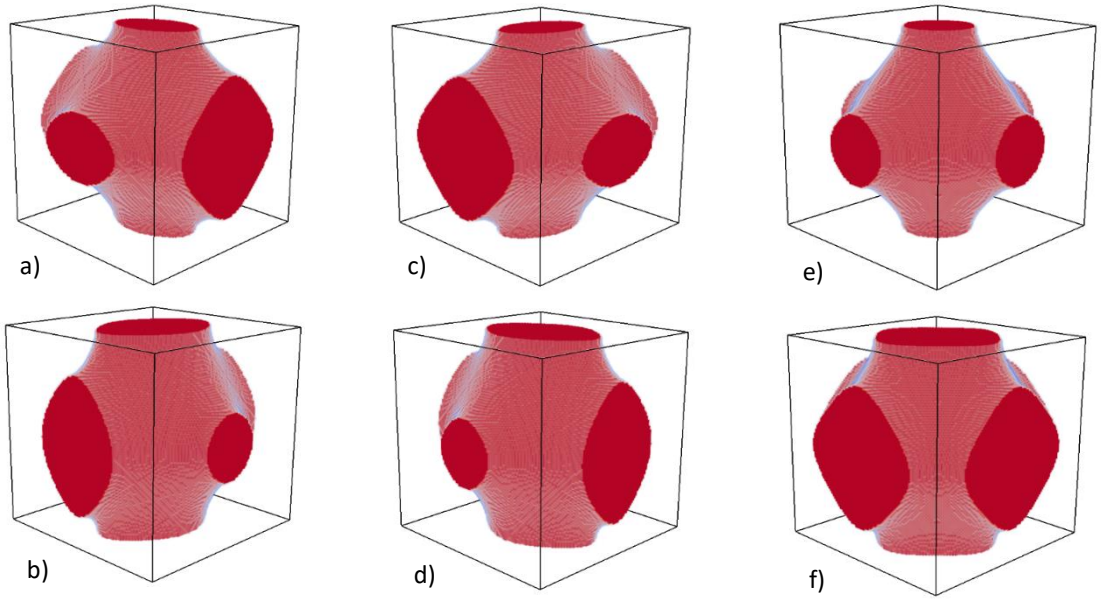

Figure 5.13. Single variable manipulations of the SP level-set equation: a) a = 0.5, b) a = 1.5, c) e = 0.5, d) e = 1.5 e) r = -0.5 and f) r = 0.5.

When approaching these limits, the connectivity between the stationary phase volume decreases, which may compromise the structural properties of medium. However, these bounding values were not able to be optimized because this would depend on the material comprising the stationary phase and the operating conditions. Variables *b*, *d*, *f* affected the periodicity of the medium in each of the respective dimensions and were not tested here, but based on the work of elongated

particle packings[46], it was expected that these variables would also alter the performance of the medium. Because the transverse dimensions in a periodic packing are identical, *c* was ignored and was assumed to have the same effect as variable *a*. Although manipulating both variables concurrently may produce an alternate result, the number of data sets that would need to be produced to compare extra variables would increase exponentially. As individual manipulations, neither the *a* nor the *e* terms affected the porosity of the medium, but instead redistributed the solid material along the axis corresponding to the coefficient (Eq. (5.5)). Conversely, the *r* term exclusively manipulated the porosity of the medium and hence, had the most pronounced effect on the system permeability (Table 5.5). Although the *a* and *e* terms did not alter the system porosity, they still altered the permeability of the medium, which was decreased as solid material was redistributed toward the transverse features of the stationary phase.

Table 5.5. Flow properties of single manipulations on the SP level set equation.

Variable	Value	T	ε	k	E
a	0.5	1.05	0.50	1.77E-03	83.5
	1.25	1.03	0.50	3.86E-03	24.1
	1.5	1.02	0.50	4.53E-03	17.4
e	0.5	1.01	0.50	6.36E-03	9.8
	0.75	1.02	0.50	4.67E-03	17.8
	1.5	1.06	0.50	1.04E-03	186
r	0.5	1.04	0.36	9.16E-04	107.2
	-0.25	1.03	0.57	5.05E-03	22.5
	-0.5	1.03	0.64	7.62E-03	15.4

The reduced plate height was also affected by these manipulations. Deviation from the standard values ($a = 1$, $e = 1$, $r = 0$) yielding a monotonic relationship between the variable and the minimum reduced plate height. Arguably the most influential variable in this analysis was *e* (Fig. 5.14b), which was the coefficient of the term containing the axial co-ordinate (*Z*) (Fig. 5.14). Note, more data is shown for the manipulations which reduced the dispersion properties of the medium.

When performing manipulations concurrently, the limits of the variables become further constrained because of how the structural integrity of the medium weakens in specific areas. Hence, the most successful variable values could not be directly combined. There were four unique combinations of the four variables: "$a + e$", "$a + r$", "$e + r$" and "$a + e + r$", which were each shown to provide benefits to both permeability and band broadening when combined appropriately (Table 5.6, Fig. 5.15).

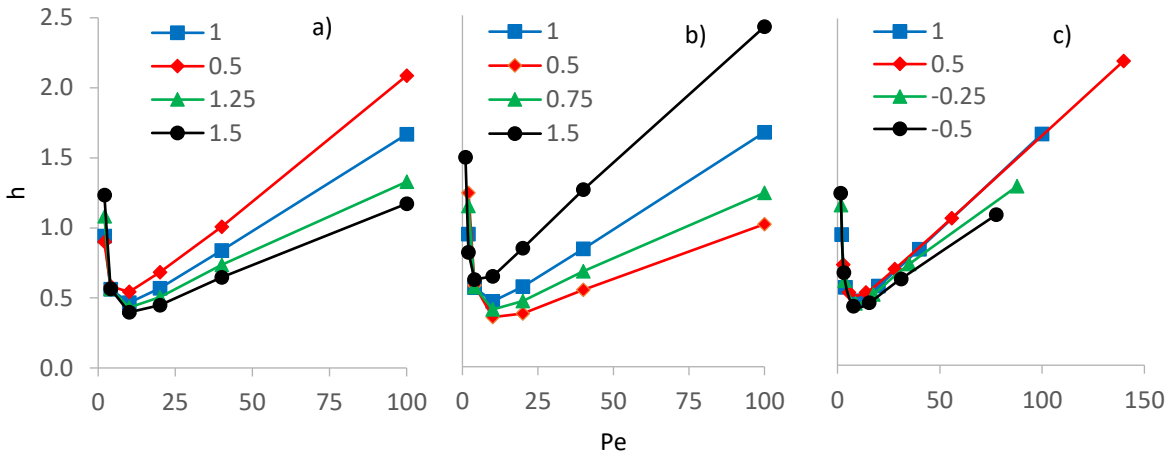

Figure 5.14. van Deemter curves of single manipulations on the SP level set equations for: a) a, b) e and c) r.

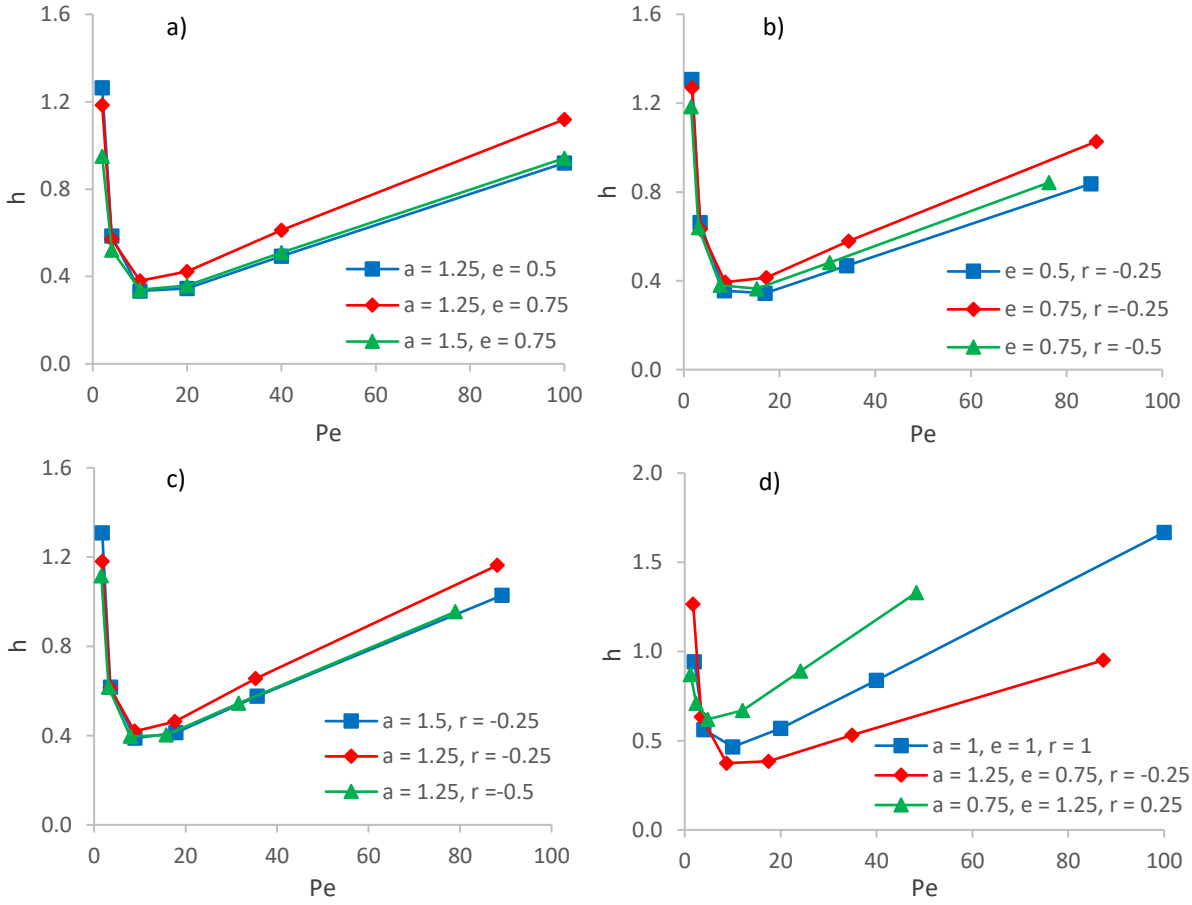

Figure 5.15. van Deemter curves of multiple concurrent manipulations on the SP level set equations for: a) a + e, b) e + r, c) a + r and d) a+ e + r.

For the combinations of variables, the structure with the highest permeability was *e = 0.5*, *r = -0.25* because of the small *e* and negative *r* term (Table 5.6), agreeing with the results from the single variable manipulations. For dispersion behaviour, the most efficient medium was *a = 1.25*, *e = 0.5* in which the *e* term was the most deviated term. The difference between this medium and *a = 1.5*, *e =*

0.75 was within the range of accuracy of the model and so it cannot be stated conclusively that the *e* term is the most influential variable here. The best "*a* + *e*" combination produced lower dispersion than the best "a + e + r" combination because the boundary limits on each variable were constricted when all three variables were used. However, the performance of *a = 1.25, e = 0.75* was improved by reducing the *r* term, showing that each term does contribute to a reduction in band broadening, but some variables have a more pronounced effect. In a practical scenario, the performance increase of the medium would therefore be heavily reliant on the structural properties of the solid phase and perhaps only a small number of variables would need to be optimized for more complex structures.

Table 5.6. Flow properties of resultant structures from multiple manipulations on the SP level set equation.

a	e	r	T	ε	k	E
1.25	0.5	1	1.01	0.50	6.20E-03	9.0
1.25	0.75	1	1.02	0.50	4.70E-03	15.4
1.5	0.75	1	1.02	0.50	5.91E-03	9.7
1	0.5	-0.25	1.01	0.59	8.87E-03	7.8
1	0.75	-0.25	1.02	0.58	6.48E-03	13.9
1	0.75	-0.5	1.02	0.65	1.04E-02	8.4
1.5	1	-0.25	1.02	0.56	5.76E-03	14.6
1.25	1	-0.25	1.03	0.57	5.08E-03	19.6
1.25	1	-0.5	1.02	0.63	8.38E-03	11.8
1.25	0.75	-0.25	1.02	0.57	6.98E-03	11.5
0.75	1.25	0.25	1.06	0.41	4.38E-04	369

Conversely, combining each of the negative coefficient values increased the reduced plate height and shifted the van Deemter curve in the opposite direction (Fig. 5.15d). This indicates that if a singular variable increases performance of a medium, then if it is combined with other beneficial variables, there will be a net gain in performance. These findings are supportive of a recent study on elongated sphere packings[46], which showed that packings that elongated particles in the axial direction showed reduced band broadening. This work suggested that these features reduced band broadening by homogenizing the velocity field and hence decreasing the mass transfer resistance of the medium. For these manipulated SP structures, the relationship of tortuosity to minimum reduced plate height is the opposite of the negatively proportional relationship which has been documented throughout this work (Fig. 5.16). This is thought to be a by-product of the SP structure specifically, because tortuosity was correlated with restriction of flow in the axial direction and hence, increasing the mass transfer resistance coefficient because of the large velocity gradients (Fig. 5.17). This was supported by the van Deemter curves, which showed an increase in the gradient at high *Pe* for the less efficient packings (Fig. 5.15d).

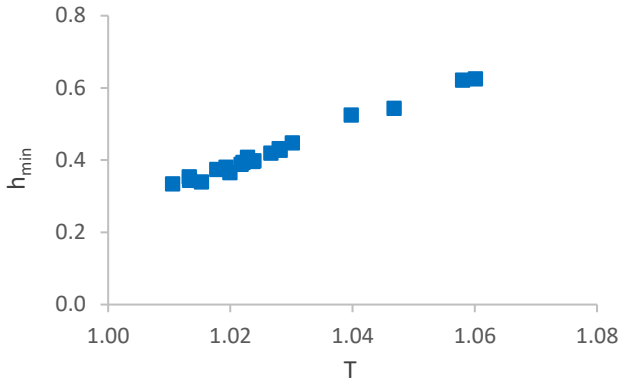

Figure 5.16. Linear correlation between tortuosity and minimum reduced plate height for numerically manipulated level-set equations of the SP surface.

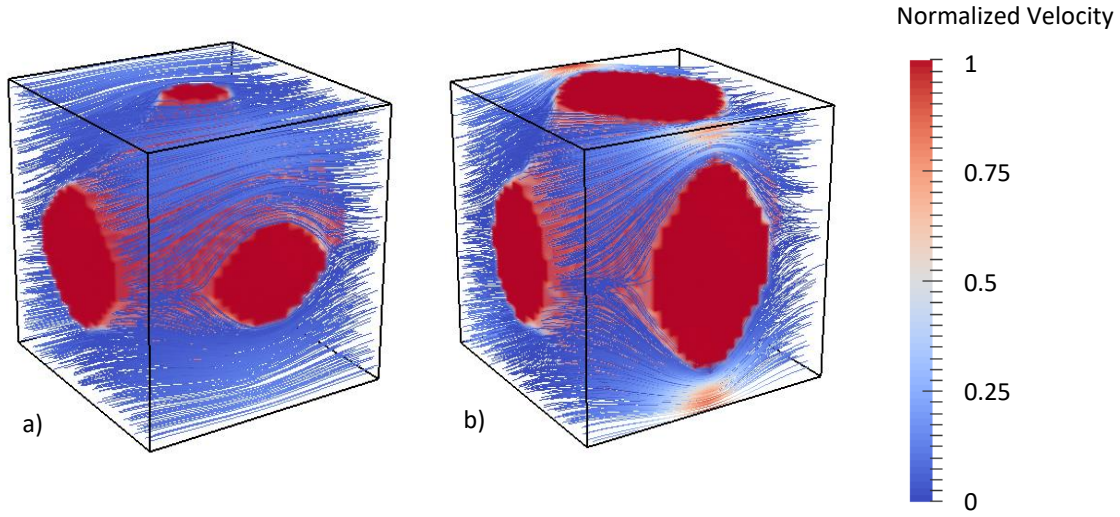

Figure 5.17. Comparison between streamlines in manipulated SP level-set equations for: a) a = 1.25, e = 0.75 and r = -0.25 and b) a = 0.75, e = 1.25 and r = 0.25.

5.3.2 Orientation

Rotations that were applied to packed beds (Chapter 3) could also be applied to monolithic structures. This was achieved by applying rotational matrices to the Cartesian inequality for each occurrence of a dimensional term (*x*, *y* and *z*), for example, the [011] orientation takes the form of Eq. (5.6). Again, three modes were investigated: [001], [011] and [111] (Fig. 5.18).

$$\cos(z * \sin(\pi/4) + x * \cos(\pi/4)) + \cos(y) +$$

$$\cos(z * \cos(\pi/4) - x * \cos(\pi/4) > 0 \qquad (5.6)$$

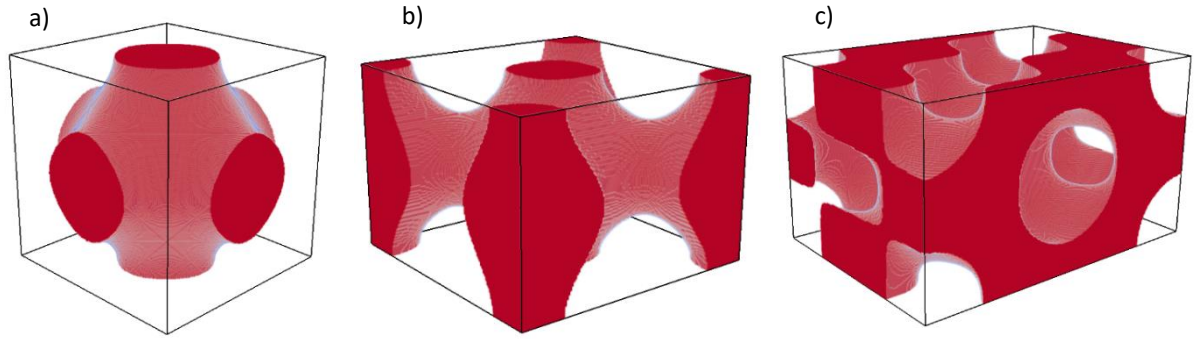

Figure 5.18. The three orientations of the SP structure: a) SP [001], b) SP [011] and c) SP [111].

The porosity and permeability of the medium is unchanged by rotation, which is the same behaviour observed in packed beds (Table 5.7). Like packed beds, particularly SC spheres, these rotations produced major reductions in band broadening which was again attributed to reducing the prevalence of straight axial flow channels with increasing degrees of rotation. Altering the orientation produced more significant performance gains than manipulating the coefficients within the level-set equation (Fig. 5.19). Furthermore, the separation impedance of the SP [111] medium was found to be equivalent to the most successful packed beds, with a value less than one. Moreover, the porosity of SP [111] is lower than these specific packed beds meaning this medium also has a higher capacity.

Table 5.7. Flow properties of the three orientations of the SP structure: a) SP [001], b) SP [011] and c) SP [111].

Orientation	T	ε	k	E
SP [001]	1.02	0.5	3.25E-03	33.3
SP [011]	1.18	0.5	3.20E-03	7.7
SP [111]	1.28	0.5	3.19E-03	0.9

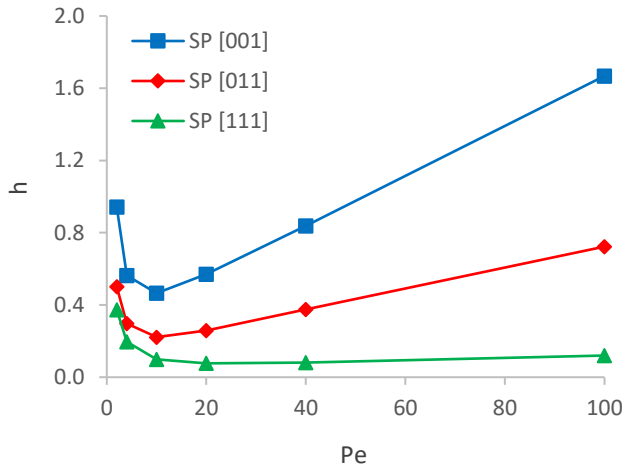

Figure 5.19. van Deemter curves for the three orientations of the SP structure: a) SP [001], b) SP [011] and c) SP [111].

Clearly, this manipulation creates a significant performance improvement over the standard SP [001] structure, a comparable result to SC sphere packing. Therefore, it stands to reason that each TPMS structure would react differently to a change in orientation, much like the various packed bed structures demonstrated in Chapter 3. For this reason, the high performing TPMS structures (such as SD and SG), are not expected to experience large performance benefits, much like FCC spheres, though this is not confirmed here.

5.3.3 Double Schwarz Primitive

Finally, elaborating on the concept of a double gyroid, as presented earlier, the novel idea of a "double primitive" structure (DP) was developed in this work. This structure comprises two discrete SP structures, mitigating the straight flow channels that are characteristic to the SP [001] packing. This was done by using two equations to define the surface (Eq. (5.7)) It is also important to note that each SP packing itself can be manipulated using other previously stated methods, though this was not investigated here. The *r* values of each section were used to control the size and shape of the flow channels through the medium.

$$\cos(x) + \cos(y) + \cos(z) < r_1 \qquad 5.7a)$$

$$\cos(x) + \cos(y) + \cos(z) > r_2 \qquad 5.7b)$$

where r_1 and r_2 relate to the two discrete components of the DP structure. The lower and upper bounds in this scenario were *-0.8* and *0.8*, respectively. In conjunction with this, the difference between the two limits was required to be at least *0.8*, otherwise the width of the void spaces became too constrictive for accurate flow simulation (Fig. 5.20). Because SP is symmetrical about $r = 0$, some DP structures are equivalent, i.e. $r_1 = a$, $r_2 = b$ is equivalent to $r_1 = -b$, $r_2 = -a$.

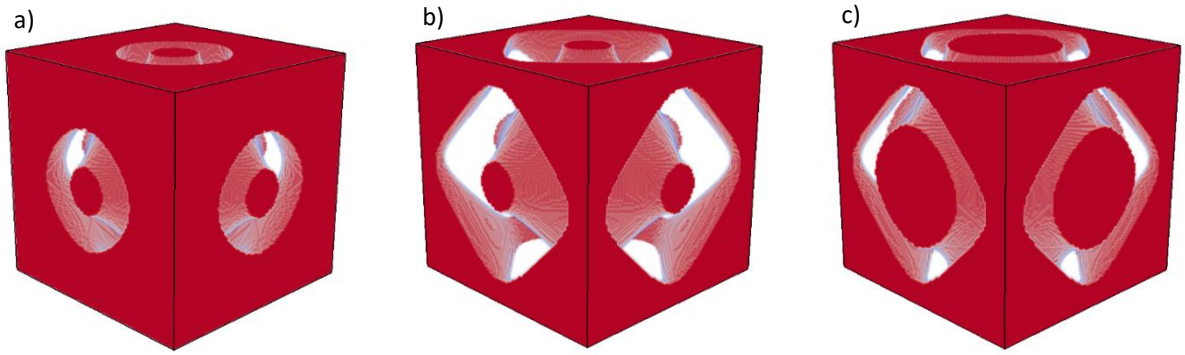

Figure 5.20. Double SP structures for varying r values: a) $r_1 = -0.8$, $r_2 = 0$, b) $r_1 = -0.8$, $r_2 = 0.8$ and a) $r_1 = 0$, $r_2 = 0.8$.

Permeability of these media was low (Table 5.8), which was caused by the low void space and high tortuosity of the morphology. However, the level of band broadening was superior to any structure

previously investigated in this study, with the most efficient medium attaining an h_{min} value of *0.035*. Although the permeability values were low, the separation impedance of these structures showed low variation and ranged between *2 – 4*, which shows good performance.

Table 5.8. Flow characteristics of the double Schwarz Primitive medium.

r_1	r_2	T	ε	k	E
-0.8	0	1.23	0.22	9.46E-05	3.6
-0.8	0.2	1.22	0.28	1.98E-04	2.9
-0.8	0.4	1.21	0.34	3.62E-04	2.4
-0.8	0.6	1.20	0.39	5.80E-04	2.3
-0.8	0.8	1.18	0.45	9.20E-04	2.1
-0.6	0.2	1.22	0.22	9.83E-05	3.0
-0.6	0.4	1.21	0.28	2.06E-04	2.6
-0.6	0.6	1.20	0.34	3.57E-04	2.4
-0.4	0.4	1.22	0.23	1.06E-04	2.7

The separation impedance was largest for the higher porosity media, meaning that the decrease in permeability had greater effect on separation impedance than the decrease in band broadening for the DP morphology. Each DP media with equivalent porosity showed identical van Deemter plots within the error of the model (Fig. 5.21). Decreasing the porosity increases the mass transfer resistance because of increased width of the flow channels meaning that radial diffusion takes longer to equilibrate the solute pulse across the flow channels.

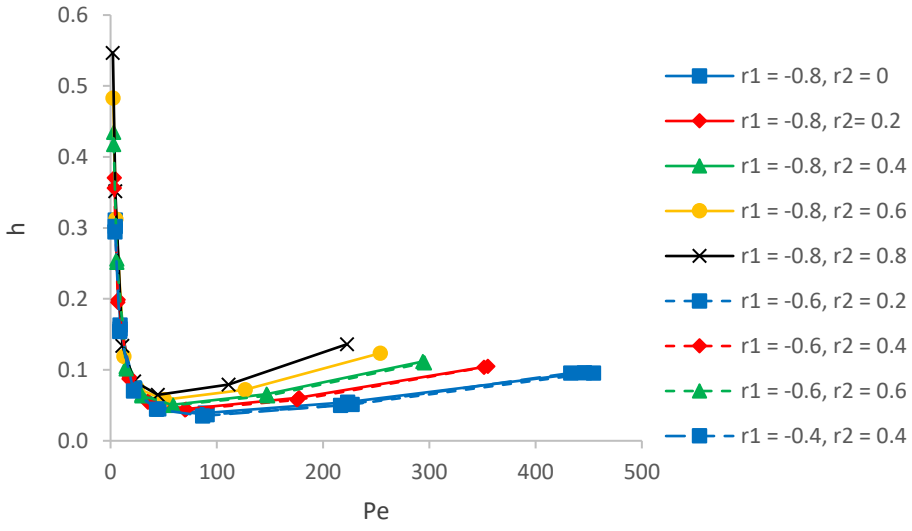

Figure 5.21. van Deemter curves for the double Schwarz Primitive medium showing how the porosity of the medium affects band broadening. Curve with the same colour and marker indicate equal porosity packings.

5.4 Channel Based Media

Using parallel straight channels, or capillaries, as a functional medium is also an example of practically used monolithic structures[209, 226]. Tortuosity has been used as an indicator of chromatographic performance throughout this work and hence, it was theorized that increasing the tortuosity of singular straight channels may improve column performance by promoting transverse mixing across the channels by using the angular momentum of the fluid.

As a starting point, flow properties (Table 5.9) and dispersion characteristics (Fig. 5.22) of cylindrical, parallel straight flow channels was examined by varying the capillary diameter with respect to the unit cell diameter, building on the validation work from Section 2.8.2, which looked at Taylor-Aris dispersion. It is known that dispersion in these systems has an axial length dependence, hence, all results are presented for the long-time limit. These systems were defined by the ratio of the capillary diameter to the distance between the capillary centres, *d'*.

Figure 5.9. Flow properties of parallel, straight cylindrical channels with varying diameter.

d'	T	ε	k	E
0.33	1.00	0.084	2.68E-04	4.1
0.66	1.00	0.33	4.35E-03	3.4
1	1.00	0.74	3.63E-02	1.9

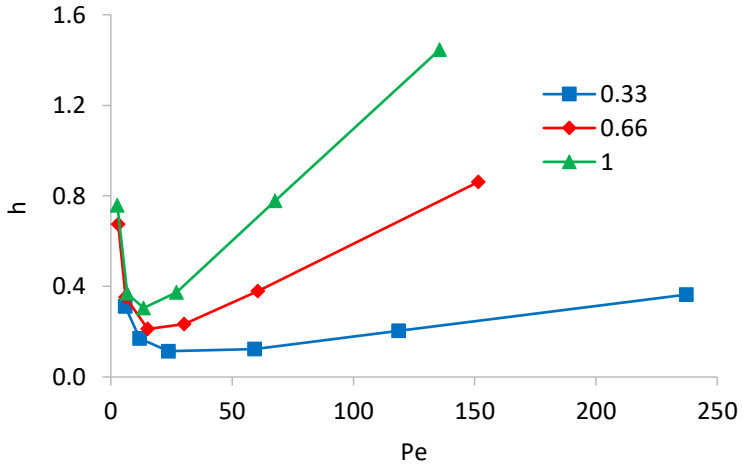

Figure 5.22. van Deemter curves for parallel, straight cylindrical channels with varying diameter. The legend describes the value of d'.

A source of ambiguity arises when non-dimensionalizing the HETP values in these systems. For packed beds, the characteristic length of the particles was used, while for periodic structures, this was replaced by periodic length in the axial dimension. However, straight channels are infinitely periodic in the axial dimension meaning that it is difficult to prescribe a parameter which is equivalent to the previous definitions for packed beds and monoliths. There are two options in this case, the first

was to use the same value as has been used for monolithic structures ($d_p = 2e^{-4}$ m) while the other option was to use the channel diameter. This second definition raised a pertinent question about the parameters used for non-dimensionalization in this work and how they affect the results presented in this work. For example, if a straight channel was slowly changed into a packed bed system using multiple intermediate morphologies, how would this parameter be defined at each step? To mitigate this concern, the periodic length equivalent was chosen to be a fairer parameter to use, because it was constant for each system.

Narrower channels exhibited lower permeability because of the large reduction in void space of the straight channels while the volumetric flow rate remained constant. Narrower channels also exhibited less dispersion, which was expected, because in parallel narrow channels the time for radial equilibration is much smaller, hence the parabolic velocity profile had less effect and the mass transfer resistance was decreased.

An important characteristic of developed laminar pipe flow, is that the velocity profile is constant in the axial direction and the transverse velocity components are both equal to zero, resulting in a system tortuosity of one. To introduce tortuosity to a straight channel, the spring geometry was used. A spring is to a helix as a cylinder is to a straight line, i.e. it gives the helical path a volume, which is necessary for fluid flow. Geometrically, a helix is created by sweeping a circle around the helix geometry (Fig. 5.23a), which can be approximated by a Cartesian equation (Eq. (5.8)).

$$(R - \sqrt{x^2 - y^2})^2 + (z + \frac{P.\tan^{-1}\left(\frac{x}{y}\right)}{\pi})^2 < r^2 \qquad (5.8)$$

where R is the distance from the centre of the tube to the centre of the spring, P defines the periodic length of the spring and r is the radius of the circle which is swept around the helix. Hence, there are three main variables which are of interest when investigating performance of these systems: R, r and P which are here normalised using the transverse length of the unit cell. Furthermore, multiple springs were used in a single morphology to create double helices (both connected (Fig. 5.23b) and discrete (Fig. 5.23c)) and a quadruple helix structure (Fig. 5.23d). It is also important to note that for this Cartesian expression, the shape of the spring is deformed as P increases.

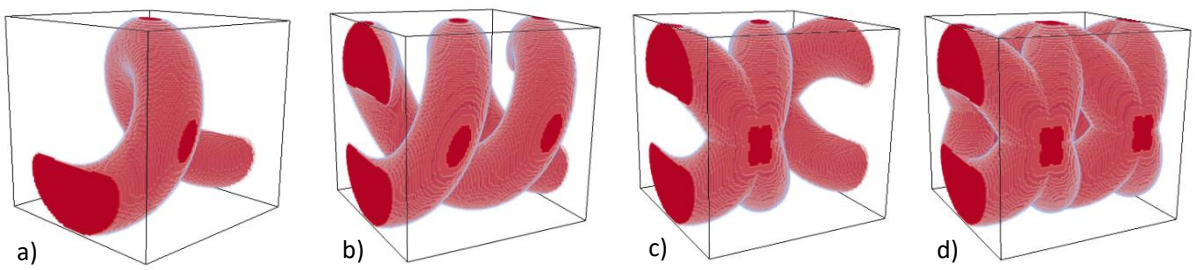

Figure 5.23. Morphology of the spring geometry using: a) a single spring, b) two discrete springs, c) two connected springs and d) four springs.

The permeability of these structures is low, which is not surprising considering that the void space is low, and the tortuosity is much greater than any previously tested morphologies (Table 5.10). These spring geometries exhibited improved performance over straight channels, but generally higher separation impedance values. For single channels, performance was proportional to *P* and *R* and inversely proportional to *r*. In this context, it is important to note that *P* directly affects the axial unit cell length and if this is chosen to be the non-dimensionalizing factor, this would alter the hierarchy of these structures. Because of the ambiguity involved with the effect of *P* maximizing performance in these channels, can be done by maximizing *R* and minimizing *r* (Fig. 5.24).

Table 5.10. Flow characteristics of each tested spring geometry.

	R	P	r	T	ε	k
Single	0.33	0.67	0.167	1.85	0.13	9.01E-05
	0.33	0.5	0.167	2.29	0.17	8.79E-05
	0.33	0.33	0.167	3.22	0.26	7.17E-05
	0.167	0.33	0.167	1.50	0.08	7.26E-05
	0.167	0.33	0.33	1.71	0.37	8.99E-04
Double - Discrete	0.33	0.5	0.167	2.29	0.34	1.76E-04
Double - Connected	0.33	0.5	0.167	1.71	0.29	2.60E-04
Quad	0.33	0.67	0.167	1.36	0.40	5.43E-04

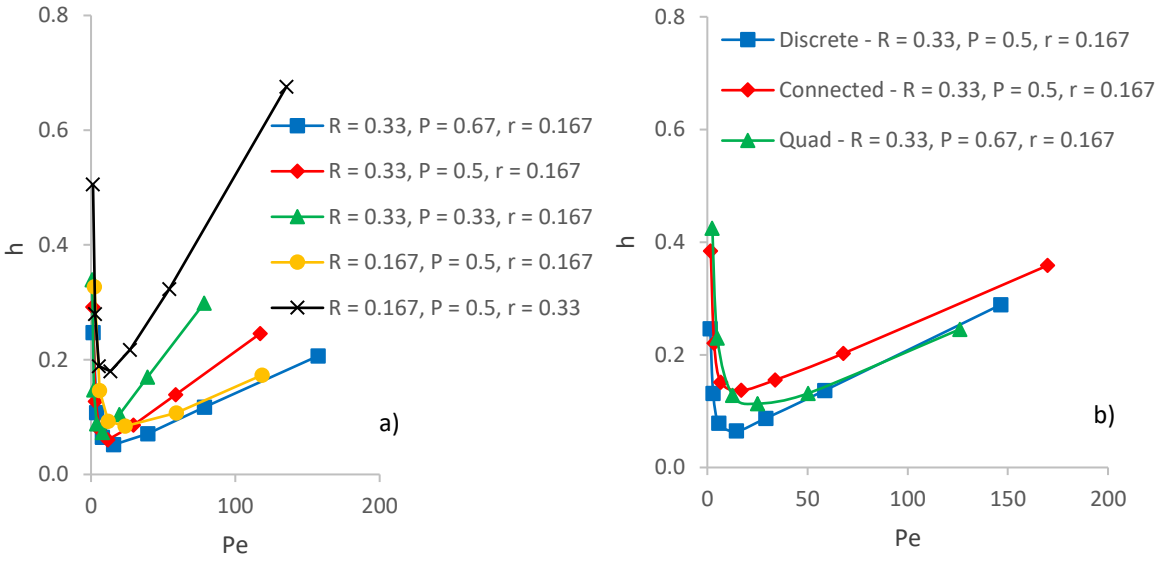

Figure 5.24. van Deemter curves for: a) single spring channels and b) multiple spring channels.

The discrete double helix showed comparable performance to the single channel structure while increasing the permeability by a factor of two, while the connected structure degraded dispersion performance because of the interaction between the two fluid channels at the connection points. For the quadruple channel structure, *P* was increased to prevent the channels from merging and creating straight axial flow channels through the medium, which has been found to degrade performance in this study.

The quadruple channel structure had lower band-broadening than the connected double spiral and showed lower mass transfer resistance than the discrete double channel structure.

When prescribing dimensions to these structures, the limits of each parameter were dependent by each other. For example, increasing *R* limits the values which can be used for *r* because channels start intersecting in the transverse dimension (although this may be an avenue for future research). Although these helical channels exhibited very low band broadening, the pressure requirements arguably made them less promising than monoliths based on TPMS – which is reflected by the separation impedance values. This is especially pertinent when observing some of the finer narrow features of these media which would not be able to withstand practical chromatography unless rigid materials were used.

5.5 Conclusions

Monolithic structures have shown superior performance to packed beds in practical modern chromatography. In the early stages of this study, it was shown that ordered packed beds decrease band broadening over randomly packed systems. In this chapter, this philosophy was applied to monolithic structures to determine whether further improvements in column performance could be attained.

The primary candidate for ordered monolithic structures were triply periodic minimal surfaces (TPMS), which minimize surface area for a given volume. The P-G-D family of TMPS are monolithic analogues of the SC, BCC and FCC cubic crystal cells and showed both lower band broadening, mass transfer resistance and separation impedance when compared to their spherical particle counterparts. The most successful packing in this family, Schwarz Diamond was attributed with a minimum reduced plate height of less than one – over five times lower than random sphere packing. Furthermore, these monolithic structures do not require overlap, a necessity in packed beds which was found to decrease system performance, providing a distinct advantage over packed beds. Using literature data, other, non-symmetrical minimal surfaces were modelled by using their level-set approximations to create geometric representations of their structure. Many of these surfaces were found to have comparable performance to Schwarz Diamond, meaning that multiple structures have the potential to be used in practical chromatographic operations. A particularly useful surface was the Double Schoen Gyroid, which could produce either two discrete stationary phases or two discrete flow channel systems, depending on how the level-set equation was defined. These structures have the potential incorporate two functionalities into the stationary phase by using 3D printing create the two discrete components with different materials. Practically, this is an interesting prospect for serial chromatographic processes which could, in theory, be performed on a single column, thus saving both time and materials.

A notable property of TPMS structures is their level-set equation and how it can be numerically manipulated to produce geometric differences. As a case study, the level-set equation of the Schwarz Primitive (SP) structure was altered in three ways to observe the effect on the chromatographic performance metrics. First, coefficients were added to the terms in the level-set equations, controlling both the distribution of the solid material along each axis and the porosity of the structure. This method substantially increased performance of the medium, which suggests that this is also applicable to other TPMS structures. Second, the concept of orientation was applied to SP using rotational matrices on the level-set equation, yielding further performance increases, as was observed for packed beds. However, like packed beds, this method would perhaps not be as effective for other, more efficient structures and could even degrade performance. Finally, the concept of a double SP surface was created, which comprised two discrete SP structures and produced reduced plate heights lower than any other medium in this study. These systems also had low permeability because of the low void space and highly tortuous flow channels.

Based on the findings in previous chapters, flow tortuosity showed inverse proportionality with the reduced plate height in any given porous medium. Furthermore, parallel straight channels perform well as monolithic structures, while having a tortuosity value of one. It was hypothesized that combining straight channels and tortuosity could create a monolithic structure with low band broadening properties. The spring geometry was created by sweeping a circular path around a helix. Spring monoliths were found to have better performance than their straight channel counterparts, but this was outweighed by the decrease in permeability and, furthermore, spring monoliths did not provide any advantage over the best TPMS structures.

Ordered monoliths were found to have improved performance over ordered packed beds, while providing more utility and opportunity for optimization. It is suggested here that TPMS structures are the future of chromatographic media, as they provide significant advantages over traditional packed beds and random monolithic structures. However, creation of these structures would not be possible by conventional means and techniques such as 3D printing would be required.

6. Numerical Model of Chromatography

6.1 Introduction

Real chromatographic systems are more complex than simulated environments because of simplifications in the latter, which are necessary to make a model computationally feasible. Furthermore, models should only be used to predict the behaviour of physical systems when they include all relevant phenomena. In the context of this work, previous chapters have included notable simplifications, such as: impermeability of the stationary phase and inert chemical behaviour of the solute tracer. Although these assumptions still provide useful results, the resulting model only describes band broadening in the mobile phase, while the crucial contribution of the stationary phase is ignored. In a chromatographic medium, the stationary phase is usually a porous or pellicular (partially porous) material, which creates a secondary porosity at a smaller scale than the main flow channels. In these smaller pores, advection is considered negligible and solute species are exclusively transported via diffusion[40]. This has an important effect on mass transport resistance, as per van Deemter's model[6] because of the slow nature of diffusion within the solid phase compared to advection via the bulk flow. To accurately describe the chromatographic separation process, these effects must be observed and quantified.

It is first noted that this section covers only non-isocratic, chemical separation methods, which have similar separation mechanisms. Isocratic methods, i.e. size exclusion, are not included, but are simpler within the numerical framework of the model because they do not require an adsorption process. Furthermore, real chromatographic processes involve many chemical species with differing flow properties and perhaps interaction with each other. Although it is numerically possible to include a multitude of phenomena, the computational requirements would be too large to produce multiple data sets for drawing relationships between relevant variables. As computational power increases, it is hoped that this work is continued to model more complex systems and continue to provide a comprehensive tool for optimizing the chromatographic process.

To create a simplified version of the chromatographic process, three chemical species were involved in simulations; the inert, selected and eluent species. Each species was prescribed with analogous diffusive properties and the stationary phase was defined as porous to both species. However, the selected species was subject to adsorption onto the stationary phase via a numerical rate equation,

while the inert species remained chemically inert. Once the selected species had been adsorbed and the inert species was eluted from the column to a specified tolerance, the eluent species was introduced into the column, inducing desorption of the selected species from the medium. The desorbed species was then eluted from the column, completing the separation process. The progress of a chromatographic separation is practically observed using a chromatogram (Section 2.5.2), which was replicated by the numerical model in this study. For a visual representation of this model, please refer to the appendices of this work.

Before using the separation model, this chapter begins by focusing the effect of introducing the internal porosity of the stationary phase on the reduced plate height of a medium using only an inert tracer. To investigate the separation process, three properties of chromatographic systems were studied using the separation model: morphology of the solid phase, eluent concentration and system Peclet number, as detailed in the proceeding sections.

6.1.1 Model Adjustments

There were three major behavioural alterations to the model: the stationary phase became a porous medium itself, binding behaviour of solute species was introduced, and multiple solute species were included in the simulation process.

To make the stationary phase porous, the bounce back boundary condition for the advection-diffusion lattice was removed and replaced with a diffusion coefficient, using the reference diffusion model[27]. This simplification was used to avoid resolving each of the internal porous channels of the stationary phase, which would require a large amount of computational power. Furthermore, advection within small pores of the stationary phase was considered negligible compared to the bulk flow channels and transport occurred solely by diffusion. In a real porous system, the diffusion coefficient of the solute within the pores of the stationary phase cannot exceed the molecular diffusion coefficient because the solute is still effectively travelling through the same fluid medium. Because of the tortuous nature of the pores in the stationary phase, which decrease the effective diffusion through the medium, the pore diffusion coefficient is defined (as introduced in Sections 1.7.2 and 2.4.2). The difference between the two diffusion coefficients is dependent on the properties of the medium, and hence will vary based on the stationary phase materials and fabrication method.

To model the adsorption behaviour, the stationary phase was numerically defined as a source/sink for the selected solute species “inside” the stationary phase, converting it to the adsorbed species (and vice versa, depending on column conditions). The concentration of the adsorbed species was stored in a scalar field which was mapped onto the simulation domain. The source/sink represented the adsorption/desorption process onto the surface of the surface of the stationary phase, within the

pores. The rate of transfer between the advection-diffusion lattice and the scalar field was governed using an adapted rate equation, which was based on the Langmuir isotherm. This formulation was introduced in Section 2.4.2 and is recalled here (Eq. (6.1)).

$$r = k_{ads} C_{aq} \left(1 - \frac{C_{ads}}{C_o}\right) - k_{des} C_{Eluent} \frac{C_{ads}}{C_o} \tag{6.1}$$

It is necessary to use an adsorption model because the length and time scales at which the molecular dynamics occur is many orders of magnitude lower than the those at the microscopic level. The Langmuir isotherm is a popular method for modelling surface adsorption because of its balance between complexity (which defines computational intensity) and accuracy[227]. For specific work, there perhaps would be more suitable isotherms for the surface reaction interactions which can be substituted into the model.

All previous chapters have considered a single inert solute species being introduced into the domain. For chromatographic simulations, three separate solute species were required, the; inert, selected and eluent species. This increased the computational demand of these systems because each species required its own advection-diffusion lattice, which increasing both memory and floating-point operations (FLOP) per global system iteration. To reduce computational requirements, iterations on the inert species were ceased after the concentration decreased below a certain level at the column outlet.

For the axial boundary conditions, all lattices used a Dirichlet inlet and Neumann outlet while for the transverse boundaries, all lattices used periodic boundary conditions to simulate an infinitely wide domain. Although this also a simplification, as seen in Chapter 4, full simulations for columns with a width larger than a single unit cell would not be completable within a feasible timescale. For all chromatographic simulations, the column length was defined as the equivalent of 10 unit cells of a SC [001] packing. This was done because not all packings had the same unit cell length, e.g. FCC [001] packing is longer by a factor of $\sqrt{2}$. Therefore, each chromatogram presented in this section is taken at the equivalent axial length, to provide fair comparison.

6.1.2 Simulation Procedure

To incorporate the phenomena discussed above, modifications were also made to the simulation procedure. During pre-processing, two further lattices (four in total) were defined for the two extra solute species (selected and eluent) along with their respective boundary and initial conditions. The simulation of the velocity field to the laminar flow field was unchanged because this process was considered independent of advection-diffusion behaviour.

When the velocity profile had converged to the specified tolerance, the inert and selected species were introduced into the column simultaneously at the inlet, with an identical pulse function

(Section 2.5.1). Both species were transported into the medium via advection and diffusion where the selected species was adsorbed onto the stationary phase, while the inert species travelled through the column without chemical interaction. When the inert species had been eluted to a specified tolerance (10% of the maximum peak height), the eluent species was introduced at the inlet. The eluent species caused the selected species to unbind from the stationary phase, via the rate equation, and be eluted from the column. The simulation was considered complete when the selected species had been eluted from the column to a specified tolerance (1% of the maximum peak height).

Measure of Performance

For practical chromatography, the normalized eluted fluid volume required to complete the separation is used as an indicator of the system efficiency. For the simulated systems, this volume was a function of the defined superficial velocity and the cross-sectional area of the column. Because different packing morphologies had different cross-sectional areas, from the size of the unit cell, this eluted volume was normalized using the total column volume (Eq. (2.17)).

6.2 Pore Diffusion Coefficient

Altering the pore diffusion coefficient was expected to have a noticeable effect on the performance of a given medium as seen in previous study which have used a solid phase retention factor[46]. To confirm this result, the Double Gyroid medium was used as the stationary phase, because it was attributed with one of the lowest amounts of mobile phase band broadening. As defined in Section 2.4.2, from the work of Grathwohl[40], the variable D' is introduced, as the ratio of pore diffusion to molecular diffusion:

$$D' = \frac{D_{pore}}{D} \tag{6.2}$$

The pore diffusion cannot be greater than the molecular diffusion because the solute is traveling through the same fluid medium in both the pores and the bulk. However, the pore diffusion coefficient is reduced from the bulk fluid value because of the factors such as, internal porosity of the stationary phase and tortuosity of the pore channels which manipulate the average diffusive distance through the medium. Furthermore, constrictivity reduces pore diffusion because of increased viscosity of the solvent at the liquid-solid boundary when the channel size becomes small, which is known as the Renkin effect[228].

The simulation time of a column with porous stationary phase increases compared to the non-porous case because the pore diffusion process is slow compared to advection and diffusion in the bulk fluid. The stationary phase porosity was modelled using the pore diffusion coefficient, meaning there was no effect on the velocity profile of the medium and factors such as system permeability and

tortuosity were unaffected. Practically, this would not be the case, because the pores in the stationary phase would decrease permeability and increase tortuosity, though this would vary with the properties of the medium. To determine the extent of this change, the porous flow channels within the stationary phase would need to be resolved, requiring a mesh with significantly higher resolution than is currently able to be simulated.

Using the pore diffusion coefficient increased the band broadening behaviour of the medium, showing that a lower rate of pore diffusion correlated to greater mass transport resistance, shown by the increase gradient of the van Deemter plot at high Pe and the translation of the global curve minima toward lower Pe (Fig. 6.1). This was expected, because a slower rate of diffusion causes greater divergence between solute in the pores and in the bulk fluid. For practical chromatography, this means that the extent of band broadening will be increased from all results presented in Chapters 3 and 5 as the pore diffusion coefficient decreases. It is also expected that the rate of degradation would depend on the morphology of the stationary phase. This difference was shown in a recent study by Li et al.[46], in which a retention factor was used to incorporate both pore diffusion and adsorption/desorption processes for sphere and ellipsoid packings.

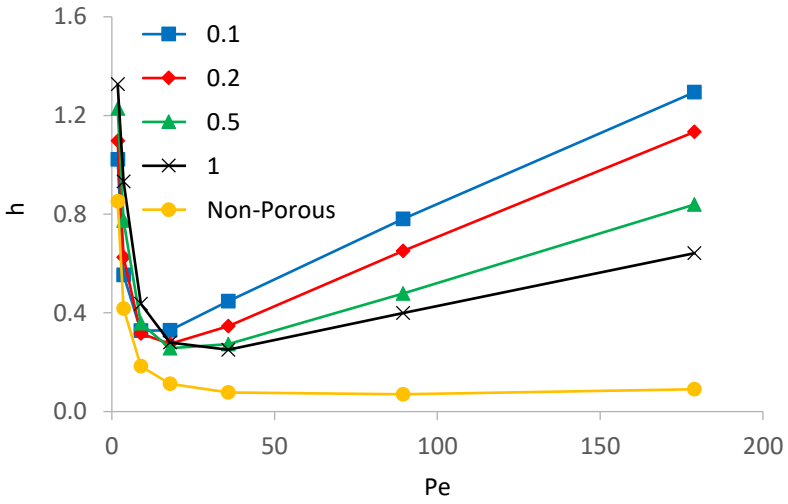

Figure 6.1. van Deemter curves for Double Schwarz Gyroid for a varying D', which is manipulated using the pore diffusion coefficient.

As the D' decreases, there are two possible outcomes for the band broadening behaviour. The first works on the assumption that a non-porous stationary phase can be thought of as the limit as $D_{pore} \rightarrow 0$ and $D' \rightarrow 0$, hence, there must be a critical value of D_{pore} at which band broadening begins to increase again. After this critical point, it is expected that the rate of diffusion decreases to the point at which that the solute matter does not reach the centre of the medium and instead diffuses back into the bulk fluid. As $D_{pore} \rightarrow 0$, the penetration distance decreases until the solid phase becomes practically impermeable. The second case would be that there is not continuous behaviour between D' and h, and the limit as $D_{pore} \rightarrow 0$ does not exist. In this case, h would increase ad infinitum and any solute which

diffuses into the stationary phase would not leave the medium within a practical timescale. Unfortunately, these hypotheses could not be explored with the current advection-diffusion model, because the system becomes unstable at the necessary diffusive rates.

From the work of Grathwohl, a wide range of pore diffusion coefficients can be observed in practice. For the proceeding comparisons, a value of 0.1 was nominally selected, as this correlated to a solid phase porosity of ~0.3. To achieve tailored results to a given system, the properties of the medium must be known before the simulation process.

6.3 Column Morphology

A central theme of this thesis has been the influence of the stationary phase morphology on solute dispersion in the flow system within its pores. It was therefore important to compare column morphologies using a model which was more comparable to a real chromatographic separation. The most successful morphologies for reduction of mobile phase band broadening (from Chapters 3 and 5) were used in this investigation, as follows: Double Schwarz Gyroid (DG), Schwarz Diamond (SD), Double Schwarz Primitive (DP), Schwarz Primitive [111] (SP [111]), Discrete Double Spring (DDS), SC [111] spheres (SC [111] S), SC [111] Octahedrons (SC [111] O), FCC [001] spheres (FCC [001] S) and FCC [001] Tetrahedrons (FCC [001] T).

It was difficult to draw direct comparison between alternative shaped morphologies because each system had an optimum efficiency at different superficial velocities, as observed for mobile phase band broadening in the previous chapters. Moreover, it has been shown in Section 6.2. that a porous material has a different van Deemter curve compared to its non-porous equivalent, therefore, the optimum *Pe* for each morphology could not be predicted based on previous results. Instead of simulating each morphology at a variety of flow rates, a constant superficial velocity was nominally selected, which was known to be in the advection dominated regime for any porous morphology. Although this did not capture the optimum efficiency of each medium, the results were considered informative because it determines which morphologies are suited to faster column conditions and subsequently more rapid separation. A constant superficial velocity ensured that the relative volumetric flowrate was constant for each medium (when normalized by the column volume).

Two important procedures of the simulation process were the introduction of the eluent (at the column entrance) at *10%* of the inert species peak height (at the column exit) and total separation time, when the concentration of the selected species had reached *< 1%* of its peak height. Though the tracer input profile and simulation process were identical for each medium, the chromatograms showed variation in chromatographic resolution, because of strong tailing in some media (Fig. 6.2). It is

important to note that the scale for the eluent concentration has been omitted, as this was constant for each medium.

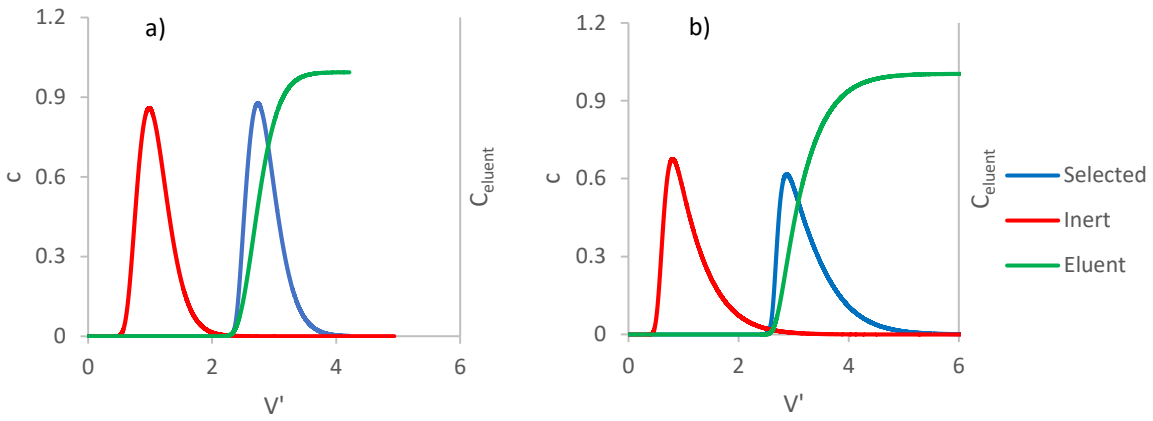

Figure 6.2. Comparison of chromatograms for: a) Schwarz Diamond and b) SC [001] spheres, illustrating the slight difference in chromatographic resolution between morphologies.

Because the reduced plate height of the medium could be calculated using the inert species, this data can be compared to the value for the inert case of each medium, at the equivalent *Pe* (Table 6.1). This agreed with the previously stated hypothesis (Section 6.2) that degradation of a medium's performance when introducing a porous stationary phase depends on the medium itself. The eluted volume for separation was also found to be proportional to the reduced plate height of the inert species (Fig. 6.3). This was expected, because the introduction of the eluent was based on how rapidly the inert species was eluted from the column, which is directly dictated by the reduced plate height for the defined operating conditions. It is important to note that these results will differ if the chromatographic resolution is required to be constant between each morphology.

Table 6.1. Difference between the reduced plate height of the non-porous and D'=0.1 for the highest performing media, at an empty column Pe = 10.

Morphology	Pe	$h_{D' = 0.1}$	$h_{non\text{-}porous}$
SC [111] S	21	2.03	0.16
FCC [001] S	39	2.53	0.10
SC [111] O	12	0.42	0.19
FCC [001] T	12	0.35	0.25
SP [111]	20	1.94	0.08
SD	20	0.68	0.09
DSG	18	0.33	0.18
DSP	22	1.07	0.08
DDS	29	1.08	0.09

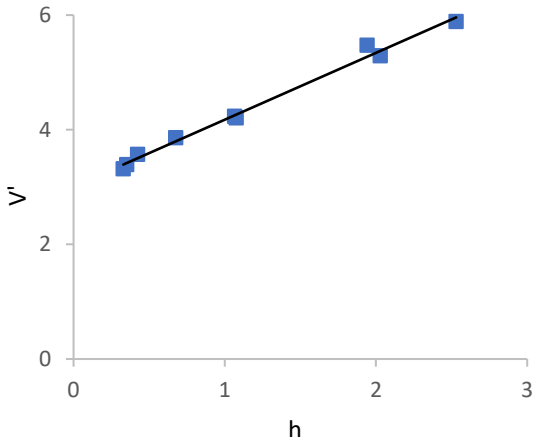

Figure 6.3. Strong correlation between the normalized eluted fluid volume and the reduced plate height at an empty column Pe =10.

Because pore diffusion was slow compared to mass transport in the bulk fluid, it was hypothesized that the distance which solute matter was required to diffuse to reach the bulk flow played an important role on system band broadening and the impact of the characteristics of the mobile phase velocity field was reduced.

To test this hypothesis, an average diffusive distance, $\underline{d}$, for each morphology was calculated as follows. Consider an arbitrary point within the stationary phase, generated using random co-ordinates (a, b, c). The distance to any point on the surface function, $f(x, y, z)$, is calculated using the distance function, g (Eq. (6.3)). To find the shortest distance to the surface, this function is minimized, using the Cartesian equation of the surface as a constraint. To solve this optimization problem, Lagrange multipliers[229] (Eq. (6.4)) were set in the three spatial dimensions and eliminated to provide three unique equations.

$$g = \sqrt{((x-a)^2 + (y-b)^2 + (z-c)^2)} \tag{6.3}$$

$$\nabla f = \lambda \nabla g \tag{6.4}$$

For example, consider a sphere, whose surface is defined as a Cartesian Equation:

$$f = x^2 + y^2 + z^2 - r^2 = 0 \tag{6.5}$$

In the x dimension, the Lagrange term considers the partial derivate in x (Eq. (6.6)), from which the terms can be substituted into the equation (Eq. (6.7)).

$$f'_x = \lambda g'_x \tag{6.6}$$

$$2x = \lambda . 2(x-a) \tag{6.7}$$

Eliminating the Lagrange Multiplier, the terms for each dimension become equivalent (Eq. (6.8)), yielding two unique equations.

$$\frac{x-a}{x} = \frac{y-b}{y} = \frac{z-c}{z} \tag{6.8}$$

To find the surface point closest to the point within the surface, the system of three equations (Two from the Lagrange relations and one being the surface function itself) was solved. For simple functions, as illustrated for the sphere, this process was found to have an analytical solution. However, for complex TPMS functions, numerical solvers were required to find the solutions. To extend this method into finding the average shortest distance for a medium, this process was repeated using 100,000 random points. Finally, $\underline{d}$ was normalized using the smallest unit cell which contains the object. Spherical particles had the largest value of all observed morphologies, which converged to a rational value of *0.125*, while the definitions of SC [001] tetrahedrons and octahedrons (as in Chapter 3). It is important to note that when using tetrahedrons in the FCC orientation that this value is decreased because of how the particles are defined within the unit cell. DSG was attributed with one of the lowest values for $\underline{d}$ while having a similar unit cell porosity to a sphere.

An important assumption used in this analysis, was that the dominant vector of diffusion at any point in within a medium is the shortest distance to the surface. This was deemed to be reasonable because this vector will always be the direction of the largest concentration gradient, as solute at the surface of the stationary phase will diffuse faster through the boundary layer of the medium and into the bulk flow where it experiences an increasing amount of advection. A linear correlation was found between the average shortest distance and the mean elution volume (Fig. 6.4), showing that the diffusion in the stationary phase has an important contribution to band broadening within the system.

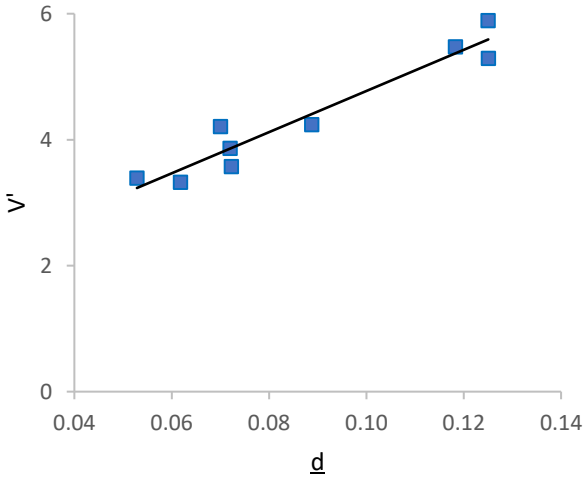

Figure 6.4. Linear correlation between the elution volume and the average minimum distance to the surface of the stationary phase.

Fig. 6.4 shows that d has an important role in the separation process. This finding can be applied to stationary phase morphologies in two ways, first, by decreasing the particle size with respect to the unit cell. However, for particles, this would compromise the structural integrity of the bed because of the lack of contact between particles. Second, the length scale of the system could be reduced. This would reduce the Peclet number, meaning that the velocity would need to be increased to compensate, subsequently increasing the pressure drop of the system. It is therefore an important consideration in practical chromatography to keep the particle size small enough to reduce the diffusion time through the medium, but large enough to keep the pressure drop of the medium in an acceptable range. This formulation of d becomes important because it enables comparison between media given a feature size within the diffusion and permeability criteria.

To further test this hypothesis, a medium with poor mobile phase band broadening was simulated using the separation model. SC [001] spheres as a chromatographic medium was attributed with one of the highest levels of mobile phase band broadening in this study. Surprisingly, this system showed a slightly poorer chromatographic resolution than SC [111] and FCC [001] spheres (Fig. 6.5) while having a comparable reduced plate height (*2.7*) and eluted volume (*5.5*). This supported the theory that mobile phase band broadening becomes less important as *D'* decreases and the relative diffusive distance through the medium becomes crucial, especially in the advection regime of the van Deemter curve.

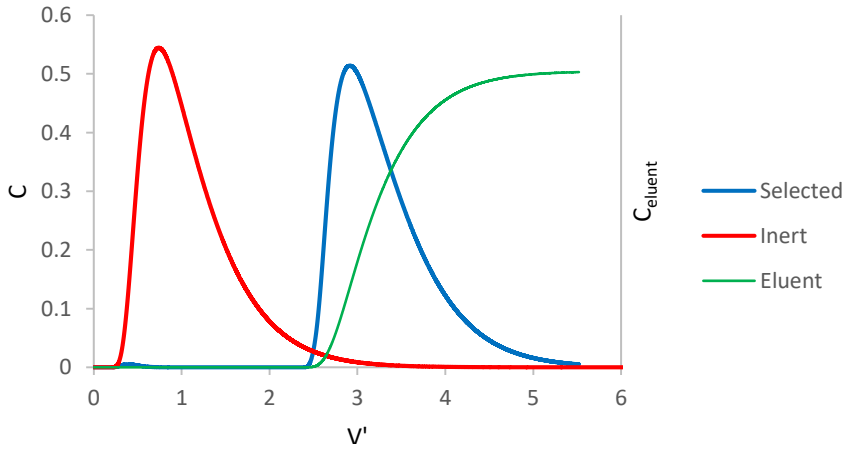

Figure 6.5. Chromatogram of a column comprising SC [001] spheres, showing a decrease in chromatographic resolution, but comparable separation time compared to other ordered sphere packings.

It was interesting to note that FCC [001] was slower than SC [001] for spherical particles, when using the defined simulation scheme, even though it was attributed with a smaller reduced plate height value for mobile phase band broadening. There are two possible explanations for this, first, the SC [001] has a lower chromatographic resolution than FCC [001] meaning that the kurtosis of the SC [001] RTD was larger because the *10%* marker was reached first, while its tail was longer. Hence, a different control scheme would be required for these systems to achieve a higher chromatographic resolution. Second,

for a medium which uses discrete particles, configurations with lower void space have an increased chance of solute diffusing from one particle into another instead of into the bulk channel flow, increasing the residence time of the solute species.

Finally, two of the media showed a noticeable premature breakthrough: SC [111] octahedrons and SC [001] spheres. This was because a fraction of the selected solute had no opportunity to interact with the stationary phase and was instead advected through the column and eluted. Media with high porosity and low tortuosity would be especially susceptible to this, because there would be a lower probability of solute particles encountering the stationary phase.

From the findings in this section, the characteristics of a successful chromatographic medium become more apparent. The average diffusive distance should be minimized while also maintaining low porosity, which are conflicting variables. It is therefore important that the stationary and mobile phases are well distributed within the unit cell of an ordered packing. However, a more uniform distribution can also correlate to both weaker structural properties and greater surface area creating the potential for column deformation and higher pressure drop across the packed bed. Finally, tortuosity should be maximized to promote transport of solute species into the boundary layer and the pores of the solid phase, which minimizes the potential of premature breakthrough in the chromatogram.

6.4 Eluent Concentration

When removing the bound solute from the column, a change in the column conditions is required. Practically, this is done by a change in pH, or introduction of a species which exhibits preferential binding to the selected species. In the simulation process, the exact mechanism of desorption is not important, and the process is incorporated into rate equation (second term on the RHS) (Eq. (6.9)).

$$r = k_{ads} C_{aq} (1 - \frac{C_{ads}}{C_o}) - k_{des} C_{Eluent} \frac{C_{ads}}{C_o} \tag{6.9}$$

For any system, it is important that $k_{ads} >> k_{des}$, meaning that the initial driving force promotes adsorption of the solute until saturation. Therefore, desorption can only occur when the product of the concentration of the eluent and the rate of desorption is greater than the rate of adsorption (ignoring the concentration terms themselves). For a system in which a step input of eluent is used, the ratio of the rate constants is defined, which is referred to as the desorption driving force, κ (Eq. (6.10)).

$$\kappa = C_{Eluent} \frac{k_{des}}{k_{ads}} \tag{6.10}$$

As the step input of the eluent permeates the medium, κ_{max} is defined when the solute concentration at a given point reaches the inlet eluent concentration meaning that κ_{max} is constant for a step input system. Varying κ_{max} shows that increasing the eluent concentration does increase the efficiency of the elution process (Fig. 6.6).

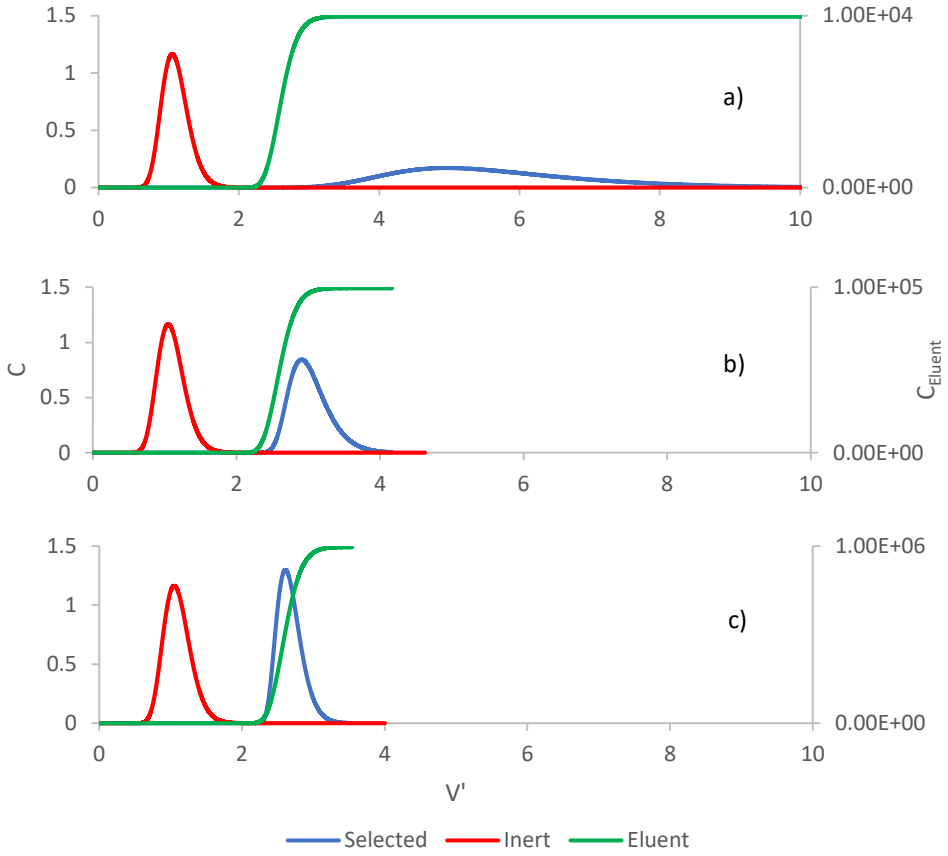

Figure 6.6. Chromatograms for DSG systems in which the desorption driving force is altered by manipulating the eluent concentration: a) $\kappa_{max} = 1$, b) $\kappa_{max} = 10$ and c) $\kappa = 100$. The eluent concentration, on the secondary vertical axis, is a theoretical numerical device which is used to define the value of κ_{max}.

From this result, it could be stated that there is no upper bound for the eluent concentration in achieving the best system performance within the simulation environment, but there are diminishing returns for using a larger eluent concentration. In this system, the decrease in eluted volume between $\kappa_{max} = 1$ and $\kappa_{max} = 10$ is significantly larger than between $\kappa_{max} = 10$ and $\kappa_{max} = 100$ and presumably this trend continues as κ increases. Higher values for κ could not be simulated because the rate of unbinding becomes too large for the time step. In the case of $\kappa = 1$, the overall driving forces were even, but solute could escape the stationary phase via the concentration gradients caused when solute was advected by the velocity field, hence shifting the equilibrium toward desorption. A driving force below one was also not simulated because this meant that the overall driving force would be for adsorption and the process time would be increased considerably. In a practical system, there are other factors to consider. For example, the eluent has a cost, meaning that the cost starts to outweigh the diminishing returns achieved

by using a higher eluent concentration. Furthermore, the eluent not only has a saturation limit in the mobile phase, but it can also influence the saturation limit of the solute species, e.g. a system with an excess of salt eluent can cause protein precipitation[230]. Furthermore, excess desorption has the potential to both alter local viscosity of the fluid and cause react with the solute species forming aggregate particles[231, 232]. Each of these factors creates an upper bound for the eluent concentration which is specific to a given separation. Hence, for most systems, it is sufficient that the process is not rate limited to reduce band broadening, but excess eluent can be detrimental to system performance.

An interesting feature of these chromatograms is that at high eluent levels, the elution of the selected species experiences a lower amount of dispersion than the inert species for some media, which can be a positive attribute within the context of the chromatographic process (assuming no viscous effects). This phenomenon occurs because the rate of desorption caused by the eluent facilitates an instantaneous unbinding of the selected species, making the elution process mass transfer limited. Because of this, as the front of the eluent step propagates through the medium, all solute is unbound instantaneously and concentrated at the eluent front. This behaviour results in a more concentrated solute pulse than the inert solute which experiences equal band broadening throughout the medium.

6.5 Peclet Number

As illustrated in Chapters 3-5 in this work, dispersion in non-porous systems is strongly governed by the channel Peclet number. This is also the case for practical chromatographic systems, which is reflected by the data produced by the model (Fig. 6.7).

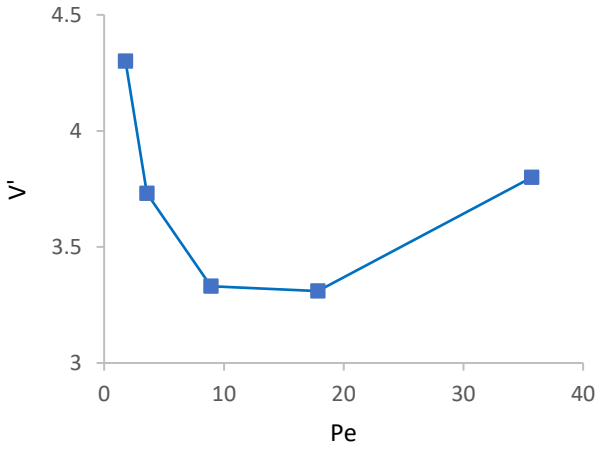

Figure 6.7. Plot of the separation efficiency, represented by V', at different flow rates for a DSG medium in which D' = 0.1.

An optimum separation efficiency was found at $10 < Pe < 20$, which reflects the van Deemter curve for the DSG medium using an inert tracer (when $D' = 0.1$). Hence, it can be argued that although the results for mobile phase band broadening do not directly correlate to separation performance, the

band broadening for porous stationary phase systems does. This is not to undermine the results presented in the previous chapters in this work, as mobile phase band broadening is relevant to improving chromatographic performance. Band broadening cannot be measured within the stationary phase alone, but it is hypothesized here that it can be considered as the difference between the mobile phase broadening and the total system broadening (Eq. (6.12)), much like the van Deemter's additive plate height model[6] and the additive model for wall effects[31].

$$h_{stat} = h_{tot} - h_{mob} \tag{6.12}$$

where h_{stat} is the band broadening in the stationary phase, h_{tot} is the total band broadening with a porous stationary phase and h_{mob} is the band broadening in the mobile phase. The CFD model began to show instability when the Peclet number was increased above the maximum reported value.

6.6 Conclusion

In this chapter, the CFD model was further developed to simulate: an approximation to a porous stationary phase, adsorption/desorption behaviour of the solute onto the stationary phase and inclusion of three solute species. These aspects of the model extended the results beyond mobile phase band broadening and showed the importance of the contribution to column inefficiency from the pores of the stationary phase. This contribution came from increasing the mass transfer resistance because of slow mass transfer within the stationary phase, as defined by the pore diffusion coefficient, compared to advection in the bulk fluid channels. Furthermore, these developments were an important precursor to performing more complex chromatographic simulations.

The numerical description of a chromatographic process was performed by introducing two species into the column simultaneous and binding one of the solutes on the stationary phase, while the other species was eluted from the column. To complete the separation process, the bound solute was eluted from the column using an eluent species which promoted desorption through the governing rate equation. The eluted volume was used as a measure of separation efficiency, which was a function of: the volumetric flow rate, total column volume and time.

Decreasing the ratio between the pore diffusion and molecular diffusion coefficients was found to decrease reduced plate height in the Double Schoen Gyroid medium, while reducing the optimum Peclet number. However, this internal porosity is a necessary feature of ion exchange and affinity media which involve surface chemical interaction with the solute, otherwise the amount of binding opportunities would be dramatically decreased, and very large columns would be required to achieve the equivalent column capacity.

It was found that the required eluted volume of an internally porous medium was directly proportional to the average shortest distance from within the medium to the surface when using a constant superficial velocity and axial column length. This relationship demonstrated the importance of the stationary phase morphology and how band broadening in these systems can be reduced by evenly distributing the mobile and stationary phases within the unit cell. This was further validated by showing that a medium which performed showed a high level of mobile phase band broadening (SC [001] spheres) had comparable separation efficiency to other sphere packings which had relatively poor mobile phase band broadening (SC [111] and FCC [001]).

By altering the concentration of a step input of eluent species into the column, the role of the desorption driving force was investigated. It was found that higher concentration of eluent increased separation performance, but this came with diminishing returns. Furthermore, there are multiple factors which limit the concentration of the eluent species, such as: cost and precipitation of solute species. Ultimately, it is important that the desorption process is not rate limited because this causes excessive band broadening of the selected species during the elution process.

Finally, altering the system Peclet number showed an optimal operating point, equivalent to the van Deemter curve for the intra-porous stationary phase, confirming that tracer studies alone can determine the optimum operating point, given that the correct system properties are used in the model. It was hypothesized that the band broadening components from the mobile and stationary phases are additive, though the band broadening within the stationary phase cannot be discretely measured using the current model.

Conclusions and Recommendations

Conclusions

Through numerical modelling, this work has illustrated the potential of 3D printed ordered packings for use as chromatographic media and created a precursor for a comprehensive numerical model of the chromatographic process. Accompanying these main achievements, there are various significant findings presented in this work which can be applied to practical chromatography and perhaps other applications of porous media, such as (but not limited to); filtration and heat exchange.

The numerical model of chromatography was developed using Palabos, an open source C++ library that uses the lattice Boltzmann method to solve fluid dynamics problems, which can be coupled with other complex physical phenomena to model real world systems. Practical chromatographic metrics, such as: bed permeability and reduced plate height were calculated from the model and used to compare the effectiveness of various stationary phase morphologies. The chromatographic model was validated using three test cases (Section 2.8), showing good agreement with accepted literature data and hence, providing evidence to support the data presented in this thesis.

Chapter 3 focused on ordered packed beds, continuing from previous investigations in the literature which have showed that ordered sphere packings can provide a performance advantage over randomly packed beds of spheres. It was suggested that ordered packing normalizes the flow patterns within a packed bed and hence, reduces eddy dispersion. This finding was confirmed by the current work, showing that both body-centred cubic (BCC) and face-centred cubic (FCC) sphere packing can achieve reduced mobile phase band broadening when compared to jammed random packing of spheres under certain operating conditions. Following from these further validation of the model, the novel concept orientation was introduced, which described the angle of incidence between the axial flow direction and the standard unit cell of the packed bed. It was found that this angle played a large role in the dispersion caused by the media but, had no effect on the system permeability meaning that the separation impedance of the medium could be decreased for relatively little effort. Furthermore, these packed beds were found to have a strong correlation between flow tortuosity and reduced plate height, suggesting that transverse dispersion is an important contributor for reducing mobile phase band broadening.

Recent literature has also suggested that spherical particles may not be the most effective particle shaped to use in ordered packed beds, contrary to the long-standing findings for randomly packed beds. This idea was further explored in Chapter 3 by replacing spherical particles with octahedral and tetrahedral particles, showing improvement of performance for numerous configurations. The packed bed system with the lowest separation impedance was found to be simple cubic (SC) [111] octahedrons, however, this system was also attributed with very high porosity and low structural integrity. For 3D printed packed beds, structural integrity of the bed is a major concern because of the low amount of contact between particles. To alleviate these concerns, the concept of overlap has been defined in the literature, which fuses discrete particles into a monolithic structure and hence increases the structural integrity of the medium. However, it was found in this work that overlap increased separation impedance for all observed cases because bed voidage and permeability were decreased.

In practical chromatography, the mobile phase is contained by the column walls. Although this is a necessity, column walls contribute to band broadening by a phenomenon known as the “wall effect”. The mechanism of the wall effect stems from the packing disruption caused by the walls, which causes decreased void space and higher velocity at the walls. Solute matter which is entrained in the faster wall flows diverges from the solute in the bulk column flow, thus elongating the system RTD curve. Literature suggests that the wall effect is an additive contribution to the reduced plate height, which is length dependent, creating: short-term (linear), transient and long-term (constant) behaviour of the reduced plate height. In this study, confined FCC sphere packing was found to agree with the two-zone plug flow model proposed in the literature, for the short-term region. The column-to-particle diameter ratio was varied, showing that wider columns have a lower rate of increase for band broadening, but a larger long-time limit. Hence, in practice, columns should have a large diameter and short axial length to reduce dispersion. Using 3D printing, particles can be printed into the walls to address the voidage issue. Embedding column walls was found to mitigate the wall effect, providing a solution to poor performance in narrow columns. Finally, embedded columns of square and circular cross section were shown to have similar performance, suggesting that the technique of embedded column walls removes the requirement of using cylindrical columns to achieve optimum performance.

Monolithic structures in practical chromatography show higher permeability than packed beds. It was therefore hypothesized that ordered monoliths may provide a similar performance advantage over ordered packed beds. Triply periodic minimal surfaces (TPMS) were an attractive candidate to this purpose because minimal surfaces are associated with high permeability. In Chapter 5, an array of TPMS structures were found to have separation impedance values equal to the best performing packed beds, while decreasing the void space and removing the requirement for overlap. Furthermore, TPMS structures could be manipulated via their level-set equation, which defines them in Cartesian space. The

worst performing TPMS structure, Schwarz Primitive was manipulated using a variety of transformations, each of which was shown to reduce band broadening by a considerable amount. It was hypothesized that these manipulations could be applied to other TPMS structures when optimizing the structure to minimize mobile phase band broadening. As a final concept for ordered monolithic structures, tortuous "spring" flow channels were investigated and were found to have very good performance, but low permeability, making them less attractive than TPMS morphologies.

Chapter 6 described the development of the basis for a full model chromatographic model. This was done by: defining the stationary phase as porous, programming an adsorption/desorption surface reaction for the solute species and including multiple species in the simulation process. Performance of these systems was evaluated using the dimensionless volume required to complete the separation process. For an inert tracer, it was found that the reduced plate height of the Double Schoen Gyroid medium increased as the pore diffusion coefficient of the stationary phase decreased, because of an increase in mass transfer resistance, as per van Deemter's plate height model. For chromatographic separations, this work correlated the average diffusive distance to the surface of a medium to the dimensionless volume, implying that mobile phase band broadening contributed little to the system efficiency as the pore diffusion coefficient decreased. It was also found that system efficiency increased with eluent concentration, though there were practical factors that were not modelled, which would restrict the maximum concentration. Varying the Peclet number in the chromatographic model also influenced the system efficiency, mirroring the van Deemter curve created when using a porous stationary phase, suggesting that the chromatographic performance of a medium can be shown using a tracer study, given that stationary porosity is used. Finally, it was hypothesized here that the mobile and stationary phase contributions to band broadening are additive effects, and that their sum is equal to the total system band broadening.

Recommendations

For the future of this body of work, there are many potential model developments and systematic studies which could provide further benefit to practical chromatography and applications of porous media, as detailed below.

There are several phenomena which could be incorporated into the model to improve its capacity as a predictive tool. As mentioned many times in this work, stationary phase deformation is critical to understanding the pressure limits of any given medium. This would be a significant addition to the model and would be able to answer many questions which have been posed about structural integrity of stationary phase morphologies in this work. Second, the current model only considers isothermal systems, meaning that the effect of temperature on system performance was not explored. This would be expected to have a large effect on the computational requirements of the model, because

of the effect which temperature has on properties of the mobile phase, such as viscosity and density, which need to be locally adjusted every time step. Continuing this line of thinking, the effect of solute concentration on the mobile phase could also be included, instead of using the current passive model.

Ignoring the above developmental prospects, there is still work of interest which could be completed with the current model, continuing from each chapter of this work. It is suggested here that ordered monolithic structures are more useful than ordered packed beds, however only three particle shapes were investigated. Hence, there may be some untested regular or irregular geometries which produce further optimizations in chromatographic efficiency.

Wall effects are a large practical concern for chromatography, although it has been shown that these can be mitigated somewhat, using 3D printing, there is still a broad scope for work which optimizes the wall-packing interface to further reduce band broadening in these systems.

TPMS structures are perhaps the most interesting prospect for future work. The most pressing aspect would be to apply the manipulations which were used on Schwarz Primitive to other TMPS structures to further optimize these systems. Furthermore, there are perhaps other TPMS structures which have not yet been discovered which further decrease band broadening.

Within the full chromatographic model, there are also many systematic studies which can be performed, such as (but not limited to): competitive surface binding for solute species, alternative isothermal binding models, resolution of the secondary porosity scale within the stationary phase, pellicular stationary phases and size exclusion chromatography.

A practical aspect of chromatography which has not been mentioned in this thesis, is the inlet distribution and outlet collection of the mobile phase. All simulations have only considered perfectly flat velocity profile at the column inlet; however, this is very difficult to achieve in practice because the column walls cause the flow to tend toward a parabolic flow profile. Furthermore, after the mobile phase leaves the column, it experiences band broadening in the flow systems present before being sampled. Each of these effects could be modelled and perhaps methods of inlet and outlet distribution could be tested to reduce dispersion involved with these processes.

Finally, with development, this model could readily be used to optimise other porous media applications outside of the chromatographic process, for unit operations such as: heat exchange and filtration. This versatility and potential makes the model a valuable tool for future research of 3D printed porous media.

References

1. Heftmann, E., *Chromatography: Fundamentals and applications of chromatography and related differential migration methods - Part A: Fundamentals and techniques*. 2004: Elsevier Science.

2. Edgar, T.F., D.M. Himmelblau, and L.S. Lasdon, *Optimization of chemical processes*. 2nd ed. 2001, New York: McGraw-Hill.

3. Segovia-Hernández, J.G. and A. Bonilla-Petriciolet, *Process intensification in chemical engineering: Design optimization and control*. 2016.

4. Poole, C.F., *The Essence of Chromatography*. 2003: Elsevier.

5. Robards, K., P.R. Haddad, and P.E. Jackson, *Principles and Practice of Modern Chromatographic Methods*. 1994: Academic Press.

6. van Deemter, J.J., F.J. Zuiderweg, and A. Klinkenberg, *Longitudinal diffusion and resistance to mass transfer as causes of nonideality in chromatography.* Chemical Engineering Science, 1956. **5**(6): p. 271-289.

7. Schotting, R.J., H.C.J. van Duijn, and A. Verruijt, *Soil Mechanics and Transport in Porous Media: Selected Works of G. de Josselin de Jong*. 2008: Springer Netherlands.

8. Tschernich, R.W., *Zeolites of the World*. 1992: Geoscience Press.

9. Crescentini, G., et al., *Preparation and evaluation of dry-packed capillary columns for high-performance liquid chromatography.* Analytical Chemistry, 1988. **60**(17): p. 1659-1662.

10. Andreolini, F., C. Borra, and M. Novotny, *Preparation and evaluation of slurry-packed capillary columns for normal-phase liquid chromatography.* Analytical Chemistry, 1987. **59**(19): p. 2428-2432.

11. Bidlingmeyer, B.A., *Preparative Liquid Chromatography*. 1987: Elsevier Science.

12. Fee, C., S. Nawada, and S. Dimartino, *3D printed porous media columns with fine control of column packing morphology.* Journal of Chromatography A, 2014. **1333**: p. 18.

13. Nawada, S., S. Dimartino, and C. Fee, *Dispersion behavior of 3D-printed columns with homogeneous microstructures comprising differing element shapes.* Chemical Engineering Science, 2017. **164**: p. 90-98.

14. Schure, M.R., et al., *Simulation of ordered packed beds in chromatography.* Journal of Chromatography A, 2004. **1031**(1–2): p. 79-86.

15. Currie, I.G., *Fundamental Mechanics of Fluids, Fourth Edition*. 2012: Taylor & Francis.

16. Doering, C.R. and J.D. Gibbon, *Applied Analysis of the Navier-Stokes Equations*. 1995: Cambridge University Press.

17. Temam, R., et al., *Navier—Stokes Equations: Theory and Numerical Analysis*. 2016: Elsevier Science.

18. Whitaker, S., *Flow in porous media I: A theoretical derivation of Darcy's law*. Transport in Porous Media, 1986. **1**(1): p. 3-25.

19. Defraeye, T., et al., *Computational fluid dynamics analysis of cyclist aerodynamics: Performance of different turbulence-modelling and boundary-layer modelling approaches.* Journal of Biomechanics, 2010. **43**(12): p. 2281-2287.

20. Defraeye, T., P. Verboven, and B. Nicolai, *CFD modelling of flow and scalar exchange of spherical food products: Turbulence and boundary-layer modelling.* Journal of Food Engineering, 2013. **114**(4): p. 495-504.

21. Parente, A., et al., *A Comprehensive Modelling Approach for the Neutral Atmospheric Boundary Layer: Consistent Inflow Conditions, Wall Function and Turbulence Model.* Boundary-Layer Meteorology, 2011. **140**(3): p. 411-428.

22. Cercignani, C., *The Boltzmann Equation and Its Applications*. 2012: Springer New York.

23. Krüger, T., et al., *The Lattice Boltzmann Method: Principles and Practice*. 2016: Springer International Publishing.

24. Rohde, M., et al., *Improved bounce-back methods for no-slip walls in lattice-Boltzmann schemes: Theory and simulations.* Physical Review E, 2003. **67**(6): p. 066703.

25. Yin, X. and J. Zhang, *An improved bounce-back scheme for complex boundary conditions in lattice Boltzmann method.* Journal of Computational Physics, 2012. **231**(11): p. 4295-4303.

26. Mountrakis, L., et al., *Parallel performance of an IB-LBM suspension simulation framework.* Journal of computational science, 2015. **9**: p. 45-50.

27. Perko, J. and R.A. Patel, *Single-relaxation-time lattice Boltzmann scheme for advection-diffusion problems with large diffusion-coefficient heterogeneities and high-advection transport.* Physical review. E, Statistical, nonlinear, and soft matter physics, 2014. **89**(5): p. 053309.

28. de Klerk, A., *Voidage variation in packed beds at small column to particle diameter ratio.* AIChE Journal, 2003. **49**(8): p. 2022-2029.

29. Knox, J.H. and J.F. Parcher, *Effect of the column to particle diameter ratio on the dispersion of unsorbed solutes in chromatography.* Analytical Chemistry, 1969. **41**(12): p. 1599-1606.

30. Shalliker, R.A., B.S. Broyles, and G. Guiochon, *Physical evidence of two wall effects in liquid chromatography.* Journal of chromatography. A, 2000. **888**(1): p. 1-12.

31. Broeckhoven, K. and G. Desmet, *Approximate transient and long time limit solutions for the band broadening induced by the thin sidewall-layer in liquid chromatography columns.* Journal of Chromatography A, 2007. **1172**(1): p. 25-39.

32. Broeckhoven, K. and G. Desmet, *Numerical and analytical solutions for the column length-dependent band broadening originating from axisymmetrical trans-column velocity gradients.* Journal of Chromatography A, 2009. **1216**(9): p. 1325-1337.

33. Bird, R.B., W.E. Stewart, and E.N. Lightfoot, *Transport phenomena*. 2007, Hoboken, New Jersey, USA: John Wiley & Sons.

34. Schoen, A.H., *Embedded Triply-Periodic Minimal Surfaces and Related Soap Film Experiments*, in *Geometric Analysis and Computer Graphics: Proceedings of a Workshop held May 23–25, 1988*, P. Concus, R. Finn, and D.A. Hoffman, Editors. 1991, Springer New York: New York, NY. p. 147-157.

35. Schoen, A.H., *Reflections concerning triply-periodic minimal surfaces.* Interface Focus, 2012. **2**(5): p. 658-668.

36. Wohlgemuth, M., et al., *Triply Periodic Bicontinuous Cubic Microdomain Morphologies by Symmetries.* Macromolecules, 2001. **34**(17): p. 6083-6089.

37. Liu, P. and G.F. Chen, *Porous Materials: Processing and Applications*. 2014: Elsevier Science.

38. Bear, J., *Dynamics of Fluids in Porous Media*. 2013: Dover Publications.

39. Vafai, K., *Porous Media: Applications in Biological Systems and Biotechnology*. 2010: CRC Press.

40. Grathwohl, P., *Diffusion in Natural Porous Media: Contaminant Transport, Sorption/Desorption and Dissolution Kinetics*. 2012: Springer US.

41. Glinski, J., *Solute Transport in Soils*. 2011, Springer.

42. Cerrolaza, M., *Computational Bioengineering: Current Trends and Applications*. 2004: Imperial College Press.

43. Narayan, R., et al., *Advances in Bioceramics and Porous Ceramics V: Ceramic Engineering and Science Proceedings, Volume 33*. 2012: Wiley.

44. Eaves, D., *Handbook of Polymer Foams*. 2004: Rapra Technology.

45. Khirevich, S., *High-Performance Computing of Flow, Diffusion, and Hydrodynamic Dispersion in Random Sphere Packings*, in *Department of Chemistry*. 2011, Philipps-Universität Marburg.

46. Li, L., et al., *Numerical investigation on band-broadening characteristics of an ordered packed bed with novel particles.* Applied energy, 2017. **185**: p. 2168-2180.

47. Gibson, I., et al., *Additive Manufacturing Technologies: 3D Printing, Rapid Prototyping, and Direct Digital Manufacturing*. 2nd 2015.;2nd 2015; ed. 2015, New York, NY: Springer New York.

48. Direktor, L.B., et al., *Theoretical and experimental studies of hydrodynamics and heat exchange in porous media.* High Temperature, 2010. **48**(6): p. 887-895.

49. Nield, D.A. and A. Bejan, *Convection in Porous Media*. 2014, New York, NY, UNITED STATES: Springer New York.

50. Darcy, H., *Les fontaines publiques de la ville de Dijon: exposition et application*. 1856: Victor Dalmont.

51. Carman, P.C., *Fluid flow through granular beds.* Transactions-Institution of Chemical Engineeres, 1937. **15**: p. 150-166.

52. Carman, P.C., *Flow of gases through porous media*. 1956: Academic press.

53. Kozeny, J., *Über kapillare leitung des wassers im boden:(aufstieg, versickerung und anwendung auf die bewässerung)*. 1927: Hölder-Pichler-Tempsky.

54. Ergun, S., *Fluid flow through packed columns.* Chem. Eng. Prog., 1952. **48**: p. 89-94.

55. Ozahi, E., M.Y. Gundogdu, and M.Ö. Carpinlioglu, *A Modification on Ergun's Correlation for Use in Cylindrical Packed Beds With Non-spherical Particles.* Advanced Powder Technology, 2008. **19**(4): p. 369-381.

56. Li, L. and W. Ma, *Experimental Study on the Effective Particle Diameter of a Packed Bed with Non-Spherical Particles.* Transport in Porous Media, 2011. **89**(1): p. 35-48.

57. Aris, R., *On the Dispersion of a Solute in a Fluid Flowing through a Tube.* Proceedings of the Royal Society of London. Series A, Mathematical and Physical Sciences, 1956. **235**(1200): p. 67-77.

58. Taylor, G., *Dispersion of soluble matter in solvent flowing slowly through a tube.* Proceedings of the Royal Society of London A: Mathematical, Physical and Engineering Sciences, 1953. **219**(1137): p. 186-203.

59. Flekkøy, E.G., *Lattice Bhatnagar-Gross-Krook models for miscible fluids.* Physical Review E, 1993. **47**(6): p. 4247-4257.

60. Guo, Z. and C. Shu, *Lattice Boltzmann Method and Its Applications in Engineering*. Vol. 3;3.;. 2013, New Jersey: World Scientfic.

61. Damodaran, S., *Food Proteins and Their Applications*. 1997: Taylor & Francis.

62. Keener, R.N., et al., *Mechanical deformation of compressible chromatographic columns.* Biotechnology progress, 2002. **18**(3): p. 587-596.

63. Lindsay, S., J. Barnes, and ACOL, *High Performance Liquid Chromatography*. 1992: Wiley.

64. Grushka, E. and N. Grinberg, *Advances in Chromatography*. 2007: CRC Press.

65. Wu, C., *Column Handbook for Size Exclusion Chromatography*. 1999: Elsevier Science.

66. Jandera, P. and J. Churácék, *Gradient Elution in Column Liquid Chromatography: Theory and Practice*. 1985: Elsevier Science.

67. Yamamoto, S., K. Nakanishi, and R. Matsuno, *Ion-Exchange Chromatography of Proteins*. 1988: Taylor & Francis.

68. Marinsky, J.A. and Y. Marcus, *Ion Exchange and Solvent Extraction: A Series of Advances*. 1995: Taylor & Francis.

69. Stenholm, Å., H. Lindgren, and J. Shaffie, *Comparison of amine-selective properties of weak and strong cation-exchangers.* Journal of Chromatography A, 2006. **1128**(1–2): p. 73-78.

70. Hage, D.S. and J. Cazes, *Handbook of Affinity Chromatography, Second Edition*. 2005: CRC Press.

71. Alves, N., et al., *Small-Molecule-Based Affinity Chromatography Method for Antibody Purification via Nucleotide Binding Site Targeting.* Analytical chemistry (Washington), 2012. **84**(18): p. 7721.

72. Fausnaugh, J., L. Kennedy, and F. Regnier, *Comparison of hydrophobic-interaction and reversed-phase chromatography of proteins.* Journal of Chromatography A, 1984. **317**: p. 141-155.

73. Mori, S. and H.G. Barth, *Size Exclusion Chromatography*. 2013: Springer Berlin Heidelberg.

74. Samuelsson, J., et al., *Development of the tracer-pulse method for adsorption studies of analyte mixtures in liquid chromatography utilizing mass spectrometric detection.* Analytical chemistry, 2008. **80**(6): p. 2105-2112.

75. Jonsson, J.A., *Chromatographic Theory and Basic Principles*. 1987: Taylor & Francis.

76. Faghri, A., Y. Zhang, and J.R. Howell, *Advanced Heat and Mass Transfer*. 2010: Global Digital Press.

77. Ganetsos, G. and P.E. Barker, *Preparative and production scale chromatography*. Vol. 61. 1992: CRC Press.

78. Gustafson, G.B. and C.H. Wilcox, *Analytical and Computational Methods of Advanced Engineering Mathematics*. 1998: Springer New York.

79. Kucera, P., *Microcolumn High-Performance Liquid Chromatography*. 2000: Elsevier Science.

80. Knox, J.H., *Band dispersion in chromatography – a new view of A-term dispersion.* Journal of Chromatography A, 1999. **831**(1): p. 3-15.

81. Seki, K. and B. Bagchi, *Relationship between entropy and diffusion: A statistical mechanical derivation of Rosenfeld expression for a rugged energy landscape.* The Journal of chemical physics, 2015. **143**(19): p. 194110.

82. Siouffi, A.M., *About the C term in the van Deemter's equation of plate height in monoliths.* Journal of Chromatography A, 2006. **1126**(1–2): p. 86-94.

83. Jacobs, P.A., et al., *Introduction to Zeolite Science and Practice*. 2001: Elsevier Science.

84. Schwarz, J.A. and C.I. Contescu, *Surfaces of Nanoparticles and Porous Materials*. 1999: CRC Press.

85. Jungbauer, A., *Chromatographic media for bioseparation.* Journal of chromatography. A, 2005. **1065**(1): p. 3-12.

86. Benes, M.J., et al., *Methacrylate-based chromatographic media.* Journal of separation science, 2005. **28**(15): p. 1855.

87. Sofer, G.K. and L. Hagel, *Handbook of process chromatography: a guide to optimization, scale up, and validation*. 1997, San Diego: Academic Press.

88. Gooding, K.M. and F.E. Regnier, *Hplc Of Biological Macro- Molecules, Revised And Expanded*. 2002: Taylor & Francis.

89. Zachariou, M., *Affinity Chromatography: Methods and Protocols*. 2008: Humana Press.

90. Cybulski, A., *Structured Catalysts and Reactors*. 1997: Taylor & Francis.

91. Weber, D., D.J. Holland, and L.F. Gladden, *Spatially and chemically resolved measurement of intra- and inter-particle molecular diffusion in a fixed-bed reactor.* Applied Catalysis A: General, 2011. **392**(1–2): p. 192-198.

92. Petro, M., F. Svec, and J.M.J. Fréchet, *Molded continuous poly(styrene- co-divinylbenzene) rod as a separation medium for the very fast separation of polymers Comparison of the chromatographic properties of the monolithic rod with columns packed with porous and non-porous beads in high-performance liquid chromatography of polystyrenes.* Journal of Chromatography A, 1996. **752**(1): p. 59-66.

93. Kirkland, J.J. and J.J. DeStefano, *The art and science of forming packed analytical high-performance liquid chromatography columns.* Journal of Chromatography A, 2006. **1126**(1–2): p. 50-57.

94. Cheng, J.H.-C., *Packing and Quality Control of a Chromatography Column*, in *Bioprocessing Network Annual Conference 2009* 2009: Brisbane, Australia.

95. Lottes, F., et al., *Hydrodynamic impact of particle shape in slurry packed liquid chromatography columns.* Journal of Chromatography A, 2009. **1216**(30): p. 5687-5695.

96. Svec, F., T.B. Tennikova, and Z. Deyl, *Monolithic Materials: Preparation, Properties and Applications*. 2003: Elsevier Science.

97. Mallik, R. and D.S. Hage, *Affinity monolith chromatography.* Journal of Separation Science, 2006. **29**(12): p. 1686-1704.

98. Lipson, H. and M. Kurman, *Fabricated: The New World of 3D Printing*. 2013: Wiley.

99. Yang, Y., et al., *3D printing of shape memory polymer for functional part fabrication.* The International Journal of Advanced Manufacturing Technology, 2016. **84**(9): p. 2079-2095.

100. Gaal, G., et al., *Simplified fabrication of integrated microfluidic devices using fused deposition modeling 3D printing.* Sensors and Actuators B: Chemical, 2017. **242**: p. 35-40.

101. Goodship, V.D., B. Middleton, and R. Cherrington, *Design and Manufacture of Plastic Components for Multifunctionality: Structural Composites, Injection Molding, and 3D Printing*. 2015: Elsevier Science.

102. Bártolo, P.J., *Stereolithography: Materials, Processes and Applications*. 2011: Springer US.

103. Limited, E.G.P., *A Focus on SLM and SLS Methods in 3D Printing*. 2015: Emerald Group Publishing Limited.

104. Gibson, I., D. Rosen, and B. Stucker, *Additive Manufacturing Technologies: 3D Printing, Rapid Prototyping, and Direct Digital Manufacturing*. 2014: Springer New York.

105. Ladyzhenskaya, O.A., *Sixth problem of the millennium: Navier-Stokes equations, existence and smoothness.* Russian Mathematical Surveys, 2003. **58**(2): p. 251-286.

106. Sarrate, J. and M. Staten, *Proceedings of the 22nd International Meshing Roundtable*. 2013: Springer International Publishing.

107. Dellar, P.J., *Incompressible limits of lattice Boltzmann equations using multiple relaxation times.* Journal of Computational Physics, 2003. **190**(2): p. 351-370.

108. Wolf-Gladrow, D.A., *Lattice-Gas Cellular Automata and Lattice Boltzmann Models: An Introduction*. 2004: Springer Berlin Heidelberg.

109. Zou, Q. and X. He, *On pressure and velocity flow boundary conditions and bounceback for the lattice Boltzmann BGK model.* Open Access, 1996.

110. Wang, M. and Q. Kang, *Modeling electrokinetic flows in microchannels using coupled lattice Boltzmann methods.* Journal of Computational Physics, 2010. **229**(3): p. 728-744.

111. Safi, M.A., N. Prasianakis, and S. Turek, *Benchmark computations for 3D two-phase flows: A coupled lattice Boltzmann-level set study.* Computers & Mathematics with Applications, 2017. **73**(3): p. 520-536.

112. De Rosis, A., et al., *Aeroelastic study of flexible flapping wings by a coupled lattice Boltzmann-finite element approach with immersed boundary method.* Journal of Fluids and Structures, 2014. **49**: p. 516-533.

113. Succi, S., *The Lattice Boltzmann Equation: For Fluid Dynamics and Beyond*. 2001: Clarendon Press.

114. Gogolin, A.O., E.G. Tsitsishvili, and A. Komnik, *Lectures on Complex Integration*. 2013: Springer International Publishing.

115. Reider, M.B. and J.D. Sterling, *Accuracy of discrete-velocity BGK models for the simulation of the incompressible Navier-Stokes equations.* Computers & Fluids, 1995. **24**(4): p. 459-467.

116. He, X. and L.-S. Luo, *A priori derivation of the lattice Boltzmann equation.* Physical Review E, 1997. **55**(6): p. R6333.

117. Pan, C., L.-S. Luo, and C.T. Miller, *An evaluation of lattice Boltzmann schemes for porous medium flow simulation.* Computers & Fluids, 2006. **35**(8–9): p. 898-909.

118. Dellar, P.J., *Lattice Boltzmann algorithms without cubic defects in Galilean invariance on standard lattices.* Journal of Computational Physics, 2014. **259**: p. 270-283.

119. Scagliarini, A., et al., *Lattice Boltzmann methods for thermal flows: Continuum limit and applications to compressible Rayleigh Taylor systems.* Physics of Fluids, 2010. **22**(5): p. 055101.

120. Elhadidi, B. and H.E. Khalifa, *Comparison of coarse grid lattice Boltzmann and Navier Stokes for real time flow simulations in rooms.* Building Simulation, 2013. **6**(2): p. 183-194.

121. Xiong, S., et al., *Numerical simulation of compressible turbulent flow via improved gas-kinetic BGK scheme.* International Journal for Numerical Methods in Fluids, 2011. **67**(12): p. 1833-1847.

122. Servan-Camas, B. and F. Tsai. *Lattice Boltzmann Method for Heterogeneous and Anisotropic Advection-Dispersion Equation in Porous Medium Flow*. in *AGU Fall Meeting Abstracts*. 2007.

123. Leonard, B.P., *The ULTIMATE conservative difference scheme applied to unsteady one-dimensional advection.* Computer Methods in Applied Mechanics and Engineering, 1991. **88**(1): p. 17-74.

124. Servan-Camas, B. and F.T.C. Tsai, *Non-negativity and stability analyses of lattice Boltzmann method for advection–diffusion equation.* Journal of Computational Physics, 2009. **228**(1): p. 236-256.

125. Steam, T.I.A.f.t.P.o.W.a., *Release on the IAPWS Formulation 2008 for the Viscosity of Ordinary Water Substance* 2008.

126. Nguyen, N.T., *Micromixers: Fundamentals, Design and Fabrication*. 2011: Elsevier Science.

127. Tyn, M.T. and T.W. Gusek, *Prediction of diffusion coefficients of proteins.* Biotechnology and Bioengineering, 1990. **35**(4): p. 327-338.

128. Kaviany, M., *Essentials of Heat Transfer: Principles, Materials, and Applications*. 2011: Cambridge University Press.

129. Rodríguez, H., et al., *Apparent Molar Volume, Isentropic Compressibility, Refractive Index, and Viscosity of DL-Alanine in Aqueous NaCl Solutions.* Journal of Solution Chemistry, 2003. **32**(1): p. 53-63.

130. Schmidt, E. and U. Grigull, *Properties of water and steam in SI-units: Thermodyamische Eigenschaften von Wasser und Wasserdampf : 0-800 C, 0-1000bar*. 2., rev. and updat printing ed. 1979, Berlin: Springer.

131. Salamon, P., D. Fernàndez-Garcia, and J.J. Gómez-Hernández, *Modeling mass transfer processes using random walk particle tracking.* Water resources research, 2006. **42**(11): p. W11417.

132. Vreugdenhil, C.B. and B. Koren, *Numerical Methods for Advection - Diffusion Problems*. 1993: Vieweg Friedr. + Sohn Ver.

133. Hassan, A.E. and M.M. Mohamed, *On using particle tracking methods to simulate transport in single-continuum and dual continua porous media.* Journal of Hydrology, 2003. **275**(3–4): p. 242-260.

134. Yoshida, H. and M. Nagaoka, *Multiple-relaxation-time lattice Boltzmann model for the convection and anisotropic diffusion equation.* Journal of computational physics, 2010. **229**(20): p. 7774-7795.

135. Chai, Z., B. Shi, and Z. Guo, *A Multiple-Relaxation-Time Lattice Boltzmann Model for General Nonlinear Anisotropic Convection–Diffusion Equations.* Journal of Scientific Computing, 2016. **69**(1): p. 355-390.

136. Kuzmin, A., I. Ginzburg, and A.A. Mohamad, *The role of the kinetic parameter in the stability of two-relaxation-time advection–diffusion lattice Boltzmann schemes.* Computers & Mathematics with Applications, 2011. **61**(12): p. 3417-3442.

137. Servan-Camas, B. and F.T.C. Tsai, *Lattice Boltzmann method with two relaxation times for advection–diffusion equation: Third order analysis and stability analysis.* Advances in Water Resources, 2008. **31**(8): p. 1113-1126.

138. Suga, K., et al., *A D3Q27 multiple-relaxation-time lattice Boltzmann method for turbulent flows.* Computers & mathematics with applications (1987), 2015. **69**(6): p. 518-529.

139. Ginzburg, I., F. Verhaeghe, and D. d'Humieres, *Two-relaxation-time lattice Boltzmann scheme: About parametrization, velocity, pressure and mixed boundary conditions.* Communications in computational physics, 2008. **3**(2): p. 427-478.

140. Ginzburg, I., D. d'Humières, and A. Kuzmin, *Optimal Stability of Advection-Diffusion Lattice Boltzmann Models with Two Relaxation Times for Positive/Negative Equilibrium.* Journal of Statistical Physics, 2010. **139**(6): p. 1090-1143.

141. Batôt, G., et al., *Analytical and numerical investigation of the advective and dispersive transport in Herschel–Bulkley fluids by means of a Lattice–Boltzmann Two-Relaxation-Time scheme.* Chemical Engineering Science, 2016. **141**: p. 271-281.

142. Liu, Q., et al., *A multiple-relaxation-time lattice Boltzmann model for convection heat transfer in porous media.* International Journal of Heat and Mass Transfer, 2014. **73**: p. 761-775.

143. Ginzburg, I., *Multiple anisotropic collisions for advection–diffusion Lattice Boltzmann schemes.* Advances in Water Resources, 2013. **51**: p. 381-404.

144. Ginzburg, I., *Equilibrium-type and link-type lattice Boltzmann models for generic advection and anisotropic-dispersion equation.* Advances in Water Resources, 2005. **28**(11): p. 1171-1195.

145. de Lemos, M.J.S., *Turbulence in Porous Media: Modeling and Applications*. 2012: Elsevier Science.

146. Barrande, M., R. Bouchet, and R. Denoyel, *Tortuosity of Porous Particles.* Analytical Chemistry, 2007. **79**(23): p. 9115-9121.

147. Ghanbarian, B., et al., *Tortuosity in Porous Media: A Critical Review.* Soil Science Society of America Journal, 2013. **77**(5): p. 1461.

148. Matyka, M., Z. Koza, and K. Vafai. *How to calculate tortuosity easily?* in *AIP Conference Proceedings 4*. 2012. AIP.

149. Latt, J., *Choice of units in lattice Boltzmann simulations.* Freely available online at http://lbmethod. org/_media/howtos: lbunits. pdf, 2008.

150. Allgower, E.L., et al., *A Mesh-Independence Principle for Operator Equations and Their Discretizations.* SIAM Journal on Numerical Analysis, 1986. **23**(1): p. 160-169.

151. Baranau, V. and U. Tallarek, *Random-close packing limits for monodisperse and polydisperse hard spheres.* Soft Matter, 2014. **10**(21): p. 3826-3841.

152. Flowkit. *Course Materials*. in *Palabos Training Course*. 2014. Laussane, Switzerland: FlowKit Ltd.

153. Krüger, T. *Unit conversion in LBM*. in *LBM Workshop 2011*.

154. Mueller, J.D., *Essentials of Computational Fluid Dynamics*. 2015: CRC Press.

155. Day, M.A., *The no-slip condition of fluid dynamics.* Erkenntnis, 1990. **33**(3): p. 285-296.

156. Rosenhead, L., *Laminar boundary layers: an account of the development, structure, and stability of laminar boundary layers in incompressible fluids, together with a description of the associated experimental techniques*. 1963: Clarendon Press.

157. Chen, L., et al., *A comparative study of lattice Boltzmann methods using bounce-back schemes and immersed boundary ones for flow acoustic problems.* International Journal for Numerical Methods in Fluids, 2014. **74**(6): p. 439-467.

158. Husain, S.Z. and J.M. Floryan, *Spectrally-accurate algorithm for moving boundary problems for the Navier–Stokes equations.* Journal of Computational Physics, 2010. **229**(6): p. 2287-2313.

159. Ginzbourg, I. and P.M. Adler, *Boundary flow condition analysis for the three-dimensional lattice Boltzmann model.* J. Phys. II France, 1994. **4**(2): p. 191-214.

160. Dai, Q. and L. Yang, *LBM numerical study on oscillating flow and heat transfer in porous media.* Applied Thermal Engineering, 2013. **54**(1): p. 16-25.

161. Manjhi, N., et al., *Simulation of 3D velocity and concentration profiles in a packed bed adsorber by lattice Boltzmann methods.* Chemical Engineering Science, 2006. **61**(23): p. 7754-7765.

162. Levesque, M., et al., *Accounting for adsorption and desorption in lattice Boltzmann simulations.* Physical Review E, 2013. **88**(1): p. 013308.

163. Zhou, L., et al., *Lattice Boltzmann simulation of gas–solid adsorption processes at pore scale level.* Journal of Computational Physics, 2015. **300**: p. 800-813.

164. Jung, S., et al., *Determination of the interparticle void volume in packed beds via intraparticle Donnan exclusion.* Journal of Chromatography A, 2010. **1217**(5): p. 696-704.

165. Gritti, F. and G. Guiochon, *Effect of the surface coverage of -bonded silica particles on the obstructive factor and intraparticle diffusion mechanism.* Chemical Engineering Science, 2006. **61**(23): p. 7636-7650.

166. Aveyard, R. and D.A. Haydon, *An Introduction to the Principles of Surface Chemistry*. 1973: Cambridge University Press.

167. Ruthven, D.M., *Principles of Adsorption and Adsorption Processes*. 1984: Wiley.

168. Liu, Y. and L. Shen, *From Langmuir kinetics to first- and second-order rate equations for adsorption.* Langmuir : the ACS journal of surfaces and colloids, 2008. **24**(20): p. 11625-11630.

169. Klaewkla, R., M. Arend, and W.F. Hoelderich, *A review of mass transfer controlling the reaction rate in heterogeneous catalytic systems*. Vol. 5. 2011: INTECH Open Access Publisher.

170. Fish, J., *Multiscale Methods: Bridging the Scales in Science and Engineering*. 2010: OUP Oxford.

171. Sassoli de Bianchi, M., *The Observer Effect.* Foundations of Science, 2013. **18**(2): p. 213-243.

172. Levenspiel, O., *Chemical reaction engineering.* Industrial & engineering chemistry research, 1999. **38**(11): p. 4140-4143.

173. Ham, B.M. and A. MaHam, *Analytical Chemistry: A Chemist and Laboratory Technician's Toolkit*. 2015: Wiley.

174. Jamshed, S., *Using HPC for computational fluid dynamics: a guide to high performance computing for CFD engineers*. 2015, Amsterdam: Elsevier/Academic Press.

175. Berry, M.W., et al., *High-Performance Scientific Computing: Algorithms and Applications*. 2012: Springer London.

176. Overill, R., *Parallel Processing and Parallel Algorithms: Theory and Computation.* Journal of Logic and Computation, 2001. **11**(2): p. 355.

177. FlowKit. *Palabos Benchmarks*. 2011 [cited 2016.

178. Mehrotra, P., et al., *Performance evaluation of Amazon EC2 for NASA HPC applications*, in *Proceedings of the 3rd workshop on Scientific Cloud Computing Date*. 2012, ACM: Delft, The Netherlands. p. 41-50.

179. Bespalko, D., A. Pollard, and M. Uddin, *Direct Numerical Simulation of Fully-Developed Turbulent Channel Flow Using the Lattice Boltzmann Method and Analysis of OpenMP Scalability*, in *High Performance Computing Systems and Applications: 23rd International Symposium, HPCS 2009, Kingston, ON, Canada, June 14-17, 2009, Revised Selected Papers*, D.J.K. Mewhort, et al., Editors. 2010, Springer Berlin Heidelberg: Berlin, Heidelberg. p. 1-19.

180. Maier, R.S. and R.S. Bernard, *Lattice-Boltzmann accuracy in pore-scale flow simulation.* Journal of Computational Physics, 2010. **229**(2): p. 233-255.

181. Zick, A.A. and G.M. Homsy, *Stokes flow through periodic arrays of spheres.* Journal of Fluid Mechanics, 2006. **115**: p. 13-26.

182. Sangani, A.S. and A. Acrivos, *Slow flow through a periodic array of spheres.* International Journal of Multiphase Flow, 1982. **8**(4): p. 343-360.

183. Frankel, I. and H. Brenner, *On the foundations of generalized Taylor dispersion theory.* Journal of Fluid Mechanics, 2006. **204**: p. 97-119.

184. Giddings, J.C., *Dynamics of Chromatography: Principles and Theory*. 2002: Taylor & Francis.

185. Schure, M.R., et al., *Simulation of packed-bed chromatography utilizing high-resolution flow fields: comparison with models.* Analytical chemistry, 2002. **74**(23): p. 6006-6016.

186. Askeland, D.R. and W.J. Wright, *Essentials of Materials Science & Engineering, SI Edition*. 2013: Cengage Learning.

187. Tilley, R.J.D., *Understanding Solids: The Science of Materials*. 2013: Wiley.

188. Nawada, S., S. Dimartino, and C.J. Fee, *The Effects of bead overlap on chromatographic performance in 3D printed packed bed columns.* International Labmate, 2014.

189. Salomon, D., *Computer Graphics and Geometric Modeling*. 2012: Springer New York.

190. Carta, G. and A. Jungbauer, *Protein chromatography: Process Development and Scale-up*. 2010, Hoboken, New Jersey, USA: John Wiley & Sons.

191. Tallarek, U., et al., *Measurement of transverse and axial apparent dispersion coefficients in packed beds.* AIChE Journal, 1996. **42**(11): p. 3041-3054.

192. Daneyko, A., et al., *From random sphere packings to regular pillar arrays: Analysis of transverse dispersion.* Journal of Chromatography A, 2012. **1257**: p. 98-115.

193. O'Toole, P.I. and T.S. Hudson, *New High-Density Packings of Similarly Sized Binary Spheres.* The Journal of Physical Chemistry C, 2011. **115**(39): p. 19037-19040.

194. Desmet, G., et al., *Merging Open-Tubular and Packed Bed Liquid Chromatography.* Analytical Chemistry, 2015. **87**(14): p. 7382-7388.

195. Wadell, H., *Volume, Shape, and Roundness of Quartz Particles.* The Journal of Geology, 1935. **43**(3): p. 250-280.

196. Guo, X., J. Lin, and D. Nie, *New formula for drag coefficient of cylindrical particles.* Particuology, 2011. **9**(2): p. 114-120.

197. Yow, H.N., M.J. Pitt, and A.D. Salman, *Drag correlations for particles of regular shape.* Advanced Powder Technology, 2005. **16**(4): p. 363-372.

198. Zastawny, M., et al., *Derivation of drag and lift force and torque coefficients for non-spherical particles in flows.* International Journal of Multiphase Flow, 2012. **39**: p. 227-239.

199. Maier, R.S., D.M. Kroll, and H.T. Davis, *Diameter-dependent dispersion in packed cylinders.* AIChE Journal, 2007. **53**(2): p. 527-530.

200. Cohen, Y. and A.B. Metzner, *Wall effects in laminar flow of fluids through packed beds.* AIChE Journal, 1981. **27**(5): p. 705-715.

201. Billingham, J.F.T., NY), Lockett, Michael James (Grand Island, NY), *Distillation column employing structured packing which reduces wall flow*. 1997, Praxair Technology, Inc. (Danbury, CT): United States.

202. Sunder, S.A., PA), *Mixed-resistance structured packing*. 2003, Air Products and Chemicals, Inc. (Allentown, PA): United States.

203. Knox, J.H., G.R. Laird, and P.A. Raven, *Interaction of radial and axial dispersion in liquid chromatography in relation to the "infinite diameter effect".* Journal of Chromatography A, 1976. **122**: p. 129-145.

204. Gu, T., *Mathematical Modeling and Scale-Up of Liquid Chromatography: With Application Examples*. 2015: Springer International Publishing.

205. Khirevich, S., et al., *Geometrical and topological measures for hydrodynamic dispersion in confined sphere packings at low column-to-particle diameter ratios.* Journal of Chromatography A, 2012. **1262**: p. 77-91.

206. Rennels, D.C. and H.M. Hudson, *Pipe Flow: A Practical and Comprehensive Guide*. 2012: Wiley.

207. Unger, K.K., R. Skudas, and M.M. Schulte, *Particle packed columns and monolithic columns in high-performance liquid chromatography-comparison and critical appraisal.* Journal of Chromatography A, 2008. **1184**(1): p. 393-415.

208. Guiochon, G., *Monolithic columns in high-performance liquid chromatography.* Journal of Chromatography A, 2007. **1168**(1): p. 101-168.

209. Williams, J.L., *Monolith structures, materials, properties and uses.* Catalysis Today, 2001. **69**(1): p. 3-9.

210. Inoue, H., et al., *Synthesis and cation exchange properties of a new porous cation exchange resin having an open-celled monolith structure.* Polymer, 2004. **45**(1): p. 3-7.

211. Chu, Y., et al., *Preparation of poly (L-lactic acid) with aligned structures by unidirectional freezing.* Polymers for advanced technologies, 2015. **26**(6): p. 606-612.

212. Koku, H., et al., *Modeling of flow in a polymeric chromatographic monolith.* Journal of Chromatography A, 2011. **1218**(22): p. 3466-3475.

213. Schwarz, H.A., *Gesammelte mathematische abhandlungen*. 1890: J. Springer.

214. Neovius, E.R., *Bestimmung zweier speciellen periodischen Minimalflächen: auf welchen unendlich viele gerade linien und unendlich viele ebene geodätische Linien liegen*. 1883: J.C. Frenckell & sohn.

215. Yan, C., et al., *Ti-6Al-4V triply periodic minimal surface structures for bone implants fabricated via selective laser melting.* Journal of the mechanical behavior of biomedical materials, 2015. **51**: p. 61-73.

216. Jung, Y. and S. Torquato, *Fluid permeabilities of triply periodic minimal surfaces.* Physical Review E, 2005. **72**(5): p. 056319.

217. Afshar, M., et al., *Additive manufacturing and mechanical characterization of graded porosity scaffolds designed based on triply periodic minimal surface architectures.* Journal of the mechanical behavior of biomedical materials, 2016. **62**: p. 481-494.

218. Abueidda, D.W., et al., *Effective conductivities and elastic moduli of novel foams with triply periodic minimal surfaces.* Mechanics of Materials, 2016. **95**: p. 102-115.

219. Lee, D.-W., K.A. Khan, and R.K. Abu Al-Rub, *Stiffness and yield strength of architectured foams based on the Schwarz Primitive triply periodic minimal surface.* International Journal of Plasticity, 2017. **95**: p. 1-20.

220. Meeks, W. and J. Pérez, *A Survey on Classical Minimal Surface Theory*. 2012: American Mathematical Society.

221. Pérez, J. and A. Ros, *The space of properly embedded minimal surfaces with finite total curvature.* Indiana University Mathematics Journal, 1996: p. 177-204.

222. Lidin, S. and S. Larsson, *Bonnet transformation of infinite periodic minimal surfaces with hexagonal symmetry.* Journal of the Chemical Society, Faraday Transactions, 1990. **86**(5): p. 769-775.

223. Brakke, K.A., *The surface evolver.* Experiment. Math., 1992. **1**(2): p. 141-165.

224. Hirzebruch, F.E.P. and M. Kreck, *On the concept of genus in topology and complex analysis.* Notices of the American Mathematical Society, 2009. **56**(6): p. 713-719.

225. Jung, Y., K.T. Chu, and S. Torquato, *A variational level set approach for surface area minimization of triply-periodic surfaces.* Journal of Computational Physics, 2007. **223**(2): p. 711-730.

226. Heibel, A.K., F. Kapteijn, and J. Moulijn, *Flooding Performance of Square Channel Monolith Structures.* Industrial & Engineering Chemistry Research, 2002. **41**(26): p. 6759-6771.

227. Wang, L.K., et al., *Environmental Bioengineering*. 2010: Humana Press.

228. Renkin, E.M., *Filtration, diffusion, and molecular sieving through porous cellulose membranes.* The Journal of general physiology, 1954. **38**(2): p. 225-243.

229. Bertsekas, D.P. and W. Rheinboldt, *Constrained Optimization and Lagrange Multiplier Methods*. 2014: Elsevier Science.

230. Nfor, B.K., et al., *High-throughput protein precipitation and hydrophobic interaction chromatography: Salt effects and thermodynamic interrelation.* Journal of Chromatography A, 2011. **1218**(49): p. 8958-8973.

231. Barnett, G.V., et al., *Aggregate structure, morphology and the effect of aggregation mechanisms on viscosity at elevated protein concentrations.* BIOPHYSICAL CHEMISTRY, 2015. **207**: p. 21-29.

232. Bauer, K.C., et al., *Impact of additives on the formation of protein aggregates and viscosity in concentrated protein solutions.* INTERNATIONAL JOURNAL OF PHARMACEUTICS, 2017. **516**(1-2): p. 82-90.

Appendices

Appendix A: Illustration of Chromatographic Model

This appendix is designed to increase comprehension of the chromatographic model which was developed from this work. First, it is important to understand which image relates to which component of the chromatographic process. From top to bottom and then left to right, each panel of all images is as follows: a) inert species in the mobile phase, b) selected species in the mobile phase, c) adsorbed species, d) inert species in the pores of the stationary phase, e) selected species in the pores of the stationary phase, f) eluent species, g) process chromatogram and h) stationary phase morphology. Furthermore, the vertical line on the chromatogram represents the current time of the snapshot. Initially, t = 0 as in Fig. A.1.

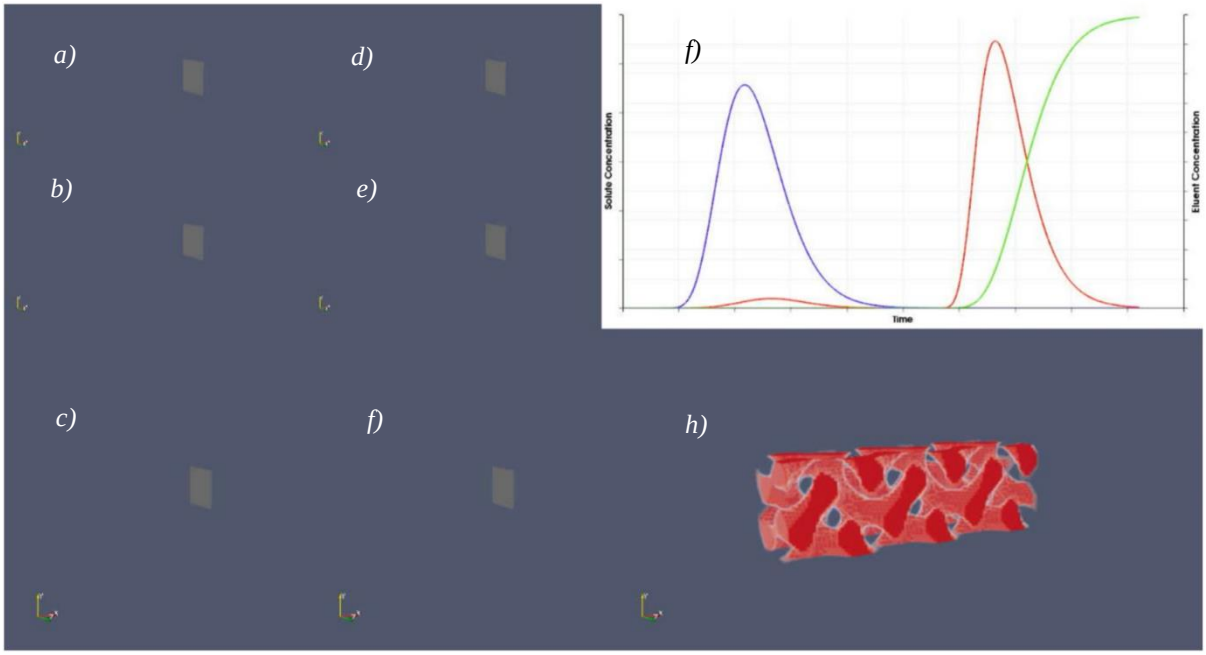

Fig. A.1. The chromatographic system at t = 0. Each panel represents: a) inert species in the mobile phase, b) selected species in the mobile phase, c) adsorbed species, d) inert species in the pores of the stationary phase, e) selected species in the pores of the stationary phase, f) eluent species, g) process chromatogram and h) stationary phase morphology.

As time begins, the inert species passes through the column, as denoted by the blue peak on the chromatogram (Fig. A. 2).

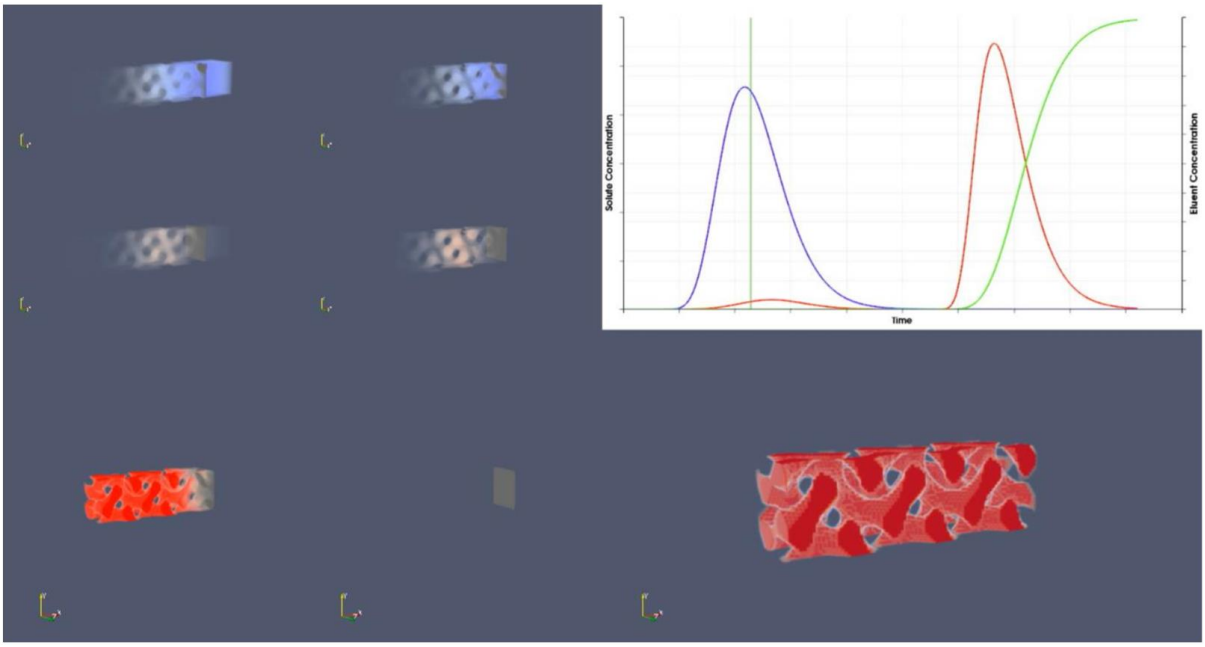

Fig. A.2. The chromatographic system as the inert species exits the column.

Most of the selected species is adsorbed onto the stationary phase, but there is a small amount of premature breakthrough of the selected species, because the medium is too short to adsorb this solute before it exits the column. After the inert species has exited the column, the only solute within the column is bound to the stationary phase (Fig. A.3).

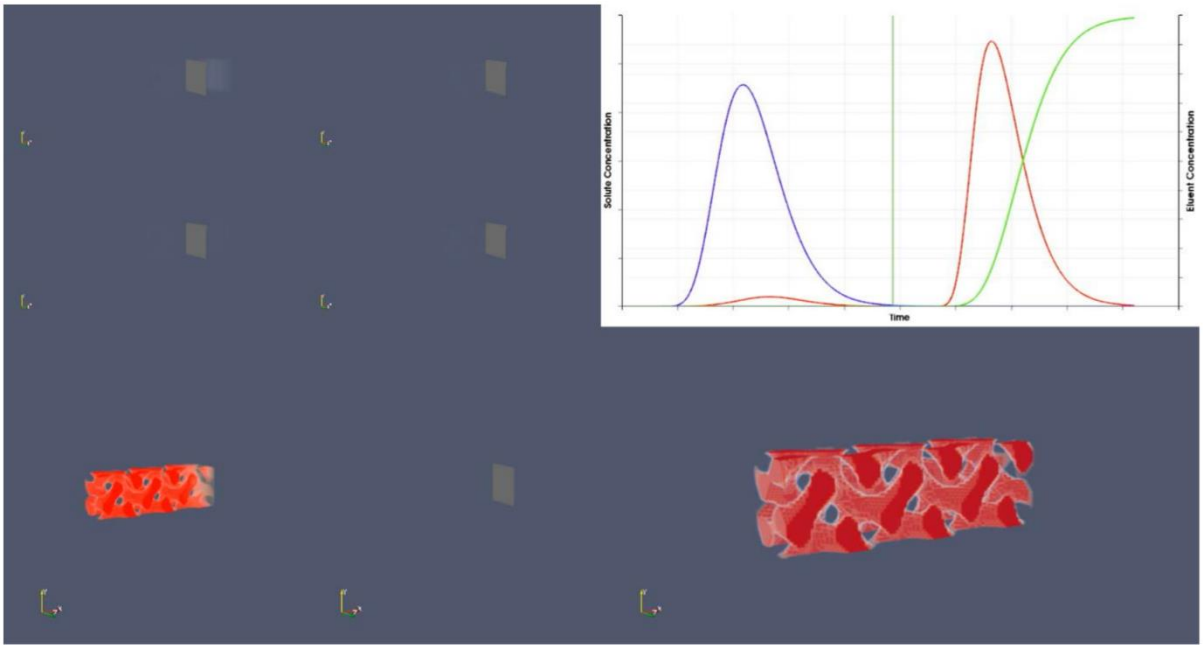

Fig. A.3. The chromatographic system when the selected species is bound to the column.

The eluent is then introduced into the column, this desorbs the selected species, which then diffuses back into the mobile phase and is eluted from the column (Fig. A.4).

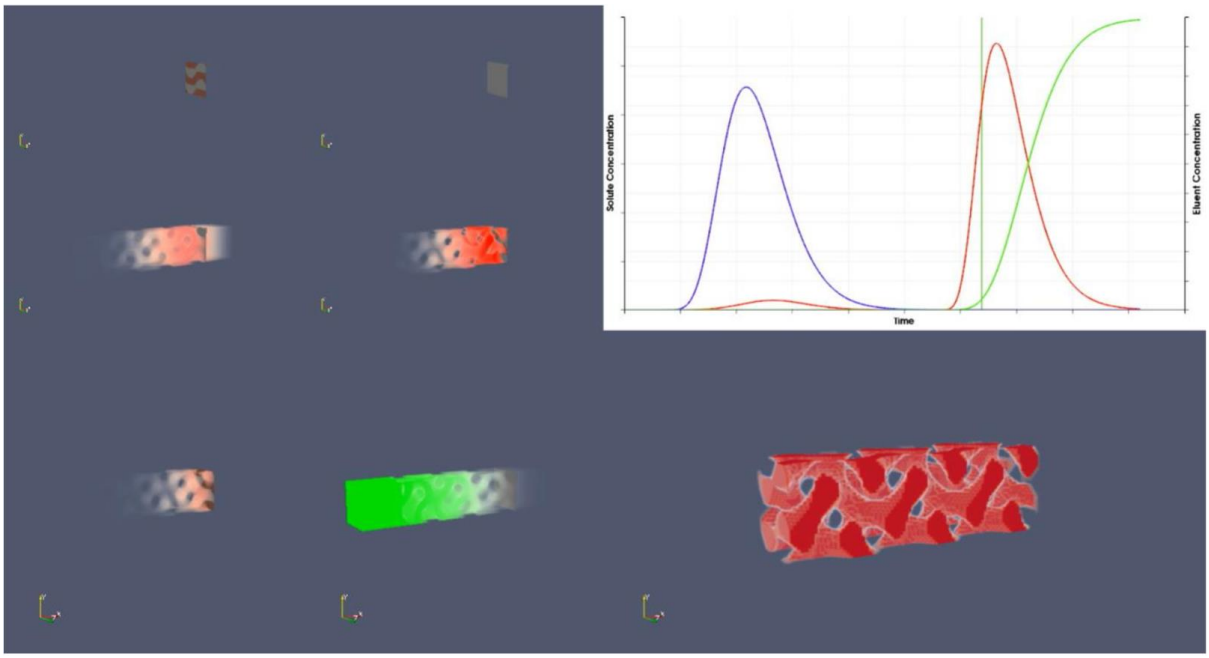

Fig. A.4. The chromatographic system as the selected species is desorbed and eluted from the column.

Finally, all solute species has been eluted from the column and only the eluent species remains, giving a complete separation of the two species, ignoring the premature breakthrough of the selected species (which is intentional for this illustration) (Fig. A.5).

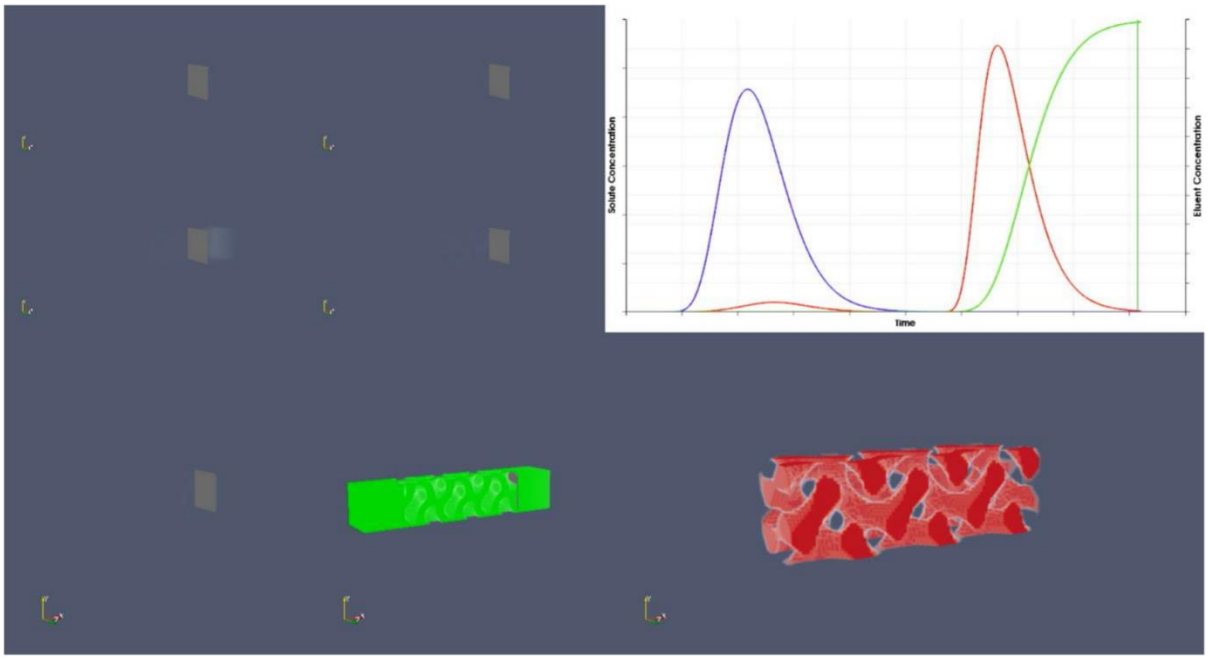

Fig. A.5. The chromatographic system after a completed separation.

Appendix B: List of Figures

Appendix C: List of Tables

Appendix D: Supplementary Resources

Both the code base and all results from this work (in spreadsheet form) are appended to this thesis, within the university database. Before attempting to use the code, please consult the README file.